



July 19, 1995

Approved for public release,  
distribution unlimited

322 Spedding Hall  
Iowa State University  
Ames, IA 50011

Professor Peele  
Southeastern Center for Electrical  
Engineering Education  
1101 Massachusetts Avenue  
St. Cloud, FL 34769

Dear Professor Peele:

Enclosed is a copy of my Ph.D. dissertation as required by the terms of the NDSEG Fellowship which expired on 2/28/95. I will graduate this summer on August 5, 1995. If desired, I could send a copy of my diploma or final transcript when they become available in mid August.

I plan to continue my dissertation research at Ames Laboratory as a postdoctoral associate for at least a year. I am currently finishing six manuscripts for publication, and additional research will likely lead to at least three more manuscripts. Following the postdoctoral associate appointment, I would prefer to secure a job in industry. I may eventually move into academia, but I strongly believe that "real-world" experience is important for a professor to incorporate practical aspects into classroom education.

I would like to thank SCEE and AFOSR for the support and administration of the fellowship. It has provided me with a unique opportunity to collaborate with the Materials Laboratory at Wright-Patterson AFB and the High Temperature Materials Laboratory at Oak Ridge National Laboratory. The generous terms of the fellowship certainly have provided for a more enjoyable graduate school experience by alleviating many financial concerns. I am excited to begin my professional career as a research scientist, and this program has made an important contribution to my education and training.

Based on my experience, I strongly support this fellowship program and urge its future continuation.

Sincerely,

*Andrew J. Thom*

Andrew J. Thom

JUL 21 1995  
am

Oxidation studies on small atom doped  $\text{Ti}_5\text{Si}_3$


by

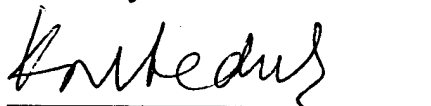
Andrew Jason Thom

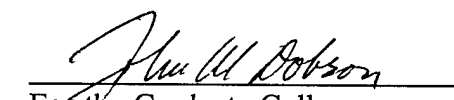
A Dissertation Submitted to the  
Graduate Faculty in Partial Fulfillment of the  
Requirements for the Degree of  
DOCTOR OF PHILOSOPHY

Department: Materials Science and Engineering  
Major: Ceramic Engineering

Approved:

  
In-Charge of Major Work

  
For the Major Department

  
For the Graduate College

Iowa State University  
Ames, Iowa

1995

## TABLE OF CONTENTS

CHAPTER 1: GENERAL INTRODUCTION	1
I. Dissertation Organization	1
II. Background	3
III. Literature Review	5
1. Oxidation of Titanium	5
2. Oxidation of Silicon	9
3. Oxidation of $Ti_5Si_3$	14
4. Oxidation of Other Engineering Materials	15
References	20
CHAPTER 2: SINGLE CRYSTAL STUDIES OF $Ti_5Si_3Z_X$	24
Abstract	24
I. Introduction	25
II. Experimental	30
III. Results	32
1. Chemical Analysis	32
2. Room Temperature Lattice Parameters	34
3. Single Crystal Results	40
IV. Discussion	42
V. Conclusions	44
Acknowledgements	45
References	45
CHAPTER 3: THERMAL EXPANSION ANISOTROPY OF $Ti_5Si_3$	49
Abstract	49
I. Introduction	50
II. Experimental	52
III. Results and Discussion	54
IV. Conclusions	62
Acknowledgements	62
References	62
CHAPTER 4: EFFECT OF PROCESSING ON OXIDATION OF $Ti_5Si_3$	64
Abstract	64



I. Introduction	65
II. Experimental	65
III. Results and Discussion	66
IV. Conclusions	73
Acknowledgements	73
References	73
 CHAPTER 5: IMPROVED OXIDATION RESISTANCE OF $\text{Ti}_5\text{Si}_3$ BY SMALL ATOM DOPING	 75
Abstract	75
I. Introduction	76
II. Experimental	77
III. Results	80
1. Composition and Structure	80
2. Oxidation of Undoped $\text{Ti}_5\text{Si}_3$	82
3. Oxidation of Carbon-Doped $\text{Ti}_5\text{Si}_3$	87
4. Oxidation of Boron-Doped $\text{Ti}_5\text{Si}_3$	91
5. Oxidation of Nitrogen-Doped $\text{Ti}_5\text{Si}_3$	93
6. Oxidation of Oxygen-Doped $\text{Ti}_5\text{Si}_3$	97
IV. Discussion	103
1. Grain Size Effects on Oxidation of Undoped $\text{Ti}_5\text{Si}_3$	103
2. Oxidation Kinetics of $\text{Ti}_5\text{Si}_3\text{C}_x$	105
3. Scale Development in $\text{Ti}_5\text{Si}_3\text{Z}_x$ ( $\text{Z}=\text{B},\text{C}$ )	109
4. Scale Development in $\text{Ti}_5\text{Si}_3\text{Z}_x$ ( $\text{Z}=\text{O},\text{N}$ )	112
V. Conclusions	112
Acknowledgements	113
References	113
 CHAPTER 6: GENERAL CONCLUSION	 117
I. Oxidation Behavior of $\text{Ti}_5\text{Si}_3\text{Z}_x$	117
II. Interstitial Chemistry of $\text{Ti}_5\text{Si}_3\text{Z}_x$	118
III. Thermal Expansion Anisotropy of $\text{Ti}_5\text{Si}_3\text{Z}_x$	119
IV. Future Research	120
1. Mechanical Properties of $\text{Ti}_5\text{Si}_3\text{Z}_x$	120
2. Characterization of Other $\text{A}_5\text{Si}_3\text{Z}_x$ Systems	121
3. Oxidation of Micro-Doped $\text{Ti}_5\text{Si}_3$	121
References	121
 ACKNOWLEDGEMENTS	 123

APPENDIX A: INTERSTITIAL CHEMISTRY EFFECTS ON PROCESSING OF $\text{Ti}_5\text{Si}_3$	124
APPENDIX B: SYNTHESIS, PROCESSING, AND PROPERTIES OF $\text{Ti}_5\text{Si}_3$	153
APPENDIX C: EVALUATION OF $\text{A}_5\text{Si}_3\text{Z}_x$ INTERMETALLICS FOR USE AS HIGH TEMPERATURE STRUCTURAL MATERIALS	183

## CHAPTER 1: GENERAL INTRODUCTION

### I. Dissertation Organization

This dissertation is organized in an alternate format. Several papers which have already been published or are to be submitted for publication have been included as separate chapters. Although the title of the dissertation implies concentration on oxidation behavior, the included papers discuss a broad range of topics. Chapter 1 is a general introduction which describes the dissertation organization, discusses the background motivation for the research, and reviews literature pertinent to Ti-Si oxidation. Chapter 2 is a paper entitled "Single Crystal Studies of  $\text{Ti}_5\text{Si}_3\text{Z}_x$ " which is to be submitted to *Journal of Materials Research* for publication<sup>1</sup>. Chapter 2 describes the synthesis and characterization of material used in the dissertation research. Victor Young, a crystallographer now working at the University of Minnesota, is listed as a co-author because of his contributions in the collection of the single crystal x-ray data.

Some general material properties of  $\text{Ti}_5\text{Si}_3$  are discussed in Chapter 3, a paper entitled "Thermal Expansion Anisotropy of  $\text{Ti}_5\text{Si}_3$ " which has been published in *Journal of Materials Science Letters*<sup>2</sup>. Burl Cavin and Camden Hubbard are included as authors for their assistance during data collection which was performed by the dissertation author at the High Temperature Materials Laboratory at Oak Ridge National Laboratory.

Finally, oxidation resistance is discussed in Chapter 4 and Chapter 5. Chapter 4 is a paper entitled "Effect of Processing on Oxidation of  $\text{Ti}_5\text{Si}_3$ " and has been published in *Materials Research Society Symposium Proceedings*<sup>3</sup>. This paper describes the oxidative stability of undoped  $\text{Ti}_5\text{Si}_3$ . Finally, Chapter 5 is a paper entitled "Improved Oxidation

Resistance of  $\text{Ti}_5\text{Si}_3$  by Small Atom Doping" which is to be submitted to *Journal of Materials Science* for publication<sup>4</sup>.

General processing, ranging from synthesis of the intermetallic silicide to hot consolidation to yield dense, crack-free material, is discussed in Appendix A and Appendix B. Appendix A is a paper entitled "Interstitial Chemistry Effects on Processing of  $\text{Ti}_5\text{Si}_3$ " which is to be submitted to *Intermetallics* for publication<sup>5</sup>. This material has been listed as an appendix since the processing issues do not directly relate to oxidation resistance of  $\text{Ti}_5\text{Si}_3$ . Appendix B is a paper entitled "Synthesis, Processing, and Properties of  $\text{Ti}_5\text{Si}_3$ " which was published in *Processing and Fabrication of Advanced Materials for High Temperature Applications-II*<sup>6</sup>. This paper contains additional information on initial processing and consolidation efforts; however, since Youngman Kim was the primary author of the work, the paper is included as an appendix. Appendix B also gives cursory details of the mechanical properties of  $\text{Ti}_5\text{Si}_3$ . Initial results of doping effects on the oxidation resistance of  $\text{Ti}_5\text{Si}_3$  are discussed in Appendix C which is a paper entitled "Evaluation of  $\text{A}_5\text{Si}_3\text{Z}_x$  Intermetallics for Use as High Temperature Structural Materials" already published in *Processing and Fabrication of Advanced Materials-III*<sup>7</sup>. This was a review-type article incorporating recent experimental results, and both Youngman Kim and Mitch Meyer were included as co-authors because of their experimental contributions.

Dr. Mufit Akinc as major professor has been included as co-author on all of the papers included in this dissertation. His guidance and oversight have been crucial during this research.

## II. Background

This research arose from an effort to bridge the research of solid state chemists and material scientists. For several years, researchers at Ames Laboratory have been investigating an interesting class of binary intermetallic materials that have a demonstrated ability to incorporate substantial quantities of ternary additions while maintaining the structure of the host material<sup>8,9,10,11</sup>. This ability arises from the presence of interstices within the  $\text{Mn}_5\text{Si}_3$ -type structure of the host binary intermetallic which can accommodate a wide variety and amount of ternary elements. This research demonstrated marked effects on the structure of the host material, namely, changes in lattice constants and bond lengths as determined by careful structural studies. With the realization that these additions may also significantly affect material properties, a window of opportunity was presented to utilize this "doping" effect and determine the potential engineering usefulness of these materials. Approximately 175 binary intermetallic compounds are known to exist in the  $\text{Mn}_5\text{Si}_3$  structure<sup>12</sup>, and considering the substantial number of possible ternary alloying elements which could be added, one is presented with an overwhelming number of material systems for investigation. Fortunately from an engineering point of view, this field can be significantly narrowed by considering some of the critical material properties required for a particular type of application. High strength, stiffness, creep resistance, and oxidation resistance are needed for high temperature structural applications. Oxidation resistance at elevated temperatures limits the potential systems to those based on silicon, aluminum, and chromium since these systems have the potential to form passivating layers of silica, alumina, and chromia, respectively. Fleischer surveyed 293 binary intermetallic compounds with melting temperatures greater than  $1500^\circ\text{C}$ <sup>13</sup>. Melting temperature was chosen as a figure of merit based on the general rule of thumb

that the upper operating temperature for a monolithic material ranges from one-half to two-thirds of the absolute melting temperature<sup>14</sup>. Density was also selected as a critical material property for applications in which component mass is important, so that correlating density to melting temperature gives a useful method for ranking potential material systems. For a given melting temperature, materials with the lowest density are most desirable. This analysis indicates that in particular,  $\text{Ti}_5\text{Si}_3$  has an attractive combination of high melting temperature (2130°C) and low density (4.32 g/cm<sup>3</sup>).

Having been established as a potential high temperature structural material,  $\text{Ti}_5\text{Si}_3$  was selected for further investigation. Most investigations of potential high temperature structural materials are centered around the development of material systems for maximized mechanical performance. Oxidation resistance is most usually measured as a secondary result of the research, and a fundamental understanding of oxidation resistance is seldom achieved. If indeed any material is someday to be used as a structural material in oxidizing environments, an understanding of the oxidation mechanism is needed. Very little information exists in the literature on the oxidative properties of  $\text{Ti}_5\text{Si}_3$ , and no attempt has been made to exploit the ternary "doping" effect to substantially improve oxidation resistance as well as other properties including strength, fracture toughness, and creep resistance. The unique and novel aspect of this research is the intentional addition of ternary interstitial alloying elements, namely boron, carbon, nitrogen, and oxygen, with the stated goal of improving critical material properties such as oxidation resistance.

As a prelude to discussion of the dissertation research, a review of the literature pertinent to the current state of understanding of oxidation in the Ti-Si system is needed.

### III. Literature Review

Critical to any high temperature oxidation process are the diffusional processes responsible for growth of the resulting oxide scale. Therefore a review of the defect chemistry and oxidation of the major constituents titanium and silicon is included. Available literature on the oxidation of  $\text{Ti}_5\text{Si}_3$  is also discussed. Finally, oxidation of other engineering materials is reviewed.

#### 1. Oxidation of Titanium

##### *a. Defect chemistry*

During the oxidation of an engineering material, one or several of the components are oxidized. Product layers are formed during this process, and for further oxidation to occur, transport must occur through the developing product layer. Formation of an oxide layer (called as "scale") may lead to diffusion limited oxidation kinetics where the scale may grow inward, outward, or in both directions. Parabolic oxidation is a diffusion limited process in which the oxidation rate decreases as thickness increases. That is,

$$\frac{dx}{dt} = \frac{k_p}{x} \Rightarrow x^2 = k_p t \quad (1)$$

where  $x$  is the scale thickness and  $k_p$  is the parabolic rate constant.

Ionic and electronic transport through the product layer occurs by diffusion of crystal defect species. Therefore consideration of defect chemistry in the developing layer is necessary. The steady state growth of an oxide layer has been treated by Wagner<sup>15</sup>. A simplified treatment given by Birks and Meier<sup>16</sup> assumes that the mobility of one of the ionic species, either cations or anions, is much larger so that transport of the slower

moving species can be ignored. Assuming that anions and electrons are the mobile species and neglecting cation transport gives a parabolic rate constant

$$k_p = \frac{1}{Z_a^2 F^2 C_x} \int_{\mu'_x}^{\mu''_x} \frac{\sigma_a \sigma_e}{\sigma_a + \sigma_e} d\mu_x \quad (2)$$

where  $\sigma_a$  and  $\sigma_e$  are the partial conductivities of the anion and electrons, X denotes oxygen, F is the Faraday constant,  $C_x$  is the concentration of the anion in the scale,  $Z_a$  is the charge of the anion, and the chemical potential of oxygen at the metal/scale and scale/gas interface are given by  $\mu'_x$  and  $\mu''_x$ , respectively. By further assuming that  $\sigma_e$  approaches unity and is much greater than  $\sigma_a$  (i.e., that the scale is an electronic conductor or semiconductor), Eq. 2 simplifies to

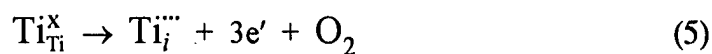
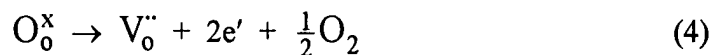
$$k_p = \frac{1}{Z_a^2 F^2 C_x} \int_{\mu'_x}^{\mu''_x} \sigma_a d\mu_x \quad (3)$$

which relates the parabolic oxidation rate constant to the partial conductivity of the oxygen ions in the growing scale. Eq. 3 shows that the rate constant is proportional to  $\sigma_a$ , and, therefore oxides which maintain low defect concentrations (and hence, low ionic conductivities) will have lower rate constants and thus are expected to be more oxidation resistant.

With regard to oxidation of titanium,  $\text{TiO}_2$  is the main oxide of concern. Rutile is a metal excess semiconductor (n-type). There is some uncertainty whether the metal-excess nature is manifested by oxygen vacancies or cation interstitials. Kofstad proposed that the defect structure simultaneously consists of doubly ionized oxygen vacancies and



triply or quadruply charged titanium interstitials<sup>17</sup>. According to Kofstad, the appropriate defect reactions are:



Neglecting intrinsic electronic equilibrium in the wide bandgap material, the electrical neutrality equation becomes:

$$3[\text{Ti}_i'''] + 4[\text{Ti}_i'''] + 2[\text{V}_0''] = n \quad (7)$$

If oxygen vacancies dominate at atmospheric oxygen pressures, Eq. 7 becomes  $n \approx 2[\text{V}_0'']$ .

The equilibrium of Eq. 4 is

$$[\text{V}_0''] n^2 = k_1 P_{\text{O}_2}^{-1/2} \quad (8)$$

and substitution of Eq. 7 (where  $n \approx 2[\text{V}_0'']$ ) into Eq. 8 gives

$$[\text{V}_0''] \propto P_{\text{O}_2}^{-1/6} \quad (9)$$

For sufficiently low impurity concentrations, data verifies this relationship<sup>18</sup>. At higher temperatures, diffusion of titanium interstitials also becomes important<sup>19</sup>.

*b. Oxidation thermodynamics and kinetics*

Considering the Ti-O binary phase diagram, the oxidation of titanium should produce a scale of oxides consisting of TiO, Ti<sub>2</sub>O<sub>3</sub>, Ti<sub>3</sub>O<sub>5</sub>, and TiO<sub>2</sub>. However, for oxidation in air at or below 1000°C, only rutile is detected, and the presence of water vapor in air can lead to the formation of lower oxides such as TiO and Ti<sub>2</sub>O<sub>3</sub><sup>20</sup>.

The oxidation of Ti is summarized in Figure 1 and has been discussed in detail by Kofstad<sup>22</sup>. A brief description of the mechanism for each of the rate equations listed in Figure 1 follows. Logarithmic oxidation ( $x \propto \log t$ ) is not well understood but is generally associated with the formation of thin oxide films on the order of a few hundred Angstroms. One such theory asserts that the rate of chemisorption of the oxidant gas on the surface is a logarithmic rate process, and thus the rate controlling step in logarithmic scale growth is chemisorption<sup>21</sup>. The mechanism of cubic oxidation ( $x^3 \propto t$ ) also has not been established. It is possible that cubic oxidation simply is a transition between logarithmic and parabolic oxidation, describing the simultaneous parabolic scale growth and oxygen dissolution<sup>22</sup>. Because of the high oxygen solubility of  $\alpha$ -Ti, parabolic oxidation above 600°C involves parabolic scale formation and oxygen dissolution. From an Arrhenius plot of the linear and parabolic rate constants, Welsch<sup>23</sup> estimated the activation energy for parabolic and linear oxidation to be 59.8 and 45.7 kcal/mol, respectively. Prolonged oxidation above 900°C leads to a decrease in the oxidation rate.

The linear regime is associated with a loss of protective behavior. As temperature increases, the transition from parabolic to linear behavior occurs at shorter times. The mass gain significantly increases in the linear regime, and the scale is characterized by a stratified growth pattern. The dense outer rutile layer reaches a limiting thickness of about 15-20  $\mu\text{m}$  and begins to spall<sup>23</sup>. Continued spalling and oxidation produces a stratified layer beneath the outer layer. Scale cracking may occur from a high Pilling and

Bedworth ratio (ratio of the volume of the oxide per metal ion to the volume of the metal per metal atom) of 1.75 which predicts compressive stress in the oxide and tension at the metal surface. Other mechanisms include stress build-up due to dissolution of oxygen into Ti, causing a large change in lattice parameters for formation of  $\text{Ti}_3\text{O}^{24}$ , and condensation of titanium vacancies at the metal/oxide interface<sup>25</sup>. A post-linear regime is reported above 900°C where the oxidation rate begins to decrease with long exposure times. The duration of the linear stage decreases with increasing temperature, and by 1200°C the linear stage is not detected. Kofstad has correlated this behavior with sintering and grain growth of the rutile scale which then acts as a diffusion barrier<sup>17</sup>. This suggests that outward diffusion of titanium interstitial ions through the rutile scale under those conditions is also important. Smeltzer has proposed that linear oxidation is indicative of oxide growth by grain boundary diffusion of oxygen<sup>25</sup>. As grain growth occurs with time, the relative contribution of grain boundary transport decreases so that the number of short circuit paths decreases. Eventually volume diffusion of oxygen vacancies dominates and the rate becomes parabolic. However, large grain growth decreases the plasticity of the scale and thus should decrease its ability to remain adherent under cyclic temperature conditions.

## 2. Oxidation of Silicon

### *a. Defect chemistry*

The principal oxide of concern is  $\text{SiO}_2$ . Silica exists in both the vitreous and crystalline states. For crystalline silica at 1 atm. there are four equilibrium polymorphs:  $\alpha$ -quartz below 573°C,  $\beta$ -quartz up to 867°C,  $\beta_2$ -tridymite up to 1470°C, and  $\beta$ -cristobalite up to the melting point of 1710°C<sup>26</sup>. The  $\beta$  to  $\alpha$ -quartz transformation is

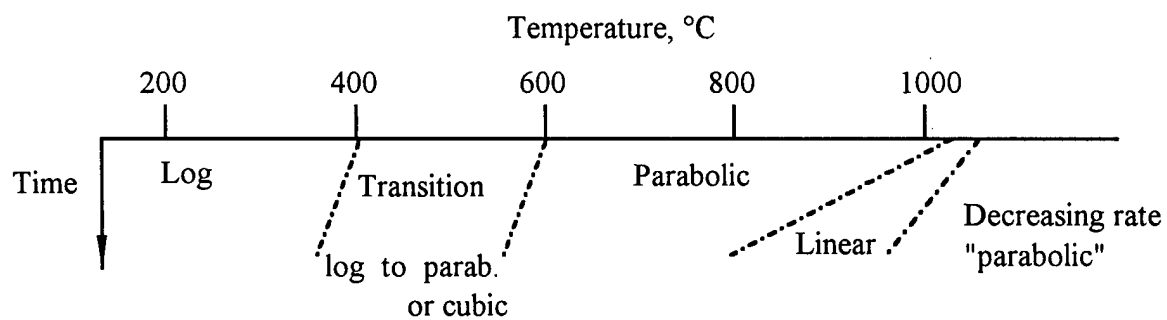
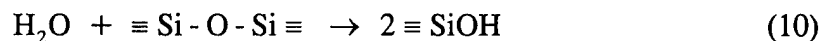


Figure 1: Schematic diagram of rate equations in oxidation of titanium<sup>22</sup>.

reversible and occurs rapidly during cooling. The  $\beta_2$ -tridymite and  $\beta$ -cristobalite transformation to quartz is slow and during cooling,  $\beta_2$ -tridymite transforms into unstable  $\beta$ -tridymite and  $\beta$ -cristobalite transforms into unstable  $\alpha$ -cristobalite. Silica glass held at elevated temperature may devitrify to form  $\beta$ -cristobalite which transforms to unstable  $\alpha$ -cristobalite during cooling. The structures of both crystalline and vitreous silica are based on  $\text{SiO}_4^{4-}$  tetrahedra. A three dimensional network is formed by corner sharing of oxygen in these tetrahedra. Vitreous silica lacks the long range order of crystalline forms, and all defects which are present in crystalline silica can exist in vitreous silica. However, not all defects found in vitreous silica are present in crystalline silica<sup>27</sup>.

Tracer diffusion studies have shown that  $D_O$  is much greater than  $D_{Si}$  in both vitreous and crystalline silica. Diffusion of molecular oxygen in quartz glass is about two orders of magnitude faster than in crystalline quartz at  $1000^\circ\text{C}$ <sup>28</sup>. The activation energy for Si diffusion is very high, reflecting the large number of directional bonds which must be broken and reformed for Si diffusion. Quartz glass has a permeability for  $\text{O}_2$  and  $\text{H}_2\text{O}$  proportional to partial pressure. Transport in quartz glass is believed to occur by two mechanisms<sup>29</sup>. Neutral oxygen molecules can diffuse through connected pores or micro channels created by the relatively open structure. This interstitial oxygen can also exchange with network oxygen for transport. Normally diffusion of neutral oxygen molecules dominates. However, the presence of  $\text{H}_2\text{O}$  vapor serves to break up the network according to the reaction



and promotes exchange between interstitial oxygen and network oxygen.

*b. Oxidation kinetics*

An important aspect of oxidation by the formation of silica scales is the transition from active to passive oxidation. Passive oxidation is diffusion-controlled parabolic growth of the silica scale. Low  $P_{O_2}$  environments lead to rapid oxidation due to  $SiO(g)$  generation, a process called active oxidation.  $P_{SiO}$  increases dramatically as  $P_{O_2}$  decreases. Consequently, if the  $SiO_2$  passivating surface is exposed to a low  $P_{O_2}$  environment, a  $SiO$  "smoke" is formed and the  $SiO_2$  layer is reduced, eventually leading to consumption of the base material. Birks and Meier<sup>16</sup> have given a simplified analysis of the process. The critical oxygen pressure below which active oxidation will occur is given as

$$P_{O_2}(\text{crit}) \approx \frac{1}{2} P_{SiO}(\text{eq}) \quad (11)$$

where  $P_{SiO}(\text{eq})$  is the equilibrium  $P_{SiO}$  above the  $Si$  surface at the temperature of interest. The consumption of  $Si$  due to the flux of  $SiO$  vapor across a boundary layer is given as

$$J_{SiO} = \frac{2P_{O_2} D_{O_2}}{\delta RT} \quad (12)$$

Increasing the flow rate of gas over the surface decreases the stagnation layer thickness,  $\delta$ , through which  $O_2$  and  $SiO$  must diffuse. This leads to linear oxidation kinetics in which the rate-determining step is the supply of  $O_2$  to and removal of  $SiO$  from the scale/gas surface. For oxygen pressures below  $P_{O_2}(\text{crit})$ , the rate of  $Si$  consumption is about 300 times faster than it is for oxygen pressures above  $P_{O_2}(\text{crit})$ . This limits the use of  $SiO_2$ -forming alloys to atmospheres containing a minimum oxygen content of about 8 Torr<sup>30</sup>.

The overall oxidation process for silicon has been described by Deal and Grove<sup>31</sup> as being divided into three processes. First, the oxidant is transported from the gaseous atmosphere to the outer surface of the scale. Second, the oxidant diffuses across the scale according to Fick's Law. Finally, it reacts at the silicon/scale interface to form  $\text{SiO}_2$ . At steady-state, the flux of the oxidant in each of the three steps is identical, leading to the following equation:

$$x^2 + Ax = B(t + \tau) \quad (13)$$

where  $x$  is the scale thickness,  $t$  is time,  $B$  is the parabolic rate constant,  $\tau$  is the time coordinate correcting for an initial oxide thickness, and  $B/A$  is the linear rate constant related to phase boundary reactions (thin oxide formation) and solubility of oxygen in  $\text{SiO}_2$ . Solving the quadratic equation in Eq. 13 yields

$$\frac{x}{\left(\frac{A}{2}\right)} = \left[ 1 + \frac{t + \tau}{\frac{A^2}{4B}} \right]^{1/2} - 1 \quad (14)$$

At large times,  $t \gg A^2/4B$  and  $t \gg \tau$ , so that  $x^2 \cong Bt$  (parabolic scale growth). For short times,  $t \ll A^2/4B$  so that  $x \cong \frac{B}{A} (t + \tau)$  or linear scale growth. The activation energy of  $B$  compares closely to that for the diffusion of molecular oxygen through fused silica, indicating that molecular oxygen diffusion through silica is rate determining during oxidation.

### 3. Oxidation of $\text{Ti}_5\text{Si}_3$

Literature on the oxidation of  $\text{Ti}_5\text{Si}_3$  is rather limited. An early investigation of oxidation in the Ti-Si system was conducted by Paine et al.<sup>32</sup> They tested sintered plates in dry air at 1260°C for 100 hours. Good oxidation resistance was reported in spite of the inability to synthesize single-phase compositions.  $\text{TiSi}_2$  was reported to experience mass gains of 2.2 and 4.4 mg/cm<sup>2</sup> in 100 hours at 1260 and 1370°C. Anton and Shah<sup>33</sup> performed cyclical oxidation testing of arc-cast  $\text{Ti}_5\text{Si}_3$  at 1149°C. Samples were lowered into a furnace for 55 minutes followed by withdrawal for 5 minutes. After 50 hours the mass gain was 30.76 mg/cm<sup>2</sup>, indicating substantial consumption of the alloy. An external brown oxide was observed, and x-ray diffraction of the oxidation products indicated 75-80 vol%  $\text{TiO}_2$  (rutile), 20 vol% hexagonal  $\text{Ti}_5\text{Si}_3$  and < 5 vol% tetragonal  $\text{SiO}_2$  ( $\alpha$ -cristobalite). The estimated rate of metal consumption based on the density of  $\text{TiO}_2$  was 1.44  $\mu\text{m}/\text{hour}$ . Good scale adherence was observed, possibly attributable to the formation of  $\text{TiO}_2$ . In future combustor liners, an estimated acceptable metal recession rate<sup>44</sup> is  $10 \times 10^{-3}$  inches per 10,000 hours or 0.025  $\mu\text{m}/\text{hour}$ . Clearly, the above tested material lacks adequate oxidation resistance at these conditions.

Liu, Lee, and Henson<sup>34</sup> produced alloys of Ti-29Si-8Cr, Ti-33Si-4Cr-4Zr, and Ti-36.5Si by arc melting and casting. Isothermal oxidation at 800°C in air showed parabolic oxidation for the last two alloys with a mass gain of 0.88 and 0.98 mg/cm<sup>2</sup> at 120 hours. The alloy of lowest silicon content showed linear oxidation with a mass gain of 1.8 mg/cm<sup>2</sup> at 120 hours. All three alloys formed adherent scales.

Eutectic alloys of  $\beta$ -Ti and  $\text{Ti}_5\text{Si}_3$  have been produced<sup>35,36,37</sup>. These composite materials show a dramatic improvement in the otherwise poor mechanical properties of  $\text{Ti}_5\text{Si}_3$ . The eutectic alloy shows parabolic oxidation kinetics after transient oxidation of 6 hours and 0.8mg/cm<sup>2</sup> at 845°C. The activation energy was 180 kJ/mol, and at longer



time tests the data did not fit well to a parabolic model. A Ti-Si solid solution containing 0.5 wt% Si showed parabolic oxidation after transient oxidation of 4 hours at 870°C. The activation energy was 182 kJ/mol, but the parabolic rate constant was about 2 times higher than the eutectic alloy. At 850°C the parabolic rate constant for the eutectic alloy was 0.256 mg<sup>2</sup>/cm<sup>4</sup>/hr. This is orders of magnitude higher than the parabolic rate constant for other common oxidation resistant silica formers such as SiC, Si<sub>3</sub>N<sub>4</sub>, and MoSi<sub>2</sub>.

#### 4. Oxidation of Other Engineering Materials

Figure 2 shows the oxidation kinetics for several of the stable oxide formers<sup>16</sup>. As shown in Eq. 3, oxides which maintain low defect concentrations are expected to have lower parabolic rate constants. Chromia, silica, and alumina scales are slower growing because of their smaller deviations from stoichiometry and therefore lower concentrations of defect species.

##### *a. Chromia formers*

Formation of chromia scales is the basis for the oxidation protection of many high-temperature stainless steels and superalloys. In the case of Ni-Cr alloys, addition of chromium to nickel above a minimum concentration promotes the selective oxidation of Cr atoms to form a slower growing, protective chromia scale. Unfortunately, chromia formers are not suitable in extreme P<sub>O<sub>2</sub></sub> environments or at temperatures in excess of 1000-1100°C. As temperature increases, the rate of chromia consumption increases since P<sub>Cr</sub> and P<sub>CrO<sub>3</sub></sub> increase. This leads to an increased rate of consumption of the base alloy. Therefore, oxidation-resistant high temperature structural materials must be based on materials which form silica or alumina scales.

### *b. Alumina formers*

For applications at higher temperatures, alumina scales provide significantly better oxidation resistance than chromia scales. Alloy 214 (FeNiCrAlY) and MA956 (FeCrAlY) are two recently developed alumina formers which maintain oxidation resistance up to 1200°C<sup>38</sup>. Intermetallic aluminides have also received considerable attention. In the Ti-Al system, the oxidation resistance of Ti is substantially improved when the Al content is greater than about 25 at.%. At temperatures up to about 950°C in pure oxygen, the oxidation rate of  $\gamma$ -TiAl is low. However, the presence of nitrogen in the atmosphere leads to a loss of oxidation resistance. The scale consists of an outer layer of rutile over a mixed layer of alumina and rutile with an internal oxidation zone below the scale<sup>39</sup>. It is believed that internal precipitates of  $\text{TiN}_x$  form which rapidly oxidize to form rutile<sup>40</sup>. These precipitates prevent formation of a continuous alumina layer and act as a path for rapid inward oxygen diffusion. In the Ni-Al system,  $\beta$ -NiAl is extremely oxidation resistant. At 1100°C in air, Doychak and Mitchell<sup>41</sup> observed parabolic mass gain with a rate constant of  $1.12 \times 10^{-4} \text{ mg}^2/\text{cm}^4/\text{hr}$ . Unfortunately, the melting point of  $\beta$ -NiAl (1650°C) substantially limits its potential high-temperature usefulness.

### *c. Silica formers*

Nickel and iron have poor high-temperature oxidation resistance. Silicon has been added to these materials to promote formation of a slow-growing silica layer.<sup>42,43</sup> Ni-Si alloys containing more than 10 wt.% Si exhibit slow linear rates, comparable to Ni-20Cr-10Al. At 1100°C in air, linear rates of  $1\text{-}2 \times 10^{-3} \text{ mg}/\text{cm}^2/\text{hr}$  are observed. Similarly for Fe-Si alloys, approximately 10 wt.% Si promotes slow linear oxidation. These rates are substantially lower than that for pure Si oxidation, and outward diffusion of Ni and Fe through the silica layer occurs.

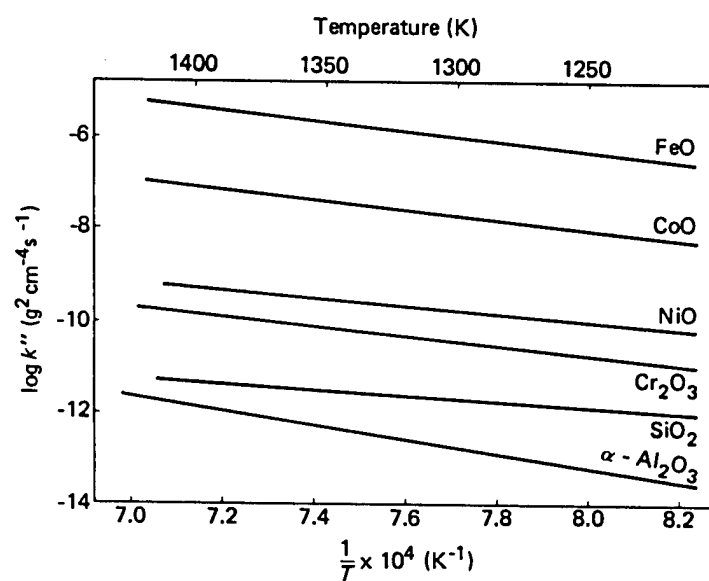
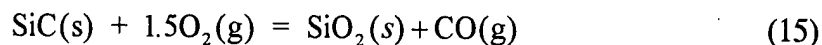


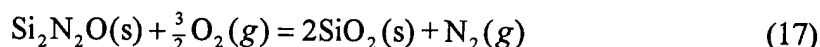
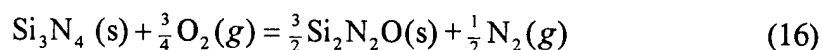
Figure 2: Parabolic rate constants for several oxides<sup>16</sup>.

Silicon-based ceramics including SiC and Si<sub>3</sub>N<sub>4</sub> exhibit excellent oxidation resistance<sup>44</sup>. According to Jacobson, SiC oxidation occurs by the following reaction:



The oxidized microstructure is characterized by formation of a single phase silica scale. Rate constants<sup>44</sup>,  $k_p = 1.3 \times 10^{-3} \text{ mg}^2/\text{cm}^4/\text{hr}$  at 1400°C in dry oxygen, are slightly less than those for silicon. As with silicon, it is believed that the rate of inward diffusion of molecular oxygen is rate determining. For temperatures below about 1450°C, the activation energy<sup>44</sup> is similar to that for silicon oxidation and molecular oxygen diffusion (120-140 kJ/mol). For temperatures above about 1500°C, the activation energy of SiC oxidation increases (260-300 kJ/mol), and this is attributed to the increasing contribution of network exchange diffusion.

Also from Jacobson, the oxidation of Si<sub>3</sub>N<sub>4</sub> occurs by the reactions:



A duplex scale forms with an underlying silicon oxynitride layer and an exterior silica layer. The activation energy for the oxidation of Si<sub>3</sub>N<sub>4</sub> is larger than for silicon, and this is reflected in the parabolic rate constant for Si<sub>3</sub>N<sub>4</sub> being about two orders of magnitude lower than for silicon and SiC. As for the case of SiC, it is believed that molecular oxygen is rate determining with considerable network exchange occurring at higher temperatures. The lower rate for Si<sub>3</sub>N<sub>4</sub> has been explained by Du et al.<sup>45</sup> In the duplex

structure, the oxide layer is about nine times thicker than the oxynitride layer. The oxynitride is proposed to act as a diffusion barrier, having a lower permeability to oxygen than silica. Luthra<sup>46</sup> has shown that the substantially lower rate of oxidation for  $\text{Si}_3\text{N}_4$  predicts an unreasonably large buildup of nitrogen pressure at the oxynitride/silica interface within the duplex scale. Since spalling of the scale is not experimentally observed, Luthra concludes that thermodynamic equilibrium is not attained. As such true diffusion control may not be rate determining, and mixed control by interfacial reaction and nitrogen outward diffusion is proposed. Clearly, there are several unanswered questions regarding the oxidation mechanism of silicon-based ceramics.

It is worth noting that while many of the above engineering materials possess good high temperature oxidation resistance, each of the materials has basic limitations preventing its use in monolithic form in high temperature structural applications. The chromia formers lose oxidation resistance above about 1000-1100°C. Alumina formers provide improved protection, but for  $\beta\text{-NiAl}$  the lower melting point ( $T < 1650^\circ\text{C}$ ) precludes use in high temperature applications exceeding about 1265°C ( $0.8T_m$ ). Silicon based ceramics including  $\text{SiC}$  and  $\text{Si}_3\text{N}_4$  have excellent oxidation resistance, but these materials lack the necessary low temperature ductility and fracture toughness required for structural applications. Considering the limitations of the mentioned engineering materials, investigation of the  $\text{Mn}_5\text{Si}_3$ -type materials such as  $\text{Ti}_5\text{Si}_3$  which allow for manipulation of critical physical properties by extensive ternary additions is clearly warranted.

## References

- <sup>1</sup>A. J. Thom, V. Young, and M. Akinc, "Single Crystal Studies of  $Ti_5Si_3Z_x$ ," to be published.
- <sup>2</sup>A. J. Thom, M. Akinc, O. B. Cavin, and C. R. Hubbard, "Thermal Expansion Anisotropy of  $Ti_5Si_3$ ", *J. Mat. Sci. Letters*, **13**, 1657-1660 (1994).
- <sup>3</sup>A.J. Thom, Y. Kim, and M. Akinc, "Effect of Processing on Oxidation of  $Ti_5Si_3$ ," *Mat. Res. Soc. Symp. Proc.*, vol. 288, edited by Baker, Darolia, Whittenberger, and Yoo (Pittsburgh, PA: Materials Research Society, 1037-1042 (1993).
- <sup>4</sup>A. J. Thom and M. Akinc, "Improved Oxidation Resistance of  $Ti_5Si_3$  by Small Atom Doping," to be published.
- <sup>5</sup>A. J. Thom and M. Akinc, "Interstitial Chemistry Effects on Processing of  $Ti_5Si_3$ ," to be published.
- <sup>6</sup>Y. Kim, A. J. Thom, and M. Akinc, "Synthesis, Processing, and Properties of  $Ti_5Si_3$ ," *Min. Met. Mater. Soc. Symp. Proc.*, edited by T. S. Srivatsan and V. A. Ravi, *Processing and Fabrication of Advanced Materials for High-Temperature Applications - II*, (1993) 189-208.
- <sup>7</sup>A. J. Thom, M. K. Meyer, Y. Kim, and M. Akinc, "Evaluation of  $A_5Si_3Z_x$  Intermetallics for Use as High Temperature Structural Materials," *Min. Met. Mater. Soc. Symp. Proc.*, edited by T. S. Srivatsan and V. A. Ravi, *Processing and Fabrication of Advanced Materials - III*, 413-438 (1994).
- <sup>8</sup>E. Garcia and J. D. Corbett, "Chemistry of Polar Intermetallic Compounds. Study of Two  $Zr_5Sb_3$  Phases, Hosts for a Diverse Interstitial Chemistry," *Inorganic Chem.*, **27**, 2353-2359, (1988).
- <sup>9</sup>E. Garcia and J. D. Corbett, "Chemistry in the Polar Intermetallic Host  $Zr_5Sb_3$ . Fifteen Interstitial Compounds," *Inorganic Chem.*, **29**, 3274-3282 (1990).
- <sup>10</sup>Y. Kwon, M. A. Rzeznik, A. Guloy, and J. D. Corbett, "Impurity Stabilization of Phases with the  $Mn_5Si_3$ -Type Structure. Questions Regarding  $La_5Sn_3$  and  $Zr_5Si_3$ ," *Chem. Mater.*, **2**, 546-550 (1990).

- <sup>11</sup>Y. Kwon and J. D. Corbett, "Chemistry in Polar Intermetallic Compounds. The Interstitial Chemistry of  $Zr_5Sn_3$ ", *Chem. Mater.*, **4**, 1348-1355 (1992).
- <sup>12</sup>P. Villars and L. D. Calvert, *Pearson's Handbook of Crystallographic Data for Intermetallic Phases*, 2nd ed., American Society for Metals Int., Metals Park, OH, 255 (1991).
- <sup>13</sup>R. L. Fleischer, "Review of High-Strength, High-Temperature Intermetallic Compounds", *J. Mat. Sci.*, **22**, 2281-88 (1987).
- <sup>14</sup>H. J. Frost and M. F. Ashby, *Deformation-Mechanism Maps: the Plasticity and Creep of Metals and Ceramics*, Pergamon Press, Oxford, (1982).
- <sup>15</sup>C. Z. Wagner, "Beitrag zur Theorie des Anlaufvorgangs," *Zeit. Physik. Chemie*, **21**, 25-41, (1933).
- <sup>16</sup>N. Birks and G. H. Meier, *Introduction to High Temperature Oxidation of Metals*, Edward Arnold Publishers, London, (1983).
- <sup>17</sup>P. Kofstad, "Note on the Defect Structure of Rutile ( $TiO_2$ )," *J. Less-Common Metals*, **13**, 635-638 (1967).
- <sup>18</sup>R.N. Blumenthal, J. Coburn, J. Baukus, and W.M. Hirthe, *J. Phys. Chem. Solids*, **27**, 643 (1966).
- <sup>19</sup>Hj. Matzke, "Diffusion in Nonstoichiometric Oxides", p206 in *Nonstoichiometric Oxides*, Edited by O.T. Sorensen (1981).
- <sup>20</sup>P. Kofstad, *High Temperature Corrosion*, Elsevier, New York, 290 (1988).
- <sup>21</sup>P.T. Landsberg, "On the Logarithmic Rate Law in Chemisorption and Oxidation," *J. Chem. Phys.*, **23**, 1079-1087 (1955).
- <sup>22</sup>P. Kofstad, *High Temp. Oxidation of Metals*, John Wiley and Sons, New York, (1966).
- <sup>23</sup>A. I. Kahueci and G. Welsch, "Oxidation of Titanium Alloys", p47 in *Environmental Degredation of Eng. Mat. III*, Edited by M.R. Louthan (1987).
- <sup>24</sup>P. Kofstad, P.B. Anderson, and J. Krudtaa, "Oxidation of Titanium in the Temperature Range 800-1200°C," *J. Less-Common Metals*, **3**, 89-97 (1961).

- <sup>25</sup>W.W. Smeltzer, R.R. Haering, and J.S. Kirkaldy, "Oxidation of Metals by Short Circuit and Lattice Diffusion of Oxygen," *Acta. Metall.*, **9**, 880-885 (1961).
- <sup>26</sup>W. D. Kingery, H. K. Bowen, and D. R. Uhlmann, *Introduction to Ceramics*, John Wiley and Sons, New York, 274 (1976).
- <sup>27</sup>F.A. Kroger, "High Temperature Corrosion", Nat. Assoc. Corr. Eng., Edited by Robert Rapp, **6**, 89 (1983).
- <sup>28</sup>P. Kofstad, *High Temperature Corrosion*, Elsevier, New York, 123 (1988).
- <sup>29</sup>A. Atkinson, *Selected Topics in High Temp. Chem.*, Edited by O. Johannesen and A. Anderson, Elsevier, 41 (1989).
- <sup>30</sup>K. Vedula, Iowa State Uni., MSE523 class notes, Spring 1993.
- <sup>31</sup>B.E. Deal and A.S. Grove, "General Relationship for the Thermal Oxidation of Silicon," *J. Appl. Phys.*, **36**, 3770-3778 (1965).
- <sup>32</sup>R. M. Paine, A. J. Stonehouse, and W. W. Beaver, WADC Tech. Rep. 59-29-Part I, January 1960 (United States Air Force, Wright-Patterson Air Force Base, OH).
- <sup>33</sup>D. L. Anton and D. M. Shah, *Development Potential of Advanced Intermetallic Materials*, US Air Force Rep. (contract no. WRDC-TR-90-4122.OH,USA) 1991.
- <sup>34</sup>C. T. Liu, E. H. Lee, and T. J. Henson, "Initial Development of High Temperature Titanium Silicide Alloys", Report, ORNL-6435; Order No. DE88007860, 1988.
- <sup>35</sup>G. Frommeyer, R. Rosendrantz, and C. Ludecke, "Microstructure and Properties of the Refractory Intermetallic  $Ti_5Si_3$  Compound and the Unidirectionally Solidified Eutectic Ti- $Ti_5Si_3$  alloy", *Z. Metallkde*, **8**, 307-313 (1990).
- <sup>36</sup>R. Rosenkranz, G. Frommeyer, and W. Smarsly, "Microstructures and Properties of High Melting Point Intermetallic  $Ti_5Si_3$  and  $TiSi_2$  Compounds," *Mater. Sci. Eng.*, **A152**, 288-294 (1992).
- <sup>37</sup>B. Pieraggi, M. Raffy, and F. Dabosi, "Oxidation of Ti- $Ti_5Si_3$  Eutectic Alloy", *Proc. of Int. Congress on Metal. Corr.*, 348-352 (1984).



- 38G. Y. Lai, High-Temperature Corrosion of Engineering Alloys, ASM International, Materials Park, OH, 44 (1990).
- 39G. H. Meier and F. S. Pettit, "The Oxidation Behavior of Intermetallic Compounds", *Mat. Sci. Eng.*, **A153**, 548-560 (1992).
- 40C. P. Stinner, G. H. Meier, and F. S. Pettit, "The Oxidation of Alloys Based on Gamma Titanium Aluminide", presented at the Fall TMS/ASM Meeting, Pittsburgh, 1993.
- 41J. K. Doychak and T. E. Mitchell, "High Temperature Oxidation of  $\beta$ -NiAl", *Mat. Res. Soc. Symp. Proc.*, **39**, 475-484 (1985).
- 42G. H. Meier, "High Temperature Oxidation and Corrosion of Metal-Silicides", *Mat. Res. Soc. Symp. Proc.*, **81**, 443-458 (1987).
- 43F. H. Stott, G. J. Gabriel, and G. C. Wood, "The Influence of Silicon on the High-Temperature Oxidation of Nickel", *Oxidation Metals*, **28**, 329-345 (1987).
- 44N. S. Jacobson, "Corrosion of Silicon-Based Ceramics in Combustion Environments", *J. Am. Ceram. Soc.*, **76** [1], 3-28 (1993).
- 45H. Du, R. E. Tressler, and C. G. Pantano, "Oxidation Studies of Crystalline CVD Silicon Nitride", *J. Electrochem. Soc.*, **136** [5], 1527-36 (1989).
- 46K. L. Luthra, "Some New Perspectives on Oxidation of Silicon Carbide and Silicon Nitride", *J. Am. Ceram. Soc.*, **74** [5], 1095-1103 (1991).

CHAPTER 2:  
SINGLE CRYSTAL STUDIES OF  $\text{Ti}_5\text{Si}_3\text{Z}_x$

A manuscript to be submitted to *Journal of Materials Research*

Andrew J. Thom, Victor Young, and Mufit Akinc

Ames Laboratory and Department of Materials Science and Engineering

**Abstract**

Several  $\text{Ti}_5\text{Si}_3\text{Z}_x$  compositions ( $\text{Z}=\text{B}, \text{C}, \text{N}, \text{O}$ ) have been synthesized by arc-melting. Powder x-ray diffraction indicates the materials maintain the  $\text{Mn}_5\text{Si}_3$ -type structure possessed by  $\text{Ti}_5\text{Si}_3$ . Calculated cell constants are correlated to ternary composition based on careful chemical analysis. Nitrogen and oxygen promote a volume decrease, while boron promotes a volume increase. Carbon causes a decrease in the  $a$ -parameter and an increase in the  $c$ -parameter with a concomitant volume increase. Room temperature x-ray single crystal structural analysis was performed on one composition for each ternary addition. Each analyzed composition has the  $\text{P6}_3/\text{mcm}$  space group (No. 193) with the  $\text{Mn}_5\text{Si}_3$ -type structure. Each ternary addition occupies the normally vacant interstitial site at the center of the trigonal antiprisms of titanium ( $\text{Ti}_2$ ) atoms ( $\text{Ti}_6\text{Z}$  polyhedra), located in chains at the corners of the unit cell. Bonding between the interstitial atoms and the titanium ( $\text{Ti}_2$ ) atoms in the  $\text{Ti}_6\text{Z}$  polyhedra is suggested by a decrease in the cavity size, and significant changes in other bond lengths also occur.

## I. Introduction

Previous experimental work by Corbett and collaborators<sup>1,2,3,4</sup> has shown that intermetallic compounds of the form  $A_5B_3$  which possess the  $Mn_5Si_3$ -type structure present a wealth of potential interstitial chemistries. Materials with the base  $A_5B_3$  composition can be doped with a wide variety and substantial amount of various Z elements. The resulting  $A_5B_3Z_x$  compound possesses the same  $Mn_5Si_3$ -type structure. The dopant Z occupies an interstitial site within the structure which contributes to a change in the lattice parameters of the material. This presents a unique opportunity to modify material properties by suitable interstitial additions.  $A_5Si_3$  silicide intermetallics<sup>5,6,7,8,9</sup>, which are potential high temperature structural materials, can be made more attractive for potential use by suitable additions which improve critical material properties<sup>10</sup>. Otherwise inferior materials can be dramatically improved by appropriate additions.

Transition metal silicides of the form  $M_5Si_3$  exist in three structures: tetragonal  $Cr_5B_3$ -type ( $T_2$  phases), tetragonal  $W_5Si_3$ -type ( $T_1$  phases), and hexagonal  $Mn_5Si_3$ -type ( $D8_8$  phases). Some  $M_5Si_3$  silicides will only exist in the  $Mn_5Si_3$ -type structure in the presence of ternary stabilizing elements such as boron, carbon, nitrogen, and oxygen. These hexagonally stabilized materials, formulated as  $M_5Si_3Z_x$ , are called Nowotny phases<sup>11</sup>. In the absence of the stabilizer, the pure binary  $M_5Si_3$  compound has the  $W_5Si_3$  structure. The voids within the  $W_5Si_3$ -type structure are not large enough to accommodate significant amount of Z interstitials, and the  $Mn_5Si_3$ -type structure becomes favored because of its ability to incorporate these additions<sup>12</sup>. As the amount of interstitial is further increased, a ternary  $T_2$  phase may form.

Parthé summarized the compositional variation of the  $M_5Si_3Z_x$  Nowotny phases<sup>13</sup>. Considering the transition metals from Group IV to VI, the amount of carbon required to stabilize the D8<sub>8</sub> phase increases with both group and period of the metal. It has yet to be established whether  $Ti_5Si_3$  is a true binary D8<sub>8</sub> phase or simply a Nowotny phase stabilized by a small amount of Z. For Group VI metal Mo, the interstitial occupancy does not sufficiently explain the observed decrease in density of the D8<sub>8</sub>  $Mo_5Si_3C$ <sup>14</sup>. Kieffer et al.<sup>15</sup> suggested a metal deficiency via silicon substitution and carbon substitution for silicon. Parthé<sup>16</sup> suggested interstitial occupancy by carbon with metal deficiency. This was later verified in a neutron diffraction study by Parthé.<sup>17</sup>

It is important to note, however, that the discovery of the interstitial stabilization effect by Nowotny was based on the accidental introduction of impurities. More recent investigations using purer starting materials and modern equipment and synthesis techniques have revealed the existence of many true binary  $A_5B_3$  compositions with the  $Mn_5Si_3$ -type structure<sup>18</sup>.

Figure 1 shows an [001] projection of the  $Ti_5Si_3$  unit cell. This is a hexagonal structure (hP16) in space group  $P6_3/mcm$  which is characterized by two distinct chains extending along the c-direction. The first chain is a linear chain of titanium atoms (Ti1) located at  $(1/3, 2/3, z)$  where  $z = 0, 1/2$ . Ti1 atoms are coordinated by six silicon atoms (Si) which form irregular trigonal antiprisms, being intermediate between trigonal prismatic and trigonal antiprismatic. The second chain is composed of titanium atoms (Ti2) which form trigonal antiprisms. Within the cavity of the (Ti2) trigonal antiprism is an interstitial site at (0,0,0) which is normally vacant in the undoped material. With two formula units per unit cell, up to two interstitial atoms can be accommodated within the cell, yielding a formula for the fully stuffed  $Mn_5Si_3$ -type structure of  $Mn_5Si_3Z_{1.0}$  which is isostructural with the  $Ti_5Ga_4$ -type structure (hP18). The silicon homogeneity range of

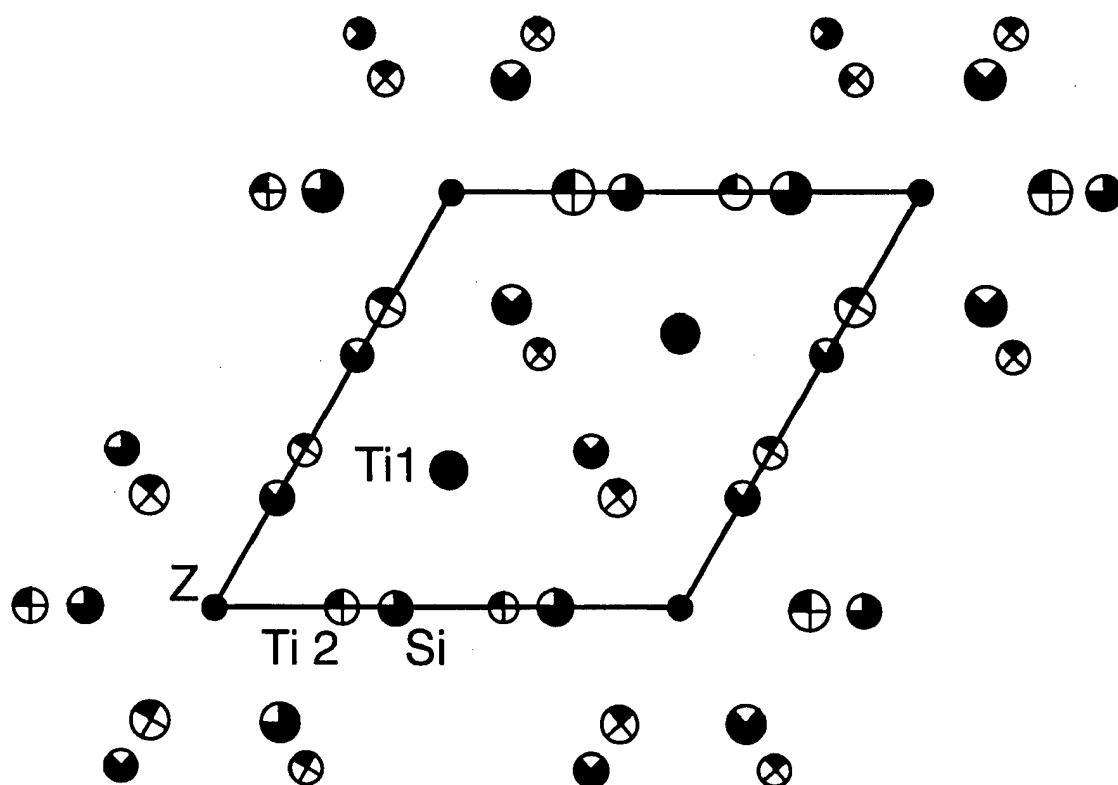


Figure 1: [001] projection of  $\text{Ti}_5\text{Si}_3$  which has the  $\text{Mn}_5\text{Si}_3$ -type structure. The large circles are Ti, medium circles are Si, and the small circles are interstitial sites. Height symbol key:  $\oplus$  ( $z=0, \frac{1}{2}$ ),  $\otimes$  ( $z=\frac{1}{4}$ ),  $\bullet$  ( $z=\frac{3}{4}$ ).

$\text{Ti}_5\text{Si}_3$  was not investigated in this work. Based on the binary Ti-Si phase diagram<sup>19</sup> which indicates  $\approx 2.5$  at% homogeneity range, a 1.25 at% addition of silicon to stoichiometric  $\text{Ti}_5\text{Si}_3$  yields a formula of  $\text{Ti}_5\text{Si}_3\text{Si}_{0.16}$ . Stuffing beyond this point promotes formation of a biphasic mixture of  $\text{Ti}_5\text{Si}_3\text{Si}_{0.16}$  and  $\text{Ti}_5\text{Si}_4$ . Tetragonal  $\text{Ti}_5\text{Si}_4$  has an unrelated  $\text{Zr}_5\text{Si}_4$ -type (tP36) structure.

The Ti2 chains are located at the corners of the hexagonal unit cell. The trigonal antiprisms can also be considered face sharing octahedra as shown in Figure 2. Silicon atoms are at the three edges of each shared face, bonding to two Ti2 atoms within the plane (in-plane) on the face edge and also bonding to two Ti2 atoms (out-of-plane), one each above and below the plane. The silicon atoms serve to bond together the structure by forming an (interchain) bond with the Ti2 atom of another trigonal antiprism within the plane and also forming the irregular trigonal antiprismatic chains about the Ti1 atoms. An ABACA stacking sequence can be envisioned by considering an A plane of the interstitial sites and Ti1 atoms. The C plane, which contains the Ti2 and Si atoms, is rotated by  $180^\circ$  with respect to the B plane.

Kajitani et al.<sup>20</sup> studied the structure of  $\text{Ti}_5\text{Si}_3$  doped with hydrogen isotopes. For the composition of  $\text{Ti}_5\text{Si}_3\text{D}_{0.9}$ , deuterium occupied the interstitial sites at (0,0,0). The c-parameter expanded about 0.3% and the a-parameter contracted about 0.16% compared to  $\text{Ti}_5\text{Si}_3$ .

The high degree of stability of this structure promoted by these strong chains is evidenced by the high melting point of many of the  $\text{Mn}_5\text{Si}_3$ -type materials. Table I shows the melting point of several  $\text{A}_5\text{Si}_3$  compositions which can be stabilized in the  $\text{Mn}_5\text{Si}_3$ -type structure.

To exploit the possibility of tailoring critical material properties,  $\text{Ti}_5\text{Si}_3$  was selected for further investigation because of its potential as a structural material. Several

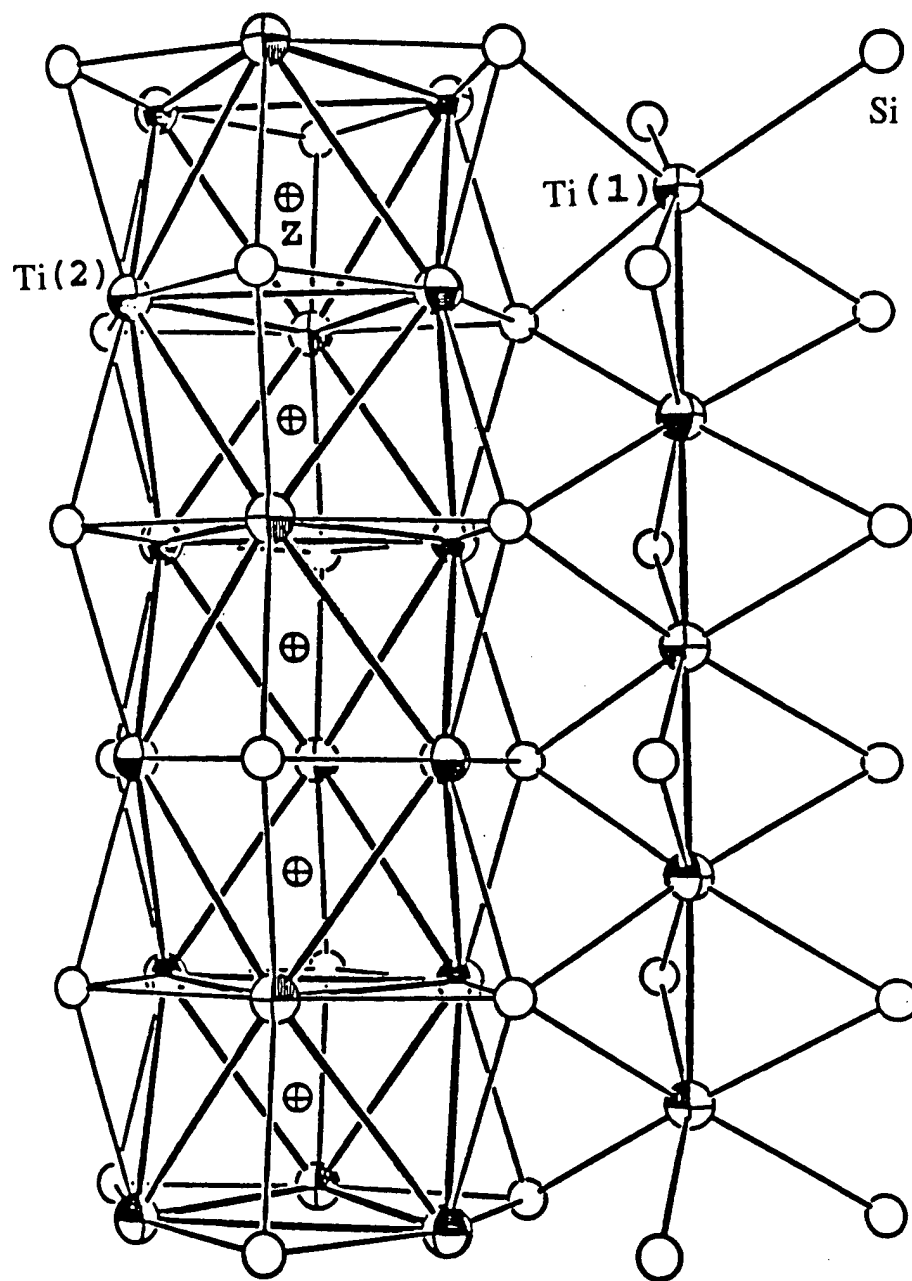


Figure 2: Ti1 linear chain and Ti2 trigonal antiprismatic chain.

light elements have been added to the base  $\text{Ti}_5\text{Si}_3$  composition, and the effect of these additions on properties such as oxidation resistance<sup>21</sup>, mechanical properties, and thermal expansion anisotropy<sup>22,23</sup> is currently being investigated. In all of the preceding experimental work in which the base composition  $\text{Ti}_5\text{Si}_3$  has been doped with ternary additions such as carbon, boron, nitrogen, and oxygen, the assumption has been made that the dopant occupies an interstitial site at (0,0,0) within the structure. In order to validate this assumption, several single crystal x-ray diffraction studies have been conducted. The goal of these studies is to verify that the dopant atom is occupying the stated interstitial position within the  $\text{Mn}_5\text{Si}_3$ -type structure.

Table I: Melting Point<sup>+</sup> (°C) of Various  
Transition Metal  $\text{A}_5\text{Si}_3$  Compositions

Group IIIB	Group IVB	Group VB	Group VIB	Group VIIB
Sc <sup>#</sup> 2200	Ti 2130	V 2125	Cr 1650	Mn 1300
Y 1855	Zr 2210	Nb 2450	Mo 2180	Tc
La	Hf 2600	Ta 2500	W 2350	Re

<sup>+</sup> Ref. 24

<sup>#</sup> Ref. 25

## II. Experimental

Nominal compositions of  $\text{Ti}_5\text{Si}_3\text{Z}_x$  ( $\text{Z} = \text{B}, \text{C}, \text{N}, \text{O}$  and  $x = 0.25, 0.50, 0.75$ ) were synthesized by the method of arc-melting. Table II shows the starting constituents for



each of the various compositions synthesized. Materials were arc-melted under argon using a non-consumable tungsten electrode. Materials were triple melted to promote chemical homogenization.

For each of the synthesized compositions, the starting  $\text{Ti}_5\text{Si}_3$  was previously arc-melted from elemental Ti and Si. Because of the high melting point of boron and graphite, prealloyed  $\text{Ti}_5\text{Si}_3$  was used as a starting material to reduce the amount of silicon volatilization compared to using elemental silicon. Carbon, nitrogen, and oxygen content were determined by combustion analysis and the inert gas fusion technique. Boron was analyzed by spark source laser mass spectroscopy. The arc-melt buttons were ground in an agate mortar and pestle and sieved to -325 mesh for x-ray diffraction. The powders were analyzed in a powder x-ray diffractometer using  $\text{Cu K}_\alpha$  radiation. Lattice parameters were calculated for each of the compositions using a method previously described<sup>22</sup>.

For each composition to be studied, a crystal of the compound was extracted from the arc-melted button and mounted on a glass fiber on a Enraf-Nonius CAD4 diffractometer. Data were collected at  $293 \pm 1\text{K}$  using monochromated  $\text{Mo K}_\alpha$  radiation.

Table II: Starting Materials for Synthesized  $\text{Ti}_5\text{Si}_3\text{Z}_x$

Composition	Starting materials
$\text{Ti}_5\text{Si}_3\text{B}_x$	$\text{Ti}_5\text{Si}_3 + \text{B}$
$\text{Ti}_5\text{Si}_3\text{C}_x$	$\text{Ti}_5\text{Si}_3 + \text{graphite}$
$\text{Ti}_5\text{Si}_3\text{N}_x$	$\text{Ti}_5\text{Si}_3 + \text{TiN} + \text{Si}$
$\text{Ti}_5\text{Si}_3\text{O}_x$	$\text{Ti}_5\text{Si}_3 + \text{TiO}_2 + \text{Si}$

The typical  $\theta$  range was from  $3.16^\circ$  to  $29.96^\circ$  with an index range of  $-10 \leq h \leq 10$ ,  $-10 \leq k \leq 10$ ,  $0 \leq l \leq 7$ . The  $\omega$ - $2\theta$  scan technique was used to collect all x-ray data.

The cell constants for the data collections were determined from reflections found from a random search routine. Lorentz and polarization corrections were applied. A nonlinear correction based on the decay in the standard reflections was applied to the data although there was no measurable radiation decay. A series of azimuthal reflections was collected for each specimen. An empirical absorption correction was applied to the data for each specimen. Details of the x-ray single crystal experiments are given in Table III.

### III. Results

#### 1. Chemical Analysis

The results of chemical analysis performed on chunks of each arc-melt composition is shown in Table IV. The level of non-doped Z is relatively constant between the various compositions, carbon ranging from 120-300 ppm and nitrogen ranging from 53-200 ppm. However, the most interesting difference is the variation in oxygen content. For undoped, boron-, and nitrogen-doped  $\text{Ti}_5\text{Si}_3$ , the oxygen level is relatively constant at around 1000 ppm. For the carbon doped material, the oxygen level significantly decreases with increasing carbon content. Carbon may act as an oxygen getter, producing a gaseous species which evolves from the material. The accompanying decrease in carbon content would not be detectable given the significantly larger level of carbon added to the sample. The potential effect on critical material properties could be significant if this level of oxygen ( $\approx 1100$  ppm wt%) is found to have deleterious effects. The location of the various non-doped Z atoms is unknown. Oxygen is presumably in the form of both surface oxide and interstitial oxygen, while carbon and nitrogen could be interstitial or perhaps substituted on another lattice site such as silicon.

Table III: X-ray Single Crystal Experimental Variables

Empirical Formula	Ti <sub>5</sub> Si <sub>3</sub> O <sub>0.09</sub> (1)	Ti <sub>5</sub> Si <sub>3</sub> B <sub>0.45</sub> (2)	Ti <sub>5</sub> Si <sub>3</sub> Co <sub>0.31</sub> (1)	Ti <sub>5</sub> Si <sub>3</sub> N <sub>0.42</sub> (1)	Ti <sub>5</sub> Si <sub>3</sub> O <sub>0.43</sub> (1)
Crystal Size (mm)	0.18x0.12x0.04	0.58x0.10x0.07	0.23x0.10x0.10	0.50x0.10x0.10	0.23x0.10x0.10
Cell Dimensions					
a (Å)	7.4521(8)	7.464(1)	7.4477(7)	7.4309(7)	7.4356(7)
c (Å)	5.1522(15)	5.165(3)	5.153(1)	5.138(1)	5.131(1)
vol. (Å <sup>3</sup> )	247.79(8)	249.2(2)	247.54(7)	245.71(7)	245.68(6)
Z	2	2	2	2	2
Formula Weight	325.21	328.64	327.49	329.65	330.65
Density (Mg/m <sup>3</sup> )	4.359	4.380	4.394	4.456	4.470
μ (mm <sup>-1</sup> )	8.258	8.214	8.268	8.333	8.339
F <sub>000</sub>	305	309	307	309	311
Ref. Collected	1463	1467	1453	1431	1431
Ind. Reflections	154	154	153	151	151
Obs. Ref.	142	152	148	149	150
Min./Max. Trans.	0.703/1.000	1.000/0.449	1.0/0.691	0.979/0.861	0.924/0.699
Extinct. Corr.	0.0070(13)	0.1365(39)	0.1185(37)	0.0394(24)	0.1749(68)
Param. Refined	15	15	15	15	15
R1[ $I \geq 2\sigma(I)$ ]	0.0108	0.0092	0.0091	0.0092	0.0128
wR2	0.0223	0.0237	0.0200	0.0221	0.0292
Goof	1.096	1.110	1.293	1.316	1.397

$$R1 = \frac{\sum |F_o| - |F_c|}{\sum |F_o|}$$

$$wR2 = \sqrt{\frac{\sum [\omega(F_o^2 - F_c^2)^2]}{\sum [\omega(F_o^2)^2]}}$$

$$\text{Goof} = \sqrt{\frac{\sum [\omega(F_o^2 - F_c^2)^2]}{(n-p)}}$$

$$\text{where } \omega = 1/\left[\sigma^2(F_o^2) + (a \cdot P)^2 + b \cdot P + d + e \cdot \sin \theta\right]$$

Table IV: Chemical Analysis of Arc-Melted  $\text{Ti}_5\text{Si}_3\text{Z}_x$ 

Nominal Composition ( $\text{Z}_x$ )	Carbon (x)	Nitrogen (x)	Oxygen (x)	Boron (x)
$\text{Z}_x = \emptyset$	120 ppm	69 ppm	1100 ppm	+
$\text{Z}_x = \text{C}_{0.25}$	(0.251)	56 ppm	674 ppm	+
$\text{C}_{0.50}$	(0.579)	53 ppm	469 ppm	+
$\text{C}_{0.75}$	(0.709)	58 ppm	186 ppm	+
$\text{B}_{0.25}$	260 ppm	58 ppm	750 ppm	(0.183)
$\text{B}_{0.50}$	200 ppm	58 ppm	1100 ppm	(0.394)
$\text{B}_{0.75}$	180 ppm	58 ppm	940 ppm	(0.746)
$\text{N}_{0.25}$	150 ppm	(0.172)	910 ppm	+
$\text{N}_{0.50}$	200 ppm	(0.376)	1100 ppm	+
$\text{N}_{0.75}$	170 ppm	(0.520)	1200 ppm	+
$\text{O}_{0.25}$	290 ppm	120 ppm	(0.267)	+
$\text{O}_{0.50}$	300 ppm	170 ppm	(0.455)	+
$\text{O}_{0.75}$	250 ppm	200 ppm	(0.647)	+

+ Not analyzed

## 2. Room Temperature Lattice Parameters

The variation of lattice parameter with level of interstitial addition is shown for  $\text{Z} = \text{B}, \text{C}, \text{N}, \text{and O}$  in Figures 3-6. The addition of boron promotes a significant expansion in both parameters, with the change in each parameter being about the same. In contrast, the addition of oxygen promotes a strong contraction in each parameter. For the introduction of nitrogen, the a-parameter significantly contracts while the c-parameter is relatively unaffected. Carbon has an intermediate effect in which the c-parameter strongly expands while the a-parameter undergoes a minimum. For carbon, nitrogen, and oxygen, the effect of increasing additions appears to decrease and may indicate a solubility limit in

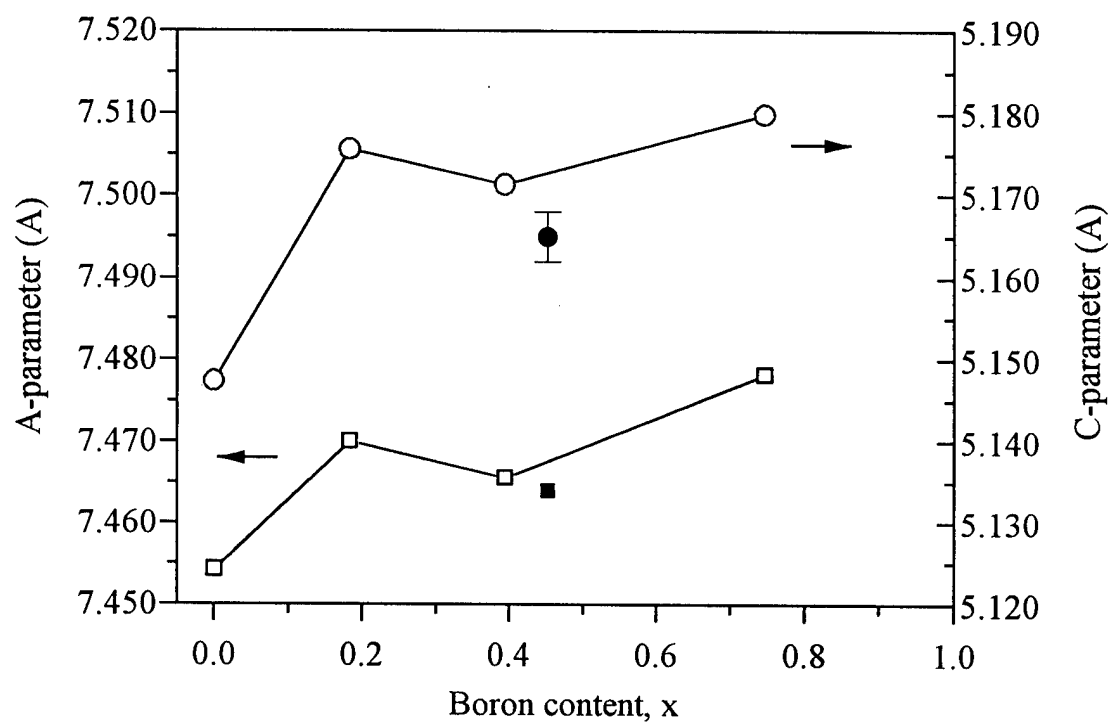


Figure 3: Variation of A and C lattice parameter with level of boron content. Open symbols denote parameters calculated from powder diffraction. Solid symbols denote parameters calculated from single crystal diffraction.

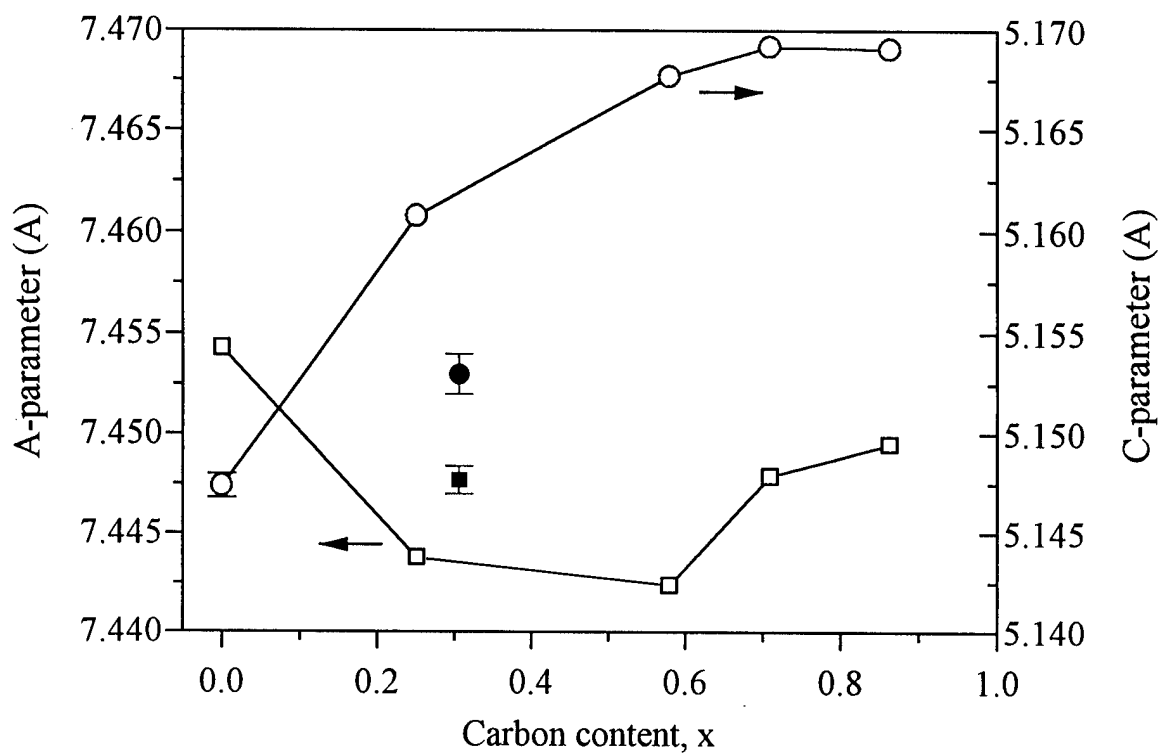


Figure 4: Variation of A and C lattice parameter with level of carbon content. Open symbols denote parameters calculated from powder diffraction. Solid symbols denote parameters calculated from single crystal diffraction.

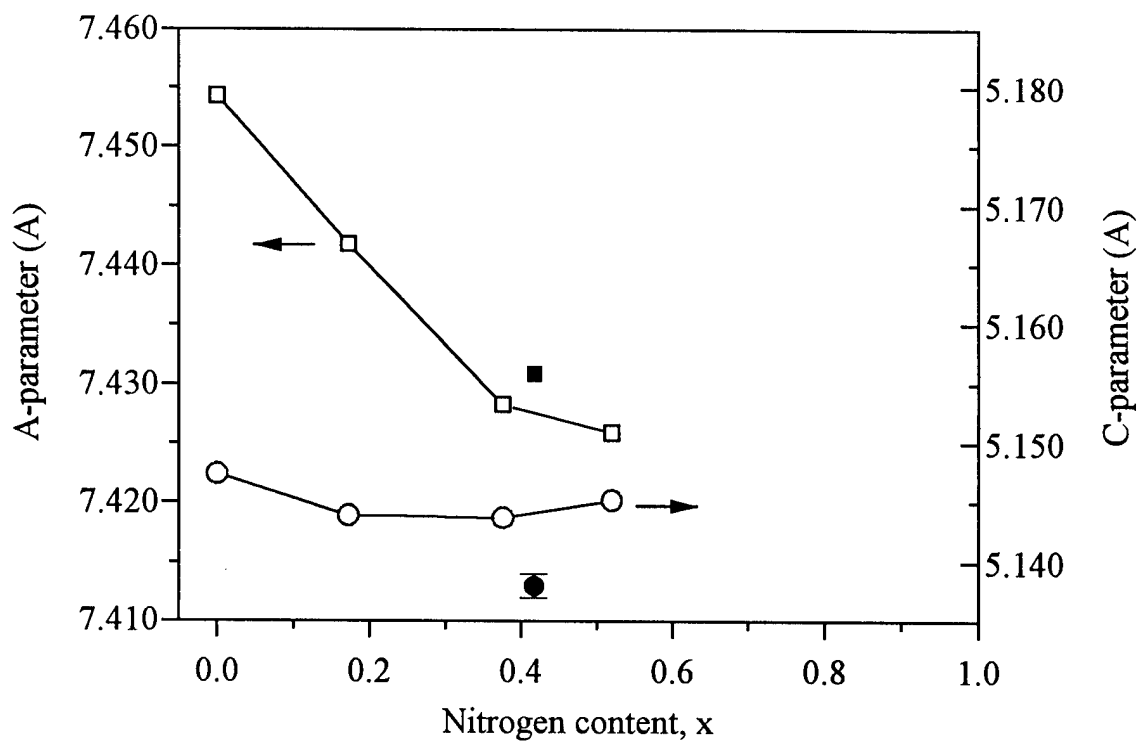


Figure 5: Variation of A and C lattice parameter with level of nitrogen content. Open symbols denote parameters calculated from powder diffraction. Solid symbols denote parameters calculated from single crystal diffraction.

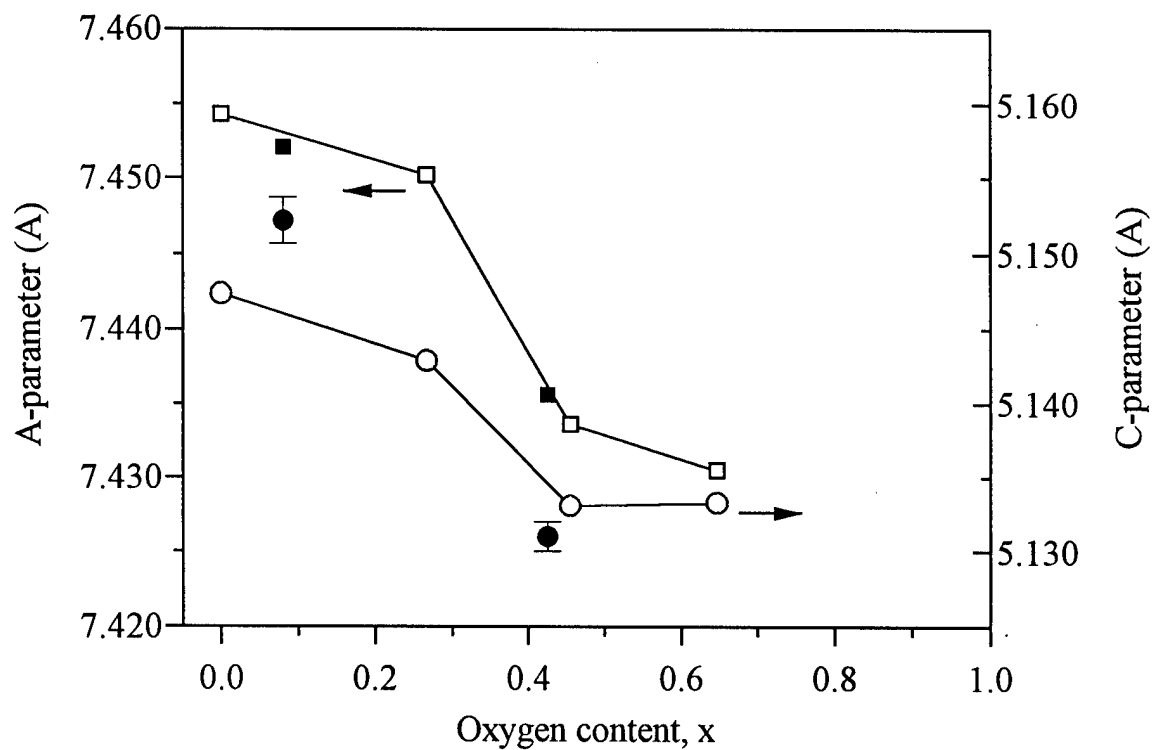


Figure 6: Variation of A and C lattice parameter with level of oxygen content. Open symbols denote parameters calculated from powder diffraction. Solid symbols denote parameters calculated from single crystal diffraction.



Ti<sub>5</sub>Si<sub>3</sub>. Boron does not exhibit this decreasing effect and so Ti<sub>5</sub>Si<sub>3</sub> may be able to incorporate additional boron.

No data exists for the direct comparison of the measured lattice parameters. However, the effect of similar interstitial additions on the lattice parameters of Zr<sub>5</sub>Si<sub>3</sub> and Zr<sub>5</sub>Sn<sub>3</sub> has been measured<sup>2,4</sup>. These data are summarized in Table V. The addition of carbon and oxygen to Zr<sub>5</sub>Si<sub>3</sub> causes behavior similar to that of Ti<sub>5</sub>Si<sub>3</sub>. Carbon causes a decrease in the a-parameter and an increase in the c-parameter with an overall volume

Table V: Unit Cell Values for A<sub>5</sub>Si<sub>3</sub>Z<sub>x</sub> Compositions

Compound	a (Å)	Δa (Å)	c (Å)	Δc (Å)	Volume (Å <sup>3</sup> )	ΔVol. (%)	Ref
Ti <sub>5</sub> Si <sub>3</sub>	7.4543(4)		5.1474(6)		247.70(3)		a
Ti <sub>5</sub> Si <sub>3</sub> C <sub>0.50</sub>	7.4424(3)	- 0.0119	5.1677(4)	+0.0203	247.89(2)	+0.077	a
Ti <sub>5</sub> Si <sub>3</sub> C <sub>0.90</sub>	7.4495(2)	- 0.0048	5.1691(3)	+0.0217	248.43(2)	+0.295	a
Ti <sub>5</sub> Si <sub>3</sub> O <sub>0.75</sub>	7.4305(4)	- 0.0238	5.1333(2)	- 0.0141	245.45(3)	- 0.908	a
Ti <sub>5</sub> Si <sub>3</sub> B <sub>0.75</sub>	7.478(1)	+0.0237	5.1799(7)	+0.0325	250.87(6)	+1.28	a
Ti <sub>5</sub> Si <sub>3</sub> N <sub>0.75</sub>	7.4259(5)	- 0.0284	5.1452(3)	- 0.0022	245.71(3)	- 0.803	a
Zr <sub>5</sub> Si <sub>3.1</sub>	7.9582(6)		5.5613(8)		305.03(6)		2
Zr <sub>5</sub> Si <sub>3</sub> C <sub>0.5</sub>	7.9409(5)	- 0.0173	5.6016(6)	+0.0403	305.90(5)	+0.285	2
Zr <sub>5</sub> Si <sub>3</sub> C	7.9400(6)	- 0.0182	5.6116(8)	+0.0503	306.38(7)	+0.443	2
Zr <sub>5</sub> Si <sub>3</sub> O	7.9200(6)	- 0.0382	5.5502(7)	- 0.0111	301.50(6)	- 1.16	2
Zr <sub>5</sub> Sn <sub>3</sub>	8.4560(7)		5.779(1)		357.86(9)		4
Zr <sub>5</sub> Sn <sub>3</sub> B	8.4936(4)	+0.0376	5.8029(5)	+0.0239	362.54(5)	+1.31	4
Zr <sub>5</sub> Sn <sub>3</sub> N	8.4040(8)	- 0.0520	5.7698(8)	- 0.0092	352.91(8)	- 1.38	4

<sup>a</sup>This work

increase. In contrast, oxygen decreases both parameters which results in a volume decrease. The addition of boron and nitrogen to  $Zr_5Sn_3$  also causes behavior similar to that of boron- and nitrogen-doped  $Ti_5Si_3$ . Boron causes a strong increase in both parameters with an increase in volume. Conversely, nitrogen decreases both parameters, as did oxygen, to decrease volume. This analysis has established that several at. % of boron, carbon, nitrogen, and oxygen can be added to  $Ti_5Si_3$  while still maintaining the  $Mn_5Si_3$ -type structure. This is consistent with available ternary phase diagrams which indicate that  $Ti_5Si_3Z_x$  may contain up to 10 at. % of carbon, nitrogen, and oxygen at 1000-1100°C<sup>26,27,28</sup>.

### 3. Single Crystal Results

The space group  $P6_3/mcm$  and the  $Mn_5Si_3$ -type structure were used for the initial structural model. All atoms were refined with anisotropic displacement parameters. Final refinements were done with SHELXL-93<sup>29,30</sup>. The (010) reflection was omitted from the refinements for each sample. Inclusion of this low-angle reflection caused problems with anisotropic refinement of the doped site.  $F_o$  was always about 20% higher than  $F_c$  for this reflection. The error is most likely due to inaccuracies in the extinction correction. Refinement calculations were performed using the SHELXTL-Plus<sup>31</sup> and SHELXL-93<sup>30</sup> programs.

The calculated stoichiometry for each analyzed single crystal is given in Table VI. There is some deviation of the refined composition from the chemically analyzed composition. This difference is likely related to the method of sampling for analysis. During the arc-melting process, rapid cooling occurs when the electrode is deenergized and the molten button solidifies in the chilled copper hearth in which it sits. This results in variation in stoichiometry within the button. Since the arc-melt buttons were not

annealed, composition of individual single crystals which were used for the x-ray analysis may vary. The composition determined by chemical analysis reflects the average composition since a larger amount of material is analyzed. Similarly, lattice parameters determined by powder x-ray diffraction are more indicative of the average composition since grinding to produce a powder sample mixes the material.

The undoped crystal refined better when including interstitial oxygen in the structure. Oxygen presence is expected because the arc-melting process does not establish an oxygen-free atmosphere, as evidenced by chemical analysis. It is possible that the added dopant does not completely displace all of the oxygen and that some oxygen may still remain interstitially within the structure. However, the overall effect would be

Table VI: Stoichiometry of Arc-Melted Materials

Nominal Composition	Chemical Analysis	Single Crystal Analysis
$\text{Ti}_5\text{Si}_3\text{O}_{0.08}$	$x = 0.022$	$x = 0.09(1)$
$\text{Ti}_5\text{Si}_3\text{B}_{0.50}$	$x = 0.41$	$x = 0.45(2)$
$\text{Ti}_5\text{Si}_3\text{C}_{0.25}$	$x = 0.25$	$x = 0.31(1)$
$\text{Ti}_5\text{Si}_3\text{N}_{0.50}$	$x = 0.38$	$x = 0.42(1)$
$\text{Ti}_5\text{Si}_3\text{O}_{0.50}$	$x = 0.46$	$x = 0.43(1)$

minimal since the concentration of the principal dopant is at least an order of magnitude larger than the residual oxygen, seen in Table IV. The effect of this residual interstitial oxygen could be determined by constraining the amount of oxygen in the structure and re-refining the single crystal data. Any statistically significant differences in the stoichiometry and bond lengths would indicate the relative effect of the residual oxygen.

The results of the single crystal analyses are shown below in Table VII, together with the results of a single crystal study of  $\text{Ti}_5\text{Si}_3\text{O}$  by Perchenek<sup>32</sup>. The results from this work agree well with those of Perchenek. In general, the data of Perchenek show a greater change in bond lengths, and this likely results from the increased oxygen content of Perchenek's material.

Table VIII shows the crystal structure refinement results by Kwon and Corbett<sup>4</sup> for  $\text{Zr}_5\text{Sn}_3\text{C}$  and  $\text{Zr}_5\text{Sn}_3\text{O}$ . The addition of carbon caused the interstitial cavity, given by  $\text{Zr2-Z}$ , to decrease by 0.08 Å, and the edges of the Zr trigonal antiprisms, given by  $\text{Zr2-Zr2}$ , to decrease by 0.10-0.12 Å. All  $\text{Zr2-Sn}$  distances increased, with the interchain and out-of-plane distances about equally affected. The in-plane distance was only slightly increased. The addition of oxygen causes similar changes in bond lengths. This behavior is also observed for  $\text{Ti}_5\text{Si}_3\text{C}_x$  and  $\text{Ti}_5\text{Si}_3\text{O}_x$ .

#### IV. Discussion

The unit cell constants determined from the single crystal study differ somewhat from the trend of unit cell constants determined from powder x-ray diffraction. Figures 3-6 show the single crystal cell constants plotted as solid symbols. The unit cell constants determined by powder x-ray diffraction reflect a sample which is not compositionally homogeneous, compared to the compositionally homogeneous single crystals. The powder data reflects an average composition of the sample taken from the arc-melted button.

The change in the  $a$  and  $c$ -parameters can be related to changes in local bonding caused by introduction of the interstitial atom. The effect of the interstitial addition can be characterized by the  $\text{Ti2-Z}$  bond length, indicating the size of the interstitial cavity, and the octahedral nature of the  $\text{Ti2}$  trigonal antiprismatic unit, indicated by the difference of

Table VII: Bond Lengths for Various Interstitial Additions (Z) to  $\text{Ti}_5\text{Si}_3\text{Z}_x$  (Å)

Bond Type	Empty	Z = B	Z = C	Z = N	Z = O	$\text{Ti}_5\text{Si}_3\text{O}^{33}$
Ti2 - Z	2.2645(4)	2.2461(5)	2.2305(3)	2.2024(4)	2.2105(4)	2.183(3)
Ti2 - Si						
interchain	2.6650(8)	2.6757(6)	2.6799(5)	2.6833(6)	2.6735(6)	2.644(3)
out-of-plane	2.7865(7)	2.8118(13)	2.8119(6)	2.8227(6)	2.8162(5)	2.851(4)
in-plane	2.5642(6)	2.5804(5)	2.5757(4)	2.5808(5)	2.5849(5)	2.609(3)
Ti1 - Si	2.6323(3)	2.6307(5)	2.6240(3)	2.6124(3)	2.6123(3)	2.593(3)
Ti2 - Ti2						
out-of-plane	3.2256	3.1697(12)	3.1550	3.1306(6)	3.1341(5)	3.118(4)
in-plane	3.1789(7)	3.1829	3.1537(6)	3.0988(7)	3.1181(7)	3.056(4)
Ti1 - Ti2	3.1241(4)	3.1458(6)	3.1470(3)	3.1563(3)	3.1512(3)	3.159(4)
Ti1 - Ti1	2.5761(7)	2.5825(14)	2.5766(6)	2.5691(7)	2.5655(5)	2.571(3)

Table VIII: Bond Distances<sup>4</sup> in  $\text{Zr}_5\text{Sn}_3\text{Z}$  (Å)

Bond Type	$\text{Zr}_5\text{Sn}_3^+$	$\text{Zr}_5\text{Sn}_3\text{C}$	$\text{Zr}_5\text{Sn}_3\text{O}$
Zr2 - Z	2.536	2.459(1)	2.4562(8)
Zr2 - Sn			
interchain	3.068	3.102(2)	3.093(1)
out of plane	3.142	3.1973(8)	3.1875(6)
in plane	2.903	2.9142(9)	2.9190(5)
Zr1 - Sn	2.984	2.9641(3)	2.9582(2)
Zr2 - Zr2			
out of plane	3.565	3.443(2)	3.445(2)
in plane	3.614	3.5118(7)	3.5017(6)
Zr1 - Zr2	3.566	3.605(1)	3.6004(6)

+ Extrapolated from data for  $\text{Zr}_5\text{Sn}_3\text{Sn}_{0.10}$  and  $\text{Zr}_5\text{Sn}_3\text{Sn}_{0.18}$ .

the Ti2-Ti2 (out-of-plane) and the Ti2-Ti2 (in-plane) bond lengths. These differences are given below in Table IX. For all additions, contraction of the interstitial cavity occurs, suggesting bonding between the Ti2 atoms and Z atoms. Even for boron in which both lattice parameters expand, the cavity contracts. As the Ti2-Ti2 difference approaches zero, the stability of the trigonal antiprismatic unit should increase due to the increased symmetry of the bonding between Ti2 atoms. This decrease is accompanied by a decrease in cavity contraction, and together they affect the a-parameter and c-parameter. Nitrogen and oxygen promote the strongest cavity contraction and thus a contraction is observed in both the a-parameter and c-parameter. Carbon promotes a smaller cavity contraction, and this contributes to a decrease in the a-parameter despite a nearly constant c-parameter. Finally, boron promotes the smallest cavity contraction, and this occurs even though both parameters increase.

While the decrease in Ti2-Z dimension suggests bonding between Ti2 and Z, bond strength does not necessarily correlate to bond length<sup>33</sup>. Extended Huckel band calculations are planned to quantify the extent of bonding between Ti2 atoms and Z atoms.

## V. Conclusions

Ti<sub>5</sub>Si<sub>3</sub> can incorporate ternary additions such as boron, carbon, nitrogen, and oxygen. X-ray single crystal diffraction studies have verified that these additions are accommodated in the interstitial sites within the trigonal antiprismatic chains of Ti2 atoms of the Mn<sub>5</sub>Si<sub>3</sub>-type structure of Ti<sub>5</sub>Si<sub>3</sub>. Bonding between the interstitial atom and Ti2 is suggested by cavity contraction. There are significant changes in bond lengths as a result of these additions. Most notably there is an increase in the Ti2-Si and decrease in the Ti2-Ti2 bond lengths.

Table IX: Influence of Interstitial Additions on Bonding Nature

Composition	(Ti2-Ti2) <sup>a</sup> Difference	(Ti2-Z) Contraction
Ti <sub>5</sub> Si <sub>3</sub> O <sub>0.09</sub>	+0.0467	0.0000
Ti <sub>5</sub> Si <sub>3</sub> N <sub>0.42</sub>	+0.0318	0.0621
Ti <sub>5</sub> Si <sub>3</sub> O <sub>0.43</sub>	+0.0160	0.0540
Ti <sub>5</sub> Si <sub>3</sub> C <sub>0.31</sub>	+0.0013	0.0340
Ti <sub>5</sub> Si <sub>3</sub> B <sub>0.45</sub>	-0.0132	0.0184

<sup>a</sup> (out-of-plane)-(in-plane)

### Acknowledgements

Ames Laboratory is operated for the U. S. Department of Energy by Iowa State University under contract number W-7405-ENG-82. This research was supported by the Office of Basic Energy Science, Materials Science Division.

### References

- <sup>1</sup>E. Garcia and J. D. Corbett, "Chemistry of Polar Intermetallic Compounds. Study of Two Zr<sub>5</sub>Sb<sub>3</sub> Phases, Hosts for a Diverse Interstitial Chemistry," *Inorganic Chem.*, **27** [13], 2353-2359 (1988).
- <sup>2</sup>Y. Kwon, M. A. Rzeznik, A. Guloy, and J. D. Corbett, "Impurity Stabilization of Phases with the Mn<sub>5</sub>Si<sub>3</sub>-Type Structure. Questions Regarding La<sub>5</sub>Sn<sub>3</sub> and Zr<sub>5</sub>Si<sub>3</sub>," *Chem. Mater.*, **2** [5], 546-550 (1990).
- <sup>3</sup>E. Garcia and J. D. Corbett, "Chemistry in the Polar Intermetallic Host Zr<sub>5</sub>Sb<sub>3</sub>. Fifteen Interstitial Compounds," *Inorganic Chem.*, **29** [18] 3274-3282 (1990).

- <sup>4</sup>Y. Kwon and J. D. Corbett, "Chemistry in Polar Intermetallic Compounds. The Interstitial Chemistry of  $Zr_5Sn_3$ ," *Chem. Mater.*, **4** [6], 1348-1355 (1992).
- <sup>5</sup>D. L. Anton, D. M. Shah, D. N. Duhal, and A. F. Giamei, "Selecting High-Temperature Structural Intermetallic Compounds: The Engineering Approach," *Jour. Metals*, 12-17, Sept. 1989.
- <sup>6</sup>A. I. Taub and R. L. Fleischer, "Intermetallic Compounds for High-Temperature Structural Use", *Science*, **243**, 616-621(1989).
- <sup>7</sup>P. J. Meschter and D. S. Schwartz, "Silicide-Matrix Materials for High-Temperature Applications", *Jour. Metals*, 52-55, Nov. 1989.
- <sup>8</sup>D. M. Shah, D. Berczik, D. L. Anton, R. Hecht, "Appraisal of other Silicides as Structural Materials", *Mat. Sci. Eng.*, **A155**, 45-57 (1992).
- <sup>9</sup>K. S. Kumar and C. T. Liu, "Ordered Intermetallic Alloys, Part II: Silicides, Trialuminides, and Others", *Jour. Metals*, 28-34, June 1993.
- <sup>10</sup>A. J. Thom, M. K. Meyer, Y. Kim, and M. Akinc, "Evaluation of  $A_5Si_3Z_x$  Intermetallics for Use as High Temperature Structural Materials," Min. Met. Mater. Soc. Symp. Proc., edited by T. S. Srivatsan and V. A. Ravi, Processing and Fabrication of Advanced Materials for High-Temperature Applications - III, 413-438 (1994).
- <sup>11</sup>H. Nowotny, "Alloy Chemistry of Transition Element Borides, Carbides, Nitrides, Aluminides, and Silicides," Electronic Structure and Alloy Chemistry of the Transition Elements, ed. P. Beck (New York, NY:, John Wiley & Sons, 1963), 179-220.
- <sup>12</sup>B. Aronsson, "Borides and Silicides of the Transition Metals", *Arkiv Kemi*, **16**, 379-423 (1960).
- <sup>13</sup>E. Parthe, "Contributions to the Nowotny Phases", *Powder Metallurgy Bulletin*, **8** [1/2] 23-34 (1957).
- <sup>14</sup>L. Brewer and O. Krikorian, "Reactions of Refractory Silicides with Carbon and Nitrogen," *J. Electrochem. Soc.*, **103**, 38-51 (1956).
- <sup>15</sup>R. Kieffer, F. Benesovsky, and B. Lux, "Untersuchungen uber NOWOTNY-Phasen," *Planseeberichte Pulvermetallurgie.*, **4**, 30-36 (1956).



- <sup>16</sup>E. Parthe, cited by B. Aronsson in "Borides and Silicides of the Transition Metals", *Arkiv Kemi*, **16**, 379-423 (1960).
- <sup>17</sup>E. Parthe and W. Jeitschko, "A Neutron Diffraction Study of the Nowotny Phase  $\text{Mo}_{1-x}\text{Si}_3\text{C}_x$ ", *Acta Cryst.*, **19**, 1031-1037 (1965).
- <sup>18</sup>A. M. Guloy and J. D. Corbett, "The Lanthanum-Germanium System. Nineteen Isostructural Interstitial Compounds of the  $\text{La}_5\text{Ge}_3$  Host," *Inorgan. Chem.*, **32** [16], 3532-3540 (1993).
- <sup>19</sup>T. B. Massalski et al., eds., *Binary Alloy Phase Diagrams*, **3**, (Materials Park, OH: American Society for Metals, 1990) 3370.
- <sup>20</sup>T. Kajitani, T. Kawase, K. Yamada, and M. Hirabayashi, "Site Occupation and Local Vibration of Hydrogen Isotopes in Hexagonal  $\text{Ti}_5\text{Si}_3\text{H(D)}_{1-x}$ ", *Trans. Japan Inst. Metals*, **27** [9], 639-647 (1986).
- <sup>21</sup>A. J. Thom and M. Akinc, "Improved Oxidation Resistance of  $\text{Ti}_5\text{Si}_3$  by Small Atom Doping," to be published.
- <sup>22</sup>A. J. Thom, M. Akinc, O. B. Cavin, and C. R. Hubbard, "Thermal Expansion Anisotropy of  $\text{Ti}_5\text{Si}_3$ ," *Jour. Mat. Sci. Lett.*, **13**, 1657-1660 (1994).
- <sup>23</sup>A. J. Thom, M. Akinc, O. B. Cavin, and C. R. Hubbard, unpublished research.
- <sup>24</sup>T. Y. Kosolapova, *Handbook of High Temperature Compounds: Properties, Production, Application*, (New York, NY: Hemisphere Publishing, 1990) 162.
- <sup>25</sup>T. B. Massalski et al., eds., *Binary Alloy Phase Diagrams*, **3**, (Materials Park, OH: American Society for Metals, 1990) 3324.
- <sup>26</sup>J. I. Goldstein, S. K. Choi, F. J. J. Van Loo, G. F. Bastin, and R. Metselaar, "Solid State Reactions and Phase Relations in the Ti-Si-O System at 1373K", *Journal Amer. Ceram. Soc.*, **78** [2], 313-322 (1995).
- <sup>27</sup>S. Arunajatesan and A. H. Carim, "Synthesis of Titanium Silicon Carbide," *Journal Amer. Ceram. Soc.*, **78** [3], 667-672 (1995).

<sup>28</sup>S. Sambasivan and W. T. Petuskey, "Phase Chemistry in the Ti-Si-N System: Thermochemical Review with Phase Stability Diagrams", *Journal Mater. Res.*, **9** [9], 2362-2369 (1994).

<sup>29</sup>SHELXL-93, G.M. Sheldrick, *J. Appl. Cryst.*, in preparation.

<sup>30</sup>All X-ray scattering factors and anomalous dispersion terms were obtained from the "International Tables for Crystallography", **C**, 4.2.6.8 and 6.1.1.4.

<sup>31</sup>SHELXTL-PLUS, Siemens Analytical Xray, Inc., Madison, WI.

<sup>32</sup>N. Perchenek, "Metallreiche Titansulfide und Die Phase  $\text{Ti}_5\text{Si}_3\text{O}$ ", thesis, Universitat Stuttgart (1988).

<sup>33</sup>J. D. Corbett, "Chevrel Phases: An Analysis of Their Metal-Metal Bonding and Crystal Chemistry," *J. Solid State Chem.*, **39**, 56-74 (1981).

CHAPTER 3:  
THERMAL EXPANSION ANISOTROPY OF  $\text{Ti}_5\text{Si}_3$

A paper published in the *Journal of Materials Science Letters*<sup>1</sup>

Andrew J. Thom and Mufit Akinc

Ames Laboratory and Department of Materials Science and Engineering

O.B. Cavin and C. R. Hubbard

High Temperature Materials Laboratory, Oak Ridge National Laboratory

**Abstract**

$\text{Ti}_5\text{Si}_3$  and  $\text{Ti}_5\text{Si}_3\text{C}_{0.85}$  were synthesized by arc-melting. The materials were characterized by chemical analysis and x-ray diffraction and were judged to be single phase. Coefficient of thermal expansion (CTE) along the a-axis and c-axis was measured by the method of high temperature x-ray diffraction. Bulk CTE of  $\text{Ti}_5\text{Si}_3$  was measured by thermomechanical analysis. The addition of carbon to  $\text{Ti}_5\text{Si}_3$  significantly reduced the intrinsic CTE anisotropy. For  $\text{Ti}_5\text{Si}_3$  from 298-873K,  $\alpha_a = 8.68 \pm 0.14$  and  $\alpha_c = 20.4 \pm 0.4$  ppm/K. For  $\text{Ti}_5\text{Si}_3\text{C}_{0.85}$  from 298-873K,  $\alpha_a = 9.43 \pm 0.29$  and  $\alpha_c = 17.9 \pm 0.6$  ppm/K.

---

<sup>1</sup>Reprinted with permission from Journal of Materials Science Letters 1994, 13, 1657-1660. Copyright © Chapman and Hall.

## I. Introduction

Intermetallics have long been considered as prospective high temperature structural materials. Advanced projects such as the National Aerospace Plane (NASP) rely on the development of a new generation of materials. Anticipated operating environments are too severe for conventional materials such as superalloys. Refractory transition metal silicides are candidate materials [1]. Among these materials,  $\text{Ti}_5\text{Si}_3$  is particularly interesting due to its low density, high melting point, and potential oxidation resistance [2, 3].

$\text{Ti}_5\text{Si}_3$  has an interesting crystal structure. It possesses a hexagonal unit cell with two formula units per unit cell. It has the  $\text{Mn}_5\text{Si}_3$ -type structure, and an [001] projection of the unit cell is shown in Figure 1. The structure is characterized by chains of titanium and silicon atoms in the [001] or c-direction. One group of titanium atoms (Ti1) forms linear chains at  $(1/3, 2/3, z)$  and  $(2/3, 1/3, z)$  with  $z=0, 1/2$  while the other group (Ti2) forms chains of trigonal antiprisms at the corners of the unit cell. Silicon atoms (Si) form trigonal layers which create chains of irregular trigonal antiprisms. The  $\text{Mn}_5\text{Si}_3$ -type structure has the ability to incorporate a wide variety of interstitial atoms at the corners of the unit cell [4,5,6,7]. Linear chains of interstitial atoms occupy the centers of trigonal antiprisms of the (Ti2) titanium atoms. These interstitial additions may significantly affect the bonding of the structure to change the thermal expansion, oxidative, and mechanical behavior.

Critical to evaluating the engineering usefulness of such materials is the ability to hot consolidate the material into a dense, crack-free body. Structure sensitive mechanical properties such as hardness, fracture toughness, and modulus are influenced by the microstructure. Materials which possess a large thermal expansion anisotropy are

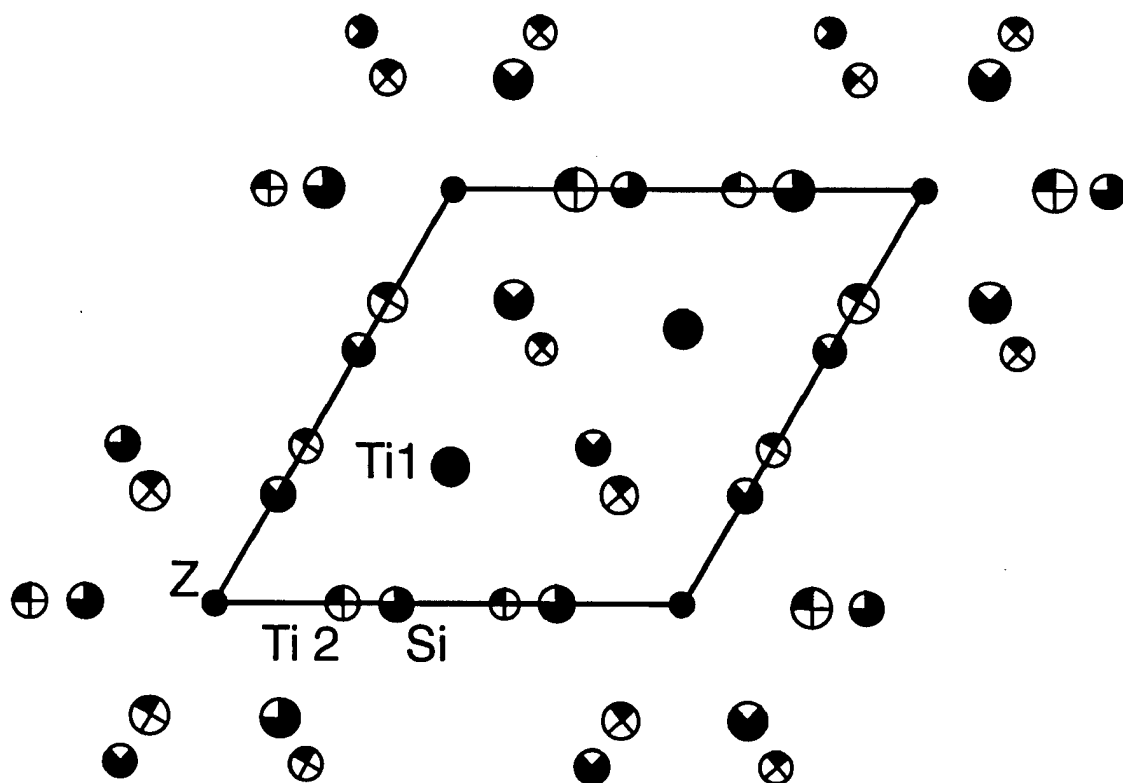


Figure 1: [001] projection of  $\text{Ti}_5\text{Si}_3$  which has the  $\text{Mn}_5\text{Si}_3$ -type structure. The large circles are Ti, medium circles are Si, and the small circles are interstitial sites. Height symbol key:  $\oplus$  ( $z=0, \frac{1}{2}$ ),  $\oplus\bullet$  ( $z=\frac{1}{4}$ ),  $\bullet$  ( $z=\frac{3}{4}$ ).

particularly difficult to process into dense, crack-free bodies. This anisotropy in coefficient of thermal expansion (CTE) contributes to residual stresses within and between grains during cooling from the consolidating temperature and contributes to transgranular and/or intergranular microcracking [8]. The extent of the microcracking can be reduced by decreasing the grain size of the consolidated body to less than some critical grain size for microcracking [9]. Any attempt to model the critical grain size necessitates knowledge of the crystallographic CTE values.

Determination of the crystallographic CTE is thus necessary to understand the processing of anisotropic materials. Previous work has shown that  $\text{Ti}_5\text{Si}_3$  exhibits transgranular microcracking [1,10]. Since  $\text{Ti}_5\text{Si}_3$  has a hexagonal unit cell, it is expected to exhibit CTE anisotropy. The CTE of  $\text{Ti}_5\text{Si}_3$  along the a-axis and c-axis, denoted as  $\alpha_a$  and  $\alpha_c$ , has been estimated from bulk CTE measurements to be 3.1 ppm/K and 10.7 ppm/K, respectively [2]. However, no data exist for the direct measurement of  $\alpha_a$  and  $\alpha_c$ . (During revision of this publication, a single crystal measurement of  $\alpha_a$  and  $\alpha_c$  was made [11]). In this study,  $\alpha_a$  and  $\alpha_c$  are measured by the technique of high temperature x-ray powder diffraction (HTXRPD).  $\text{Ti}_5\text{Si}_3$  and carbon doped  $\text{Ti}_5\text{Si}_3$  are investigated. Bulk CTE measurements are made to correlate with the HTXRPD measurements.

## II. Experimental

The material to be measured was prepared by arc-melting under argon.  $\text{Ti}_5\text{Si}_3$  was produced from a stoichiometric mixture of titanium and silicon, and a nominal  $\text{Ti}_5\text{Si}_3\text{C}_{0.9}$  composition was produced from a stoichiometric mixture of  $\text{Ti}_5\text{Si}_3$  and graphite. Zirconium metal was first melted inside the arc-melter to getter oxygen prior to melting the elements. Batches were then triple melted to promote homogenization.

The high-temperature x-ray powder diffractometer used has a stationary sample holder within an atmospheric controlled x-ray diffraction furnace. The sample holder also functions as a resistive heater strip. Typical heater strip materials include platinum, molybdenum, tungsten, and tantalum. However, since silicon forms binary compounds with all of these metals, a thin quartz wedge was used as a setter plate. A quantity of the arc-melted  $\text{Ti}_5\text{Si}_3$  was ground in an agate mortar and pestle to -325 mesh ( $<43\text{ }\mu\text{m}$ ). A small amount of the -325 mesh powder was floated onto the quartz wedge using ethanol. The quartz wedge was then placed on the platinum heater strip, and the system was evacuated to  $1.3 \times 10^{-4}$  Pa for 18 hours. X-ray diffraction patterns using  $\text{Cu K}\alpha$  radiation were then collected using a  $0.02^\circ$  step size at a scan rate of  $1^\circ 2\theta/\text{minute}$ . Patterns were collected during heating and cooling over the temperature range 298-873 K. The temperature was measured using a Pt/Pt10Rh thermocouple placed in contact with the Pt heating strip. Temperature calibration was achieved by measuring the thermal expansion of MgO under identical experimental conditions [12].

Peak positions and intensities were determined using the profile-fitting capabilities of the diffractometer software. Deconvolution of  $\text{K}\alpha_1$  and  $\text{K}\alpha_2$  peaks was achieved by use of the software. Lattice parameters were determined using a least-squares refinement program [13]. Bulk CTE was measured from 298-873 K using a thermomechanical analyzer (TMA). Samples for bulk CTE measurements were hot isostatically pressed from arc-melted powders and cut into  $3.5 \times 3.5 \times 6.5$  mm specimens. Samples were measured on the long dimension and heated at 5 K/min in flowing argon.

### III. Results and Discussion

Room temperature powder x-ray diffraction patterns of the arc-melted powders of  $\text{Ti}_5\text{Si}_3$  and  $\text{Ti}_5\text{Si}_3\text{C}_{0.9}$  are shown in Figure 2. The patterns match closely, and no unmatched peaks were found in the  $\text{Ti}_5\text{Si}_3$  pattern.  $\text{Ti}_5\text{Si}_3\text{C}_{0.9}$  contained six additional minor peaks which could not be matched. Chemical analysis of both compositions is shown in Table I.

Table I: Chemical Analysis of Arc-Melted Compositions

	$\text{Ti}_5\text{Si}_3$	$\text{Ti}_5\text{Si}_3\text{C}_{0.85}$
Ti	73.02%	
Si	26.38%	
C	120 ppm	3.10%
N	69 ppm	58 ppm
O	1100 ppm	186 ppm

The major impurity is oxygen, and it is believed that this oxygen is incorporated into the interstitial sites of the structure. The analysis of the carbon containing sample indicated an actual composition of  $\text{Ti}_5\text{Si}_3\text{C}_{0.85}$ , assuming all carbon occupies the interstitial sites. The oxygen content has decreased presumably due to carbon substituting for some of the interstitial oxygen.

Measured room temperature lattice parameters are shown in Table II. These compare well with the reported values for  $\text{Ti}_5\text{Si}_3$  [14]. For all measured lattice parameters, the standard errors are less than 0.00010 nm which corresponds to less than half the symbol size used in figures. Therefore the error bars have been omitted.



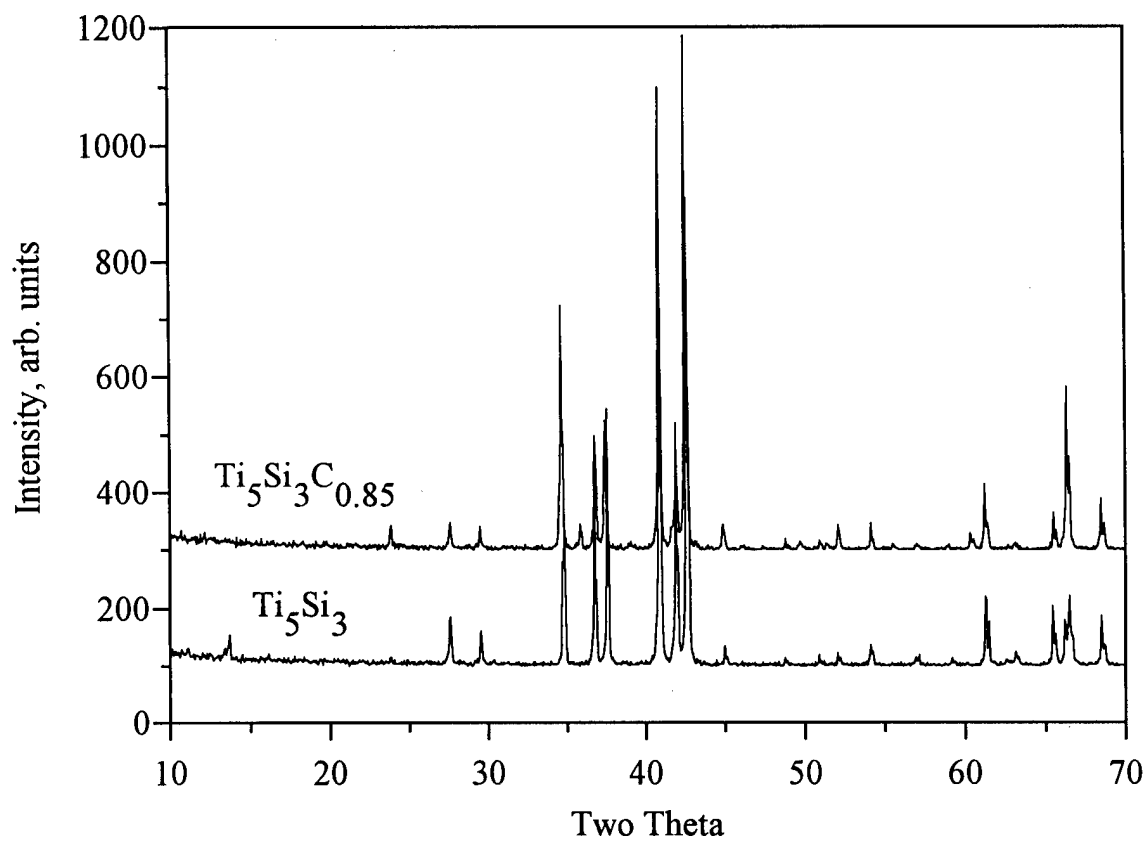


Figure 2: X-ray diffraction pattern of arc-melted  $\text{Ti}_5\text{Si}_3$  and  $\text{Ti}_5\text{Si}_3\text{C}_{0.85}$ .

Table II: Room Temperature Lattice Parameters

	a (nm)	c (nm)
Ti <sub>5</sub> Si <sub>3</sub> (this study)	0.74514(4)	0.51464(3)
Ti <sub>5</sub> Si <sub>3</sub> (literature)	0.74440(4)	0.51430(5)
Ti <sub>5</sub> Si <sub>3</sub> C <sub>0.85</sub> (this study)	0.74438(4)	0.51643(4)

Figure 3 shows the linear temperature dependence of the a-parameter and c-parameter of Ti<sub>5</sub>Si<sub>3</sub> and Ti<sub>5</sub>Si<sub>3</sub>C<sub>0.85</sub>. There appears to be some curvature in the plots, but higher order terms are not statistically significant. The linear thermal expansion coefficient is defined as

$$\alpha = \frac{1}{l_0} \frac{dl}{dT} \quad (1)$$

where  $l$  is a function of temperature and  $l_0$  is the lattice parameter at 298 K. The Ti<sub>5</sub>Si<sub>3</sub> unit cell expands at a greater rate in the c-direction. There has been expansion in the c-direction and contraction in the a-direction due to the addition of carbon to Ti<sub>5</sub>Si<sub>3</sub>. Table III gives the slope and standard error for the plots in Figure 3. For both compositions, the calculated linear thermal expansion coefficients in the c-direction are much larger than in the a-direction. The calculated thermal expansion coefficients are independent of temperature and are listed in Table III.

For a hexagonal crystal, the upper and lower bound of the bulk CTE can be estimated by the Voight and Reuss methods, respectively [15] :

$$\alpha_v = \frac{2\alpha_a + \alpha_c}{3} \quad (2)$$

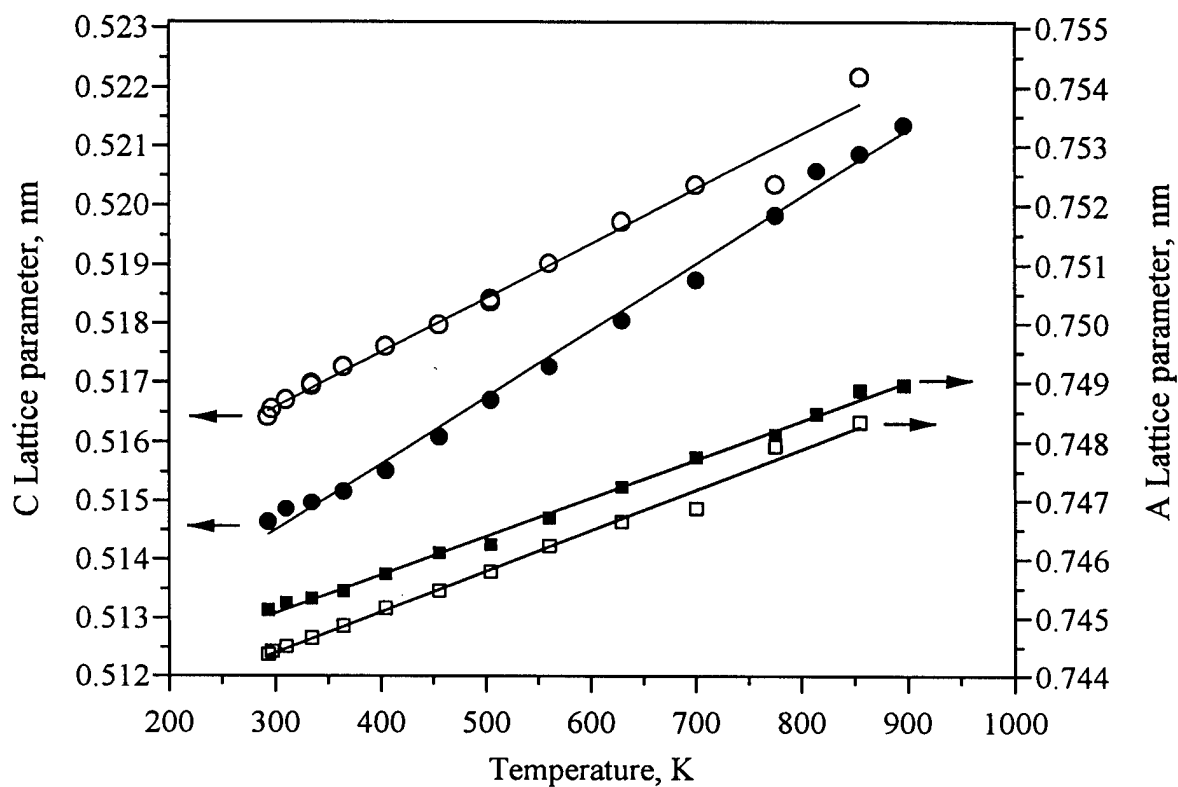


Figure 3: Lattice parameters of  $\text{Ti}_5\text{Si}_3$  and  $\text{Ti}_5\text{Si}_3\text{C}_{0.85}$  versus temperature. Symbol key:  
 ■  $\text{Ti}_5\text{Si}_3$  a-parameter, □  $\text{Ti}_5\text{Si}_3\text{C}_{0.85}$  a-parameter, ●  $\text{Ti}_5\text{Si}_3$  c-parameter,  
 ○  $\text{Ti}_5\text{Si}_3\text{C}_{0.85}$  c-parameter.

Table III: Thermal Expansion Data

	Slope $\pm$ Std. Err. (nm/K) $\times 10^6$	CTE $\pm$ Std. Err. (ppm/K)
$\text{Ti}_5\text{Si}_3$		
a-axis	$6.47 \pm 0.10$	$8.68 \pm 0.14$
c-axis	$10.5 \pm 0.2$	$20.4 \pm 0.4$
$\text{Ti}_5\text{Si}_3\text{C}_{0.85}$		
a-axis	$7.02 \pm 0.21$	$9.43 \pm 0.29$
c-axis	$9.23 \pm 0.33$	$17.9 \pm 0.6$

$$\alpha_r = \frac{3}{\frac{2}{\alpha_a} + \frac{1}{\alpha_c}} \quad (3)$$

The mean of the Reuss and Voigt estimates gives a good approximation of the true bulk CTE. From the values of  $\alpha_a$  and  $\alpha_c$  obtained by HTXRPD, the bulk CTE of  $\text{Ti}_5\text{Si}_3$  and  $\text{Ti}_5\text{Si}_3\text{C}_{0.85}$  is estimated to be  $11.6 \pm 0.1$  and  $11.7 \pm 0.2$  ppm/K, respectively. Figure 4 shows the expansion of a bulk  $\text{Ti}_5\text{Si}_3$  sample. The approximately linear temperature dependence gives a constant bulk CTE value of  $10.4 \pm 0.1$  ppm/K. Summarized in Table IV, the measured bulk CTE value of  $\text{Ti}_5\text{Si}_3$  compares reasonably well to the estimated value.

The measured room temperature lattice parameters listed in Table II show that the unit cell measured in this study was slightly larger than the unit cell of the reference value. Quakernaat and Visser made their measurements on a relatively pure sample which fit the theoretical composition and showed an impurity content of carbon, boron, nitrogen, and

oxygen of less than 500 ppm, 1000 ppm, 10000 ppm, and 1000 ppm, respectively. They were unable to determine either the presence or absence of nitrogen by emission spectrographic analysis. The samples used in this study were essentially nitrogen free, and nitrogen levels up to 10000 ppm might cause a contraction of the a-parameter and c-parameter of Quakernaat and Visser's sample.

Table IV: Bulk CTE Values

	Estimated	Measured	Literature
$\text{Ti}_5\text{Si}_3$	$11.6 \pm 0.1$	$10.4 \pm 0.1$	$11.0^a$ $7.1-9.1^b$
$\text{Ti}_5\text{Si}_3\text{C}_{0.85}$	$11.7 \pm 0.2$	not measured	not available

<sup>a</sup>450-1350 K; Ref. 16

<sup>b</sup>293-1273 K; Ref. 2

The addition of carbon to  $\text{Ti}_5\text{Si}_3$  caused expansion in the c-parameter and contraction in the a-parameter. No data exist for the direct comparison of these results. However, the effect of interstitial additions on the lattice parameters of  $\text{Zr}_5\text{Si}_3$  and  $\text{Zr}_5\text{Sn}_3$  has been measured [5,7]. These data are summarized in Table V. The addition of carbon to  $\text{Zr}_5\text{Si}_3$  and  $\text{Zr}_5\text{Sn}_3$  causes behavior similar to that of  $\text{Ti}_5\text{Si}_3$ . The unit cell contracts in the a-direction and expands in the c-direction.  $\text{Zr}_5\text{Si}_3$  also exhibits an increase in unit cell volume with the addition of carbon.  $\text{Zr}_5\text{Sn}_3$  shows a decrease in unit cell volume, which occurs due to the proportionately larger decrease in the a-parameter. This change in volume is not of great concern since the  $\text{Zr}_5\text{Sn}_3$  unit cell volume is about 40% larger than that of  $\text{Ti}_5\text{Si}_3$ .

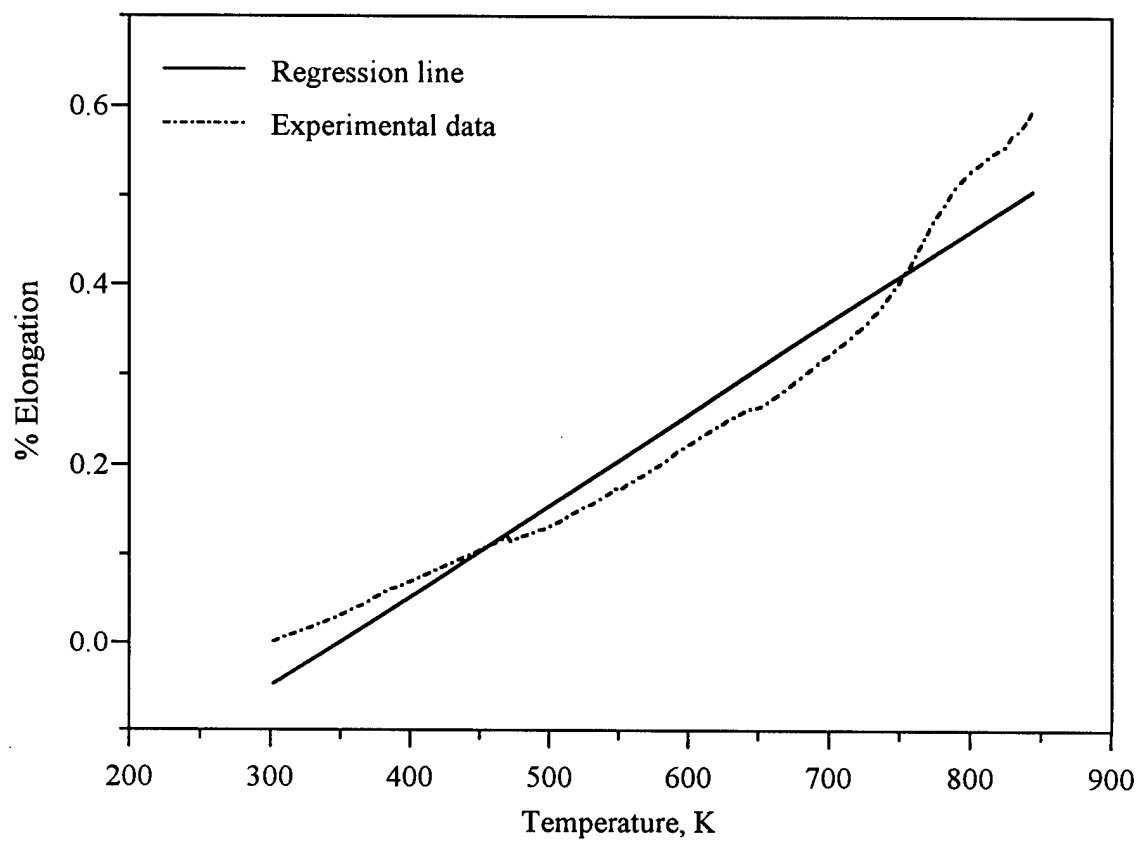


Figure 4: Bulk CTE measurement of  $\text{Ti}_5\text{Si}_3$  versus temperature.

Table V: Effect of Carbon on  $A_5Si_3C_x$  Compositions

Compound	a (nm)	$\Delta a$ (nm)	c (nm)	$\Delta c$ (nm)	Volume (nm <sup>3</sup> )	$\Delta Vol$ (%)
$Ti_5Si_3$	0.74514(4)		0.51464(3)		0.24746(4)	
$Ti_5Si_3C_{0.85}$	0.74438(4)	-0.00076	0.51643(4)	+0.00182	0.24782(3)	+0.15
$Zr_5Si_3$	0.79582(9)		0.55638(8)		0.30518(8)	
$Zr_5Si_3C_{1.0}$	0.79400(6)	-0.00182	0.56116(8)	+0.00478	0.30638(7)	+0.39
$Zr_5Sn_3$	0.84560(7)		0.5779(1)		0.35786(9)	
$Zr_5Sn_3C_{1.0}$	0.84268(9)	-0.00292	0.58001(8)	+0.00211	0.35669(9)	- 0.33

From Table IV the estimated and measured bulk CTE value of  $Ti_5Si_3$  compare well to the value given by Kosolapova [16] but are larger than that measured by Frommeyer, Rosenkranz, and Ludecke [2]. If the measured bulk CTE is considered as non-constant, it varies from 6.4 to 11.9 ppm/K from 298 to 873 K which compares better to Frommeyer et al. It is unclear whether the value from Kosolapova is truly independent of temperature or simply an average over the temperature range. In general, the thermal expansion measured by linear bulk expansion may not equal the thermal expansion measured by change in the unit cell or lattice parameter. The presence of thermally generated defects such as vacancies can cause the linear bulk expansion to be less than the linear expansion measured by the change in length of the unit cell. However, the measurements made in this study were at low homologous temperatures of less than  $0.4T_m$  ( $T_m=2403$  K). The equilibrium concentration of defect species is expected to be low. Thus a significant difference between the two methods is not expected.

#### IV. Conclusions

The addition of carbon to  $\text{Ti}_5\text{Si}_3$  changed the thermal expansion behavior. A decrease in  $\alpha_c$  was observed while  $\alpha_a$  increased. The overall net effect of the increase and decrease was no predicted change in the bulk CTE. While there is little expected change in the overall bulk behavior, CTE anisotropy was significantly reduced from  $\Delta\alpha = 11.7$  to  $\Delta\alpha = 8.5$ .

#### Acknowledgements

Ames Laboratory is operated for the U.S. Department of Energy by Iowa State University under contract number W-7405-ENG-82. This research was supported by the Office of Basic Energy Science, Materials Science Division. A portion of the work was conducted at the High Temperature Materials Laboratory User Program at Oak Ridge National Laboratory, sponsored by the Office of Transportation Technologies under contract DE-AC05-84OR21400 with Martin Marietta Energy Systems, Inc.

#### References

1. D.M. Shah, D. Berczik, D.L. Anton, and R. Hecht, "Appraisal of other Silicides as Structural Materials," *Mater. Sci. and Eng.* **A155** (1992) 45-57.
2. G. Frommeyer, R. Rosenkranz, C. Ludecke, "Microstructure and Properties of the Refractory Intermetallic  $\text{Ti}_5\text{Si}_3$  Compound and the Unidirectionally Solidified Eutectic Ti-Ti $_5\text{Si}_3$  Alloy," *Z. Metallkde.* **81** (1990) 307-313.
3. R. Rosenkranz, G. Frommeyer, and W. Smarsly, "Microstructures and Properties of High Melting Point Intermetallic  $\text{Ti}_5\text{Si}_3$  and  $\text{TiSi}_2$  Compounds," *Mater. Sci. Eng.* **A152** (1992) 288-294.



4. E. Garcia and J.D. Corbett, "Chemistry of Polar Intermetallic Compounds. Study of Two  $Zr_5Sb_3$  Phases, Hosts for a Diverse Interstitial Chemistry," *Inorgan. Chem.* **27** (1988) 2353-2359.
5. Y. Kwon, M.A. Rzeznik, A. Guloy, and J.D. Corbett, "Impurity Stabilization of Phases with the  $Mn_5Si_3$ -Type Structure. Questions Regarding  $La_5Sn_3$  and  $Zr_5Si_3$ ," *Chem. Mater.* **2** (1990) 546-550.
6. E. Garcia and J.D. Corbett, "Chemistry in the Polar Intermetallic Host  $Zr_5Sb_3$ . Fifteen Interstitial Compounds," *Inorgan. Chem.* **29** (1990) 3274-3282.
7. Y. Kwon and J.D. Corbett, "Chemistry in Polar Intermetallic Compounds. The Interstitial Chemistry of  $Zr_5Sn_3$ ," *Chem. Mater.* **4** (1992) 1348-1355.
8. A.G. Evans, "Microfracture from Thermal Expansion Anisotropy - I. Single Phase Systems" *Acta. Metall.* **26** (1978) 1845-1853.
9. R.W. Rice and R.C. Pohanka, "Grain-Size Dependence of Spontaneous Cracking in Ceramics," *J. Am. Ceram. Soc.* **62** (1979) 559-563.
10. C.T. Liu, E.H. Lee, T.J. Henson, "Initial Development of High-Temperature Titanium Silicide Alloys," Report, ORNL-6435; Order No. DE88007860, (1988).
11. T. Nakashima and Y. Umakoshi, "Anisotropy of Electrical Resistivity and Thermal Expansion of Single-Crystal  $Ti_5Si_3$ ," *Philos. Mag. Lett.* **66** (1992) 317-321.
12. Y.S. Touloukian, R.K. Kirby, R.E. Taylor, and T.Y.R. Lee, in "Thermophysical Properties of Matter, Vol. 13: Thermal Expansion, Non-Metallic Solids" (Plenum Press, New York, 1977) p. 289.
13. D.E. Appleman and H.T. Evans, NTIS Document No. PB-216188, (1973).
14. J. Quakernaat and J.W. Visser, "Lattice Dimensions of Low-Rate Metalloid-Stabilized  $Ti_5Si_3$ ," *High Temp. - High Pres.* **6** (1974) 515-517.
15. P. Scardi, R.D. Maggio, and L. Lutterotti, "Thermal Expansion Anisotropy of Ceria-Stabilized Tetragonal Zirconia," *J. Am. Ceram. Soc.* **75** (1992) 2828-2832.
16. T. Y. Kosolapova, in "Handbook of High Temperature Compounds: Properties, Production, Applications" (Hemisphere Publishing Corp., New York, 1990) p. 392.

CHAPTER 4:  
EFFECT OF PROCESSING ON OXIDATION OF  $\text{Ti}_5\text{Si}_3$

A paper published in *Materials Research Society Symposium Proceedings*<sup>1</sup>

Andrew J. Thom, Youngman Kim, and Mufit Akinc

Ames Laboratory and Department of Materials Science and Engineering

**Abstract**

The mechanical properties and oxidation resistance of HIPed  $\text{Ti}_5\text{Si}_3$  have been measured. HIPing submicron size powder compacts produces a crack-free, fine-grained microstructure with significantly higher hardness and toughness than a coarse-grained microstructure which contains microcracks within larger grains. Oxidation resistance is influenced by the grain size. Coarse-grained material has much lower mass gain than fine-grained material in an oxidizing atmosphere and exhibits parabolic oxidation kinetics. The oxidation resistance of fine-grained material was measured between 700°C and 1000°C in air. Mass gain at 120 hours was measured to be 0.07 mg/cm<sup>2</sup> at 700°C. At 900°C cracking of the scale leads to linear oxidation kinetics and significantly higher mass gain.

---

<sup>1</sup>Reprinted with permission from Materials Research Society Symposium Proceedings 1993, 288, 1037-1042. Copyright © Materials Research Society.

## I. Introduction

Silicides have received considerable attention as potential high temperature structural materials. Of the less commonly investigated silicides[1],  $\text{Mo}_5\text{Si}_3$ ,  $\text{Nb}_5\text{Si}_3$ ,  $\text{Cr}_5\text{Si}_3$ ,  $\text{Zr}_5\text{Si}_3$ ,  $\text{Ti}_5\text{Si}_3$ ,  $\text{V}_5\text{Si}_3$ , and  $\text{Ta}_5\text{Si}_3$  are particularly interesting as potential high temperature materials. Among this group of materials,  $\text{Ti}_5\text{Si}_3$  is attractive due to its low density, high melting point, potential oxidation resistance, and interesting interstitial chemistry. The previous work indicates that the monolithic material suffers from microcracking [2-7] which degrades the mechanical properties. Additionally, the oxidative behavior of  $\text{Ti}_5\text{Si}_3$  has received only limited attention[2,7,8].

In this paper, the effect of processing upon the mechanical and oxidative behavior of  $\text{Ti}_5\text{Si}_3$  is studied. In particular, the influence of grain size on the mechanical and oxidative behavior is discussed.

## II. Experimental

$\text{Ti}_5\text{Si}_3$  was synthesized in 125g batches. A stoichiometric mixture of titanium and silicon was arc-melted under an argon atmosphere using a non-consumable electrode. The buttons were milled to -325 mesh ( $<43\text{ }\mu\text{m}$ ) powder in a WC-lined mill. X-ray diffraction patterns indicated the powders were single phase  $\text{Ti}_5\text{Si}_3$  with the  $\text{Mn}_5\text{Si}_3$ -type structure. Powders were then milled for up to an additional six hours. Submicron size powders were pressed into 15mm x 15mm x 60mm bars, coated with boron nitride, and HIPed in a borosilicate encapsulating glass at 206 MPa at 1250°C for 10 hours. A slow cooling rate of 1-2°C/min was used to minimize bulk thermal stresses and reduce

cracking. Room temperature hardness and fracture toughness were measured by Vickers indentation technique.

Specimens for thermal oxidation studies were prepared by cutting 10mm x 5mm x 2mm coupons from the HIPed bar. These coupons were polished through 0.05 $\mu$ m Al<sub>2</sub>O<sub>3</sub> abrasive. Samples were suspended from a sapphire hangdown wire in a TGA and heated at 20°C/min in a flowing stream of synthetic air (mixture of 79%N<sub>2</sub>-21%O<sub>2</sub>, free of H<sub>2</sub>O). Continuous isothermal oxidation was measured for up to 120 hours.

### III. Results and Discussion

The grain size of the HIPed monoliths varied significantly with initial powder size. A starting powder of -325 mesh produced a coarse-grained microstructure of 10-25 $\mu$ m which exhibited transgranular microcracks. A starting powder which was milled for an additional six hours produced a fine-grained microstructure of 1-2 $\mu$ m and was free of microcracks. The room temperature hardness and fracture toughness increased as the grain size decreased. The fine-grained material had hardness and toughness values up to 17.1 $\pm$ 0.7 GPa and 2.9 $\pm$ 0.2 MPa $\cdot$ m<sup>1/2</sup>, respectively, for an indentation load of 500 g. The corresponding values for the coarse-grained material were 9.1 $\pm$ 0.5 GPa and 1.6 $\pm$ 0.2 MPa $\cdot$ m<sup>1/2</sup>. The lower values of hardness and fracture toughness exhibited by the large-grained material are attributed to the transgranular microcracking. This microcracking is believed to arise from the large thermal expansion anisotropy of the material [9]. The coefficient of thermal expansion (CTE) as measured by high temperature x-ray diffraction is:  $\alpha_a = 8.7 \pm 0.2$  ppm/K and  $\alpha_c = 20.4 \pm 0.4$  ppm/K. The large difference between  $\alpha_a$  and  $\alpha_c$  (thermal expansion anisotropy) results in large thermal stresses during processing which may exceed the strength of the material when the grain size exceeds a critical

value[10]. Residual stresses which develop during cooling from the processing temperature are believed to cause transgranular microcracking in large-grained microstructures.

Oxidation resistance measurements indicated that the coarse-grained material showed good oxidation resistance at 1000°C. The mass gain after 72 hours was 1.5 mg/cm<sup>2</sup> and was parabolic with a rate constant of 0.027 mg<sup>2</sup>/cm<sup>4</sup>/hr. Fine-grained material showed significantly lower oxidation resistance, experiencing nearly an order of magnitude increase in mass gain at 1000°C after 72 hours. The fine-grained material showed a complex scale development. An outer 10 μm thick layer of TiO<sub>2</sub> formed. Below this layer was a 10 μm layer composed of TiO<sub>2</sub> particles mixed with a discontinuous silicon rich, titanium depleted phase, presumably SiO<sub>2</sub>. The lower oxidation resistance of fine-grained material is likely related to the increased grain boundary area. A continuous, protective SiO<sub>2</sub> layer was not observed to form.

The oxidative behavior of the fine-grained material was further investigated from 700°C-1000°C in air. For each temperature, two flow rates were used, 30 and 150 ml/min. If linear oxidation kinetics occurred, a dependence of the linear rate on gas flow would indicate that the supply of oxygen at the surface is the rate determining step[11]. Figure 1 shows the isothermal oxidation at 700°C. The mass gain is quite small, less than 0.07 mg/cm<sup>2</sup> after 120 hours. Figure 2 shows the isothermal oxidation at 800, 900, and 1000°C. Mass gain increases as temperature increases. The complex nature of the scale development is evident from the changing oxidation kinetics outlined in Table I. Two equations are listed when the data are intermediate between two rate equations. There is similar behavior in the oxidation kinetics between flow rates at each temperature except at 800°C which indicates reproducibility of the data.

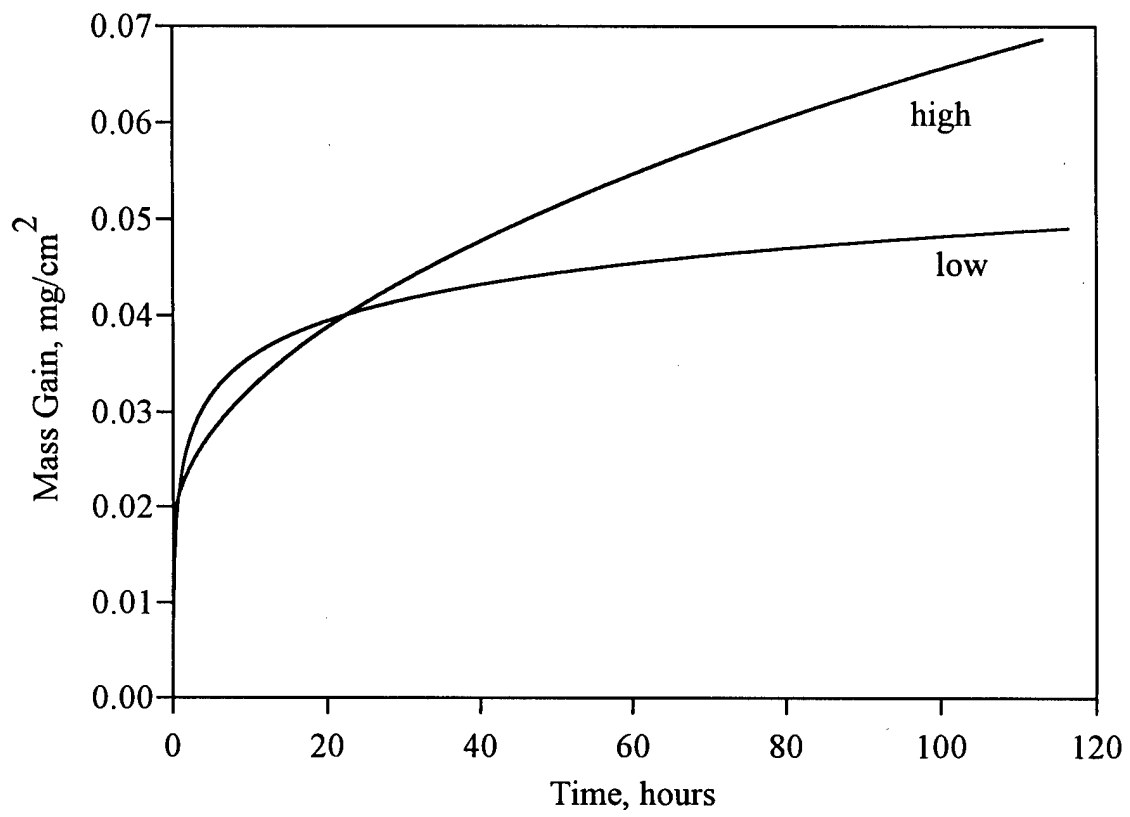


Figure 1: Isothermal oxidation of fine-grained  $\text{Ti}_5\text{Si}_3$  at  $700^\circ\text{C}$  in air at low and high flow rate (30 and 150 ml/min).

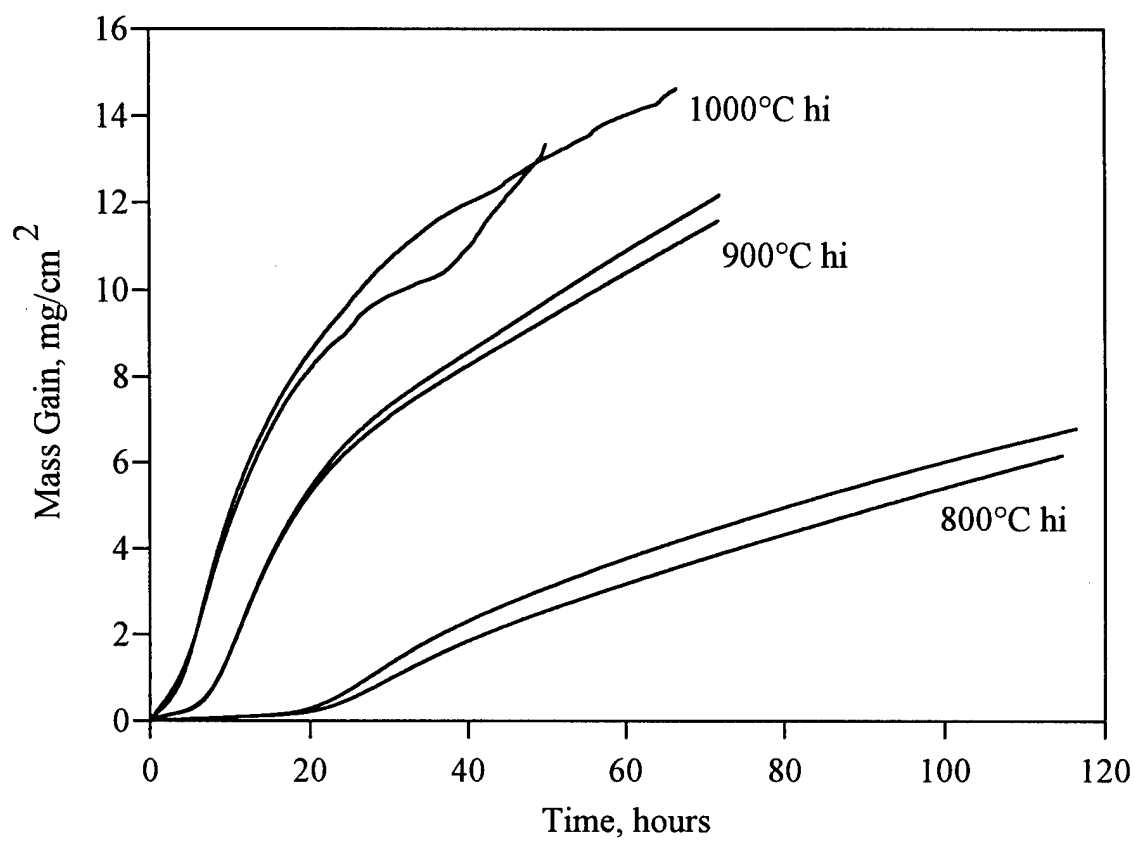


Figure 2: Isothermal oxidation of fine-grained  $\text{Ti}_5\text{Si}_3$  in air from 800°C-1000°C at low and high flow (30 and 150 ml/min). Curves for high flow rate at each temperature are labeled.

All samples show an initial transient oxidation. This initial rate changes as the scale grows inward, and a second rate-controlling mechanism dominates. At 700°C and 800°C, the steady state oxidation rate is between parabolic and cubic. The low level of mass gain at 700°C approaches the sensitivity of the microbalance and prevents an accurate determination of the steady state reaction kinetics. At 800°C and low flow, transient paralinear oxidation occurs up to 15 hours and changes to cubic oxidation at 22 hours. At 800°C and high flow, the transient oxidation is parabolic and changes to a higher parabolic rate after 22 hours. Since these are not linear mechanisms, flow rate is not expected to cause this different behavior.

Table I: Oxidation Kinetics<sup>+</sup>

Temp (°C)	Flow Rate	Time Scale/ Rate Equation	Time Scale/ Rate Equation	Time Scale/ Rate Equation
700	low	0-3 hrs/Log	3-120 hrs/PB,C	
	high	0-3 hrs/Log	3-120 hrs/PB,C	
800	low	0-15 hrs/PL	22-70 hrs/C	
	high	0-15 hrs/PB	22-70 hrs/PB	
900	low	0-3 hrs/PL,PB	10-30 hrs/Log	> 30 hrs/L
	high	0-3 hrs/PL,PB	10-30 hrs/Log	> 30 hrs/L
1000	low	0-3 hrs/L	7-35 hrs/Log	> 40 hrs/L
	high	0-3 hrs/L	7-35 hrs/Log	> 40 hrs/L

<sup>+</sup> Abbreviations used for the rate equations fit to the data are as follows: Log=direct logarithmic, C=cubic, PB=parabolic, PL=paralinear, and L=linear.



The linear rate constants at 900°C for long times ( $t \geq 30$  hours) and 1000°C for short times ( $t = 0-3$  hours) for low and high flow rate are nearly identical, indicating that the rate determining step is not associated with an adsorption of oxygen. The increased rate for 1000°C for low flow and ( $t > 40$  hours) may be due to formation of stress cracks in the scale which exposed large amounts of new surface. The linear rate at ( $t > 40$  hours) is slightly less than the initial rate for ( $t = 0-3$  hours), indicating this to be a plausible event. For both 900 and 1000°C, the linear rates are associated with the cracking of the scales, causing short circuit paths to the base material and allowing for an increased rate of mass gain.

No scale formation was observed for samples exposed to air at 700°C. The external surface was slightly tarnished, indicating the presence of a thin film. The scale formation from 800 to 1000°C is shown in Figure 3. A dense outer 15  $\mu\text{m}$  thick layer forms at 800°C. Dendrites about 12  $\mu\text{m}$  wide grow from this outer layer into the base material. The total thickness of the layer and dendrites is about 150  $\mu\text{m}$ . At 900°C the dense outer layer has grown to 35  $\mu\text{m}$ . The dendrites have coarsened to about 50  $\mu\text{m}$  in width, and the total thickness is about 275  $\mu\text{m}$ . At 900°C the mass gain is about twice that at 800°C. The increased thickness at 900°C accounts for most of the mass gain. By 1000°C the dense outer layer has separated into a two phase region as seen in the previous oxidation study of the fine-grained material. The dendrites have grown in width to consume all of the base material so that no base material extends to the dense outer scale. The total thickness is about 300  $\mu\text{m}$ . The mass gain has increased by 15% from 900°C, and this increase is reflected in the increase in total thickness to 300  $\mu\text{m}$  and the coarsening of the dendrites.

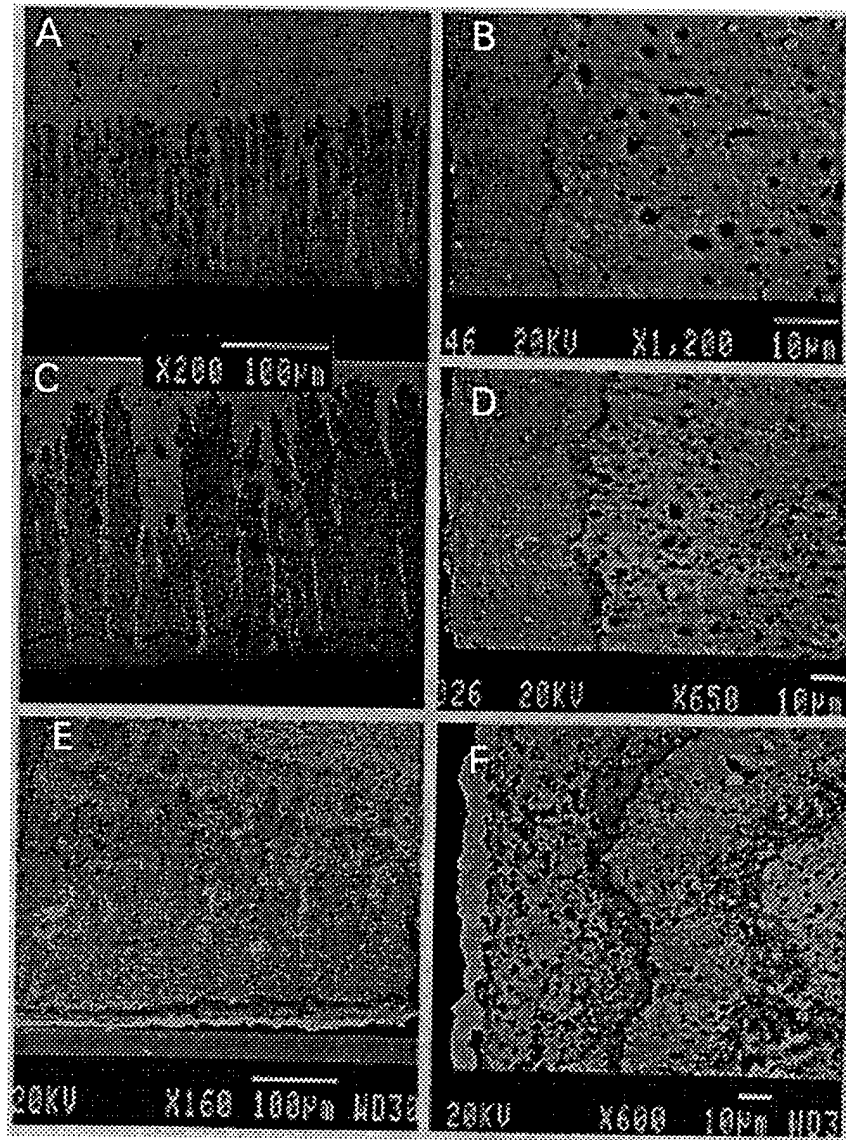


Figure 3: Microstructures of fine-grained  $\text{Ti}_5\text{Si}_3$  oxidized in air. (a),(b) 800°C for 115 hours, (c),(d) 900°C for 72 hours, (e),(f) 1000°C for 60 hours.

#### IV. Conclusions

Dense, microcrack-free  $\text{Ti}_5\text{Si}_3$  was produced by HIPing powder milled to submicron size. Hardness and fracture toughness improves as grain size decreases. Oxidation resistance appears to decrease as grain size decreases, presumably due to increased grain boundary diffusion. For fine grained material, oxidation resistance at 700°C is excellent. Above 700°C oxygen uptake increases significantly as temperature increases. By 900°C substantial cracking occurs to prevent the formation of a protective scale and linear oxidation kinetics dominate.

#### Acknowledgements

Ames Laboratory is operated for the U.S. Department of Energy by Iowa State University under contract number W-7405-ENG-82. This research was supported by the Office of Basic Energy Science, Materials Science Division.

#### References

1. D.M. Shah, D. Berczik, D.L. Anton, and R. Hecht, "Appraisal of other Silicides as Structural Materials," Mater. Sci. Eng., **A155**, 45-57 (1992).
2. D.L. Anton and D.M. Shah, US Air Force Rep., contract no. WRDC-TR-90-4122.OH,USA (1991).
3. R. Rosenkranz, G. Frommeyer, and W. Smarsly, "Microstructures and Properties of High Melting Point Intermetallic  $\text{Ti}_5\text{Si}_3$  and  $\text{TiSi}_2$  Compounds," Mater. Sci. Eng., **A152**, 288-294 (1992).

4. G. Frommeyer, R. Rosenkranz, and C. Ludecke, "Microstructure and Properties of the Refractory Intermetallic  $Ti_5Si_3$  Compound and the Unidirectionally Solidified Eutectic Ti- $Ti_5Si_3$  Alloy," *Z. Metallkde.*, **81**, 307-313 (1990).
5. C. T. Liu, E.H. Lee, and T.J. Henson, "Initial Development of High Temperature Titanium Silicide Alloys," Report, ORNL-6435; Order No. DE88007860, 1988.
6. S. Reuss and H. Vehoff, "Temperature Dependence of Fracture Toughness of Single Phase and Two Phase Intermetallics," *Scripta Met.*, **24**, 1021-1026 (1990).
7. Y. Kim, A.J. Thom, and M. Akinc, in Processing and Fabrication of Advanced Materials for High Temperature Applications-II, edited by T.S. Srivatsan and V.A. Ravi (The Min., Met., and Mater. Soc. Proc. Chicago, IL, 1992) In Press.
8. R.M. Paine, A.J. Stonehouse, and W.W. Beaver, WADC Tech. Rep. 59-29-Part I (1960).
9. A.J. Thom and M. Akinc, Iowa State University, C.R. Hubbard and O.B. Cavin, Oak Ridge National Laboratory, Unpublished data.
10. J.A. Kuszyk and R.C. Bradt, "Influence of Grain Size on Effects of Thermal Expansion Anisotropy in  $MgTi_2O_5$ ," *J. Am. Ceram. Soc.*, **56**, 420-423 (1973).
11. P. Kofstad, High-Temperature Oxidation of Metals, John Wiley and Sons, Inc., New York, 1966, p.13.

CHAPTER 5:  
IMPROVED OXIDATION RESISTANCE OF  $\text{Ti}_5\text{Si}_3$  BY SMALL ATOM DOPING

A manuscript to be submitted to *Journal of Materials Science*

Andrew J. Thom and Mufit Akinc

Ames Laboratory and Department of Materials Science and Engineering

**Abstract**

Refractory intermetallic silicides are receiving increasing consideration for use as high temperature structural materials.  $\text{Ti}_5\text{Si}_3$ -based compositions are attractive due to their ability to incorporate a variety of ternary interstitial additions. These ternary additions present a unique opportunity to potentially tailor physical properties. Previous experimental work by the authors has shown that these additions significantly increase the otherwise poor oxidation resistance of undoped  $\text{Ti}_5\text{Si}_3$  above  $700^\circ\text{C}$ . Recent experimental work by the authors on the oxidation of small atom doped  $\text{Ti}_5\text{Si}_3$  is discussed. Interstitial additions of boron, carbon, and oxygen substantially improve the isothermal oxidation resistance of  $\text{Ti}_5\text{Si}_3$  up to  $1079^\circ\text{C}$ . In contrast, added nitrogen does not provide significant improvement. Even up to  $1306^\circ\text{C}$ , interstitial oxygen imparts excellent oxidation resistance with a mass gain of  $1.1 \text{ mg/cm}^2$  after 240 hours.

## I. Introduction

The need for improved-performance high temperature structural materials has generated considerable interest in the processing and properties of advanced intermetallics. The status of intermetallic research pertaining to high temperature structural applications has been summarized by several authors (1,2,3,4,5). Anton et al. have recommended several selection criteria for determining candidate material systems (1). One of these criteria is adequate oxidation resistance, and thus silicon-bearing intermetallics are candidate materials since they are more likely to form protective scales.  $A_5Si_3$  intermetallic silicides (A=transition metal) are particularly interesting since this phase is typically the highest melting phase in the respective A-Si binary phase diagram. The compound  $Ti_5Si_3$  is particularly attractive because of its high melting point of  $2130^{\circ}C$ , adequate oxidation resistance at moderate temperatures, and low density of  $4.32\text{ g/cm}^3$ .

Liu et al. (6) produced alloys of Ti-29Si-8Cr, Ti-33Si-4Cr-4Zr, and Ti-36.5Si by arc melting and casting. Isothermal oxidation of these alloys at  $800^{\circ}C$  in air showed parabolic oxidation for the last two alloys with a mass gain of 0.88 and 0.98  $\text{mg/cm}^2$  at 120 hours. The alloy of lowest silicon content showed linear oxidation with a mass gain of 1.8  $\text{mg/cm}^2$  at 120 hours. All three alloys formed adherent scales. Anton and Shah (7) performed cyclical oxidation testing of arc-cast  $Ti_5Si_3$  at  $1149^{\circ}C$ . After 50 hours the mass gain was about 31  $\text{mg/cm}^2$ . An external brown oxide was observed, and x-ray diffraction of the oxidation products indicated 75-80 vol.%  $TiO_2$  (rutile), 20 vol.% hexagonal  $Ti_5Si_3$  and less than 5 vol.% tetragonal  $SiO_2$  ( $\alpha$ -cristobalite).

While  $Ti_5Si_3$  has adequate oxidation resistance up to about  $800^{\circ}C$ , use temperatures for new high temperature structural applications extend well in excess of  $1000^{\circ}C$ . A key to the potential usefulness of  $Ti_5Si_3$ -based materials lies in the ability to

vary composition by the incorporation of ternary interstitial additions. This capability arises from the ability of the hexagonal  $\text{Mn}_5\text{Si}_3$ -type structure to incorporate a wide variety and amount of atoms in interstitial sites at the corners of the unit cell (8,9,10,11). This presents an opportunity to tailor properties such as oxidation resistance by making the proper interstitial addition.

## II. Experimental

Nominal compositions of  $\text{Ti}_5\text{Si}_3\text{Z}_x$  ( $\text{Z} = \text{B}, \text{C}, \text{N}, \text{O}$  and  $x = 0.25, 0.50, 0.75$ ) were synthesized. The details of the synthesis and characterization of these materials are discussed elsewhere (12). Arc-melted buttons were milled to produce fine powders. Atmospheric control is necessary because finely milled  $\text{Ti}_5\text{Si}_3$  will visibly combust when exposed to ambient air. Therefore, during powder processing of  $\text{Ti}_5\text{Si}_3$ , material must be handled in an inert atmosphere. To accomplish this, operations were performed inside a glovebox which contained an argon atmosphere and an attached recirculating purification system to maintain a low water and oxygen content, with oxygen measured to be less than 0.5 parts per million (ppm).

Powders ( $\text{Z} = \text{B}, \text{N}, \text{O}$ ) were prepared by loading arc-melt material into a WC-lined mill inside the glovebox and milling within the glovebox for 90 minutes. Aspirin was used as a grinding additive to reduce caking of the powders and increase grinding efficiency. The milled powder was sieved to -635 mesh (less than 20  $\mu\text{m}$ ). Pellets were cold-pressed inside the glovebox in a 13 mm diameter die at 87 MPa, yielding typical green densities of about 62% of theoretical ( $\rho_{\text{th}} = 4.32 \text{ g/cm}^3$ ). The pellets containing a grinding additive were slowly heated at 2°C/min. and prefired at 1000°C, in flowing

ultra-high purity (UHP) argon, to burnout the grinding additive prior to encapsulation for hot isostatic pressing (HIPing).

The green bodies were then embedded in boron nitride powder and sealed into borosilicate tubes at  $10^{-1}$  Torr argon. Material was HIPed at 206 MPa and 1200°C for 10 hours. A slow cooling rate of 1-2°C/min. was used to minimize bulk thermal stresses and reduce cracking.

The undoped and carbon-doped material discussed in this paper was produced prior to the availability of the above mentioned facilities, and processing of the material has been discussed elsewhere (13,14,15). In summary, the arc-melt material was ground in a Spex mill inside an argon filled glovebox. Oxygen was judged to be less than 10 ppm based on the exposed light bulb filament test. The material was milled without a grinding aid which contributed to significant caking of the powder. Milled material was sieved to -325 mesh and pressed into a pellet in a die using a hydraulic press outside the glovebox. The powder was handled within an argon-filled glove bag during the pressing operation to minimize exposure to ambient air. Samples of coarse-grained, undoped material were similarly prepared by using commercially available, unmilled -325 mesh powder. HIPing was performed as described above with the exception that the pellets were sprayed-coated with a BN solution and embedded in borosilicate powder. Material was then HIPed as described above.

Specimens for isothermal oxidation studies were prepared by cutting coupons from HIPed material. A 0.5 mm diameter hole was EDM-drilled in the coupons from which to suspend the samples in a vertical tube thermogravimetric analyzer (TGA) using a 125  $\mu\text{m}$  diameter sapphire fiber. Test coupons were polished through 0.05  $\mu\text{m}$   $\text{Al}_2\text{O}_3$  abrasive, rinsed in acetone, and dried at 105°C for 24 hours. The coupons were then loaded into the TGA and heated at 20°C/min. in flowing synthetic 'zero' air ( $\text{H}_2\text{O} < 3.5$  ppm and



total hydrocarbons < 0.8 ppm). Sample surface area varied from 1-2 cm<sup>2</sup>. Continuous isothermal weight change was measured for up to 240 hours.

Steady state oxidation rate constants were determined from the mass gain data using the following equations:

$$\left(\frac{\Delta m}{A}\right) = k_p^{1/2} t^{1/2} + c_1 \quad (1)$$

$$\left(\frac{\Delta m}{A}\right) = k_l t + c_1 \quad (2)$$

$$\left(\frac{\Delta m}{A}\right) = k_p^{1/2} t^{1/2} + k_l t + c_1 \quad (3)$$

In Eqs. 1-3,  $\Delta m$  is the mass change which occurs in the time interval  $t$  after attainment of the isothermal temperature and  $A$  is the initial surface area. The linear and parabolic rate constants are given by  $k_l$  and  $k_p$ , respectively, while  $c_1$  is simply the intercept calculated from the regression analysis. Equation 3 describes paralinear kinetics in which a parabolic and linear process are simultaneously acting as rate determining mechanisms. It should be noted that a negative linear rate constant in paralinear kinetics indicates that a net mass loss process is occurring. However, the linear rate constant calculated from Equation 3 for such a process is not correct and can only be used as a relative indicator. The rate constant is dependent on scale growth and volatilization, and calculation of such constants has been recently discussed by Opila (16). As indicated by Pieraggi (17), parabolic rate constants determined from plots of  $(t^{1/2}, m)$  have lower relative error and can be determined in much shorter time durations than from plots of  $(t, m)$ .

The scales of the oxidized samples were analyzed by x-ray diffraction (XRD). Cross-sections of selected oxidized samples were analyzed by optical and scanning electron microscopy (SEM), including elemental analysis by x-ray dot mapping and spot analysis by energy dispersive spectroscopy (EDS).

### III. Results

#### 1. Composition and Structure

The synthesis and characterization of the arc-melted material used in this study has been discussed elsewhere (12). Table I shows the chemical analysis of the arc-melted materials, indicating the presence of the intended dopant at levels reasonably close to the nominal (batched) composition. Powder x-ray diffraction (XRD) indicates that each composition maintains the  $Mn_5Si_3$ -type structure of the undoped  $Ti_5Si_3$ . Chemical analysis for silicon content was performed on selected arc-melted samples. Silicon was measured by a wet chemistry technique, and all samples lost silicon, probably from volatilization during arc-melting.

Table I: Chemical Analysis of Arc-Melted  $Ti_5Si_3Z_x$

Nominal Composition	Alloy Designation	Analyzed Composition (x)
$Ti_5Si_3$	--	--
$Ti_5Si_3C_{0.25}$	C25	0.25
$Ti_5Si_3C_{0.50}$	C50	0.58
$Ti_5Si_3C_{0.75}$	C75	0.71
$Ti_5Si_3B_{0.25}$	B25	0.18
$Ti_5Si_3B_{0.75}$	B75	0.75
$Ti_5Si_3N_{0.25}$	N25	0.17
$Ti_5Si_3N_{0.75}$	N75	0.52
$Ti_5Si_3O_{0.25}$	O25	0.27
$Ti_5Si_3O_{0.75}$	O75	0.65

By assuming that the amount of Ti and Z is the same as originally batched, the proportion of Ti, Si, and Z can be calculated for each composition. These compositions are shown in Table II. These calculated compositions were compared to available phase diagrams for Ti-Si-Z systems (18,19,20), and the phases predicted to be present are listed in Table III. With the exception of  $\text{Ti}_5\text{Si}_3\text{N}_{0.25}$ , each composition is predicted to contain additional

Table II: Chemical Composition Based on Silicon Analysis

Nominal Composition	Ti (at%)	Si (at%)	Z (at%)
$\text{Ti}_5\text{Si}_3$	67.5	32.5	
$\text{Ti}_5\text{Si}_3\text{C}_{0.24}$	63.3	33.7	3.04
$\text{Ti}_5\text{Si}_3\text{C}_{0.85}$	58.9	31.1	10.0
$\text{Ti}_5\text{Si}_3\text{B}_{0.25}$	63.3	33.5	3.17
$\text{Ti}_5\text{Si}_3\text{B}_{0.50}$	61.6	32.3	6.16
$\text{Ti}_5\text{Si}_3\text{N}_{0.25}$	63.7	33.1	3.18
$\text{Ti}_5\text{Si}_3\text{N}_{0.75}$	59.3	31.8	8.90

Table III: Predicted Phases for Selected Arc-Melted Compositions

Nominal Composition	Predicted phases based on chemical analysis
$\text{Ti}_5\text{Si}_3$	$\text{Ti}_5\text{Si}_3 + \beta\text{-Ti}$
$\text{Ti}_5\text{Si}_3\text{C}_{0.24}$	$\text{Ti}_5\text{Si}_3\text{C}_x + \text{TiC}_y$ and/or $\beta\text{-Ti}$
$\text{Ti}_5\text{Si}_3\text{C}_{0.85}$	$\text{Ti}_5\text{Si}_3\text{C}_x + \text{TiC}_y$
$\text{Ti}_5\text{Si}_3\text{N}_{0.25}$	$\text{Ti}_5\text{Si}_3\text{N}_x$
$\text{Ti}_5\text{Si}_3\text{N}_{0.75}$	$\text{Ti}_5\text{Si}_3\text{N}_x + \text{TiN}_y$ and/or $\text{TiSi}$

phase(s). Generally, the composition points lie close to the  $\text{Ti}_5\text{Si}_3\text{Z}_x$  phase field so that only small amounts of additional phase(s) are predicted. However, about 8%  $\text{TiC}_y$  is predicted for  $\text{Ti}_5\text{Si}_3\text{C}_{0.85}$ . Figure 1 shows an optical micrograph of HIPed C85 in which a precipitate phase is clearly visible. The precipitate phase is also observed in C75, C50, and C25, decreasing in proportion to carbon content. Visual inspection indicates that the proportion of the precipitate phase in C85 is somewhat greater than in C75. The proportion in C50 is somewhat less than in C25, with both substantially less than C85. EDS spot analysis indicates the precipitates to be Ti-rich and nearly Si-void with measurable carbon. A XRD scan of -635 mesh C85 powder from  $34\text{--}44^\circ 2\theta$  with 10 seconds counting time is shown in Figure 2 and clearly indicates the (100) and (110) peaks for  $\text{TiC}_y$ . However,  $\text{TiC}_y$  is not detected in C75, C50, or C25 by similar XRD analysis. Based on the microstructural observations,  $\text{TiC}_y$  precipitates are judged to be present in each of the carbon-doped materials.  $\text{TiC}_y$  has poor oxidation resistance at elevated temperatures, and its effect on oxidation resistance of the carbon-doped material will be discussed later.

## 2. Oxidation of Undoped $\text{Ti}_5\text{Si}_3$

The isothermal oxidation of undoped  $\text{Ti}_5\text{Si}_3$  has been previously investigated from  $700\text{--}1000^\circ\text{C}$  in zero air (13,15). In summary, material at  $700^\circ\text{C}$  showed mass gains of less than  $0.1\text{ mg/cm}^2$  after 120 hours. For temperatures from  $800\text{--}1000^\circ\text{C}$ , the samples showed initial transient oxidation followed by onset of a higher rate of mass gain. Figure 3 shows the mass gain of  $\text{Ti}_5\text{Si}_3$  oxidized from  $967^\circ\text{--}1191^\circ\text{C}$  in the present work. Coarse-grained (CG1) material at  $1079^\circ\text{C}$  behaves like fine-grained (FG1) material at  $967^\circ\text{C}$ . While mass gain increases with increasing temperature from  $967\text{--}1079^\circ\text{C}$ , mass gain significantly decreases at  $1191^\circ\text{C}$ . This behavior is consistent with that observed for

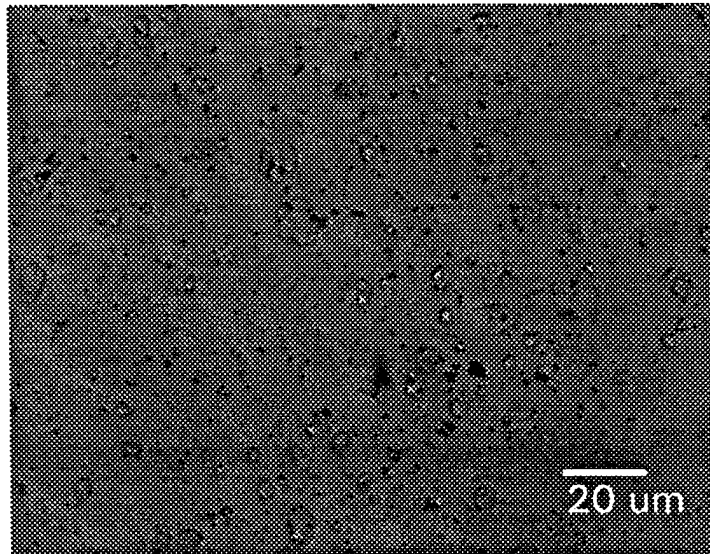


Figure 1: Optical micrograph of HIPed  $\text{Ti}_5\text{Si}_3\text{C}_{0.85}$  showing precipitate phase.

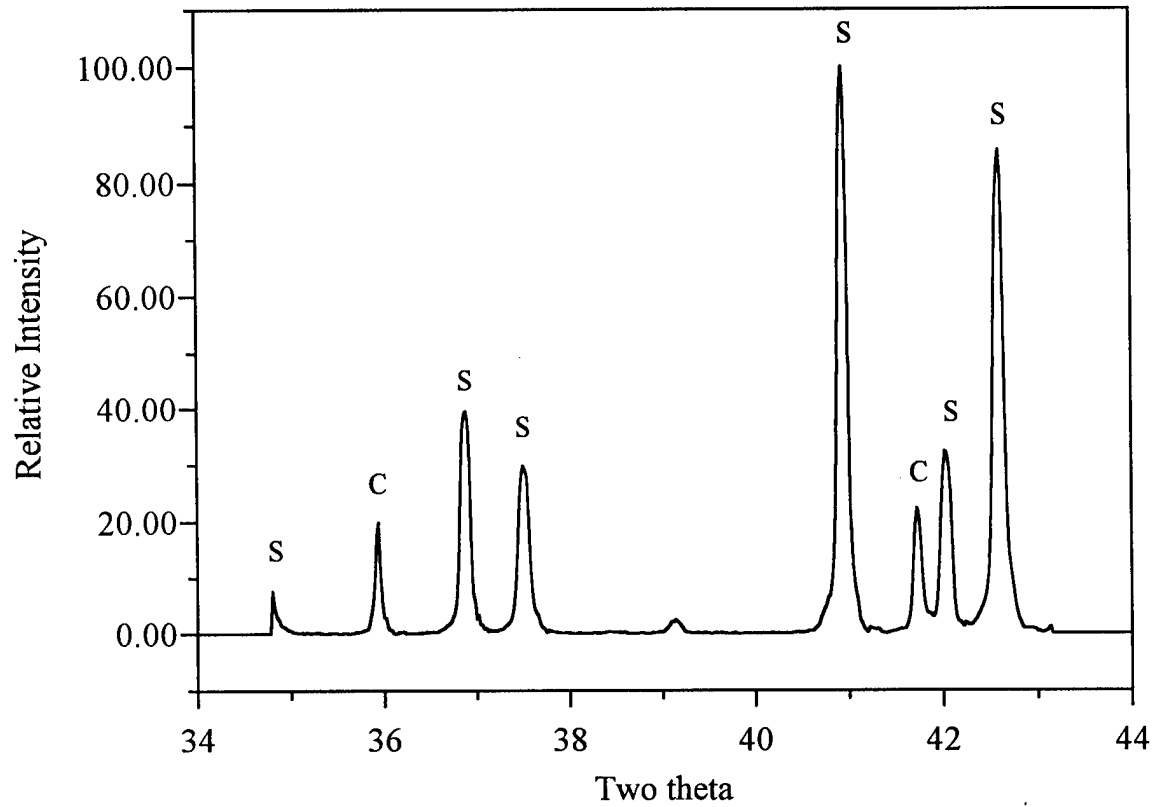


Figure 2: X-ray diffraction pattern of  $\text{Ti}_5\text{Si}_3\text{C}_{0.85}$ , indicating presence of  $\text{TiC}_y$  (S denotes silicide and C denotes carbide phases).

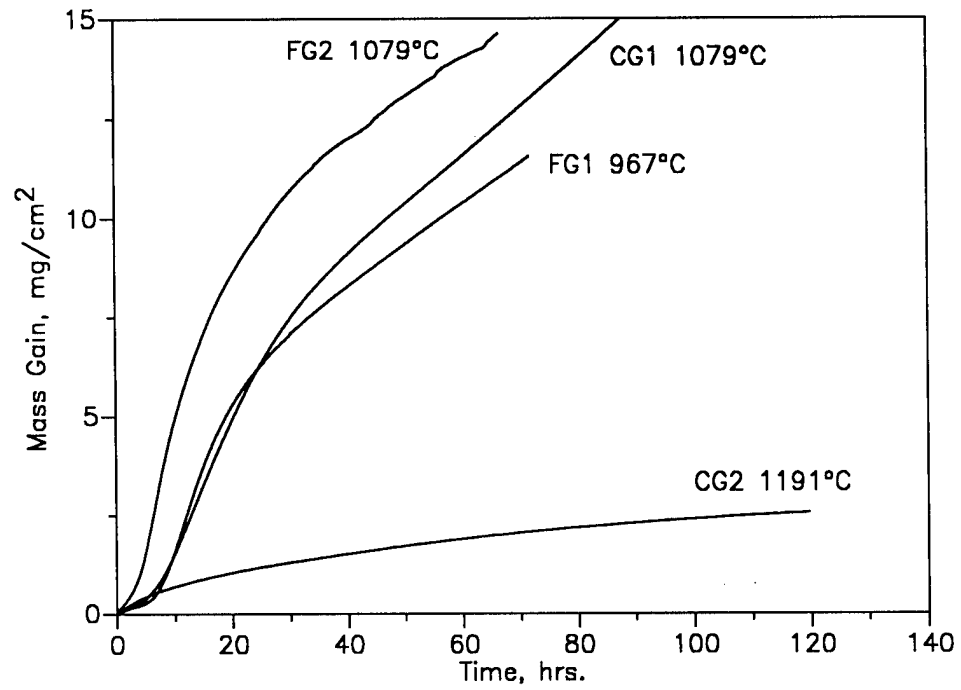


Figure 3: Isothermal oxidation of  $\text{Ti}_5\text{Si}_3$  in zero air from 967°-1191°C.

oxidation of titanium (21) in which the outer rutile scale coarsens from sintering, decreasing the relative contribution of inward grain boundary diffusion of oxygen so that slower inward volume diffusion of oxygen becomes the rate limiting step.

Steady state oxidation kinetics are given in Table IV. Between 967°-1079°C, steady state linear kinetics are achieved after about 40 hours. The linear rate constants for the three samples are approximately 0.1 mg/cm<sup>2</sup>/hr. However, at 1191°C parabolic kinetics are observed as mass gain significantly decreases.

Table IV: Steady State Rate Constants for Oxidation of Undoped Ti<sub>5</sub>Si<sub>3</sub>

Material	Alloy Designation	Temp.(°C)	Rate <sup>a</sup>	Value <sup>b</sup>	Time (hrs)
Fine-grained	FG1	967	L	0.10	t > 45
Fine-grained	FG2	1079	L	0.099	t > 40
Coarse-grained	CG1	1079	L	0.13	t > 40
Coarse-grained	CG2	1191	P	0.10	t > 4

<sup>a</sup>L=linear; P=parabolic

<sup>b</sup>L(mg/cm<sup>2</sup>/hr), P(mg<sup>2</sup>/cm<sup>4</sup>/hr)

X-ray diffraction of the exterior scale of FG1, FG2, and CG1 reveals a well developed rutile scale with no indication of the underlying Ti<sub>5</sub>Si<sub>3</sub>. A rutile scale is also detected on CG2, and the decreased mass gain is evidenced by presence of the underlying Ti<sub>5</sub>Si<sub>3</sub>-based peaks. Crystalline silica as  $\alpha$ -cristobalite is also present in the CG2 scale.



### 3. Oxidation of Carbon-Doped $\text{Ti}_5\text{Si}_3$

The addition of carbon to  $\text{Ti}_5\text{Si}_3$  dramatically improves oxidation resistance at  $1000^\circ\text{C}$  (15). Figure 4 shows the oxidation behavior of  $\text{Ti}_5\text{Si}_3\text{C}_x$  ( $x=0.25, 0.50$ ) from  $1000^\circ\text{C}$ - $1306^\circ\text{C}$  for the present work. For temperatures up to  $1191^\circ\text{C}$ , carbon additions promote a significant decrease in mass gain compared to undoped material. For both compositions, increasing temperature to  $1079^\circ\text{C}$  results in a lowering of overall mass gain. This behavior is similar to the trend observed for the undoped material in which increasing temperature from  $1079^\circ\text{C}$  to  $1191^\circ\text{C}$  produced a reduction in overall mass gain. Table V gives the steady state oxidation kinetics of carbon-doped  $\text{Ti}_5\text{Si}_3$ . The rate constant for C25 decreases as temperature is increased to  $1079^\circ\text{C}$  while the duration of transient oxidation also decreases. C50 changes from linear to parabolic kinetics as temperature is increased from  $1000^\circ\text{C}$ - $1079^\circ\text{C}$ . This change indicates a change in the rate controlling process. However, protective behavior is lost at  $1306^\circ\text{C}$  where C50 experiences rapid mass gain.

XRD of the oxidized scale of C25 shows that rutile is present and that the relative amount increases from  $1079^\circ\text{C}$ - $1191^\circ\text{C}$ . The scale is thin since  $\text{Ti}_5\text{Si}_3$ -based peaks are detected through the rutile scale, although no crystalline silica is detected. The relative amount of rutile in C50 decreases as temperature increases from  $1000^\circ\text{C}$ - $1079^\circ\text{C}$ , and once again visible  $\text{Ti}_5\text{Si}_3$ -based peaks indicate the thin nature of the external scale. As temperature is increased to  $1306^\circ\text{C}$ , only rutile is detected, consistent with the substantial mass gain observed.

Higher levels of carbon promote similar improvements in oxidation resistance with overall mass gain increasing as temperature increases. The oxidative behavior of  $\text{Ti}_5\text{Si}_3\text{C}_x$  ( $x=0.75, 0.85$ ) is shown in Figure 5. As seen in Table V, both C75 and C85 exhibit linear kinetics at  $1191^\circ\text{C}$ , with C85 transforming from parabolic to linear behavior while

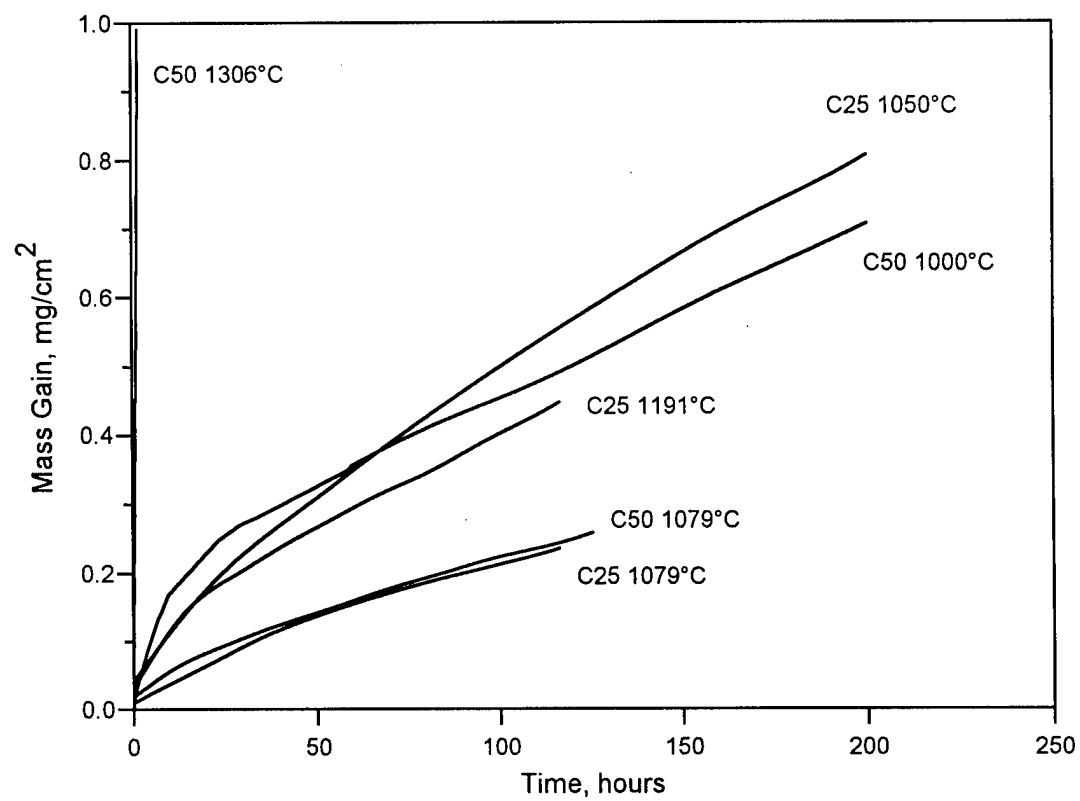


Figure 4: Isothermal oxidation of  $\text{Ti}_5\text{Si}_3\text{C}_{0.25}$  and  $\text{Ti}_5\text{Si}_3\text{C}_{0.50}$  in zero air at 1000°-1306°C.

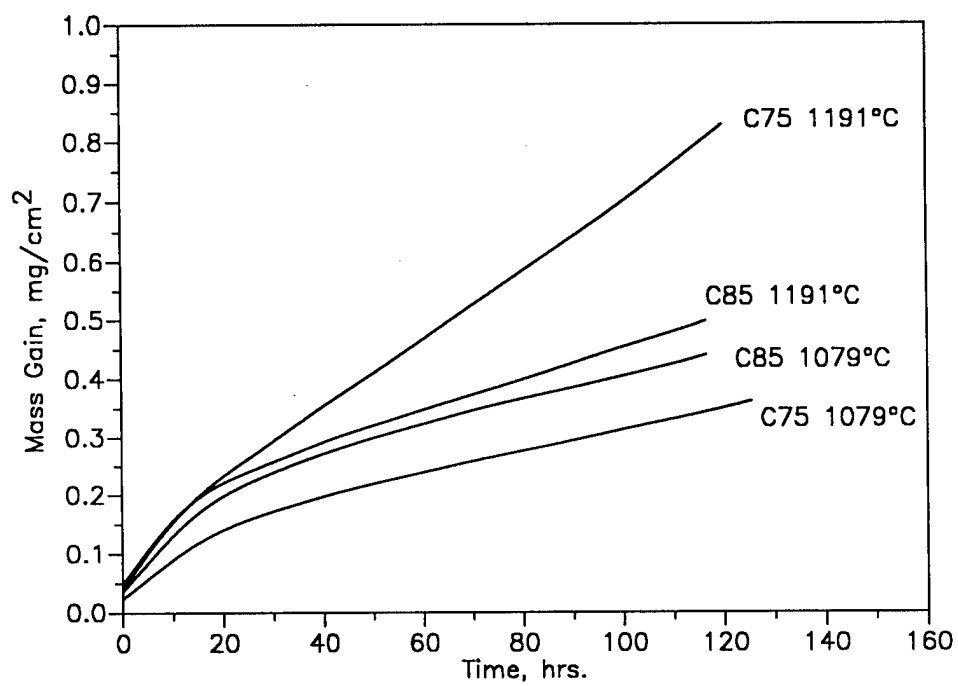


Figure 5: Isothermal oxidation of  $\text{Ti}_5\text{Si}_3\text{C}_{0.75}$  and  $\text{Ti}_5\text{Si}_3\text{C}_{0.85}$  in zero air at 1079°-1191°C.

the linear rate constant of C75 increases. The linear kinetics for C75 at 1079°C distinguish it from C25, C50, and C85 which all exhibit parabolic kinetics.

XRD of oxidized C75 indicates that the amount of rutile increases from 1079°-1191°C, and  $\text{Ti}_5\text{Si}_3$ -based peaks are visible at both temperatures. No crystalline silica is detected at 1079°C, but at 1191°C cristobalite is indicated by the faint peak (101) at  $22^\circ 2\theta$ . XRD of C85 shows the amount of rutile is about the same, consistent with the small difference in mass gain from 1079°-1191°C. Cristobalite is present at 1191°C, and  $\text{Ti}_5\text{Si}_3$ -based peaks are visible at both temperatures for C85. The small increase in mass

Table V: Steady State Rate Constants for Oxidation of  $\text{Ti}_5\text{Si}_3\text{C}_x$

Alloy	Temp.(°C)	Rate <sup>a</sup>	Value <sup>b</sup>	Time (hrs)
C25	1050	P	$5.3 \times 10^{-3}$	$t > 81$
	1079	P	$6.6 \times 10^{-4}$	$t > 36$
	1191	L	$2.7 \times 10^{-3}$	$t > 40$
C50	1000	L	$2.6 \times 10^{-3}$	$t > 100$
	1079	P	$7.6 \times 10^{-4}$	$t > 50$
C75	1079	L	$1.8 \times 10^{-3}$	$t > 60$
	1191	L	$5.9 \times 10^{-3}$	$t > 20$
C85	1079	P	$1.3 \times 10^{-3}$	$t > 36$
	1191	L	$2.7 \times 10^{-3}$	$t > 60$

<sup>a</sup>L=linear; P=parabolic

<sup>b</sup>L(mg/cm<sup>2</sup>/hr), P(mg<sup>2</sup>/cm<sup>4</sup>/hr)

gain for C85 at 1191°C relative to 1079°C may indicate the formation of a protective layer of crystalline silica.

#### 4. Oxidation of Boron-doped $\text{Ti}_5\text{Si}_3$

The addition of boron promotes an increase in oxidation resistance similar to that observed with the addition of carbon. Figure 6 shows the oxidation behavior of boron containing material. As with carbon additions, the overall mass gain of B75 decreases as temperature increases from 1000-1079°C, while B25 does not experience a similar temperature effect. Considering the steady state oxidation kinetics given in Table VI, B25 has a lower parabolic rate constant at 1000°C compared to the significantly larger linear rate constant for B75. As temperature is further increased to 1306°C, both compositions exhibit significant increases in mass gain.

XRD of B25 oxidized at 1000°C indicates rutile with underlying  $\text{Ti}_5\text{Si}_3$  peaks. The coupon contains a 'stain' on one side which corresponds to a substantial increase in rutile compared to the 'nonstained' side of the coupon. This difference may be related to differences in surface preparation of the coupon prior to oxidation. At 1306°C, B25 shows substantial mass gain which coincides with the growth of discrete 1-2 mm diameter patches of rutile on the coupon surface. The non-patchy areas presumably contain a thin rutile scale, since underlying  $\text{Ti}_5\text{Si}_3$  peaks are visible through the scale. No crystalline silica is detected at either temperature.

The scale on B75 at 1000°C contains rutile and underlying  $\text{Ti}_5\text{Si}_3$  peaks are still visible. As temperature is increased to 1079°C and mass gain decreases, both rutile and crystalline silica are detected, the latter presumably present as devitrified borosilicate glass. By 1306°C the underlying  $\text{Ti}_5\text{Si}_3$  peaks are no longer visible, and this corresponds to a uniform, thick scale which covers the entire surface, in contrast to B25. Silica is still

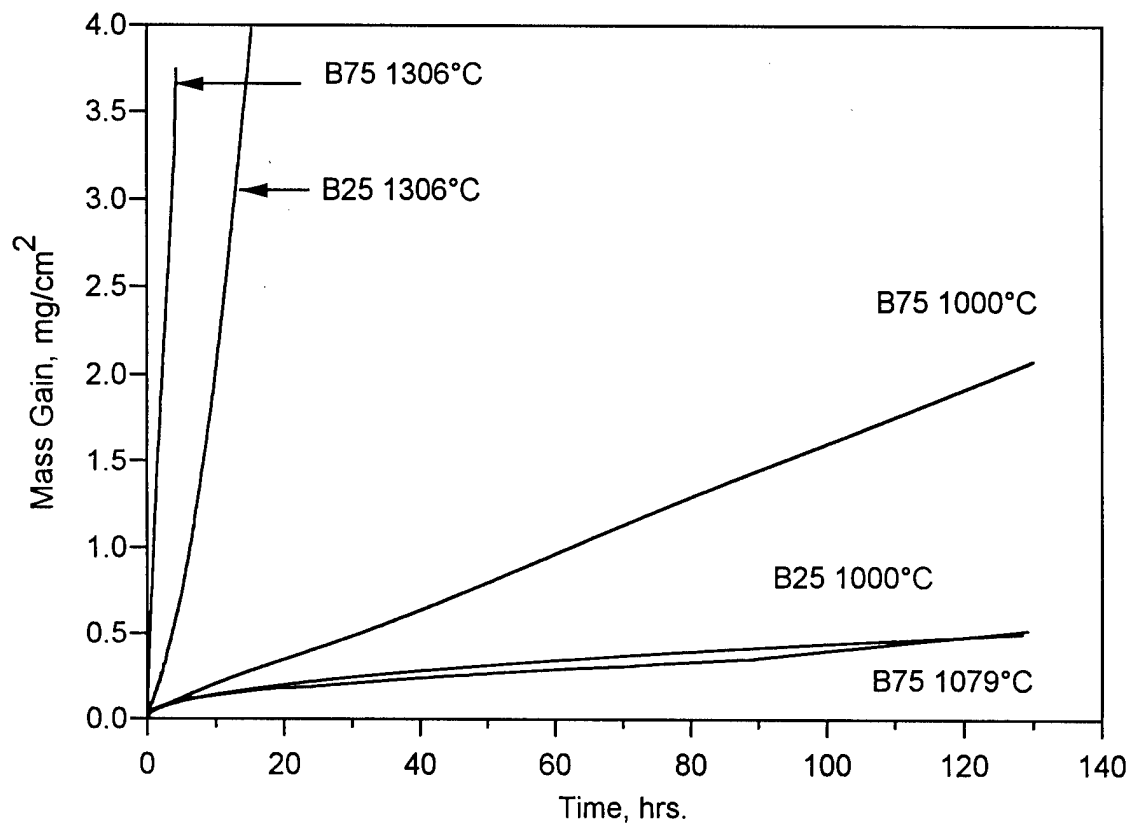


Figure 6: Isothermal oxidation of  $\text{Ti}_5\text{Si}_3\text{B}_x$  in zero air from 1000-1306°C.

Table VI: Steady State Rate Constants Oxidation of  $\text{Ti}_5\text{Si}_3\text{B}_x$ 

Alloy	Temp.(°C)	Rate <sup>a</sup>	Value <sup>b</sup>	Time (hrs)
B25	1000	P	$1.5 \times 10^{-3}$	$16 < t < 81$
		P	$2.6 \times 10^{-3}$	$t > 64$
	1306	L	$2.4 \times 10^{-1}$	$t > 30$
B75	1000	L	$1.6 \times 10^{-2}$	$t > 30$
	1079	L	$4.2 \times 10^{-3}$	$t > 90^c$
	1306	L	$1.9 \times 10^{-2}$	$t > 40$

<sup>a</sup>L=linear; P=parabolic<sup>b</sup> L(mg/cm<sup>2</sup>/hr), P(mg<sup>2</sup>/cm<sup>4</sup>/hr)<sup>c</sup> data mostly lost before 90 hrs

present, and the scale is observed to be less adherent, as pieces spalled from the edges of the oxidized coupon during handling at room temperature.

Figure 7 shows a composition backscattered electron (BSE) image of the scale which develops on B75 oxidized at 1079°C. Due to the fine nature of the scale, EDS spot analysis and x-ray dot mapping were inconclusive. However, coupling the XRD scale analysis with the BSE image contrast observed in the duplex phase assemblage indicates that the scale consists of a crystalline silica matrix (presumably borosilicate) forming a thin continuous layer with a substantial volume fraction of rutile particles. The total scale thickness is 2-3  $\mu\text{m}$  with 1  $\mu\text{m}$ -sized irregular-shaped rutile particles.

### 5. Oxidation of Nitrogen-doped $\text{Ti}_5\text{Si}_3$

Nitrogen doped material has about the same oxidative stability as undoped material. Figure 8 shows that nitrogen-containing material behaves nearly identically to

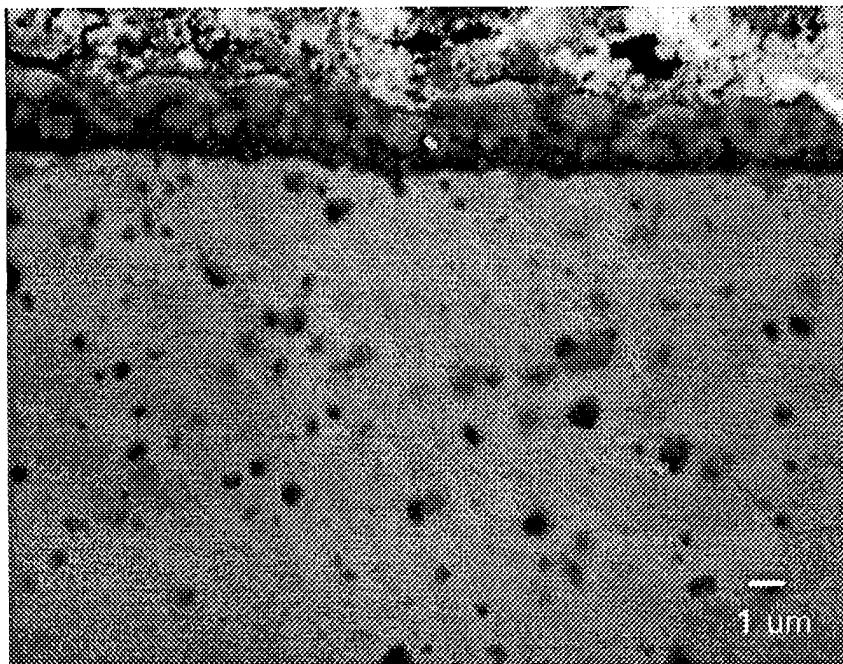


Figure 7: Backscattered electron image of  $\text{Ti}_5\text{Si}_3\text{B}_{0.75}$  oxidized at  $1079^\circ\text{C}$  for 130 hours.



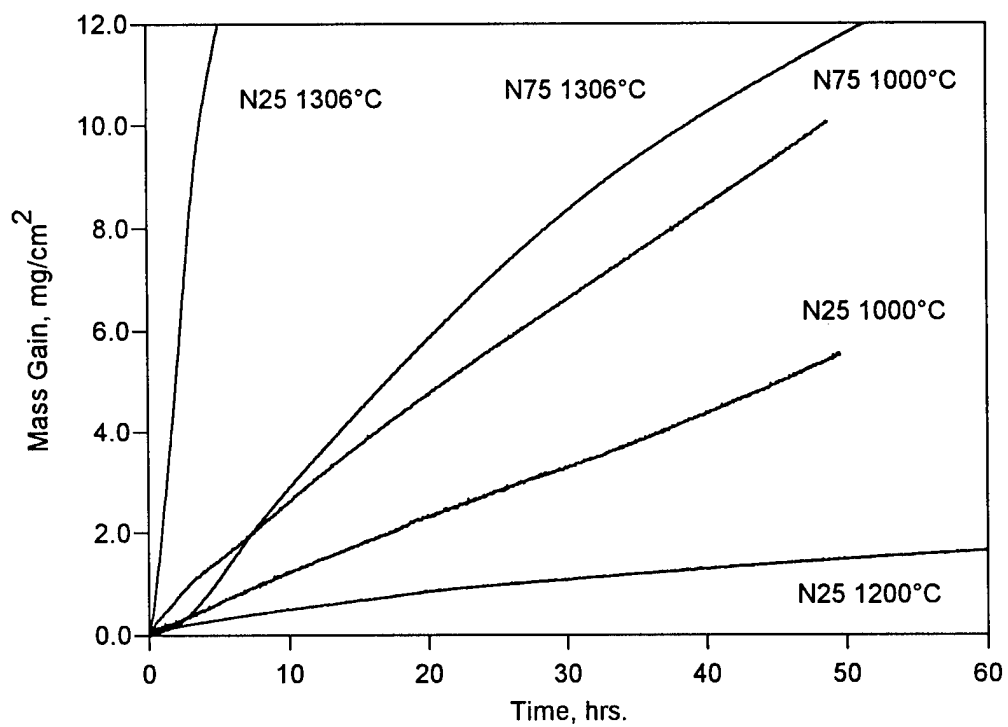


Figure 8: Isothermal oxidation of  $\text{Ti}_5\text{Si}_3\text{N}_x$  from 1000-1306°C in zero air.

undoped material. N25 shows a decrease in overall mass gain as temperature is increased from 1000°-1200°C with substantial increase in mass gain at 1306°C. N75 behaves somewhat differently in that mass gain at 1000°C and 1306°C is similar. Comparing the steady state rate constants given in Table VII, both N25 and N75 at 1000°C have linear rate constants similar to that of undoped material between 967°-1079°C (Table IV).

Table VII: Steady State Rate Constants for Oxidation of  $\text{Ti}_5\text{Si}_3\text{N}_x$

Alloy	Temp.(°C)	Rate <sup>a</sup>	Value <sup>b</sup>	Time (hrs)
N25	1000	L	$1.1 \times 10^{-1}$	$t > 0$
	1200	P	$6.3 \times 10^{-2}$	$t > 20$
	1306	L	$4.0 \times 10^{-1}$	$t > 8$
N75	1000	L	$1.8 \times 10^{-1}$	$t > 25$
	1306	L	$1.4 \times 10^{-1}$	$t > 50$

<sup>a</sup>L=linear; P=parabolic

<sup>b</sup> L(mg/cm<sup>2</sup>/hr), P(mg<sup>2</sup>/cm<sup>4</sup>/hr)

Similar to undoped material, N25 exhibits parabolic kinetics at 1200°C, although the undoped material tended toward parabolic kinetics. Interestingly, the linear rate constant of N75 at 1306°C is lower than the linear rate constant at 1000°C. However, no statistical uncertainty is associated with the rate constants, and given the substantial mass gain observed for N75 at both temperatures, the significance of this observation is overshadowed.

From 1000°-1200°C, XRD shows that N25 is covered with a thick rutile scale with no crystalline silica detected and through which no  $\text{Ti}_5\text{Si}_3$  peaks are detected. By

1306°C silica is present and the relative amount of rutile has significantly decreased.  $\text{Ti}_5\text{Si}_3$  peaks are present, and it is likely that some of the scale spalled during handling at room temperature. N75 at 1000°C is covered by a rutile scale and no  $\text{Ti}_5\text{Si}_3$  or silica peaks are detected. At 1306°C the rutile pattern changes significantly and the peaks no longer match their expected relative intensities, likely reflecting texturing and grain growth.

Figure 9 shows the scale developed on N75 at 1000°C. The dendritic phase is highly Si-deficient and is contained in a matrix phase that is Si-enriched and slightly Ti-depleted, probably  $\text{Ti}(\text{N},\text{O})_x$  dendrites within a  $\text{TiSi}_2$  matrix. The outer 5  $\mu\text{m}$  of the scale is Ti-rich and Si-void, presumably rutile. The dendritic microstructure is very similar to that developed on undoped material at 800°C (13,14,15).

## 6. Oxidation of Oxygen-Doped $\text{Ti}_5\text{Si}_3$

The oxidative behavior of O75 and O25 is shown in Figures 10 and 11, respectively. The behavior of oxygen-containing material is distinctly different than the other compositions tested. No transition to a lower mass gain regime at increasing temperature is observed, as was seen in Figures 4, 6, and 8 for C25, C50, B75, and N25. In particular, the overall mass gain is seen to increase from 1000°-1306°C for both O25 and O75. The mass gain for O75 is larger than that for O25 at each temperature. Particularly interesting is that protective behavior maintained by O25 up to 1306°C.

As described in Table VIII, O25 undergoes a transition from linear to parabolic oxidation kinetics as temperature is increased from 1000°-1200°C. Oxidation of O25 at 1306°C is slightly better described by parabolic kinetics. O75 maintains reasonable protective behavior during oxidation at 1079°C, but at 1306°C the large linear rate constant reflects that extremely rapid mass gain is occurring. The scale on O25 contains

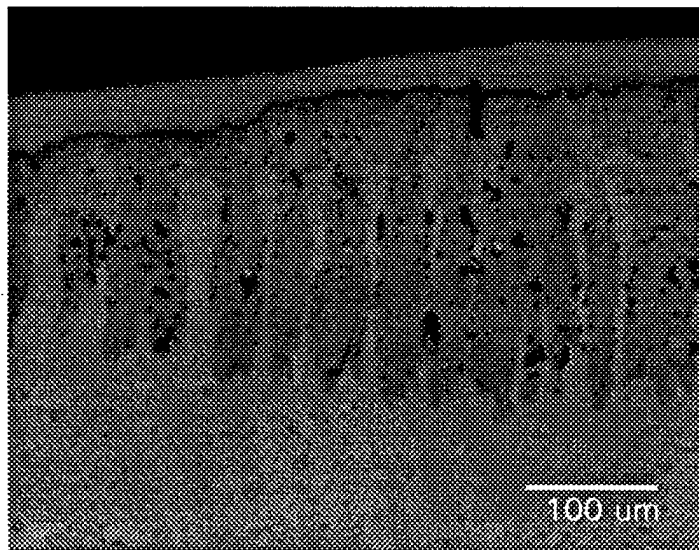


Figure 9: Backscattered electron image of  $\text{Ti}_5\text{Si}_3\text{N}_{0.75}$  oxidized at  $1000^\circ\text{C}$  for 50 hours.

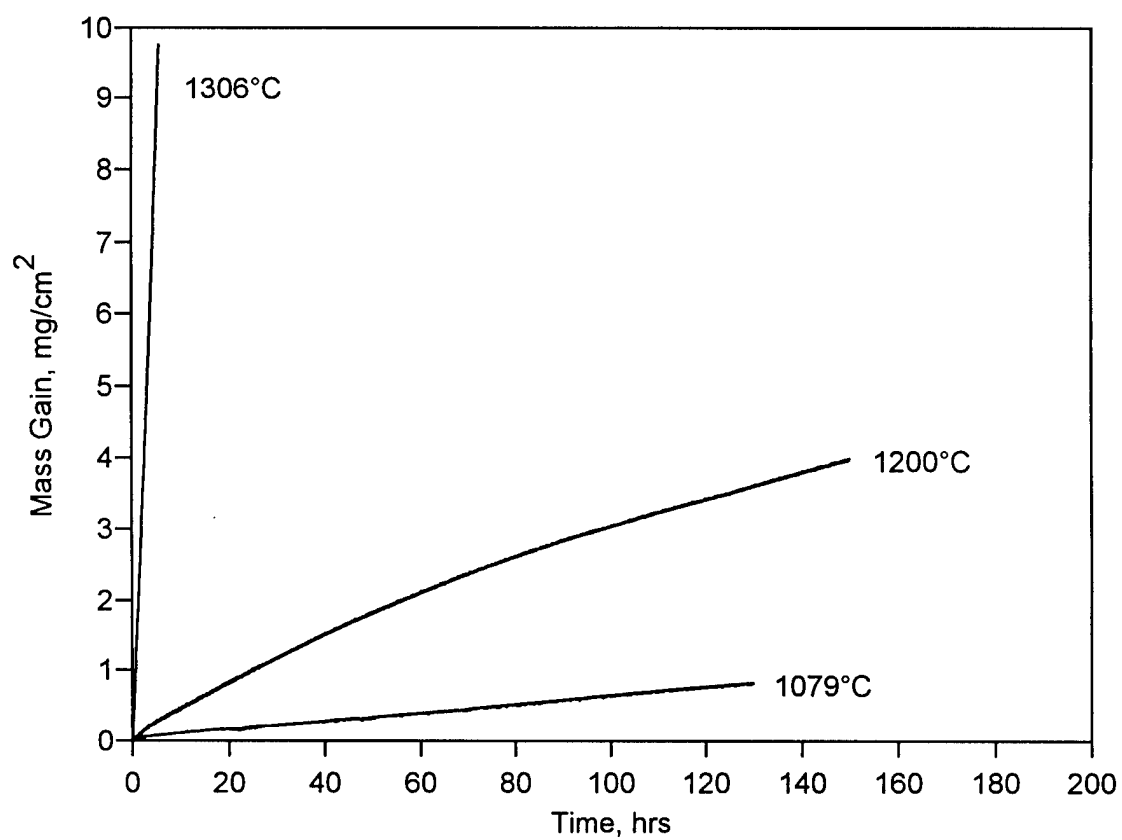


Figure 10: Isothermal oxidation of  $\text{Ti}_5\text{Si}_3\text{O}_{0.75}$  in zero air from 1079-1306°C.

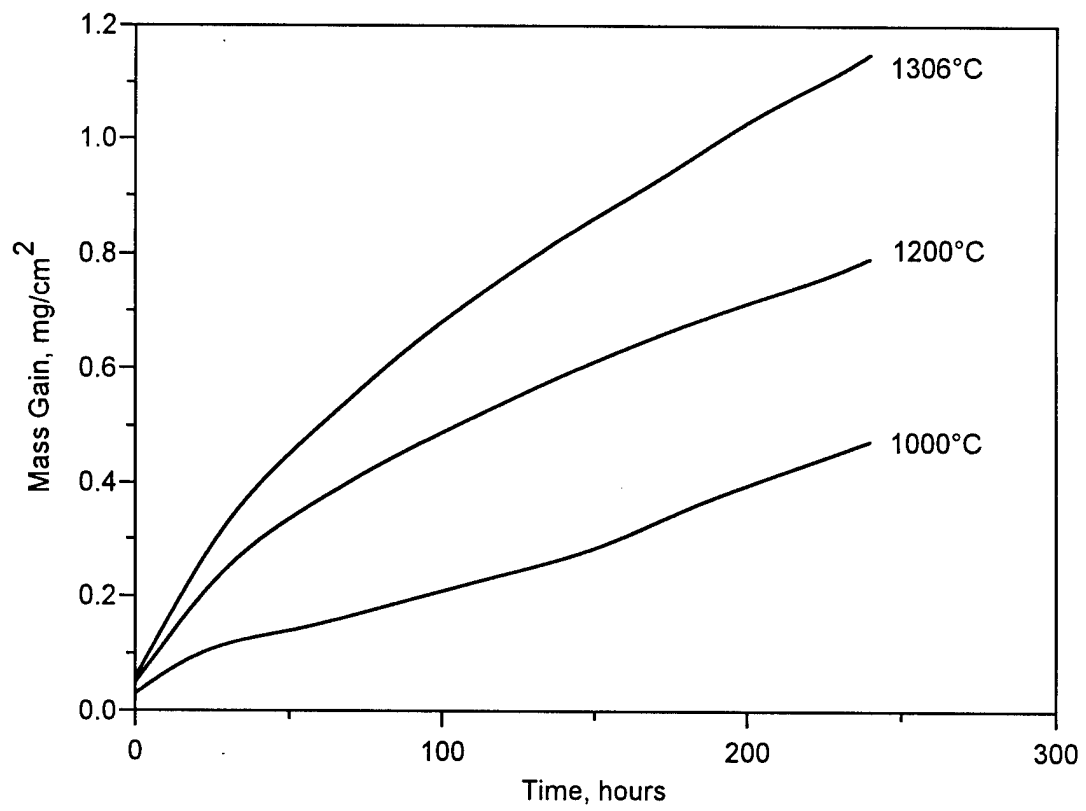


Figure 11: Isothermal oxidation of  $\text{Ti}_5\text{Si}_3\text{O}_{0.25}$  in zero air from 1079-1306°C.

rutile in increasing amounts as oxidation temperature increases from 1000°-1306°C. Underlying  $\text{Ti}_5\text{Si}_3$  peaks are present after oxidation at each temperature, and cristobalite is detected after oxidation at 1200° and 1306°C. As was observed for B75, this indicates that the vitreous silica layer is crystallizing between 1000°-1200°C. For O75 oxidized at 1079°C, a substantial amount of rutile is present in the scale. After oxidation at 1200°C,  $\text{Ti}_5\text{Si}_3$  peaks are not detected through the rutile, but after oxidation at 1306°C, spalling of the scale during coupon handling at room temperature leads to presence of underlying  $\text{Ti}_5\text{Si}_3$  peaks. Cristobalite is faintly visible after oxidation at 1200°-1306°C.

Figure 12 shows a compositional BSE image of the scale which developed on O25 oxidized at 1306°C for 240 hours. The small bright spots correspond to charging of

Table VIII: Steady State Rate Constants for Oxidation of  $\text{Ti}_5\text{Si}_3\text{O}_x$

Alloy	Temp.(°C)	Rate <sup>a</sup>	Value <sup>b</sup>	Time (hrs)
O25	1000	L	$1.8 \times 10^{-3}$	$t > 50$
	1200	P	$2.9 \times 10^{-3}$	$t > 30$
	1306	PL	$4.1 \times 10^{-3}$ (P), $8.2 \times 10^{-4}$ (L)	$t > 36$
		P	$6.7 \times 10^{-3}$	$t > 36$
O75	1079	L	$6.3 \times 10^{-3}$	$t > 60$
	1200	L	$1.9 \times 10^{-2}$	$t > 100$
	1306	L	1.6	$t < 3.5$
			accelerating	$t > 3.5$

<sup>a</sup>L=linear, P=parabolic, PL=paralinear

<sup>b</sup> L(mg/cm<sup>2</sup>/hr), P(mg<sup>2</sup>/cm<sup>4</sup>/hr)

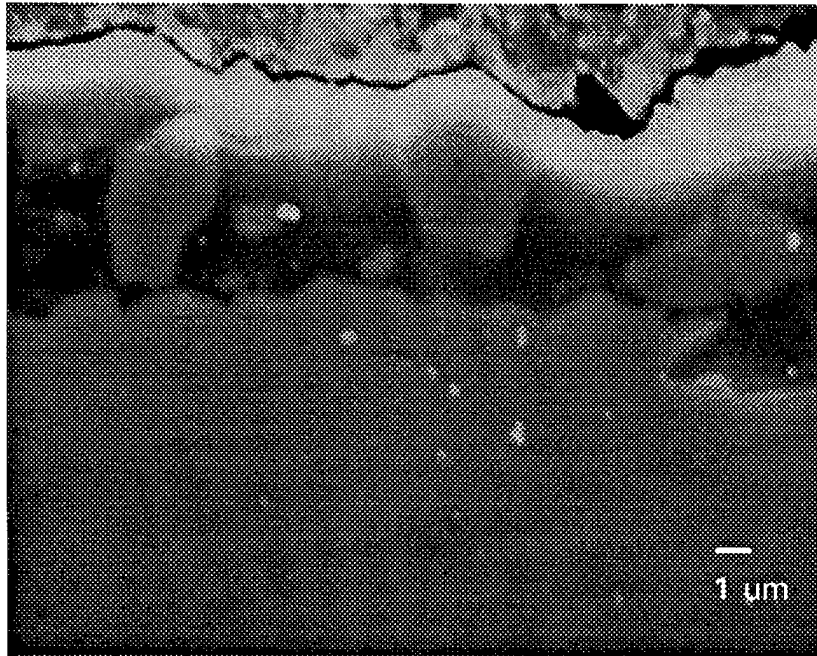


Figure 12: Compositional BSE image of  $\text{Ti}_5\text{Si}_3\text{O}_{0.25}$  oxidized at  $1306^\circ\text{C}$  for 240 hours.



residual alumina polishing media. EDS spot analysis and x-ray dot mapping indicate that the scale is composed of Ti-rich, Si-deficient particles in a matrix phase which is Si-rich and Ti-deficient. EDS analyses and XRD scale analyses indicate the scale consists of a continuous layer made up of a crystalline silica matrix containing rutile particles. The total scale thickness is 5-10  $\mu\text{m}$  with 3-8  $\mu\text{m}$  regularly-shaped rutile particles. The continuous silica matrix imparts protective behavior to the material. The scale morphology resembles that of B75 oxidized at 1079°C (Figure 7) with the exception that a higher density of rutile particles exists in the scale on B75.

The oxidative stability of the various  $\text{Ti}_5\text{Si}_3\text{Z}_x$  compositions at 1306°C are compared in Figure 13. C25 was tested only up to 1191°C, but it is included for completeness. At this highest test temperature of 1306°C, there is a general loss of protective behavior with a few notable exceptions. B75 undergoes rapid transient oxidation but assumes linear kinetics after about ten hours. The linear rate constant,  $1.9 \times 10^{-2} \text{ mg/cm}^2/\text{hr}$ , is about one-fifth the linear rate constant of undoped  $\text{Ti}_5\text{Si}_3$  from 967°-1079°C. In addition, protective behavior is maintained for O25 up to 1306°C as previously described. Mass gain after 240 hours is about  $1.1 \text{ mg/cm}^2$ .

## IV. Discussion

### 1. Grain Size Effects on Oxidation of Undoped $\text{Ti}_5\text{Si}_3$

CG1 had a lower mass gain than FG2 at the same temperature (1079°C) and was comparable to FG1 at a lower temperature (967°C). The effect of grain size of the substrate on mass gain may be explained by considering the grain size of the external scale. Caplan and Sproule (22) have shown that etched polycrystalline Cr forms a scale composed of areas of single crystal and polycrystalline chromia. The single crystal areas

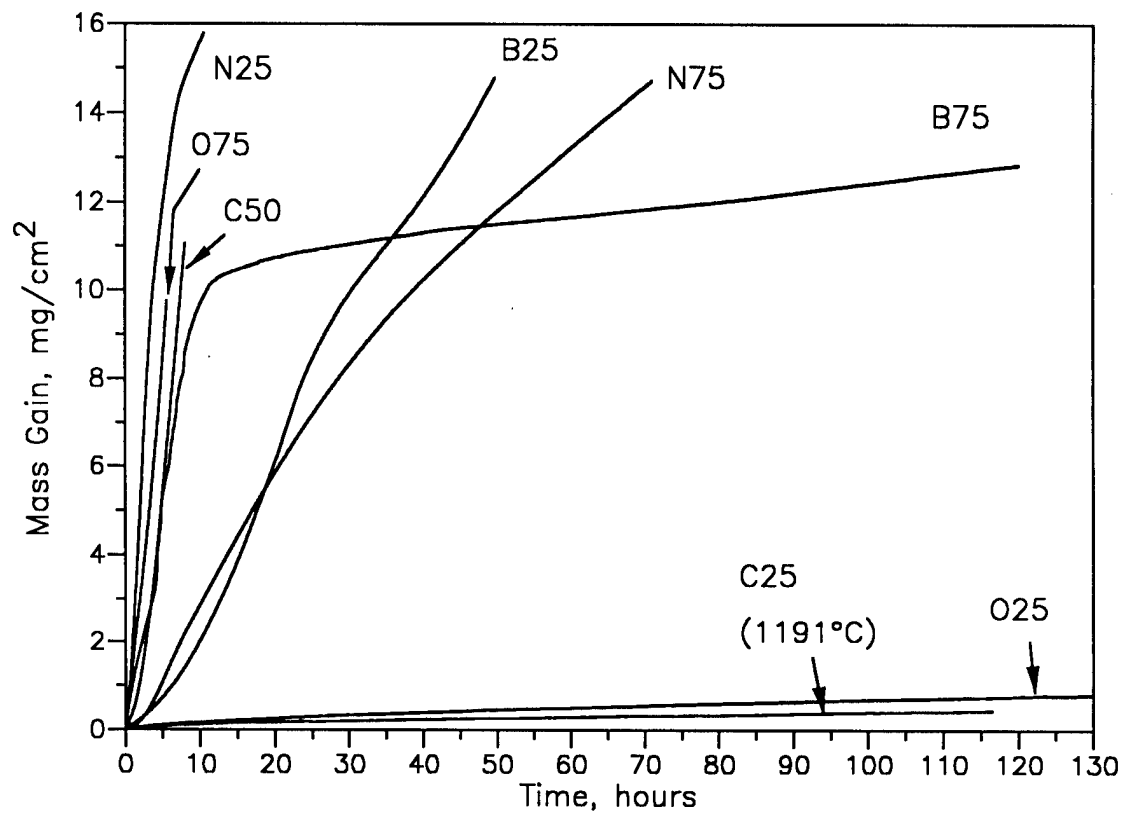


Figure 13: Isothermal oxidation of  $\text{Ti}_5\text{Si}_3\text{Z}_x$  in zero air at 1306°C.  
(Data for C25 for oxidation at 1191°C)

corresponded to epitaxial growth of the chromia on certain grain orientations of the polycrystalline Cr substrate. These single crystal chromia areas persisted during high temperature oxidation to 1200°C. This significantly reduced scale growth on the polycrystalline Cr substrate by limiting inward grain boundary diffusion of oxygen. The single crystal chromia imparted improved oxidation resistance to the polycrystalline Cr substrate. The increased grain size of the  $\text{Ti}_5\text{Si}_3$  substrate of CG1 and CG2 compared to the smaller substrate grain size in FG1 and FG2 may contribute at least limited regions of increased grain size of the developing rutile scale on CG1 and CG2. The rate of inward grain boundary diffusion of oxygen and thus overall mass gain in CG1 and CG2 would also be smaller than that in FG1 and FG2.

The parabolic kinetics observed for CG2 have been observed for titanium oxidation (21). Sintering and grain growth of the rutile scale decreases the relative contribution of inward oxygen grain boundary diffusion in the scale, allowing volume diffusion to dominate with the consequent assumption of parabolic kinetics.

## 2. Oxidation Kinetics of $\text{Ti}_5\text{Si}_3\text{C}_x$

The presence of  $\text{TiC}_y$  precipitates in  $\text{Ti}_5\text{Si}_3\text{C}_x$ , as previously discussed, will influence the overall measured mass gain for  $\text{Ti}_5\text{Si}_3\text{C}_x$  (Figures 4 and 5) and calculated oxidation kinetics (Table V). The morphological effect of the oxidation of the  $\text{TiC}_y$  precipitates is seen in Figure 14. The oxidized particles form nodules which protrude from the surface, probably as the result of the 54% volume increase which occurs during formation of rutile from  $\text{TiC}_y$ . The presence of  $\text{TiC}_y$  in the  $\text{Ti}_5\text{Si}_3\text{C}_x$  specimens tested suggests that the measured steady state oxidation rate constants given in Table V do not accurately describe the intrinsic oxidation characteristics of single-phase  $\text{Ti}_5\text{Si}_3\text{C}_x$ . The oxidation of  $\text{TiC}_y$  proceeds linearly after a transient oxidation period of up to one hour

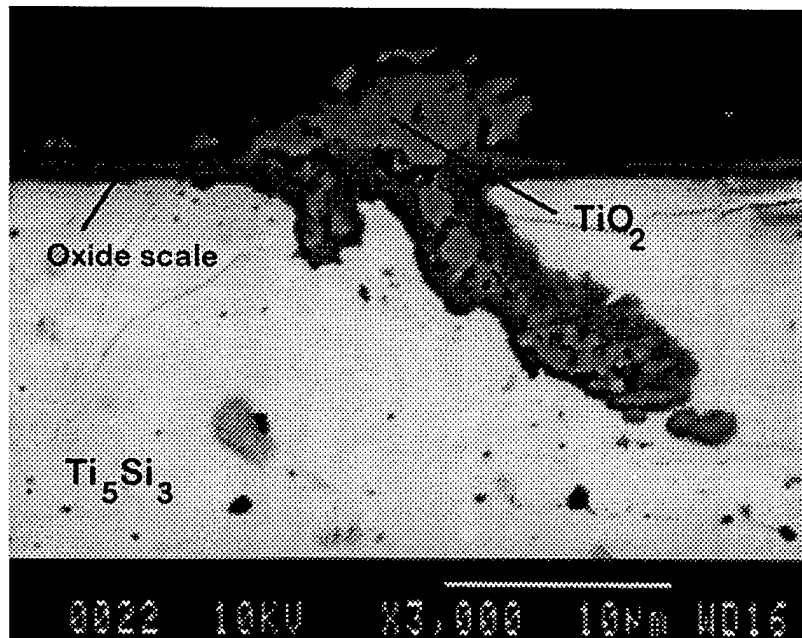


Figure 14: Compositional BSE image of  $\text{Ti}_5\text{Si}_3\text{C}_{0.25}$  oxidized at  $1079^\circ\text{C}$  for 120 hours. The nodule protruding from the surface is the remains of a  $\text{TiC}_y$  particle.

(23,24). For  $\text{TiC}_y$  contained within a  $\text{Ti}_5\text{Si}_3\text{C}_x$  matrix, the oxidation process may proceed as either (i) rapid oxidation of  $\text{TiC}_y$  leading to complete consumption of all  $\text{TiC}_y$  with no further contribution to the experimentally measured mass gain, or (ii) oxidation of  $\text{TiC}_y$  as a steady state linear process concurrently with steady-state  $\text{Ti}_5\text{Si}_3\text{C}_x$  oxidation. The following observation rules out case (i). Lavrenko et al. oxidized hot-pressed  $\text{TiC}_y$  and measured a linear rate constant of  $3.1 \text{ mg/cm}^2/\text{hr}$  in 740 Torr oxygen at  $1100^\circ\text{C}$  with a corresponding mass gain of  $13.4 \text{ mg/cm}^2$  after 3 hours. This mass gain data predicts that C85, which contains about 8 vol%  $\text{TiC}_y$ , would experience an approximate mass gain, based on a  $2 \text{ cm}^2$  sample, of  $13.4(2)(0.08) = 2.1 \text{ mg}$  after 3 hours at  $1100^\circ\text{C}$ . Experimental data for C85 at  $1079^\circ\text{C}$  for 3 hours shows a mass gain of about  $0.1 \text{ mg/cm}^2$  on a  $2 \text{ cm}^2$  sample or about  $0.2 \text{ mg}$ . The observed mass gain of C85 is about an order of magnitude lower than that predicted due to  $\text{TiC}_y$  oxidation, suggesting oxidation of  $\text{TiC}_y$  is proceeding much slower than expected. This clearly rules out case (i), and so composite oxidation can be approximated according to case (ii). Neglecting the transient oxidation of the composite, the steady state mass gain is given by:

$$\left(\frac{\Delta m}{A}\right) = (1 - f_c) k_p^{1/2} t^{1/2} + \left(f_c k_l^c + (1 - f_c) k_l^s\right) t \quad (4)$$

where  $f_c$  and  $k_l^c$  are the area fraction and linear rate constant of  $\text{TiC}_y$ , and  $k_p$  and  $k_l^s$  are the parabolic and linear rate constants for  $\text{Ti}_5\text{Si}_3\text{C}_x$ . The experimental data can be modeled as a second order polynomial of the form:

$$\left(\frac{\Delta m}{A}\right) = c_0 + c_1 \left(t^{1/2}\right)^1 + c_2 \left(t^{1/2}\right)^2 \quad (5)$$

which is parallel in form to Eq. 4 where  $c_o$  is an intercept calculated from the regression analysis,  $c_1 = (1-f_c) k_p^{1/2}$ , and  $c_2 = f_c k_l^c + (1-f_c) k_l^s$ . If  $f_c$  is known and assumed constant, then  $k_p$  can be uniquely determined from  $c_1$ . The values of  $c_1$  and  $c_2$  determined from multiple linear regression analysis for carbon-doped material at 1079°C are given in Table IX. This analysis predicts that C75 has the lowest parabolic rate constant, and this is expected since linear steady state oxidation was originally predicted in Table V. Although  $k_l^s$  and  $k_l^c$  cannot be uniquely determined from  $c_2$ , the sign of  $c_2$  indicates the relative contribution that each linear process makes to the overall mass change. The negative value of  $c_2$  implies that  $k_l^s$  is negative, suggesting a net mass loss event is occurring. The decrease in  $c_2$  with decreasing carbon composition may simply reflect the decrease in  $\text{TiC}_y$  content.

Table IX: Parabolic Rate Constants from Eq. 5 for  $\text{Ti}_5\text{Si}_3\text{C}_x$  Oxidized at 1079°C

Alloy	$c_1$	$c_2$	$f_c$	$k_p$ (mg <sup>2</sup> /cm <sup>4</sup> /hr)
C25	2.65e-2	-3.71e-5	0.01	7.2e-4
C50	1.71e-2	6.05e-4	0.01	3.0e-4
C75	1.21e-2	1.17e-3	0.08	1.7e-4
C90	1.74e-2	1.16e-3	0.08	3.6e-4

As the amount of  $\text{TiC}_y$  decreases, the mass gain due to  $\text{TiC}_y$  oxidation decreases and the net mass loss event becomes more significant, driving  $c_2$  toward zero.

A net mass loss event corresponds to formation of a volatile species. Considering the scale which is observed to form, carbon-doped material has a continuous, external rutile layer covering an underlying Si-rich layer, assumed to be silica (15). The

continuous external rutile layer may effect an equilibrium oxygen partial pressure at this silica/rutile interface which is low enough to reduce the silica layer and lead to formation of volatile SiO vapor (i.e., induce active oxidation). There must be an escape route for the vapor, likely through cracks locally developed in the scale.

Figure 15 shows an Auger Electron Microscopy (AEM) line scan profile across the scale developed on C25 oxidized at 1079°C after 120 hours. The presence of an oxide scale is evident from the enrichment of oxygen at the exterior of the sample. The Ti signal closely follows the trend of oxygen in the exterior scale, indicating the presence of rutile at the scale exterior. The shallow minimum in the Ti signal at 19  $\mu\text{m}$  should coincide with a maximum in the Si signal, corresponding to formation of a silica layer. However, the Si signal linearly decreases from the constant level in the alloy to zero at the scale surface. This lack of a clear maximum in the Si peak indicates that the underlying layer, seen in Figure 14 as a dark phase and previously ascribed as silica, is in fact a layer of continuously varying Si content. The simultaneous formation of silica at the scale/alloy interface and volatilization of SiO in the outer layers as previously hypothesized might produce such a concentration gradient. An intermetallic  $\text{Ti}_x\text{Si}_y(\text{C},\text{O})$  layer is also suggested by the increasing Ti and Si signals between the external scale and interior  $\text{Ti}_5\text{Si}_3\text{C}_x$ .

### 3. Scale Development in $\text{Ti}_5\text{Si}_3\text{Z}_x$ ( $\text{Z}=\text{B},\text{C}$ )

Carbon-containing material experiences lower mass gain than boron-doped material up to 1200°C. In particular, a difference is noted in the morphology of the scales which develop on boron- and carbon-doped materials. B75 at 1079°C was characterized by discrete particles of rutile throughout a borosilicate matrix, while carbon-doped material has a continuous, external rutile layer. As mentioned above, the continuous rutile scale

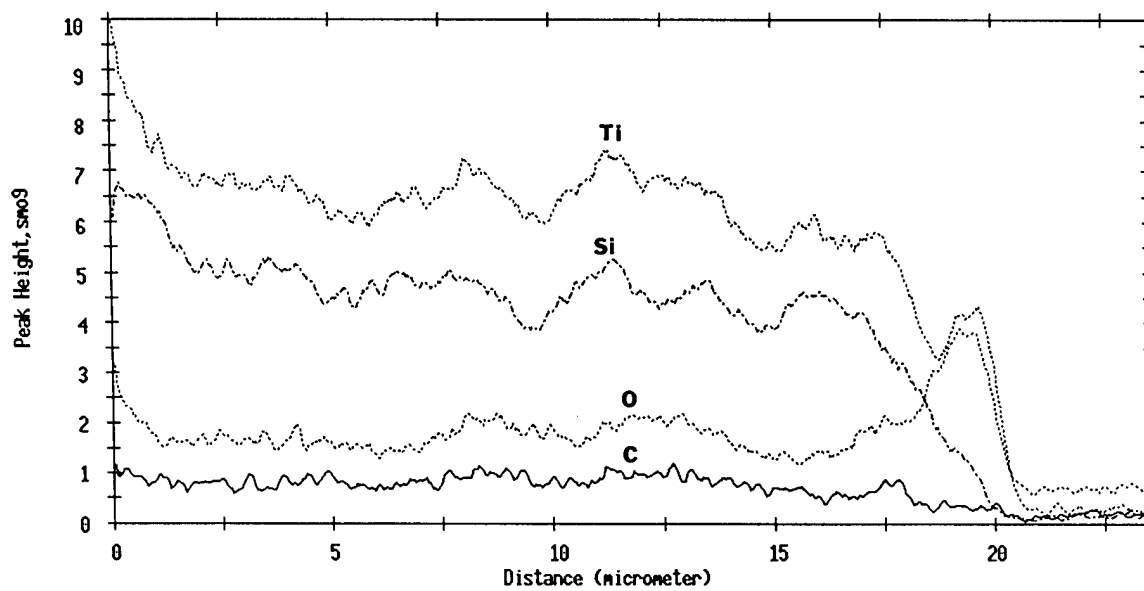


Figure 15: Auger line scan profile of  $\text{Ti}_5\text{Si}_3\text{C}_{0.25}$  oxidized at  $1079^\circ\text{C}$ .



should fix the oxygen partial pressure present at the rutile/silica interface to a significantly lower value. Oxygen diffusion through silica is directly proportional to the gradient in oxygen partial pressure across the layer (25), and this would predict a lower oxygen flux through the silica layer on carbon-doped material. Also, oxygen transport through pure silica is much slower than through borosilicate glass (26). These two observations combine to predict that the carbon-doped material should be more oxidation resistant than boron-doped material. An additional experiment to test this theory would be to oxidize both C25 and B25 in pure oxygen. The oxidation rate of B25 should increase in proportion to the oxygen partial pressure increase. On the other hand, the increase in oxygen partial pressure should have little effect on the oxidation rate of C25 since the oxygen partial pressure at the rutile/silica interface should be fixed for a constant temperature and substantially lower than the oxygen partial pressure at the scale/gas interface.

The development of an external rutile scale suggests relatively rapid outward diffusion of titanium through the silica layer. The outward diffusion of titanium through silica is observed in the oxidation of  $\text{TiSi}_2$  (27). The lack of formation of a continuous layer of rutile on boron-doped material may indicate decreased outward diffusion of titanium through the borosilicate layer.

For both boron- and carbon-doped material, increasing temperature from about  $1000^\circ\text{--}1050^\circ\text{C}$  to  $1079^\circ\text{C}$  results in a lowering of overall mass gain. Below some threshold temperature, a continuous rutile scale is observed, suggesting the rate of formation of rutile due to outward diffusion of titanium is too rapid for silica formation which leads to increased scale growth and mass gain. After the temperature is sufficiently raised, the relative increase in Si diffusion must be sufficient so that silica formation

becomes rapid relative to rutile formation and allows for formation of a continuous protective silica layer.

#### 4. Scale Development in $\text{Ti}_5\text{Si}_3\text{Z}_x$ ( $\text{Z}=\text{O},\text{N}$ )

As with boron-containing material, a continuous external rutile scale does not form on oxygen-doped material. The outward diffusion of Ti in oxygen-doped material is apparently smaller than in boron- or carbon-doped material as evidenced by the decreased formation of rutile at the scale/gas interface, even at  $1306^\circ\text{C}$ . Unlike boron- and carbon-doped material which lost protective behavior at  $1306^\circ\text{C}$ , a thin silica layer was maintained on O25. As observed for boron-doped material, decreased outward Ti diffusion as suggested by the decreased presence of rutile at the scale/gas interface suggests the interstitial effect in O25 to be strongest.

Perhaps the biggest question is the cause of the poor oxidation resistance of nitrogen-doped material. The similar oxidation behavior of undoped and nitrogen-doped material indicates that nitrogen additions cause little change in the diffusion of Si and Ti in nitrogen-doped material. It is conceivable that the supply of Si/Ti remains relatively constant if nitrogen promotes a simultaneous increase or decrease in the diffusion of both Ti and Si.

### V. Conclusions

The low density and high melting temperature of  $\text{Ti}_5\text{Si}_3$  defines the material to be a potential high temperature structural material. However,  $\text{Ti}_5\text{Si}_3$  losses oxidation resistance above  $700^\circ\text{C}$  and thus cannot be used in applications requiring exposure to high temperature oxidizing environments. The addition of small interstitial atoms,

including boron, carbon, and oxygen, dramatically improves oxidation resistance with significantly reduced mass gains in air up to about 1200°C. Boron- and oxygen-doped  $\text{Ti}_5\text{Si}_3$  form a thin, continuous layer of silica with discrete rutile particles at the scale/gas interface. Carbon-containing material also forms a thin, adherent duplex layer with a continuous external rutile layer. The formation of rutile at the scale/gas interface in  $\text{Ti}_5\text{Si}_3\text{Z}_x$  ( $Z=\text{B,C,O}$ ) suggests outward diffusion of titanium through the underlying silica layer. On the other hand, nitrogen additions promote only slight improvements in the oxidation resistance of  $\text{Ti}_5\text{Si}_3$ . Although oxidation resistance for  $\text{Ti}_5\text{Si}_3\text{Z}_x$  ( $Z=\text{B,C,N}$ ) significantly decreases as temperature is further increased to 1306°C,  $\text{Ti}_5\text{Si}_3\text{O}_{0.25}$  maintains protective behavior. It is believed that the mechanism of improved oxidation resistance is related an increasing interstitial effect in which outward Ti diffusion from  $\text{Ti}_5\text{Si}_3\text{Z}_x$  to the external scale decreases in the order  $Z=\text{N,C,B,O}$ .

### Acknowledgements

Ames Laboratory is operated for the U. S. Department of Energy by Iowa State University under contract number W-7405-ENG-82. This research was supported by the Office of Basic Energy Science, Materials Science Division. The authors would like to thank Dr. Mitch Meyer for many helpful discussions and Dr. M. F. Berard for reviewing the manuscript. The authors also thank Tammy Bloomer for AEM measurements.

### References

1. D. L. Anton, D. M. Shah, D. N. Duhl, and A. F. Giamei, "Selecting High-Temperature Structural Intermetallic Compounds: The Engineering Approach," Journal of Metals, Sept. (1989), 12-17.

2. A. I. Taub and R. L. Fleischer, "Intermetallic Compounds for High-Temperature Structural Use," Science, 243 (1989), 616-621.
3. P. J. Meschter and D. S. Schwartz, "Silicide-Matrix Materials for High-Temperature Applications," Journal of Metals, Nov. (1989), 52-55.
4. D. M. Shah, D. Berczik, D. L. Anton, and R. Hecht, "Appraisal of other Silicides as Structural Materials," Mat. Sci. Eng., A155 (1992), 45-57.
5. K. S. Kumar and C. T. Liu, "Ordered Intermetallic Alloys, Part II: Silicides, Trialuminides, and Others," J. Metals, June (1993), 28-34.
6. C.T. Liu, E. H. Lee, and T. J. Henson, "Initial Development of High Temperature Titanium Silicide Alloys," (Report ORNL-6435; Order No. DE88007860, 1988).
7. D. M. Shah, Private communication with author, Pratt and Whitney, 15 September 1992.
8. E. Garcia and J. D. Corbett, "Chemistry of Polar Intermetallic Compounds. Study of Two  $Zr_5Sb_3$  Phases, Hosts for a Diverse Interstitial Chemistry," Inorganic Chem., 27 (1988), 2353-2359.
9. Y. Kwon, M. A. Rzeznik, A. Guloy, and J. D. Corbett, "Impurity Stabilization of Phases with the  $Mn_5Si_3$ -Type Structure. Questions Regarding  $La_5Sn_3$  and  $Zr_5Si_3$ ," Chem. Mater., 2 (1990), 546-550.
10. E. Garcia and J. D. Corbett, "Chemistry in the Polar Intermetallic Host  $Zr_5Sb_3$ . Fifteen Interstitial Compounds," Inorganic Chem., 29 (1990), 3274-3282.
11. Y. Kwon and J. D. Corbett, "Chemistry in Polar Intermetallic Compounds. The Interstitial Chemistry of  $Zr_5Sn_3$ ," Chem. Mater., 4 (1992), 1348-1355.
12. A. J. Thom, V. Young, and M. Akinc, "Single Crystal Studies of  $Ti_5Si_3Z_x$ ," to be published.
13. A.J. Thom, Y. Kim, and M. Akinc, "Effect of Processing on Oxidation of  $Ti_5Si_3$ ," Mat. Res. Soc. Symp. Proc., vol. 288, edited by Baker, Darolia, Whittenberger, and Yoo (Pittsburgh, PA: Materials Research Society, (1993), 1037-1042.

14. Y. Kim, A. J. Thom, and M. Akinc, "Synthesis, Processing, and Properties of  $Ti_5Si_3$ ," Min. Met. Mater. Soc. Symp. Proc., edited by T. S. Srivatsan and V. A. Ravi, Processing and Fabrication of Advanced Materials for High-Temperature Applications - II, (1993), 189-208.
15. A. J. Thom, M. K. Meyer, Y. Kim, and M. Akinc, "Evaluation of  $A_5Si_3Z_x$  Intermetallics for Use as High Temperature Structural Materials," Min. Met. Mater. Soc. Symp. Proc., edited by T. S. Srivatsan and V. A. Ravi, Processing and Fabrication of Advanced Materials for High-Temperature Applications - III, (1994), 413-438.
16. E. J. Opila and R. E. Hann, "Paralinear Oxidation of CVD SiC in Water Vapor," submitted to Journal Amer. Ceram. Soc..
17. B. Pieraggi, "Calculations of Parabolic Reaction Rate Constants," Oxidation Metals, 27 [3/4] (1987), 177-185.
18. J. I. Goldstein, S. K. Choi, F. J. J. Van Loo, G. F. Bastin, and R. Metselaar, "Solid State Reactions and Phase Relations in the Ti-Si-O System at 1373K", Journal Amer. Ceram. Soc., 78 [2] (1995), 313-322.
19. S. Arunajatesan and A. H. Carim, "Synthesis of Titanium Silicon Carbide," Journal Amer. Ceram. Soc., 78 [3] (1995), 667-672.
20. S. Sambasivan and W. T. Petuskey, "Phase Chemistry in the Ti-Si-N System: Thermochemical Review with Phase Stability Diagrams", Journal Mater. Res., 9 [9] (1994), 2362-2369.
21. P. Kofstad, P. B. Anderson, and O. J. Krudtaa, "Oxidation of Titanium in the Temperature Range of 800-1200°C," Jour. Less-Common Metals, 3 (1961), 89-97.
22. D. Caplan and G. I. Sproule, "Effect of Oxide Grain Structure on the High-Temperature Oxidation of Cr," Oxidation Metals, 9 [5] (1975), 459-472.
23. V. A. Lavrenko, L. A. Glebov, A. P. Pomitkin, V. G. Chuprina, and T. G. Protsenko, "High-Temperature Oxidation of Titanium Carbide in Oxygen," Oxidation Metals, 9 [2] (1975), 171-179.
24. R. F. Voitovich and E. A. Pugach, "High-Temperature Oxidation of Titanium Carbide," Poroshkovaya Metallurgiya, 11 [1] (1972), 132-136.

25. B. E. Deal and A. S. Grove, "General Relationship for the Thermal Oxidation of Silicon," Jour. Applied Physics, 36 [12] (1965), 3770-3778.
26. J. Schlichting, "Oxygen Transport Through Glass Layers Formed by a Gel Process," Jour. Non-Crystalline Solids, 63 (1984), 173-181.
27. T. Sandwick and K. Rajan, "The Oxidation of Titanium Silicide," Jour. Electronic Mater., 19 [11] (1990), 1193-1199.

## CHAPTER 6: GENERAL CONCLUSION

I. Oxidation Behavior of  $\text{Ti}_5\text{Si}_3\text{Z}_x$ 

In general, oxidation kinetics of  $\text{Ti}_5\text{Si}_3$  are similar those of titanium, reflecting the dominant effect of preferential titanium oxidation due to insufficient silicon activity. The oxidation resistance of  $\text{Ti}_5\text{Si}_3$  in air is adequate up to about  $800^\circ\text{C}$ . ESCA analysis shows the material forms a thin passivating layer of  $\text{TiO}_2$  and  $\text{SiO}_2$  with small mass gain. However as temperature is increased above  $800^\circ\text{C}$ , mass gain increases significantly, and for temperatures above  $900^\circ\text{C}$ , the material assumes rapid linear oxidation kinetics ( $k_l \approx 0.1 \text{ mg/cm}^2/\text{hr}$ ). The rapid linear kinetics are associated with cracking of the external scale which creates short circuit diffusion paths for the rapid inward flux of oxygen. As temperature is further increased to  $1200^\circ\text{C}$ , mass gain significantly decreases and the material behaves parabolically ( $k_p \approx 0.1 \text{ mg}^2/\text{cm}^4/\text{hr}$ ). This likely reflects the decreased contribution of grain boundary diffusion of oxygen through  $\text{TiO}_2$  resulting from sintering and grain growth of the external rutile scale.

The oxidation resistance of  $\text{Ti}_5\text{Si}_3$  is dramatically improved by the addition of certain small atom ternary elements. Boron, carbon, and oxygen all improve oxidation resistance as evidenced by decreased mass gain and development of thin, adherent scales. Boron and oxygen doped material form crystalline silica above about  $1079^\circ\text{C}$ . SEM and XRD analysis show both materials contain continuous silica scales with discrete dispersed rutile particles at the scale/gas interface. Failure to form a continuous rutile scale is evidence of the decreased outward diffusion of Ti through silica promoted by the these additions. As temperature is further increased to  $1306^\circ\text{C}$ , protective behavior is generally lost with a few exceptions. Slow linear oxidation kinetics ( $k_l \approx 0.02 \text{ mg/cm}^2/\text{hr}$ ) develop

in  $\text{Ti}_5\text{Si}_3\text{B}_{0.75}$  after rapid, transient oxidation. The increased boron content may promote formation of a viscous borosilicate glass which can flow to heal the scale<sup>1</sup>.  $\text{Ti}_5\text{Si}_3\text{O}_{0.25}$  maintains protective behavior up to 1306°C. The mass gain after 240 hours is about 1.1 mg/cm<sup>2</sup> with kinetics tending toward parabolic behavior ( $k_l = 8.2 \times 10^{-4}$  mg/cm<sup>2</sup>/hr and  $k_p = 4.1 \times 10^{-3}$  mg<sup>2</sup>/cm<sup>4</sup>/hr). These kinetics compare reasonably well to SiC at 1300°C in dry oxygen<sup>2</sup> ( $k_p = 5 \times 10^{-4}$  mg<sup>2</sup>/cm<sup>4</sup>/hr).

Carbon-doped material also shows significant improvement in oxidation resistance. Unlike boron- and oxygen-doped material, a continuous external rutile layer forms and crystalline silica is not observed. This indicates that outward diffusion of titanium to the scale/gas interface is fast enough to allow formation of the continuous rutile scale. As temperature is further increased to 1306°C, protective behavior is lost and substantial mass gain occurs. The extent of Ti<sub>2</sub>-Z bonding in carbon- and boron-containing  $\text{Ti}_5\text{Si}_3$  is evidently not large enough to suppress  $\text{TiO}_2$  formation.

Nitrogen containing material behaves almost identically to undoped material. This may simply indicate that the diffusion of Ti and Si remains approximately similar to that of undoped material by simultaneous increase or decrease of both Si and Ti diffusion with N additions.

## II. Interstitial Chemistry of $\text{Ti}_5\text{Si}_3\text{Z}_x$

$\text{Ti}_5\text{Si}_3$  can incorporate several atomic percent of ternary additions such as boron, carbon, nitrogen, and oxygen. These additions produce significant changes in the lattice constants of the host  $\text{Ti}_5\text{Si}_3$ . Single crystal x-ray diffraction studies have verified that these additions are accommodated in the interstitial sites within the trigonal antiprismatic chains of Ti<sub>2</sub> atoms. Bonding between the interstitial atom and Ti<sub>2</sub> is suggested by cavity



contraction. There are significant changes in bond lengths as a result of these additions. Most notably there is an increase in the Ti2-Si bond lengths and a decrease in Ti2-Ti2 bond lengths.

Interstitial chemistry has a pronounced effect on sintered material. Nitrogen and oxygen additions to  $\text{Ti}_5\text{Si}_3$  produce an increase in density since mass increases from interstitial occupancy and unit cell volume decreases. During sintering, the theoretical density of the material may significantly increase when nitrogen and oxygen surface contaminants of the powder become interstitially incorporated into the structure. This interstitial incorporation suggests a robust process in which the system may be "self-correcting" for limited levels of nitrogen and oxygen contamination introduced during milling. Particularly for oxygen contaminated powder, interstitial incorporation during sintering may be extremely beneficial since the oxidation resistance of oxygen-doped material is greatly improved.

### III. Thermal Expansion Anisotropy of $\text{Ti}_5\text{Si}_3\text{Z}_x$

$\text{Ti}_5\text{Si}_3$  is inherently anisotropic because of its hexagonal crystal structure. The coefficient of thermal expansion along the c-axis is substantially larger than along the a-axis ( $\alpha_a=8.68\pm0.14$  and  $\alpha_c=20.4\pm0.4$  ppm/K from 298-873 K). This results in severe microcracking in coarse-grained  $\text{Ti}_5\text{Si}_3$  with an average grain size of about 12  $\mu\text{m}$ . Reducing the grain size of the HIPed material to 1-2  $\mu\text{m}$  eliminates microcracking and nearly doubles hardness to  $17.1\pm0.7$  GPa. The addition of carbon to  $\text{Ti}_5\text{Si}_3$  reduces the CTE anisotropy ( $\alpha_a=9.43\pm0.29$  and  $\alpha_c=17.9\pm0.6$  ppm/K from 298-873 K).

#### IV. Future Research

While this research has established the great improvement in oxidation resistance realized by ternary doping of  $\text{Ti}_5\text{Si}_3$ , questions still remain about the exact mechanism of improvement. Similarly, questions still remain about the effect of doping on critical mechanical properties. As indicated by the results of single crystal x-ray diffraction, further analysis is needed to qualify any correlation between changes in bonding and changes in the diffusion of Ti and Si. With these comments in mind, some suggestions for future research are outlined below.

##### 1. Mechanical Properties of $\text{Ti}_5\text{Si}_3\text{Z}_x$

The creep resistance, strength, and fracture toughness of the doped material needs to be determined. The compressive creep rate of undoped  $\text{Ti}_5\text{Si}_3$  is somewhat high<sup>3</sup>, about  $10^{-7} \text{ s}^{-1}$  at  $1200^\circ\text{C}$  and 44 MPa. Single crystal studies have shown that doping may promote significant changes in directional bonding, and the predicted effect of any bonding changes on creep resistance and strength is not obvious. However, the predicted effect on fracture toughness may be more evident. Frommeyer et al.<sup>3</sup> have shown the deleterious effect of impurities on the fracture toughness of  $\text{Ti}_5\text{Si}_3$ . Values of  $2.0\text{--}3.5 \text{ MPa}\cdot\sqrt{\text{m}}$  were measured up to  $700^\circ\text{C}$ . Oxygen precipitation at the grain boundaries was determined by Auger depth profiling, and above  $700^\circ\text{C}$  the oxygen was found to diffuse into  $\text{Ti}_5\text{Si}_3$  with a corresponding increase in toughness to  $7 \text{ MPa}\cdot\sqrt{\text{m}}$  at  $1050^\circ\text{C}$ . As previously observed, carbon-doped material shows a much lower oxygen content than undoped material, 186 and 1100 ppm wt%, respectively. This may correspond to a lower grain boundary oxide content and impart increased fracture toughness, particularly important at lower temperatures.

## 2. Characterization of Other $A_5Si_3Z_x$ Systems

Extended Huckel band calculations are planned to quantify the extent of bonding between Ti2 and Z atoms. If the correlation of structural analysis to diffusion can be made, then a powerful tool exists for rapidly accessing the potential usefulness of several other material systems in which the base  $A_5Si_3$  binary can be stabilized in the  $Mn_5Si_3$  structure. Those candidates which are identified could then be synthesized in bulk quantity and consolidated into specimens for oxidation testing and mechanical property assessment. In fact, this screening could be broadened to include non-silicide based systems.

## 3. Oxidation of Micro-Doped $Ti_5Si_3$

The general trend of increased oxidation resistance with decreasing interstitial content must be further investigated. Experiments are currently underway to characterize the oxidation process for  $Ti_5Si_3C_x$  where  $0 < x < 0.24$ . Similar experiments are planned for  $Ti_5Si_3O_x$  where excellent oxidation resistance was observed for  $Ti_5Si_3O_{0.25}$  up to  $1306^\circ C$ . Material will be oxidized for increasing time intervals to track scale development.

## References

- <sup>1</sup>M. K. Meyer and M. Akinc, "Oxidation Behavior of Boron Modified  $Mo_5Si_3$  at  $800^\circ$ - $1300^\circ C$ ," *J. American Ceramic Society*, accepted for publication.
- <sup>2</sup>E. J. Opila, "Oxidation Kinetics of Chemically Vapor-Deposited Silicon Carbide in Wet Oxygen," *J. American Ceramic Society*, **77** [3], 730-736 (1994).

<sup>3</sup>G. Frommeyer, R. Rosenkrantz and C. Ludecke, "Microstructure and Properties of the Refractory Intermetallic  $\text{Ti}_5\text{Si}_3$  Compound and the Unidirectionally Solidified Eutectic Ti- $\text{Ti}_5\text{Si}_3$  Alloy", *Z. Metallkde*, **81**[5], 307-313 (1990).

## ACKNOWLEDGEMENTS

Ames Laboratory is operated for the U.S. Department of Energy by Iowa State University under contract number W-7405-ENG-82. This research was supported by the Office of Basic Energy Science, Materials Science Division. The United States government has assigned the DOE report number IS-T 1743 to this thesis.

This research was also supported by the Air Force Office of Scientific Research. A three year fellowship through the National Defense Science and Engineering Graduate Fellowship Program was granted to the dissertation author.

I would like to dedicate this dissertation to my family. My wife Lisa has been infinitely patient with me throughout this long journey which began several years ago. I will never comprehend the extent of her sacrifices. My two children, Trevor and Trisha, have been very patient with me, always giving a warm welcome home with a resounding 'Daddy!' when I get home late. My mother, Catherine, and my mother-in-law, Joyce, have been very supportive. It is with a sad note that I cannot thank in person my father, Philip, and my father-in-law, Arlen, for their support. I cannot help feeling some remorse about their early departure from this Earth during this otherwise happy occasion. I love my family dearly.

I would like to thank Dr. Mitch Meyer for his common sense, practical advise on a variety of both scientific and non-scientific issues.

I would like to thank Dr. Michael Berard for his kind 'welcome' to an undecided freshman student over ten years ago which convinced me to join the MSE Department.

Finally, I would like to thank my major professor Dr. Mufit Akinc. I have appreciated the great deal of latitude extended to me, allowing me learn by my mistakes without harsh criticism and quick to complement me when things go well.

APPENDIX A:  
INTERSTITIAL CHEMISTRY EFFECTS ON PROCESSING OF  $\text{Ti}_5\text{Si}_3$

A manuscript to be submitted to *Intermetallics*

Andrew J. Thom and Mufit Akinc

Ames Laboratory and Department of Materials Science and Engineering

**Abstract**

Hot consolidation of refractory intermetallic silicides is usually accomplished by hot isostatic pressing (HIPing). However, the expense of the equipment and difficulty associated with encapsulation of the material makes this method less attractive than pressureless densification. The pressureless sintering behavior of  $\text{Ti}_5\text{Si}_3$  was investigated to determine the viability of consolidating the material by this technique. Processing parameters such as initial particle size, temperature, and atmosphere were investigated. High density and small grain size material was produced, but assessment of theoretical density is difficult due to changes in interstitial chemistry which occur during firing. Density is predicted for varying interstitial nitrogen and oxygen content. Silicon volatilization may occur during sintering in low oxygen partial pressure atmospheres, and this presents additional difficulties in maintaining stoichiometry and accessing theoretical density.

## I. Introduction

Transition metal silicides of the form  $A_5Si_3$  ( $A=Ti, Mo, Nb, V, Y, Zr$ ) are potential high temperature structural materials. Synthesis and fabrication of these intermetallic materials presents processing challenges because of their high melting points and inherent crystal anisotropy. A common technique of synthesis for these materials has been arc-melting. The starting materials (typically elements) are placed on a water-cooled copper hearth and melted under argon by striking an arc from a non-consumable tungsten electrode to the copper hearth. Arc-melt material is usually not directly usable because of its large grain size which contributes to severe microcracking in fabricated parts. Residual porosity and severe microcracking contribute to an increased surface area which significantly decreases oxidation resistance of parts. Previous research has shown that hot isostatic pressing (HIPing) can produce fine-grained, dense, microcrack-free samples of  $Ti_5Si_3$ <sup>1</sup>. The HIPed product is produced by milling the arc-melt material to micron-sized powder, cold-pressing the milled powder into a pellet, coating the pellet with boron nitride powder, encapsulating the pellet in borosilicate glass, and HIPing it.

The process of HIPing adds considerable expense to the fabrication process. Encapsulation requires several time consuming steps to complete. Sample geometries are also limited by the requirement for encapsulation and by the internal dimensions of the HIP vessel, which are usually small due to the significant expense associated with HIP equipment. Furthermore, uncontrolled process variables may severely limit densification and render the part unusable.

In order to simplify processing and allow for cheaper and greater quantity of production of densified material, pressureless sintering was investigated for the consolidation of  $Ti_5Si_3$ .

## II. Experimental

Because arc-melting is a relatively inexpensive and fast method to synthesize large quantities of intermetallic material, arc-melted material was used for all consolidation efforts. The synthesis and characterization of arc-melted  $\text{Ti}_5\text{Si}_3$  used in this study has been previously discussed<sup>2</sup>. Sintering of milled arc-melt material was investigated in detail to determine appropriate processing parameters. Densification of  $\text{Ti}_5\text{Si}_3$  by hot-pressing was also investigated for comparative purposes.

### 1. Hot Pressing

The arc-melt ingots were milled for 4 minutes in a Spex Shatterbox mill using a WC-lined container. The powders were handled in an argon filled glovebox (no active gettering of oxygen or water). The milled powder was sieved to -325 mesh (less than 43  $\mu\text{m}$ ) and characterized by chemical analysis, x-ray diffraction (XRD), and scanning electron microscopy (SEM). Samples were hot pressed in an induction heated vacuum furnace at 0.1 Torr in a graphite die lined with Ta foil. One inch diameter pellets of 20 g of powder were hot pressed at 34 MPa for 4 hours at 1300, 1580, and 1700°C. Typical ramp time to processing temperature was 2 hours, followed by natural cooling to room temperature. The die was loaded with powder in the glovebox and quickly transported to the hot press furnace to minimize powder exposure to ambient atmosphere.

### 2. Sintering

The milled powders used for sintering are discussed elsewhere<sup>3</sup>. In general, arc-melt material was milled using varying levels of atmospheric control. Table I gives the various grinding and sintering conditions used in this study. In experiments i-III, material



was milled in ambient atmosphere in a Spex Shatterbox WC-lined container. In experiments IV-VII, material was milled in a Spex Mixer-mill WC-lined container under argon inside a glovebox with a purification system that maintains the oxygen level to less than one part per million (ppm). Methylcellulose was used as a grinding additive during Mixer-milling to reduce powder caking so that outgassing prior to sintering is required to burn out the additive.

Table I: Grinding/Sintering Conditions Investigated

Experiment	Grinding Conditions <sup>a</sup>	Sintering Conditions
i	0-10 min(SB)	1750°C, 2 hrs
I	60 min (SB);opened 15 times	1800°C, 2 hrs
II	60 min (SB);opened 3 times	1800°C, 2 hrs
III	60 min (SB);opened 1 time	1800°C, 2 hrs
IV	10 min (SB), 90 min (MM)	1800°C, 2 hrs
V	90 min (MM)	1800°C, 2 hrs
VI	90-180 min (MM)	1800°C; 10,120 min
VII	90 min (MM)	1500-1800°C, 10 min <sup>b</sup>

<sup>a</sup> SB=Shatterbox (air), MM=Mixer-mill (purified Ar)

<sup>b</sup> outgassing & sintering atmosphere varied

The milled powder was sieved to -635 mesh (less than 20  $\mu\text{m}$ ) and cold-pressed in a 13 mm diameter die at 175 MPa, yielding typical geometric bulk densities of about 62% of theoretical ( $\rho_{\text{th}} = 4.32 \text{ g/cm}^3$ ). The pellets were sintered in a tungsten mesh resistance heated furnace under flowing argon. Powders from Experiments IV-VII were exclusively processed under purified Ar so that powder was not exposed to ambient atmosphere until after sintering. Powders from Experiments IV-VII contained a grinding additive and were slowly heated and prefired at 1000°C under flowing argon to burnout the grinding

additive prior to sintering. Thermogravimetric analysis of the additive shows nearly complete pyrolysis with about 200 ppm wt% char, probably residual carbon.

### 3. Characterization

Microstructures were evaluated by optical microscopy using polarized light and scanning electron microscopy (SEM). Microhardness was measured using the Vickers indentation technique. X-ray diffraction (XRD) was performed on a powder diffractometer using filtered copper  $K_{\alpha}$  radiation. Density of the powders was measured by helium gas pycnometry. Apparent density of the fired pellets was measured using an Archimedes liquid immersion technique. Nitrogen and oxygen content was determined by inert gas fusion analysis.

## III. Results

### 1. Hot Pressing Behavior

Chemical analysis of milled powder used for hot-pressing is shown in Table II. The powder is slightly silicon rich,  $Ti_5Si_{3.08}$ , and contains an appreciable oxygen impurity of 3900 ppm. XRD of the powder identifies the material as  $Ti_5Si_3$  with a few minor unidentified peaks. Table III shows the effect of temperature on the apparent density and grain size of hot pressed specimens. Extensive grain growth occurs at elevated temperature. XRD of powder from material hot-pressed at 1580°C verified the presence of  $Ti_5Si_3$ .

Figure 1 shows an optical micrograph in polarized light of material hot pressed at 1300°C. Substantial grain pullout is seen in the bright regions. Some intragranular porosity can be seen, and microcracking is visible in larger grains. Figure 2 shows a backscattered electron image (BEI) of material hot pressed at 1580°C, and the extent of

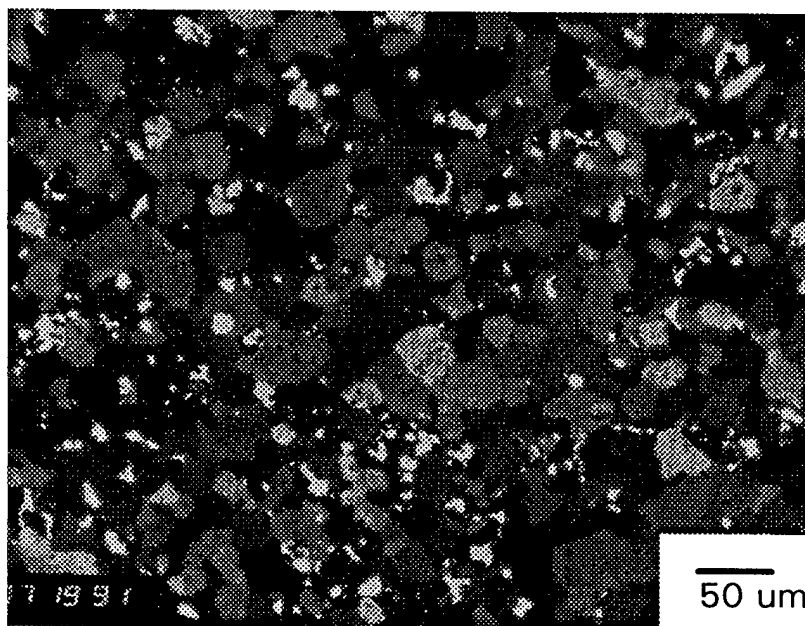


Figure 1: Polarized light micrograph of  $\text{Ti}_5\text{Si}_3$  hot pressed at  $1300^\circ\text{C}$  for 4 hours at 34 MPa in vacuum.

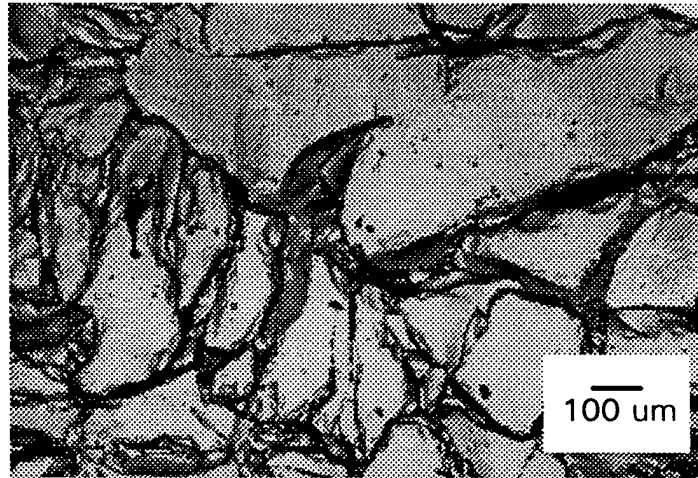


Figure 2: BEI of  $\text{Ti}_5\text{Si}_3$  hot pressed at  $1580^\circ\text{C}$  for 4 hours at 34 MPa in vacuum.

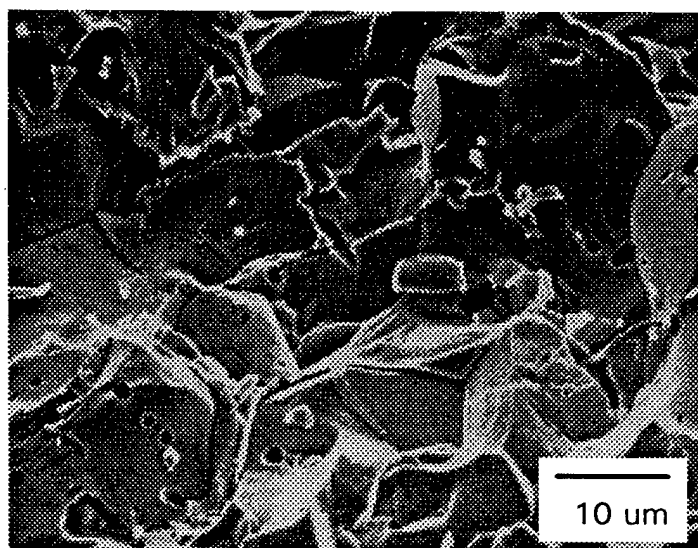


Figure 3: Fracture surface of  $\text{Ti}_5\text{Si}_3$  hot pressed at  $1300^\circ\text{C}$  for 4 hours at 34 MPa in vacuum.

Table II: Chemical Analysis of -325 Mesh Powder

Element	Weight %
Si	26.38
Ti	73.02
O	0.391
C	0.0290
N	0.0770
Nb	0.0306
Fe	0.0711
Cr	0.0035
Al	0.0023

Table III: Density and Grain Size of Hot Pressed  $\text{Ti}_5\text{Si}_3$ 

Temp(°C)	$\rho_a$ (g/cm <sup>3</sup> )	Grain Size Range ( $\mu\text{m}$ )
1300	4.31	15-40
1580	4.36	200-500
1700	4.35	250-750

grain pullout is quite evident. Figure 3 shows a fracture surface of material hot-pressed at 1300°C. Intergranular and transgranular cracking are visible, and a small amount of porosity is present.

## 2. Sintering Behavior

### a. Experiments i-III

Table IV gives the apparent density and nitrogen/oxygen content of sintered pellets prepared from powder in Experiments i-III. Powder from Experiment i was milled for 5, 7, and 9 minutes, while powder from Experiments I-III were milled 60 minutes. With the exception of Experiment III, all samples show a higher than theoretical density<sup>4</sup> for pure material ( $\rho_{th} = 4.32 \text{ g/cm}^3$ ), and this is later attributed to interstitial incorporation of

Table IV: Properties of Sintered Pellets from Experiments i-III

Experiment	Grinding time (min.)	$\rho_a$ (g/cm <sup>3</sup> )	Prefired Nitrogen (wt %)	Postfired Nitrogen (wt %)	Prefired Oxygen (wt %)	Postfired Oxygen (wt %)
i	5	4.397	0.0302	0.100	0.535	2.08
i	7	4.389	0.0382	0.0834	0.705	1.64
i	9	4.373	0.0455	0.0746	0.853	1.95
I	60	4.476	0.771	0.890	2.31	2.98
II	60	4.415	0.830	1.47	1.92	2.12
III	60	4.233	0.901	1.08	1.03	1.28

oxygen and/or nitrogen (solid solution oxygen). Sintered pellets prepared from powders i, I, and II gave indication of poor mechanical properties as evidenced by rapid cutting and poor polishing characteristics. Extensive grain pullout prevented adequate polishing for optical micrographs.

Pellets prepared from powder III exhibited improved cutting and polishing characteristics, and Figure 4 shows a polarized light micrograph. The Vickers hardness for 200 g loading was  $6.94 \pm 0.49$  GPa (95% confidence interval). The average grain size, as measured by the linear intercept method, is about 6  $\mu\text{m}$ . However, there is a wide size distribution with many grains up to 20  $\mu\text{m}$ . Grain pullout is evident, and microcracking occurs in several of the larger grains. CTE anisotropy<sup>1</sup> has been previously shown to cause microcracking in large-grained  $\text{Ti}_5\text{Si}_3$ .

Pellets from Experiments I, II, and III involved identical processing with the exception of the number of container openings during grinding. The grain size of all three materials should be similar, thus the excessive grain pullout observed for pellets from powders I and II may be due to their elevated post-fired oxygen level. The high oxygen level contributes to low intergranular strength by coating grain boundaries with prior

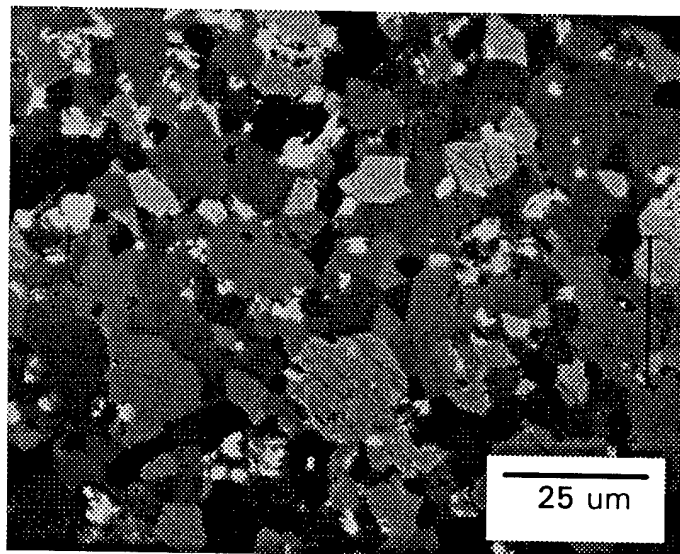


Figure 4: Polarized light micrograph of  $\text{Ti}_5\text{Si}_3$  sintered at  $1800^\circ\text{C}$  for 2 hours. Starting powder from Exp. III (Shatterbox milled 60 minutes in air).



formed oxides. Reuss and Vehoff<sup>5</sup> showed that segregation of oxygen to grain boundaries resulted in decreased fracture toughness of  $\text{Ti}_5\text{Si}_3$ .

Grinding conditions in experiment III produced powders of sufficiently small particle size and oxygen content for adequate sintering of pellets. However, the measured hardness of 6.94 GPa is significantly less than that for fine-grained  $\text{Ti}_5\text{Si}_3$  produced by HIPing. Previous research<sup>1</sup> has shown that the hardness of microcrack-free  $\text{Ti}_5\text{Si}_3$  with average grain size 1-2  $\mu\text{m}$  to be 17.1 GPa. These observations indicate that the grain size material from powder III, as evidenced by microcracking, and possibly oxygen content are still too large.

#### *b. Experiments IV-VI*

To further reduce oxygen content of the sintered pellets, arc-melt material was milled under increasing levels of atmospheric control. In experiments IV-VI, milling time was increased to decrease initial particle size, and in VI sintering time was decreased to determine grain growth characteristics. Powder in experiment IV was initially loaded into the Shatterbox mill inside the glovebox and milled outside the glovebox for 10 minutes, followed by 90 minutes of Spex-milling inside the glovebox. This procedure was used to determine the feasibility of using the large capacity Shatterbox mill for initial grinding. For experiments IV-VI all powder processing, with the exception of the Shatterbox milling in IV, was performed inside the glovebox. Table V gives microhardness (95% confidence intervals) for 200 g loading, Archimedes apparent density, and nitrogen/oxygen chemistry of sintered pellets prepared from powder in Experiments IV-VI.

Material prepared from IV and V possessed sufficient mechanical strength to allow preparation of metallographic samples. Polarized light micrographs of IV and V, shown

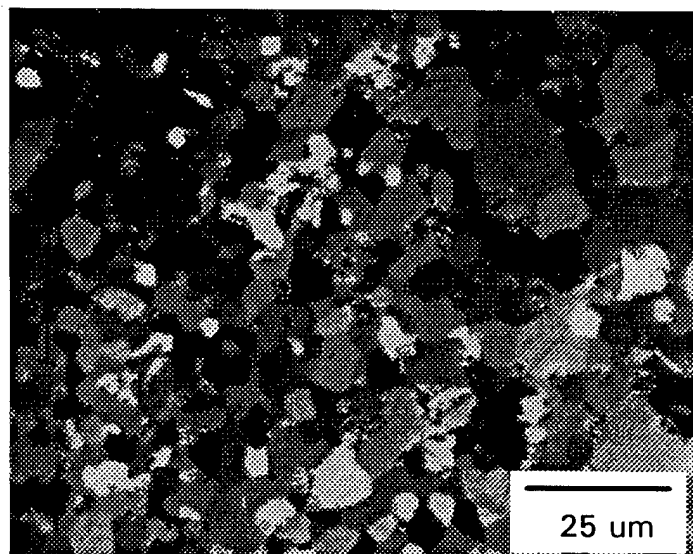


Figure 5: Polarized light micrograph of  $\text{Ti}_5\text{Si}_3$  sintered at  $1800^\circ\text{C}$  for 2 hours. Starting powder from Exp. IV (10 minute Shatterbox milled in argon, 90 minute Mixer-milled in glovebox).

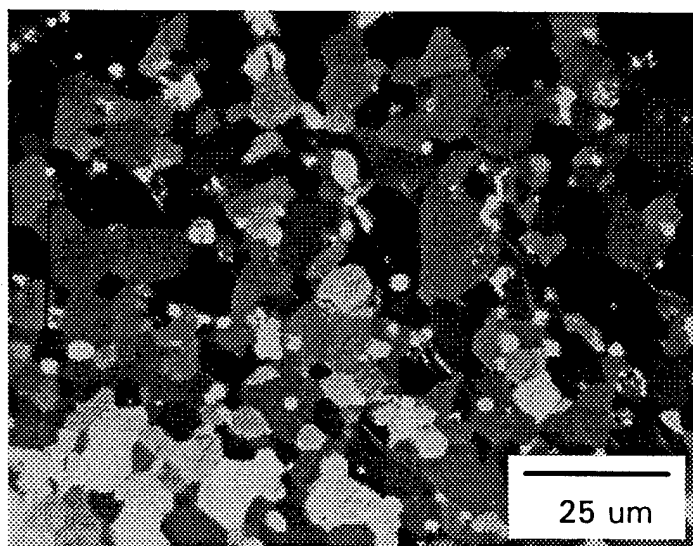


Figure 6: Polarized light micrograph of  $\text{Ti}_5\text{Si}_3$  sintered at  $1800^\circ\text{C}$  for 2 hours. Starting powder from Exp. V (90 minute Mixer-milled in glovebox).

in Figures 5 and 6, respectively, reveal a comparable grain size to that from experiment III, seen in Figure 4. The hardness measurements of III, IV, and V are statistically indistinguishable, and this is consistent with the similar extent of pullout and microcracking seen in each sample. These results indicate that either additional milling is needed to further reduce initial particle size or sintering temperature must be decreased to reduce possible grain growth. Because of the tendency of the density of these materials to

Table V: Properties of Pellets from Experiments IV-VI Sintered at 1800°C

Experiment	Grinding time(min.)	Sintering time(min.)	Hardness (GPa)	$\rho_a$ (g/cm <sup>3</sup> )	Postfired Nitrogen (wt %)	Postfired Oxygen (wt %)
IV	100 <sup>a</sup>	120	7.10±0.65	4.197	0.0783	1.20
V	90	120	7.58±0.71	4.269	0.0575	1.62
VI	90	10	b	4.389	0.551	0.972
VI	180	10	b	4.392	0.864	1.41
VI	90	120	b	4.406	0.531	1.02
VI	180	120	b	4.421	0.769	1.52

<sup>a</sup> 10 min.(SB)+90 min.(SP)

<sup>b</sup> could not be measured

increase due to incorporation of interstitial nitrogen and oxygen, no conclusions can be made based on apparent density.

Interestingly, the oxygen content of V, and to a lesser extent IV, were as high as III. Since the oxygen content of the arc-melt material was low prior to processing ( $\approx 1100$  ppm wt%), oxygen contamination occurred during inert processing. Apparently, the oxygen in IV and V acquired during inert processing was not detrimental as evidenced by the similarity in hardness of III, IV, and V.

Material produced from experiment VI is substantially different than that produced from experiment IV and V. This sintered material possesses poor mechanical properties as indicated by rapid cutting and poor polishing characteristics which prevented measurement of grain size and hardness. The apparent density of all samples from experiment VI was higher than theoretical, suggesting interstitial incorporation of nitrogen and/or oxygen. The similar oxygen level in IV, V, and VI would predict a similar density for the three materials. However, the nitrogen level of VI is about an order of magnitude higher than IV and V which indicates that a substantial amount of nitrogen may also be accommodated into the structure.

Material from III (see Table IV) and VI (see Table V) have similar postfired oxygen and nitrogen levels. The poor mechanical behavior of VI suggests that nitrogen contamination occurring during inert processing inside the glovebox is responsible for poor mechanical behavior of the material. To determine the source of nitrogen contamination, powder from VI (milled for 90 minutes) was pressed into a pellet and outgassed in UHP argon. The pellet was removed from the glovebox and exposed to ambient air. The nitrogen content of the pellet was 480 ppm, indicating that no appreciable nitrogen contamination occurs during thermal processing in UHP argon.

### *c. Experiment VII*

Recognizing the potential effect of glovebox atmosphere purity on the properties of the sintered material, an experimental matrix was constructed in which stricter control was exercised over the atmosphere present during sample outgassing and sintering. Four groups of samples were prepared by sintering for 10 minutes at temperature and controlling outgassing atmosphere and sintering atmosphere. Sample outgassing was controlled using UHP argon gas and placing Ti-sponge near the pellet to act as an oxygen

and nitrogen getter. Samples were sintered in UHP argon by first evacuating the furnace prior to heating to completely remove any residual glovebox argon. Finally, pellets were wrapped in Ta foil during sintering to reduce exchange with the furnace atmosphere and thus further reduce nitrogen and oxygen contamination. The experimental matrix is shown in Table VI. Group A was fired at 1600°C and 1800°C while Group B was fired only at 1500°C. Both Group C and D were fired at 1500° and 1800°C. The apparent density (95% confidence interval) and nitrogen/oxygen content of these samples are given in Table VII.

The effect of outgassing and sintering atmosphere is quite pronounced. Both Group C and D, which were outgassed and sintered in UHP argon, have nitrogen levels varying from one to two orders of magnitude lower than Group A and B. Group C has a processing route nearly identical to material from experiment IV and V, and the nitrogen and oxygen levels of material from the three experiments are also nearly identical. This clearly indicates that a source of nitrogen contamination is thermal processing with glovebox argon. Since the glovebox purification system does not remove nitrogen, the nitrogen partial pressure can become quite high. According to the manufacturer's recommendations, the glovebox must be periodically purged with argon to reduce the elevated nitrogen level which develops<sup>6</sup>. The 0.38 mm thick gloves on the glovebox leak approximately 10 ppm N<sub>2</sub>/glovepair/hour, or about 1680 ppm/week (168 hours). After three months of continuous operation, the nitrogen level could be as high as 2%.

An interesting observation within each group is the decrease in apparent density with increasing temperature. Since the amount of porosity is not expected to increase as temperature increases, the decrease in apparent density reflects a change in chemistry or phase of the sample. For group C and D, the nitrogen and oxygen content are approximately constant

Table VI: Experimental Matrix Utilized during Sintering in Experiment VII

Group	Outgass Atmosphere	Sintering Atmosphere	Ta Envelope Used?
A	Glovebox Ar	Glovebox Ar	No
B	Glovebox Ar	UHP Ar	No
C	UHP Ar	UHP Ar	No
D	UHP Ar	UHP Ar	Yes

Table VII: Properties of Sintered Material from Experiment VII

Group	Sintering Temp (°C)	Density (g/cm <sup>3</sup> )	Oxygen content (wt%)	Nitrogen content (wt%)
A	1600	4.443(±0.037)	1.40	8.38
	1800	4.389(±0.021)	1.04	0.651
B	1500	4.508(±0.017)	1.84	7.35
C	1500	4.415(±0.026)	1.66	0.0760
	1800	4.332(±0.014)	1.66	0.0794
D	1500	4.386(±0.060)	1.65	0.0820
	1800	4.368(±0.011)	1.54	0.0557

as temperature changes so that any chemistry change must involve either titanium or silicon.

A possible explanation for the decrease in density of the sintered material is loss of Si. Material was sintered in a low oxygen partial pressure atmosphere (UHP argon), and loss of Si in  $Ti_5Si_3$  may occur via Si and SiO vapor formation. The critical oxygen partial pressure for rapid SiO vapor formation in pure Si (i.e., active oxidation) at 1527°C is about  $5 \times 10^{-3}$  bar<sup>7</sup>, and the UHP argon<sup>8</sup> used during sintering has a significantly lower

oxygen partial pressure of about  $4 \times 10^{-6}$  bar. Thus SiO formation is thermodynamically favored. As temperature is increased within each group, the hypothesized Si loss would increase significantly and contribute to a decrease in density. The relative decrease in density with increasing temperature for C is substantially larger than for D. Group D was contained within a crimped Ta pouch which would serve to reduce the extent of Si loss. The pouch would reduce the exchange of gas with the surrounding furnace atmosphere, and the Si and SiO partial pressures within the pouch would increase and thus decrease the extent of volatilization. The density of C and D sintered for 10 minutes is higher than the density of IV and V sintered for 2 hours, and this would correspond to a larger loss of Si in IV and V because of their longer sintering times.

The change in density which occurs due to interstitial incorporation of nitrogen/oxygen and possible Si loss greatly complicates assessing the progression of densification during sintering studies. Without an accurate estimate of the theoretical density of the material, density determined by the liquid immersion technique cannot be converted to %theoretical density. However, a clear understanding of the change in density due to interstitial nitrogen/oxygen allows prediction of theoretical density, and the density measured by the liquid immersion technique can then be used to judge the extent of densification.

## IV. Discussion

### 1. Effect of Interstitial Oxygen on Density

Interstitial oxygen significantly increases the density of  $\text{Ti}_5\text{Si}_3$ . Table VIII gives the analyzed oxygen content for various  $\text{Ti}_5\text{Si}_3\text{O}_x$  compositions in both chunk and powder form. The synthesis and characterization of these compositions has been previously



Table VIII: X-ray Density of  $\text{Ti}_5\text{Si}_3\text{O}_x$ 

Sample ID	Sample Form	Nominal content (x)	Analyzed content (x)	A-lattice Parameter (Å)	C-lattice Parameter (Å)	X-ray Density ( $\text{g}/\text{cm}^3$ )	Ref.
POW788	chunk	0	0.022	7.4543	5.1474	4.346	2
	powder	0	0.10	7.4543	5.1474	4.362	2
POW988	chunk	0.25	0.27	7.4502	5.1429	4.408	2
POW986	chunk	0.50	0.46	7.4336	5.1331	4.477	2
POW985	chunk	0.75	0.65	7.4305	5.1333	4.522	2
94STR486	crystal	0	0.08	7.4521	5.1522	4.357	2
94STR466	crystal	0.5	0.43	7.4356	5.131	4.470	2
JCPDS	powder	+	0.01	7.444	5.143	4.359	4

+ Estimated oxygen content &lt; 1000 ppm

described<sup>2</sup>. Using lattice parameters determined by x-ray diffraction, x-ray density of each composition was determined, assuming stoichiometric  $\text{Ti}_5\text{Si}_3$  and all of the analyzed oxygen occupies interstitial sites. Addition of oxygen promotes contraction of both lattice parameters, and coupled with an increase in mass due to interstitial oxygen, density increases significantly. Table VIII shows that density increases from about 4.35 to 4.52  $\text{g}/\text{cm}^3$ . These data are plotted in Figure 7 and indicate a reasonable model for predicting density based on interstitial oxygen content.

The nominal oxygen content of  $x=0$  indicates the "undoped" material in which no extra oxygen was intentionally added during arc-melting. Note that a substantial difference exists in the oxygen level of the chunk form and powder form of the "undoped" material, ranging from about 1100 to 5000 ppm wt%, respectively. It is unknown how much of the measured oxygen is in the form of interstitial oxygen and how much is in the form of surface oxide formed during passivation of surface area.

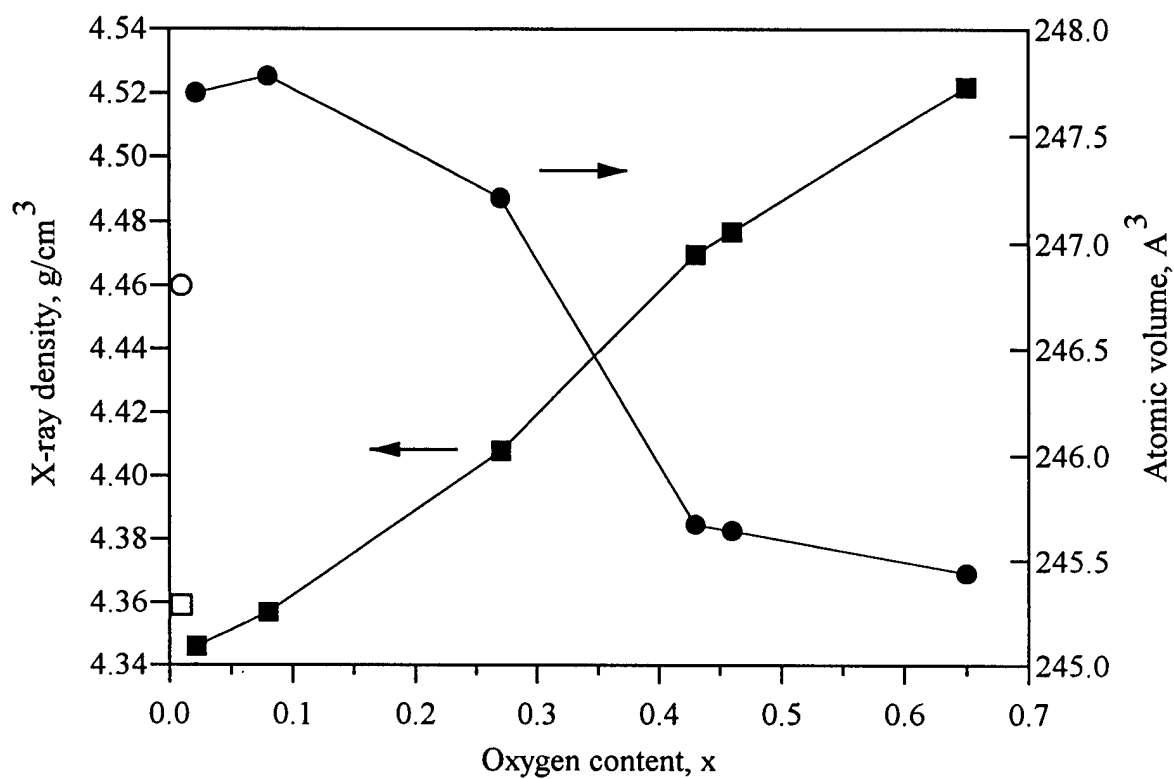


Figure 7: X-ray density and atomic volume for  $\text{Ti}_5\text{Si}_3$  with interstitially incorporated oxygen ( $\text{Ti}_5\text{Si}_3\text{O}_x$ ).

The chunk material would be expected to have a low specific surface area (SSA). Assuming a SSA of  $0.001 \text{ m}^2/\text{g}$ , the equivalent spherical diameter would be  $1400 \text{ }\mu\text{m}$ . With a surface oxide thickness range of  $100\text{-}1000 \text{ }\text{\AA}$ , the expected oxygen content of the material would be less than  $100 \text{ ppm}^3$ . Thus, most of the  $1100 \text{ ppm}$  oxygen is expected to be interstitial oxygen. Assuming that the  $1100 \text{ ppm}$  oxygen for the chunk form is entirely interstitial oxygen and using the cell volume measured from the undoped powder, the resulting x-ray density is  $4.346 \text{ g/cm}^3$ . This agrees well with the observed trend. Even if all of the oxygen is in the form of surface oxide, then the density only slightly decreases to  $4.341 \text{ g/cm}^3$ .

Considering the lattice parameters for  $\text{Ti}_5\text{Si}_3$  given by Quakkernaut and Visser<sup>4</sup> ( $a=7.444 \text{ }\text{\AA}$ ,  $c=5.143 \text{ }\text{\AA}$ ), the indicated level of boron, carbon, nitrogen, and oxygen was less than  $1000$ ,  $500$ ,  $10000$  and  $1000 \text{ ppm}$ , respectively. The predicted density using these lattice parameters and assuming a  $500 \text{ ppm}$  level of interstitial oxygen is  $4.359 \text{ g/cm}^3$ . This value is higher than expected from the trend in Figure 7. Also, the unit cell volume of Quakkernaut and Visser is much smaller than expected for  $500 \text{ ppm}$  of interstitial oxygen. These data are plotted as open symbols in Figure 7. This indicates that another type of interstitial such as nitrogen was present in the sample.

## 2. Effect of Interstitial Nitrogen on Density

The x-ray density of  $\text{Ti}_5\text{Si}_3$  for various levels of interstitial nitrogen is shown in Table IX. As observed for oxygen, nitrogen promotes contraction of the unit cell. Figure 8 shows x-ray density and unit cell volume versus nitrogen level, and similar trends are observed. In this case, the difference in nitrogen level between the powder and chunk form of the "undoped" material,  $69$  and  $177 \text{ ppm}$ , respectively, was negligible and leads to negligible differences in density. The atomic volume determined by Quakkernaut and

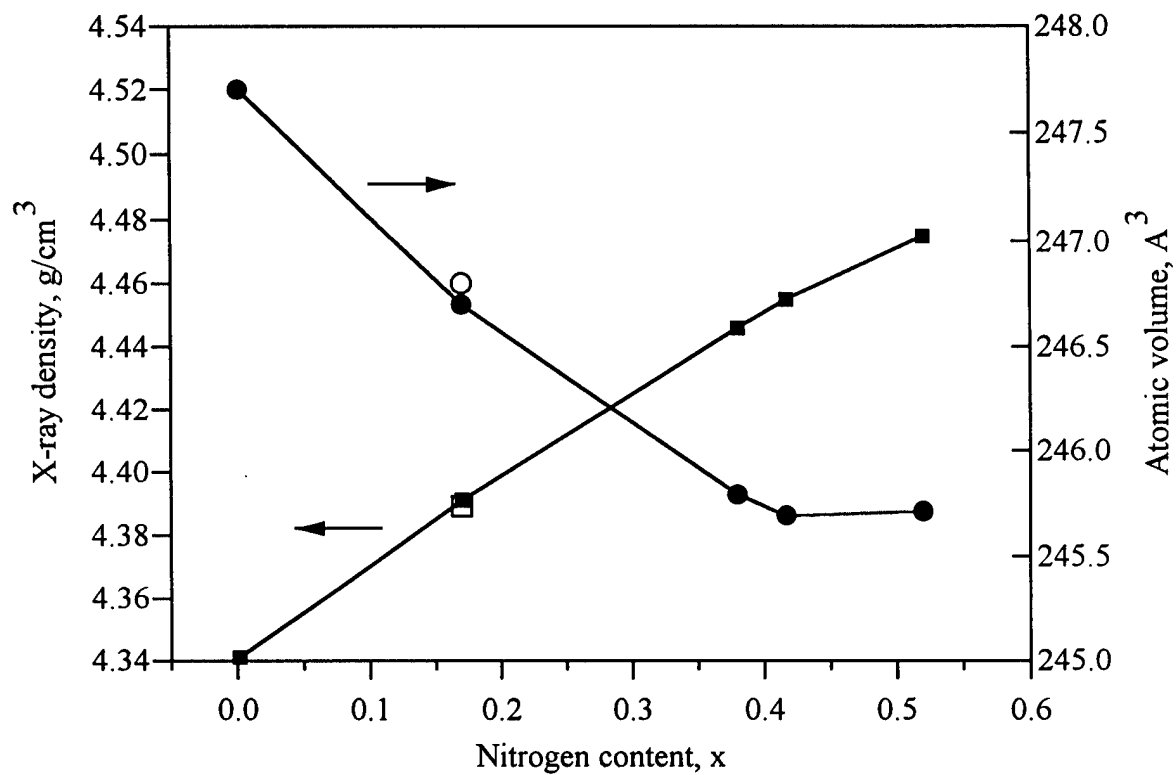


Figure 8: X-ray density and atomic volume for  $\text{Ti}_5\text{Si}_3$  with interstitially incorporated nitrogen ( $\text{Ti}_5\text{Si}_3\text{N}_x$ ).

Table IX: X-ray Density of  $\text{Ti}_5\text{Si}_3\text{N}_x$ 

Sample ID	Sample Form	Nominal content (x)	Analyzed content (x)	A-lattice Parameter ( $\text{\AA}$ )	C-lattice Parameter ( $\text{\AA}$ )	X-ray Density ( $\text{g/cm}^3$ )	Ref.
POW788	chunk	0	0.0016	7.4543	5.1474	4.341	2
	powder	0	0.0041	7.4543	5.1474	4.342	2
POW1041	chunk	0.25	0.17	7.4418	5.1439	4.391	2
POW1042	chunk	0.50	0.38	7.4283	5.1337	4.446	2
POW1043	chunk	0.75	0.52	7.4259	5.1452	4.475	2
94STR471	crystal	0.5	0.42	7.4309	5.138	4.455	2
JCPDS	powder	+	0.17	7.444	5.143	4.389	4

+ Estimated nitrogen content < 10000 ppm wt%

Table X: Pycnometer and X-ray Density of Selected  $\text{Ti}_5\text{Si}_3\text{Z}_x$  Compositions

Composition	$\rho_{\text{pyc}}$ ( $\text{g/cm}^3$ )	$\rho_{\text{xrd}}$ ( $\text{g/cm}^3$ )
undoped	4.34	4.34
$\text{Ti}_5\text{Si}_3\text{N}_{0.50}$	4.48	4.45
$\text{Ti}_5\text{Si}_3\text{O}_{0.50}$	4.47	4.48

Visser was  $246.81 \text{ \AA}^3$ , and the predicted nitrogen level based on this volume, according to Figure 8, is about  $x=0.17$ , or 7500 ppm. Given that the lower level of nitrogen detectability in their analysis was 10000 ppm, this is a reasonable possibility.

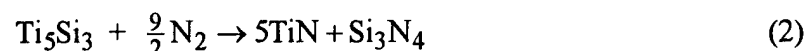
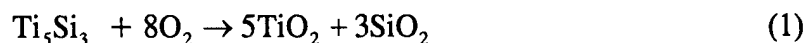
Thus, the lattice parameters of  $\text{Ti}_5\text{Si}_3$  given by Quakkernaut and Visser are likely small due to presence of interstitial nitrogen. The lattice parameters for "undoped" material are closer to that given in this paper, and perhaps even slightly larger due to the presence of residual interstitial oxygen in the powder, at least 1000 ppm. Extrapolating

both Figures 7 and 8 to zero interstitial content predicts a theoretical density for "undoped"  $\text{Ti}_5\text{Si}_3$  closer to  $4.34 \text{ g/cm}^3$ .

Table X gives the measured powder density from helium gas pycnometry. These values are in reasonable agreement with the previously determined x-ray densities and indicate the overall validity of predicting density from analyzed nitrogen and oxygen content.

### 3. Predicted Density Based on Nitride/Oxide Formation

Alternatively, some of the total oxygen and/or nitrogen assumed as interstitial may be in the form of a higher density phase material. If all of the measured nitrogen and oxygen react to form nitrides and oxides as given in Eqs. (1) and (2), the density of the resulting material can be calculated, using the measured nitrogen and oxygen content from Table IV and the predicted density of  $4.34 \text{ g/cm}^3$  for  $\text{Ti}_5\text{Si}_3$  as determined above. Table XI gives the volume fraction of products formed and predicted density for both sample (i9) and II60.



Although TiN, density  $5.22 \text{ g/cm}^3$ , will contribute to a density increase, the overall decrease in calculated density is the result of the formation of three less dense phases,  $\text{TiO}_2$ ,  $\text{SiO}_2$ , and  $\text{Si}_3\text{N}_4$  having respective densities of  $4.26$ ,  $2.64$ , and  $3.2 \text{ g/cm}^3$ . This analysis shows that formation of additional phases of higher density cannot account for the increase in density of the sintered material.

Table XI: Nitride and Oxide Product Formation

	Sample i9	Sample II60
% Volume Fraction		
TiO <sub>2</sub>	3.07	3.34
SiO <sub>2</sub>	2.24	2.43
TiN	0.15	2.97
Si <sub>3</sub> N <sub>4</sub>	0.11	2.20
Ti <sub>5</sub> Si <sub>3</sub>	94.43	89.06
Calculated Density (g/cm <sup>3</sup> )	4.300	4.297

#### 4. Predicted Density from Atomic Volume

The previous discussion described the expected increase in density due to the incorporation of interstitial nitrogen and oxygen within the  $\text{Mn}_5\text{Si}_3$  structure of  $\text{Ti}_5\text{Si}_3$ . In order to demonstrate this behavior in the sintered material, the lattice parameters of selected sintered pellets were measured by XRD, and these results are listed in Table XII. The calculated atomic volume was used to predict density for each sample from the plots in Figures 7 and 8. The analyzed chemistry and atomic volume were used to calculate the XRD density, assuming stoichiometric  $\text{Ti}_5\text{Si}_3$  and either the analyzed nitrogen or oxygen is interstitially incorporated. Sample (i9) was prepared from powder from experiment (i) milled nine minutes, and sample II60 was prepared from powder from experiment II milled for 60 minutes. Both of these materials were listed in Table IV.

Comparing the measured atomic volumes given in Table XII to the volume trends in Figures 7 and 8 shows that the unit cells have significantly contracted. The contraction suggests that significant amounts of nitrogen and/or oxygen have been interstitially incorporated.

Table XII: Density Properties of Sintered  $\text{Ti}_5\text{Si}_3$ 

	Sample (i9)	Sample II60
XRD Data		
A parameter (Å)	7.4300(4)	7.4261(3)
C parameter (Å)	5.1357(4)	5.1373(5)
Atomic Volume (Å <sup>3</sup> )	245.53(3)	245.35(2)
Predicted Density (g/cm <sup>3</sup> )	4.49	4.53
Analyzed Chemistry		
N content (wt%)	0.0746	1.47
O content (wt%)	1.95	2.12
XRD Density (g/cm <sup>3</sup> )	4.47	4.45/4.48 <sup>a</sup>
Apparent Density (g/cm <sup>3</sup> )	4.37	4.42
% Theoretical Density	97.3	97.6

<sup>a</sup>Density for only interstitial nitrogen/only interstitial oxygen.

Based on analyzed chemistry, it is clear that for sample (i9) the principal interstitial is oxygen, and the measured atomic volume gives a predicted density of 4.49 g/cm<sup>3</sup> based solely on interstitial oxygen. Sample II60 has an appreciable nitrogen and oxygen content. The predicted density for only interstitial oxygen is 4.53 g/cm<sup>3</sup>, while density for interstitial nitrogen cannot be predicted since the observed atomic volume is less than the observed trend in Figure 8. This suggests that the increased density is mainly due to interstitial oxygen.

The XRD density of sample (i9) based on the analyzed oxygen content is 4.47 g/cm<sup>3</sup>. The XRD density of sample II60 varies from 4.45 to 4.48 g/cm<sup>3</sup> for nitrogen and oxygen, respectively. Both the predicted density and the XRD density of both samples are larger than the measured apparent density, and this indicates that the sintered material is less than theoretically dense.



For both samples, the predicted density is larger than the XRD density. This difference can be explained by considering the hypothesized Si loss from the samples during sintering as discussed previously. The densities given in Figures 7 and 8 were calculated assuming stoichiometric  $\text{Ti}_5\text{Si}_3$ . Silicon loss during sintering should result in both lower unit cell mass and volume so that the artificially small unit cell volume predicts a higher than expected density. Additionally, the larger difference noted between predicted and XRD density for II60 reflects the higher sintering temperature of  $1800^\circ\text{C}$  (compared to  $1750^\circ\text{C}$  for (i9)) and thus greater Si loss. The XRD density estimate will also decrease somewhat due to Si loss.

The percent theoretical density for each sample as approximated by apparent density/predicted density is given in Table XII. This is a conservative estimate since the theoretical density should be closer to the XRD density. Microstructural analysis, including hardness and toughness measurements and phase analysis, is the topic of current research.

## V. Conclusions

High density samples of  $\text{Ti}_5\text{Si}_3$  have been prepared by sintering. Strict consideration of processing parameters is essential to obtain usable material. In particular, careful control of atmosphere during thermal processing is crucial to reduce the contamination of material due to glovebox atmosphere. Although processing inside an inert glovebox controls the level of oxygen contamination, the potential effect of uncontrolled nitrogen level must also be considered. The increased density of sintered material reflects principally the interstitial incorporation of oxygen. This provides for a robust process in which the system may be "self-correcting" for nitrogen and oxygen

contamination. Additional considerations are necessary due to potential silicon loss which occurs during sintering in low oxygen partial pressure environments.

### Acknowledgements

Ames Laboratory is operated for the U. S. Department of Energy by Iowa State University under contract number W-7405-ENG-82. This research was supported by the Office of Basic Energy Science, Materials Science Division.

### References

- 1 Y. Kim, A. J. Thom, and M. Akinc, "Synthesis, Processing, and Properties of  $Ti_5Si_3$ ," Min. Met. Mater. Soc. Symp. Proc., edited by T. S. Srivatsan and V. A. Ravi, Processing and Fabrication of Advanced Materials for High-Temperature Applications - II, (1993) 189-208.
2. A. J. Thom, V. Young, and M. Akinc, "Single Crystal Studies of  $Ti_5Si_3Z_x$ ," to be published.
3. A. J. Thom and M. Akinc, "Communion of  $Ti_5Si_3$  Prior to Sintering," to be published.
4. J. Quakernaat and J. W. Visser, "Lattice Dimensions of Low-Rate Metalloid-Stabilized  $Ti_5Si_3$ ," High Temp.-High Press., 6, (1974) 515-517.
5. S. Reuss and H. Vehoff, "Temperature Dependence of the Fracture Toughness of Single Phase and Two Phase Intermetallics," Scripta Metallurgica Mater., 24, (1990) 1021-1026.
6. J. Hamilton, private communication, Vacuum Atmospheres Company, 17 October 1994.
7. N. S. Jacobson, "Corrosion of Silicon-Based Ceramics in Combustion Environments" Journal Amer. Ceram. Soc., 76 [1], (1993) 3-28.
8. Specialty Gases and Equipment, Air Products Company, p16.

APPENDIX B:  
SYNTHESIS, PROCESSING, AND PROPERTIES OF  $\text{Ti}_5\text{Si}_3$

A paper published in *Processing and Fabrication of Advanced Materials for High Temperature Applications-II*<sup>1</sup>

Youngman Kim, Andrew J. Thom, and Mufit Akinc  
Ames Laboratory and Department of Materials Science and Engineering

Abstract

$\text{Ti}_5\text{Si}_3$  was synthesized by arc melting of Ti and Si elemental powders. The  $\text{Ti}_5\text{Si}_3$  buttons were milled and sieved to -325 mesh size powders, which were densified using HIPing. Microcracks in larger grains are observed for the HIPed microstructures with initial powder size of -325 mesh. Six hour milling of -325 mesh powder resulted in fine grain size (about 1  $\mu\text{m}$  in diameter) with no microcracks after HIPing. Mechanical properties, such as hardness and fracture toughness, were measured for HIPed  $\text{Ti}_5\text{Si}_3$ . The thermal expansion coefficients along the a and c axis were measured as a function of temperature using a high temperature x-ray technique. The anisotropy in thermal expansion coefficient is believed to be one of the major causes for microcracks in larger grains. The oxidation behavior of consolidated  $\text{Ti}_5\text{Si}_3$  was investigated in terms of weight changes at 1000°C in air.

---

<sup>1</sup>Reprinted with permission from *Processing and Fabrication of Advanced Materials for High Temperature Applications-II* 1993, 189-208. Copyright © The Minerals, Metals & Materials Society.

## I. Introduction

Intermetallic compounds generally combine the advantages in material properties between ceramics and metals. Ceramics show higher thermal capabilities, lower density, and better environmental stability than Ni-based high-temperature structural metal alloys. But ceramics have lower toughness and ductility than metal alloys, which make ceramics vulnerable to damage induced by mechanical and thermal loadings. Intermetallic compounds generally exhibit a ductile-to-brittle transition, and they can show ductility in the engineering use temperature range of 1000°-1500°C.

The high thrust-to-weight ratios of proposed high performance aircraft engines will require operating temperatures up to 1500°C. Material systems must combine light weight, high melting point, strength, creep resistance, fracture toughness, oxidation resistance and mechanical and microstructural stability over the service temperature range. Titanium silicide ( $\text{Ti}_5\text{Si}_3$ ) has been identified as a potential candidate due to the combination of low density (4320 Kg/m<sup>3</sup>), high melting temperature (2130°C) and adequate oxidation resistance. The silicide  $\text{Ti}_5\text{Si}_3$  has an ordered hexagonal crystal structure, D8-type with 16 atoms in its unit cell:  $a = 0.7444$  nm,  $c = 0.5143$  nm [1]. This silicide is expected to be very brittle due to its low crystal symmetry.

In this study titanium silicide was prepared from Ti and Si elemental powders using arc melting, subsequently ground in WC-lined mill and densified using hot isostatic pressing (HIPing). The mechanical properties and oxidation resistance were investigated.

## II. Experimental Procedure

Titanium silicide ( $\text{Ti}_5\text{Si}_3$ ) powder was prepared by grinding buttons made by arc melting elemental titanium and silicon powders with proper stoichiometry. Titanium silicide powder of -325 mesh size was milled using a Spex Mill™ for 0.25, 0.5 and 6 hours to study the effect of initial powder size on the final microstructure of the specimen. The powders were analyzed by X-ray diffraction with  $\text{Cu K}_\alpha$  radiation. Particle size distributions for the powders were measured using a centrifugal particle size analyzer (Shimadzu, Model SA-CP3, Kyoto, Japan). The powders were compacted uniaxially at 200 MPa at room temperature under argon atmosphere using WC lined steel dies 0.9 cm in diameter. The cold pressed pellets were spray-coated with an aqueous solution of BN and polyvinyl-pyrrolidone. The coated pellets were encapsulated in Pyrex™ glass powder (-10+30 mesh) and placed in a BN or alumina crucible. The crucible containing BN coated pellets and Pyrex glass powder was outgassed at 500°C for 10 hours under vacuum (about 1.3 Pa). The crucible (primary crucible) containing BN-coated discs and Pyrex™ glass powder was then loaded in another crucible (secondary crucible) to protect the HIP chamber from the accidental fracture of primary crucible at high temperature. Tantalum foil of 0.254 mm thickness was placed as a getter in between primary and secondary crucibles. Samples and crucibles were arranged as shown in Figure 1 during HIPing.

The samples were hot isostatically pressed at 1250°C using ultra high purity argon gas at the pressure of 206 MPa for 10 hours. To investigate the effect of cooling rate on the microstructure of titanium silicide two different rates were used: (1) slow cooling rate of 1°C/min from 1250°C to 800°C, 2°C/min from 800°C to room temperature; or (2) a fast cooling rate of about 50°C/min from 1250°C to room temperature. The profiles of temperature and pressure during the HIPing cycles are given in Figure 2.

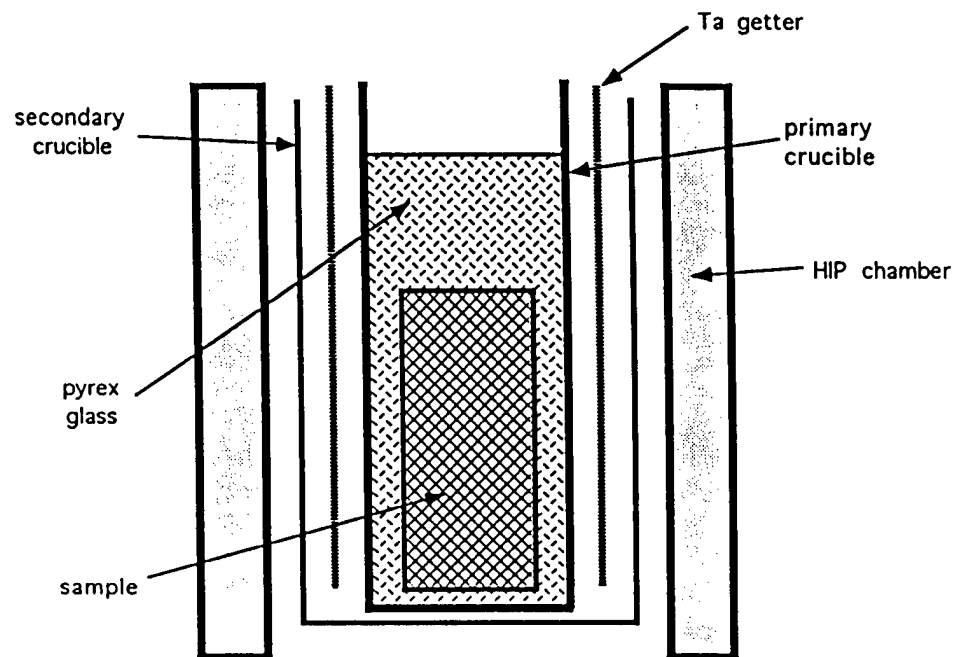


Figure 1: The schematic showing sample and crucible arrangement during HIPing.

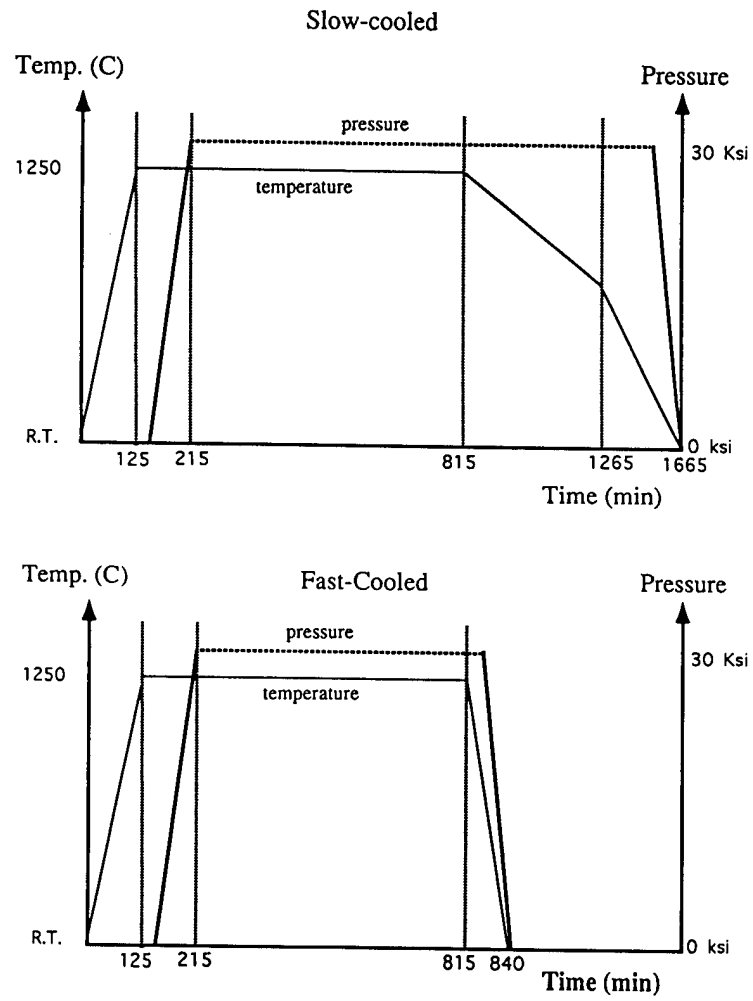


Figure 2: Temperature and pressure profile during HIPing. (a) slow cooling, (b) rapid cooling.

The apparent density of the samples was measured using a liquid immersion method. Microstructure of metallographically prepared specimens was observed using an optical microscope with polarized light. Average grain size was obtained using the linear-intercept method on the micrographs of samples. Hardness and indentation toughness were measured using Vickers microhardness tester.

The thermal expansion coefficient was measured using high temperature x-ray diffraction [2]. A thin layer of -325 mesh powder was applied to a 0.3 mm thick quartz wedge by mixing a small amount of powder with ethanol on the wedge. The wedge was placed on the platinum heater strip of the diffractometer. A Pt-10Rh thermocouple was placed in contact with the heater strip. The furnace chamber was evacuated for 18 hours to a pressure of  $1.3 \times 10^{-3}$  Pa. The sample was heated under dynamic vacuum and an x-ray diffraction pattern was collected at fixed temperature increments during heating and cooling.

Isothermal oxidation of  $\text{Ti}_5\text{Si}_3$  was measured by thermogravimetric analysis (TGA). Hot isostatically pressed bulk samples of  $\text{Ti}_5\text{Si}_3$  were cut into coupons of 6 mm x 6mm x 1.5 mm. Coupons were then rough polished with 600 grit SiC paper, and a 0.5 mm diameter hole was electric discharge machined in the coupons with a copper electrode. Coupons were then cleaned in acetone and dried for 24 hours in an oven at 120°C.

The coupons were loaded into the TGA and suspended in the vertical furnace with a sapphire wire. High purity helium gas was flowed overnight to establish an inert atmosphere. Samples were heated to 1000°C at 10°C/min, and gas flow was then switched to air. The mass was continuously monitored to determine isothermal oxidation characteristics.



### III. Results and Discussion

#### 1. Powder Characterization

The -325 mesh powder produced by grinding and sieving of arc melted buttons showed bimodal particle size distribution (Figure 3) with median particle diameter of 4.1  $\mu\text{m}$ . The reduction in particle size by Spex<sup>TM</sup> milling could not be detected by the centrifugal particle size analyzer due to powder agglomeration. However scanning electron microscope (SEM) micrographs showed particle size reduction as the milling time increased, where the submicron size powders were somewhat agglomerated (Figure 3). Na-metaphosphate was used to disperse milled powders for particle size measurement, but the powders remained agglomerated.

The X-ray diffraction pattern for the powder produced by grinding and sieving of arc melted buttons is shown in Figure 4, which indicates that predominantly  $\text{Ti}_5\text{Si}_3$  is present. Table I gives the peak positions and intensities for the pattern in Figure 4.

Table I: Peak Positions and Intensities for Arc-Melted  $\text{Ti}_5\text{Si}_3$

2 $\theta$ (degree)	d-spacing ( $\text{\AA}$ )	Relative Intensity (%)
27.730	3.2144	12
29.653	3.0102	11
34.943	2.5656	13
36.921	2.4327	47
37.727	2.3825	26
41.011	2.1990	100
42.066	2.1462	46
42.777	2.1122	74
54.311	1.6877	6

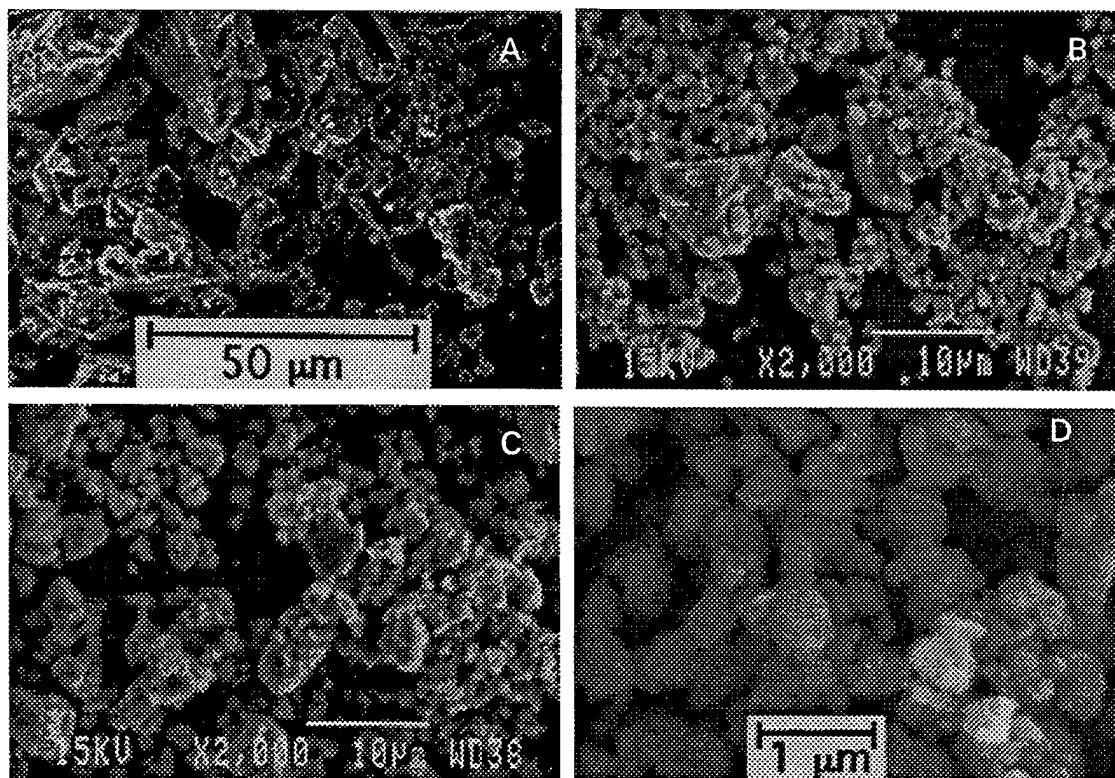


Figure 3: SEM micrographs showing (a) as-sieved -325 mesh powder, (b) 15 min milled -325 mesh powder, (c) 30 min milled -325 mesh powder, and (d) 6 hour milled -325 mesh powder.

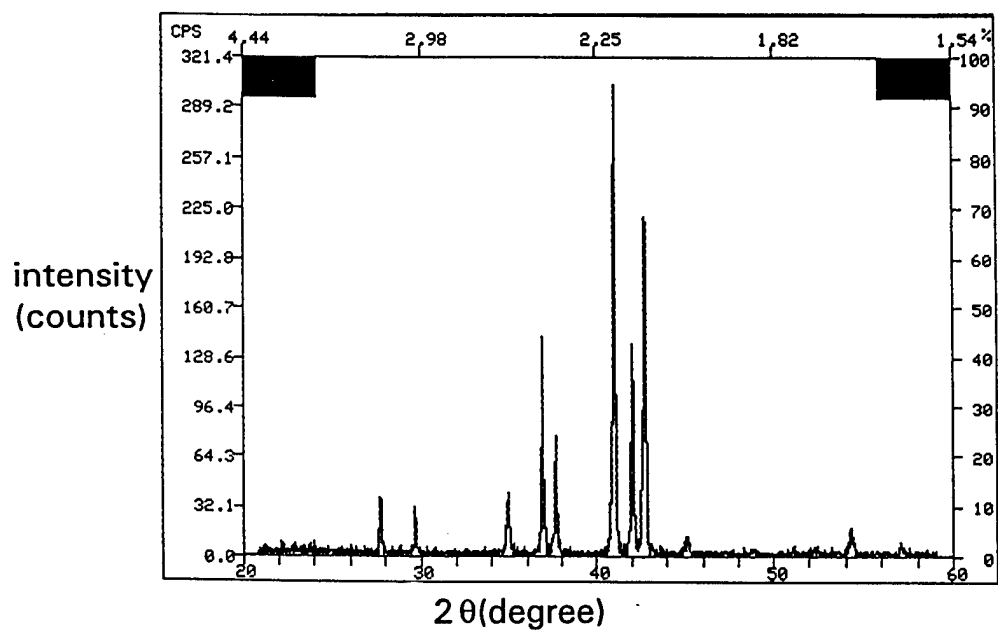


Figure 4: X-ray diffraction intensity as a function of diffraction angle for the  $\text{Ti}_5\text{Si}_3$  powder produced by arc melting.

## 2. Microstructures

Optical micrograph of HIPed  $\text{Ti}_5\text{Si}_3$  with -325 mesh initial powder is shown in Figure 5. The mean size of the grains is on the order of  $12\text{ }\mu\text{m}$  irrespective of cooling rate. Transgranular microcracks were observed, which implied a poor cleavage strength. Multiple transgranular cracks were parallel to one another (larger grains showed more transgranular cracks while smaller grains showed less cracks), indicating thermal stress caused by anisotropy in both thermal expansion coefficient and elastic modulus of the silicide during cooling. The severity of microcracking was affected by cooling rate. The number density of microcracks in rapidly cooled specimen has increased regionally but not homogeneously throughout the specimen. Since cracks are observed inside of grains, the grain boundaries appear to be stronger than one or more crystallographic directions within grains.

HIPed  $\text{Ti}_5\text{Si}_3$  with 6 hour milled -325 mesh powder and slow cooling produced microcrack free specimen with average grain size of 1 to  $2\text{ }\mu\text{m}$  (Figure 6).

## 3. Density, Hardness, and Toughness

The density of HIPed sample was measured to be 98.5 to 99.0% of theoretical density. The Vicker's hardness of the slowly cooled microcracked specimen with initial powder size of -325 mesh was measured to be  $9.1 \pm 0.5\text{ GPa}$  ( $924.2 \pm 56.1\text{ Hv}$ ) under 1.96 N indentation load. The specimen cooled rapidly showed slightly lower hardness (Figure 7). The Vickers hardness of the non-microcracked specimen processed with 6 hour-milled -325 mesh powder was  $17.1 \pm 0.7\text{ GPa}$  ( $1748.7 \pm 67.8\text{ Hv}$ ). Hardness for various specimens under an applied load of 1.96 N is shown as a function of grain size in Figure 7. As the average grain size of HIPed sample decreased (as milling time increased), the hardness increased.



Figure 5: Optical micrographs of HIPed Ti<sub>5</sub>Si<sub>3</sub> with -325 mesh initial powder, which shows microcracks in grains.

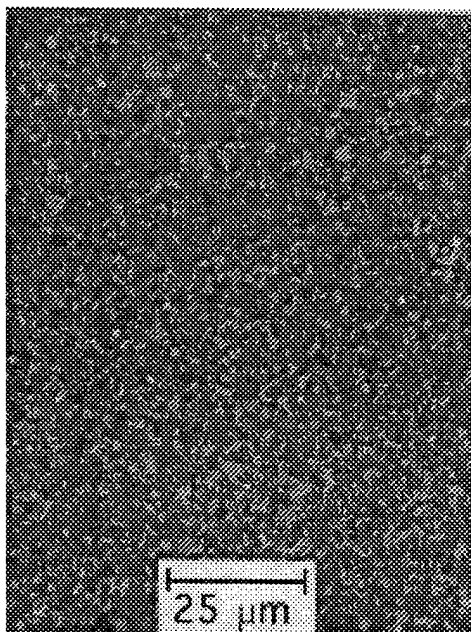


Figure 6: Optical micrographs of HIPed Ti<sub>5</sub>Si<sub>3</sub> with reduced initial powder size (6 hour milling of -325 mesh powder), which shows microcrack free specimen with average grain size of 1 to 2 μm.

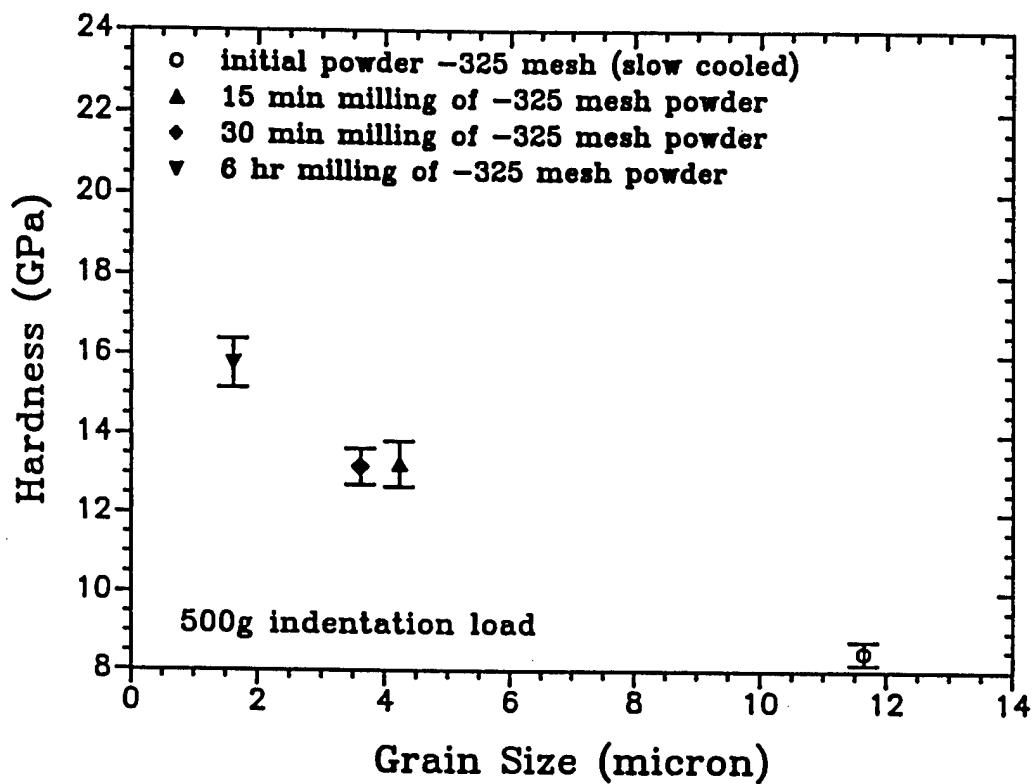


Figure 7: Hardness of  $\text{Ti}_5\text{Si}_3$  as a function of average grain size.

Hardness values for  $\text{Ti}_5\text{Si}_3$  were reported in literatures as 980 [3], 1150 [4],  $968 \pm 30$  [5],  $1283 \pm 67$  Hv [6]. The hardness obtained in this study was lower for the microcracked specimen, and higher for the non-microcracked specimen than the values reported in the literatures.

Indentation fracture toughness ( $K_{\text{IC}}$ ) for the non-microcracked specimen was found using the following expression [7]:

$$K_{\text{IC}} = \zeta (E/H)^{1/2} (P/C_0^{3/2}) \quad (1)$$

where  $\zeta$  is a calibration constant of  $0.016 \pm 0.004$ ,  $E$  is Young's modulus,  $H$  the hardness,  $P$  the peak load, and  $C_0$  the half of radial crack size. Measured indentation fracture toughness varies from  $1.6 \pm 0.2 \text{ MPa} \cdot \sqrt{\text{m}}$  for the sample with initial powder size of -325 mesh, to  $2.94 \text{ MPa} \cdot \sqrt{\text{m}}$  for the specimen with 6 hour milled -325 powder utilizing Young's modulus value of 225 GPa [8] (Figure 8).

For  $\text{Ti}_5\text{Si}_3$  with mixed grain size of 10 and 30  $\mu\text{m}$ , fracture toughness was obtained using a single edge-notched beam method in an alumina-four-point bending fixture as  $2 \text{ MPa} \cdot \sqrt{\text{m}}$  [9]. For  $\text{Ti}_5\text{Si}_3$  with grain size of 6  $\mu\text{m}$ , fracture toughness was  $6 \text{ MPa} \cdot \sqrt{\text{m}}$  at room temperature [9]. The toughness values of 2.0 - 3.5  $\text{MPa} \cdot \sqrt{\text{m}}$  at room temperature up to 700°C were reported using four-point bend test [5]. Therefore the fracture toughnesses measured for  $\text{Ti}_5\text{Si}_3$  in this study (Figure 8) agree reasonably well with the toughness values reported in the literatures [5, 9].

#### 4. Measurement of Thermal Expansion Coefficient

Because heater strip materials such as platinum, molybdenum, tungsten, and tantalum form binary silicide intermetallics, a quartz wedge was used as a plate for the



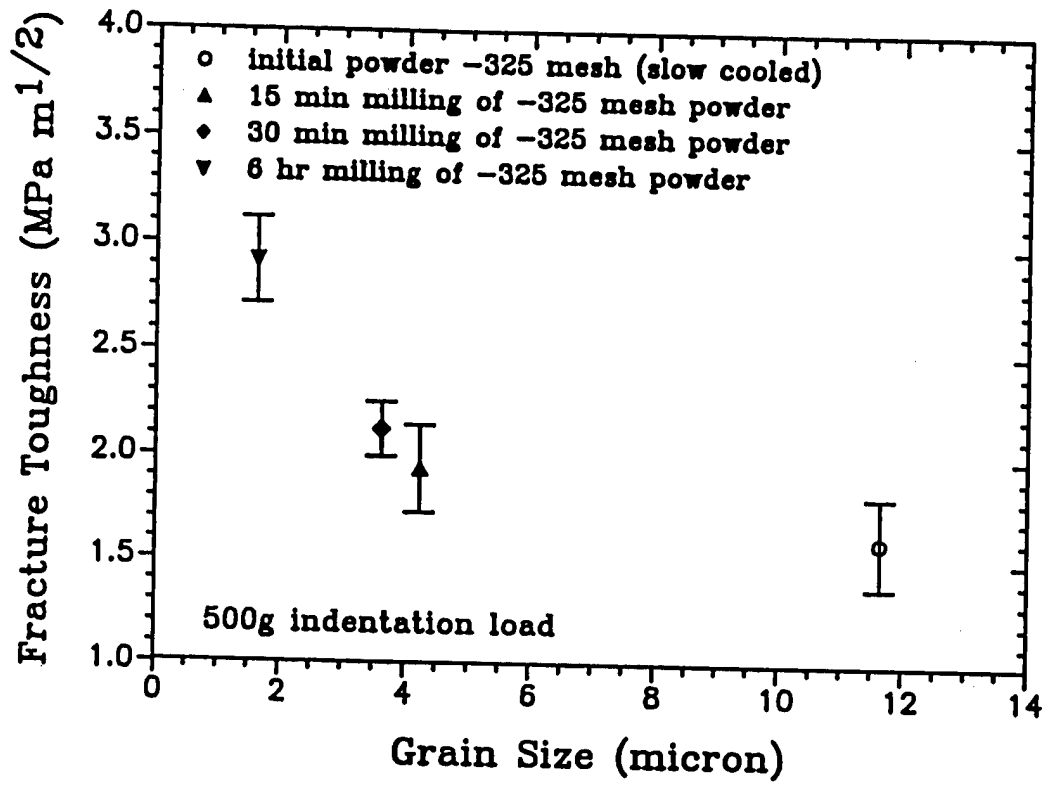


Figure 8: Fracture toughness of Ti<sub>5</sub>Si<sub>3</sub> as a function of average grain size.

Ti<sub>5</sub>Si<sub>3</sub> powder. Since the Pt-10Rh thermocouple could not be placed in contact with the Ti<sub>5</sub>Si<sub>3</sub> powder, the sample temperature was calibrated by measuring the thermal expansion coefficient of a well characterized cubic material, MgO, under similar experimental conditions.

Diffraction pattern peak locations were identified using the profile-fitting function of the diffractometer software. A least-squares lattice parameter refinement program was used to calculate the parameters [10]. The calculated room temperature parameters are:  $a=0.74514\pm0.00004$  nm,  $c=0.51464\pm0.00003$  nm. The calculated values compare well to the literature values:  $a=0.7444$  nm,  $c=0.5143$  nm [1].

Figure 9 shows the linear temperature dependence of the lattice parameters. The standard error of all calculated lattice parameters is less than 0.00010 nm. The error bars are smaller than the symbol size and were omitted from Figure 9. The linear thermal expansion coefficients estimated from the curve are approximately constant over the temperature range of 298-873K and are:  $\alpha_a=8.7\pm0.2$  ppm/K and  $\alpha_c=20.4\pm0.4$  ppm/K. No values of  $\alpha_a$  and  $\alpha_c$  are available in the literature. The estimated bulk CTE value is 11.6 ppm/K, compared to the literature value of 11.0 ppm/K from 450-1350 K [11].

## 5. Thermal Stress during Cooling

When a specimen is cooled from processing temperature, thermal stress in the specimen arises in two different ways: microscopic stress developing on the microstructural scale because of thermal expansion anisotropy for non-cubic materials, and macroscopic thermal gradient stress which develops because of uneven cooling of the body.

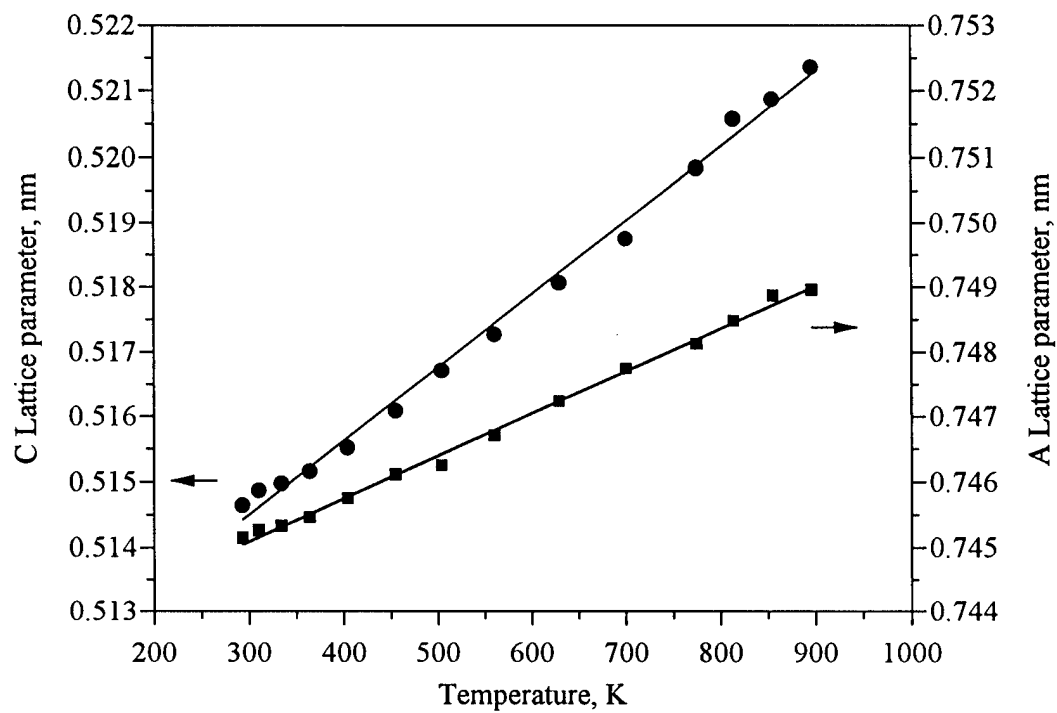


Figure 9: Lattice parameters of  $\text{Ti}_5\text{Si}_3$  as a function of temperature.

## 6. Thermal Expansion and Elastic Anisotropies

Thermal expansion anisotropy is found to be a potential source of microcracking during thermal cycling [12-14]. For a noncubic polycrystalline body, microscopic stresses develop as a result of the thermal expansion anisotropy and crystallographic orientation mismatch across grain boundaries during cooling from processing temperature.

The stress intensity factor was presented based on a three dimensional model for an annular crack around a spherical second phase particle [15] (Figure 10)

$$K_I = \frac{2PR^{1/2}}{\pi^{1/2}} \left\{ \left( \frac{R}{a} \right)^{1/2} \left( 1 - \left( 1 - \frac{R^2}{a^2} \right)^{1/2} \right) + \frac{1}{2} \left( \frac{R}{a} \right)^{3/2} \left( 1 - \frac{R^2}{a^2} \right)^{1/2} \right\} \quad (2)$$

$$-\sigma_r = 2\sigma_\theta = (\alpha_m - \alpha_p) \Delta T \left[ \left\{ (1 + \nu_m) / 2E_m \right\} + \left\{ (1 - 2\nu_p) / E_p \right\} \right]^{-1} \left( \frac{R}{r} \right)^3 = P \left( \frac{R}{r} \right)^3 \quad (2')$$

where P represents a uniform thermoelastic stress which acts along the particle-matrix interface [16], R, radius of the spherical particle, a, radius of the annular crack around spherical particle (Figure 10). The model may be applied for the case of thermal expansion anisotropy induced spontaneous cracking in a single phase material. For the simplicity of calculation the isotropic elasticity was assumed for single phase material ( $E_m = E_p$  and  $\nu_m = \nu_p$ ). For a brittle material the fracture toughness  $K_{Ic}$  has the following relationship with the surface energy,  $\gamma$

$$K_{Ic} = (2E\gamma)^{1/2} \quad (3)$$

The critical grain size  $D_c$  ( $=2R_c$ ) is expressed in terms of material properties and temperature difference,  $\Delta T$  when no annular crack is present ( $R=a$ ) around a spherical particle.

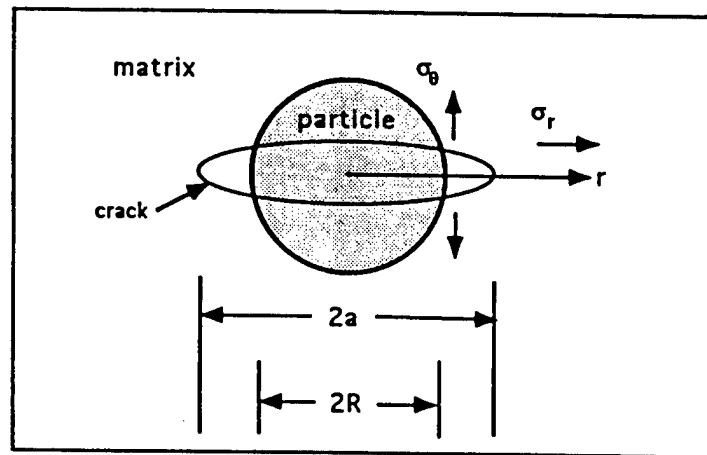


Figure 10: Schematic of an annular crack around a spherical particle under a uniform thermoelastic stress.

$$D_c = \frac{9\pi(1-\nu)^2\gamma}{4E(\Delta\alpha\Delta T)^2} \quad (4)$$

where,  $\Delta\alpha$  = the difference between bulk CTE and smaller of  $\alpha_a$  or  $\alpha_c$ . Figure 11 shows critical grain size as a function of  $\Delta\alpha$  based on equation 4 with an estimated surface energy of 5 J/m<sup>2</sup>, Young's modulus of 225 GPa [8], Poisson's ratio of 0.25, and  $\Delta T$  of 1230°C, which was the case for HIPing. When a specific hexagonal grain along a-axis contracts less than the average randomly oriented neighboring grains do, the specific hexagonal grain along the a-axis will experience a compressive stress while the neighboring grains will be subject to a tensile stress. Equation 4 predicts critical grain size of about 4  $\mu\text{m}$  for  $\Delta\alpha$  (estimated bulk CTE -  $\alpha_a$ ) of 3.9 ppm/K. The estimated bulk CTE value is 12.6 ppm/K ( $= [2\alpha_a + \alpha_c]/3$ ) and the measured  $\alpha_a$  is 8.7 ppm/K. The theoretical prediction for the critical grain size agrees with the experimental results which showed microcracks in grains for the sample with grain size of 10 to 20  $\mu\text{m}$ , and no microcracks for the sample with average grain size of 1 to 2  $\mu\text{m}$ .

### 7. The Maximum Tensile Surface Stress during Cooling.

Let us consider  $\sigma_{\text{max}}$ , the maximum tensile surface stress for a specimen [17].

$$\sigma_{\text{max}} = \frac{E\alpha\Delta T}{(1-\nu)} \cdot f(B) \quad (5)$$

where,  $f(B)$  = a function of Biot modulus, B [17],

$$f(B) = (1.5 + 3.25/B - 0.5 e^{-16/B})^{-1} \quad \text{when } 0 < B < 20 \quad (6)$$

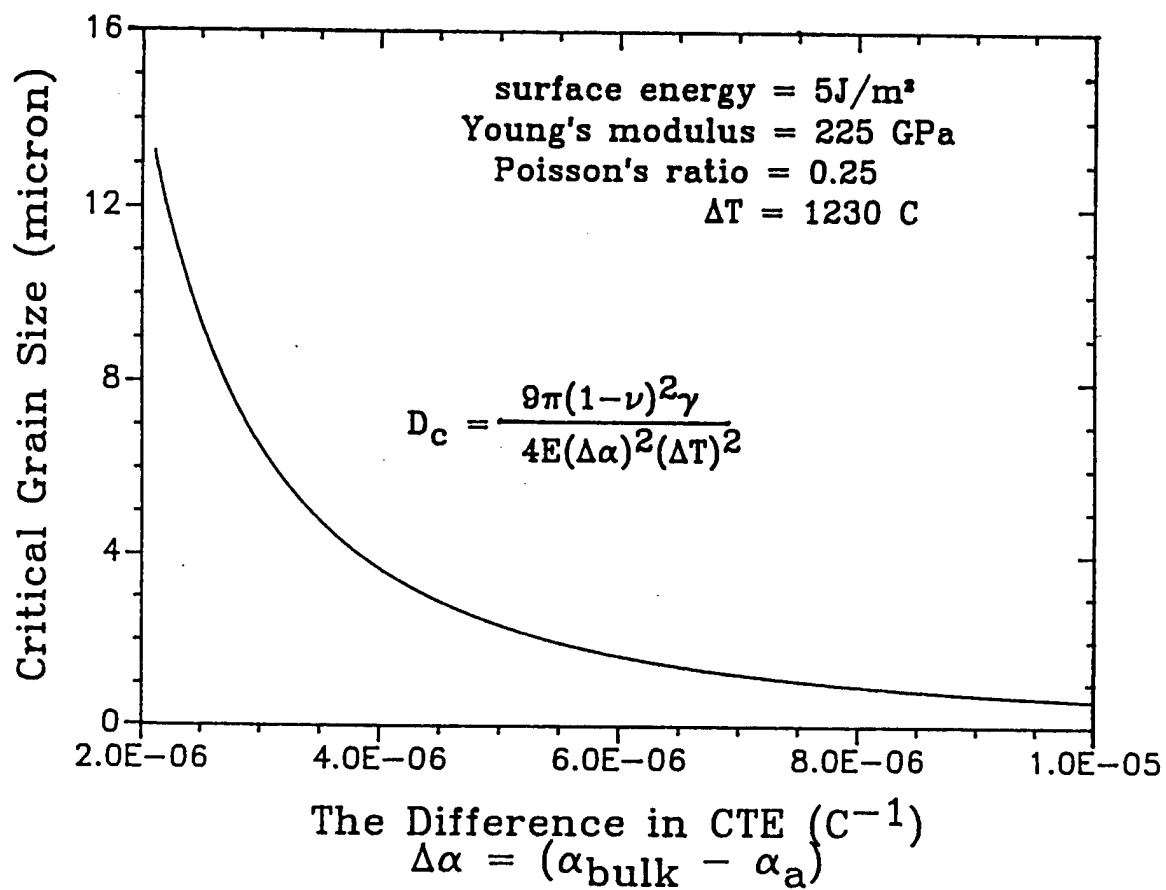


Figure 11: Calculated critical grain size as a function of  $\Delta\alpha$ .

The Biot modulus,  $B$ , is defined as  $hl/k$ , where  $h$  is surface heat transfer coefficient,  $l$  is the half thickness of the plate, and  $k$  is the thermal conductivity of the plate. Surface heat transfer coefficient,  $h$ , may be determined from the measurement of surface temperature as a function of time during cooling [18]. Thus  $h$  is a function of cooling rate. Equations 5 and 6 imply that higher stress is developed when the sample is cooled more rapidly. Higher stress can account for the fact that more cracks were observed locally for a fast cooled specimen. Equation (5) assumes an infinite thin plate geometry.

## 8. Oxidation Study

Figure 12 shows the isothermal oxidation of three  $Ti_5Si_3$  samples in air. Sample 1 had a relatively large grain size, up to 25  $\mu m$ , and exhibited intragranular microcracking. After 24 hours the parabolic oxidation rate was  $0.027 \text{ mg}^2/\text{cm}^4/\text{hr}$ . Sample 2 and 3 had a finer grain size with no intragranular microcracking. Flow rates for sample 2 and 3 were 50 and 120 ml/min, respectively. The oxidation behavior of sample 2 and 3 during the initial 48 hours was similar. Both samples progressed into an accelerated stage of oxidation, with sample 3 at the higher flow rate entering the accelerated stage quicker than sample 2 at the lower flow rate.

The oxygen uptake of the large-grained material is an order of magnitude less than the fine-grained material, and the oxidation process may be influenced by grain boundary diffusion. The apparent affect of flow rate indicates the oxidation process could be reaction limited. A test matrix incorporating temperature, grain size, and gas flow rate as factors has been designed to better characterize the oxidation process. These experiments are currently being conducted.

The microstructure of sample 2 is seen in Figure 13a. The SEM backscattered image reveals several phases. The unoxidized  $Ti_5Si_3$  phase is the bright



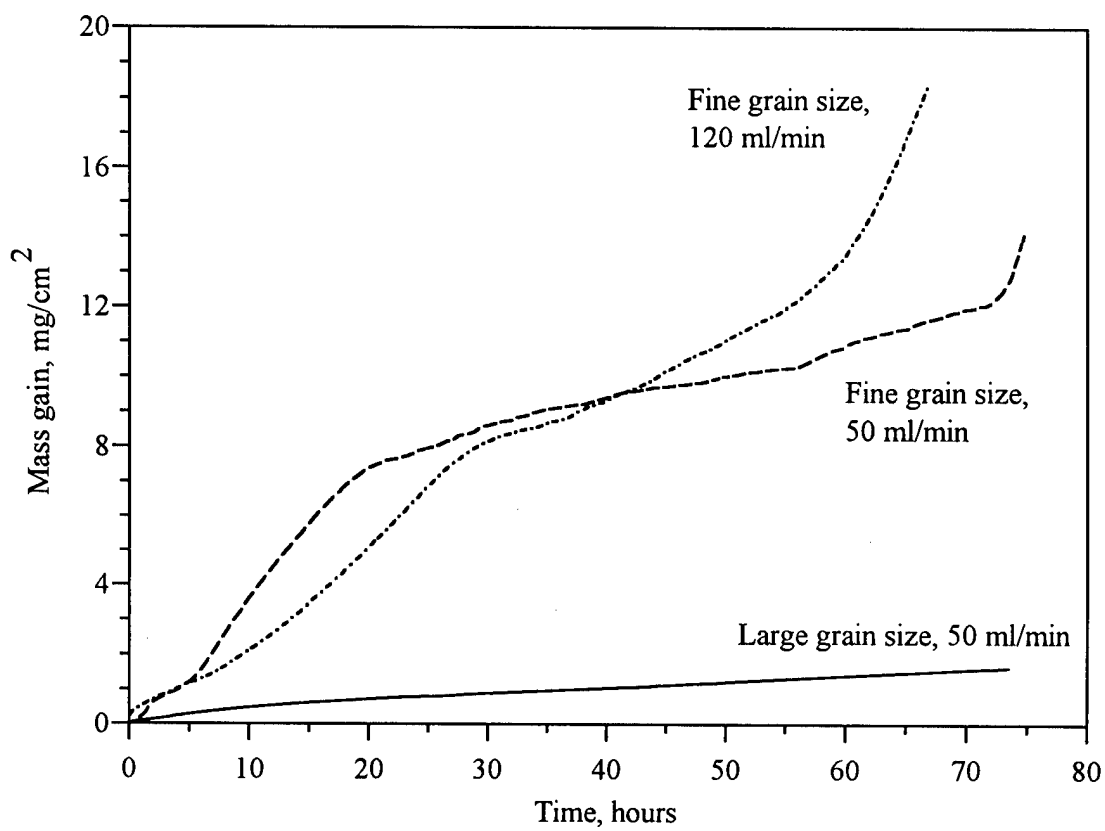


Figure 12: Isothermal oxidation of  $\text{Ti}_5\text{Si}_3$  in air at  $1000^\circ\text{C}$ .

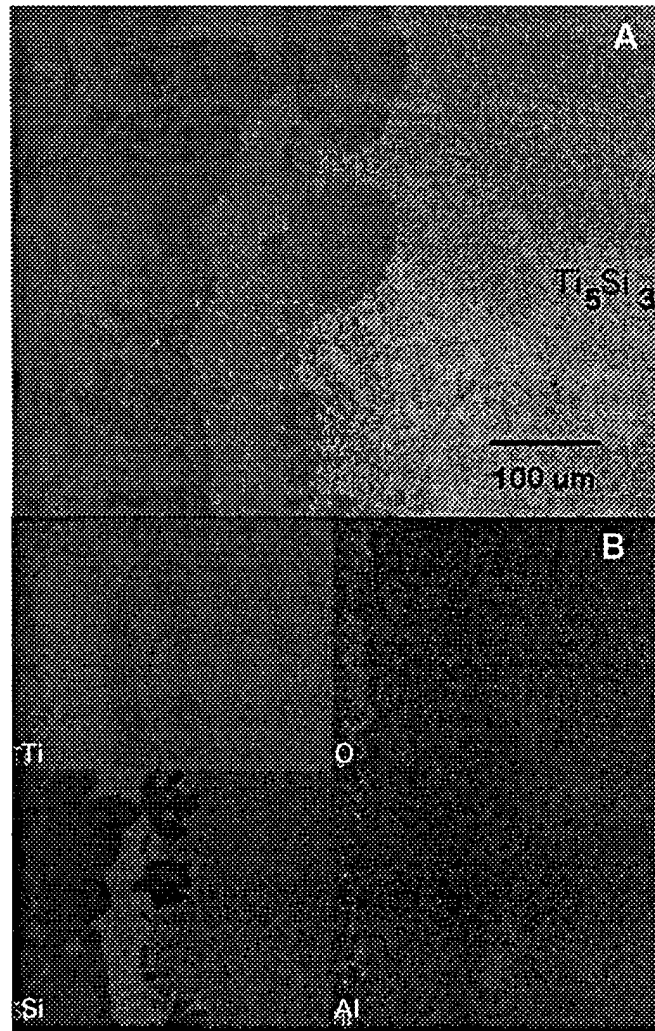


Figure 13: SEM micrographs of cross section of oxidized Sample 2.  
(a) backscattered image (b) x-ray dot map of Ti, Si, O, Al.

interior region. An x-ray dot map showing titanium, silicon, oxygen, and aluminum is seen in Figure 13b. Aluminum is probably present because alumina abrasives were used for final polishing. Qualitatively subtracting aluminum signal from the oxygen signal should give a rough idea of oxygen signal due to the sample alone.

Next to the unoxidized  $\text{Ti}_5\text{Si}_3$  is a dark dendritic phase. These dendrites are connected to a middle oxidation layer and also form large isolated islands. These regions are highly silicon depleted with about the same amount of titanium as the unoxidized  $\text{Ti}_5\text{Si}_3$ . The lack of higher oxygen content in these areas indicated these could be regions of a titanium rich phase such as  $\text{TiO}$  or some other oxide of titanium. Also next to the unoxidized  $\text{Ti}_5\text{Si}_3$  is a layer of a silicon rich phase which is interrupted by the titanium rich dendrites and islands. This discontinuous layer has a slightly decreased titanium content without an appreciable oxygen content, indicating possibly a titanium silicide intermetallic such as  $\text{TiSi}$  or  $\text{TiSi}_2$ .

Figures 14a and 14b show the titanium rich layer from which the titanium rich dendrites grew. The outer 30-50  $\mu\text{m}$  of the sample has a higher oxygen content. This outer layer is seen in more detail in Figures 15a and 15b. A dense outer 10  $\mu\text{m}$  layer of  $\text{TiO}_2$ , verified by x-ray diffraction of the outer scale, forms. The next 10  $\mu\text{m}$  appears to be a mix of the  $\text{TiO}_2$  and a silicon and oxygen rich phase, perhaps  $\text{SiO}_2$ . A 10  $\mu\text{m}$  silicon rich layer forms, but it contains  $\text{TiO}_2$  particles and doesn't form a continuous layer. This lack of a continuous protective  $\text{SiO}_2$  layer may account for the significant growth for the oxide layers.

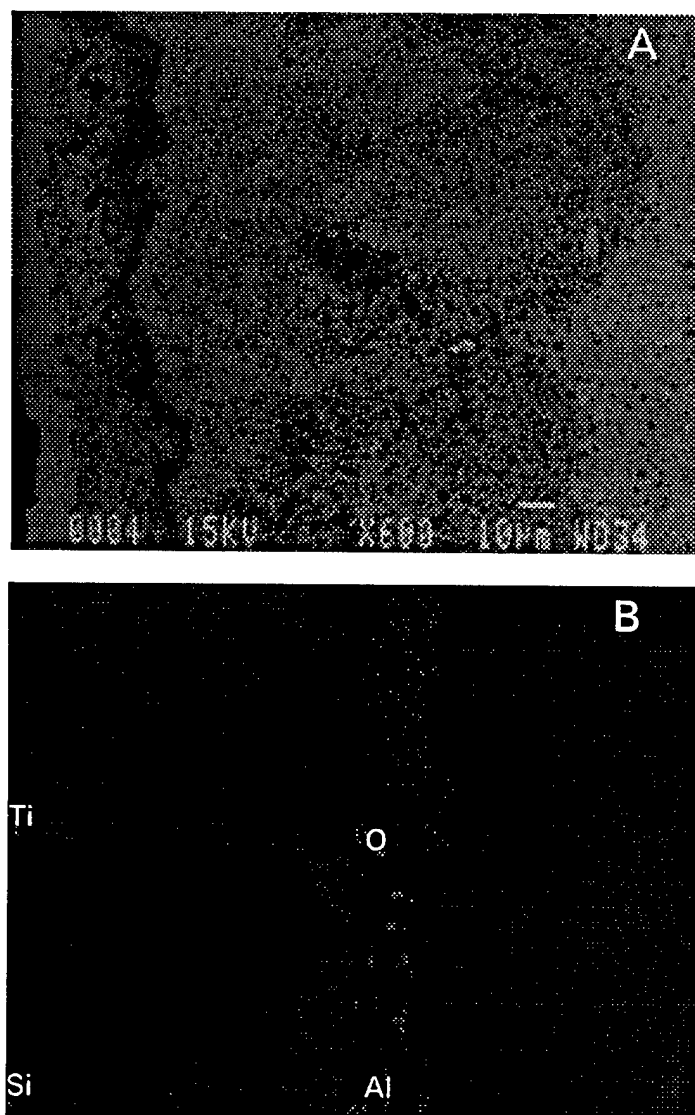


Figure 14: SEM micrographs of cross section of oxidized Sample 2.  
(a) backscattered image (b) x-ray dot map of Ti, Si, O, Al.

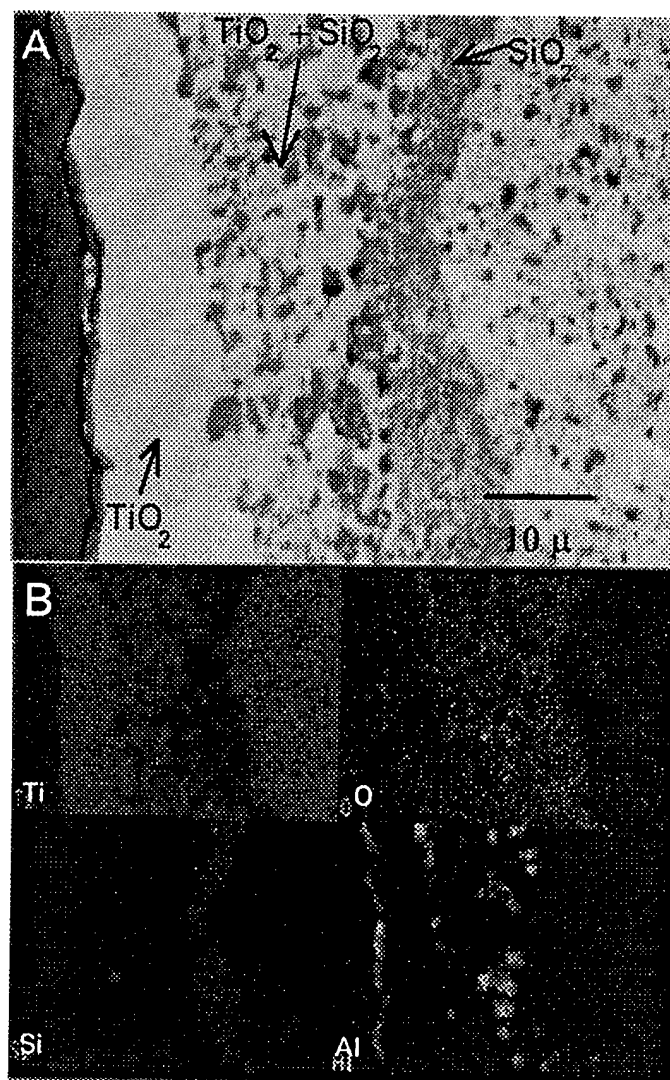


Figure 15: SEM micrographs of cross section of oxidized Sample 2.  
(a) backscattered image (b) x-ray dot map of Ti, Si, O, Al.

#### IV. Summary and Conclusions

Crack free, dense  $\text{Ti}_5\text{Si}_3$  monoliths were produced with 6 hour milled -325 mesh powder using HIPing.  $\text{Ti}_5\text{Si}_3$  HIPed with initial powder size of -325 mesh showed microcracking in grains, which had an average grain size of 10 to 20  $\mu\text{m}$ . Crack free monoliths with average grain size of 1 to 2  $\mu\text{m}$  had hardness values up to 17.1 GPa and fracture toughness values up to  $2.9 \text{ MPa} \cdot \sqrt{\text{m}}$ . For large grain size material, a parabolic oxidation rate of  $0.027 \text{ mg}^2/\text{cm}^4/\text{hr}$  was observed at  $1000^\circ\text{C}$  in air.  $\text{Ti}_5\text{Si}_3$  with larger grains exhibited microcracking, lower hardness and toughness, and higher oxidation resistance. Anisotropy in thermal expansion coefficients, measured by high temperature x-ray diffraction, is thought to be one of the major causes for the microcracking.

#### Acknowledgements

Ames Laboratory is operated for the U. S. Department of Energy by Iowa State University under contract number W-7405-ENG-82. This research was supported by the Office of Basic Energy Science, Materials Science Division.

The authors are thankful to C. R. Hubbard and O. B. Cavin for their assistance in the high temperature x-ray diffraction study. These facilities were made available to the authors through the High Temperature Materials Laboratory (HTML) User Program at Oak Ridge National Laboratory, Oak Ridge, TN.

#### References

1. J. Quakernaat and J. W. Visser, "Lattice Dimensions of Low-Rate Metalloid-Stabilized  $\text{Ti}_5\text{Si}_3$ ", High Temperatures-High Pressures, 6:515-517, 1974.

2. A. J. Thom and M. Akinc, Iowa State University, C. R. Hubbard, and O. B. Cavin, Oak Ridge National Laboratory, Unpublished Data.
3. C. T. Liu, E. H. Lee and T. J. Henson, "Initial Development of High-Temperature Titanium Silicide Alloys", Report, ORNL-6435; Order No. DE88007860, 1988.
4. H. E. N. Stone, "The Oxidation Resistance and Hardness of Some Transition Metal Silicides", *J. Mat. Sci. Lett.*, 2: 609-611, 1980.
5. G. Frommeyer, R. Rosenkrantz and C. Ludecke, "Microstructure and Properties of the Refractory Intermetallic  $Ti_5Si_3$  Compound and the Unidirectionally Solidified Eutectic Ti- $Ti_5Si_3$  alloy", *Z. Metallkde*, 81[5]: 307-313, 1990.
6. G. V. Samsonov, et al, "Relations between the Electron Work Function and Certain Physical Properties in Silicides of Group IV Transition Metals", *Izvestiya Akademii Nauk SSSR, Neorganicheskie Materialy*, 12[5]: 850-853, 1976.
7. G. R. Antis, et al, "A Critical Evaluation of Indentation Techniques for Measuring Fracture Toughness: I, Direct Crack Measurements", *J. Am. Ceram. Soc.*, 64[9]: 533-538, 1981.
8. P. J. Meschter and D. S. Schwartz, "Silicide-Matrix Materials for High Temperature Applications", *JOM*, Nov., 52-55, 1989.
9. S. Reuss and H. Vehoff, "Temperature Dependence of Fracture Toughness of Single Phase and Two Phase Intermetallics", *Scripta Met.*, 24: 1021-1026, 1990.
10. D. E. Appleman and H. T. Evans. NTIS Document No. PB-216188. 1973.
11. T. Y. Kosolapova, *Handbook of High Temperature Compounds: Properties, Production, Applications*. Hemisphere Publishing Corp., New York, 1990.
12. J. A. Kuszyk and R. C. Bradt, "Influence of Grain Size on Effects of Thermal Expansion Anisotropy in  $MgTi_2O_5$ ", *J. Am. Ceram. Soc.*, 56: 420-423, 1973.
13. R. W. Rice and R. C. Pohanka, "Grain-Size Dependence of Spontaneous Cracking in Ceramics", *J. Am. Ceram. Soc.*, 62: 559-563, 1979.
14. A. G. Evans, "Microfracture from Thermal Expansion Anisotropy - I. Single Phase Systems", *Acta Metall.*, 26: 1845-1853, 1978.

APPENDIX C:  
EVALUATION OF  $A_5Si_3Z_x$  INTERMETALLICS  
FOR USE AS HIGH TEMPERATURE STRUCTURAL MATERIALS

A paper published in *Processing and Fabrication of Advanced Materials-III*<sup>1</sup>

Andrew J. Thom, Mitchell K. Meyer, Youngman Kim, and Mufit Akinc  
Ames Laboratory and Department of Materials Science and Engineering

**Abstract**

Refractory intermetallic silicides are receiving increasing consideration for use as high temperature structural materials.  $A_5Si_3$  compositions are particularly interesting due to their ability to incorporate a variety of interstitial ternary additions. These ternary additions present a unique opportunity to potentially tailor physical properties. Previous experimental work has shown that these additions can decrease the inherent thermal expansion anisotropy of  $Ti_5Si_3$ . This paper reviews some of the literature with respect to binary and ternary silicides of the form  $A_5Si_3Z_x$ . Recent experimental work by the authors on two promising compositions,  $Ti_5Si_3$  and  $Mo_5Si_3$ , is discussed. Interstitial additions substantially improve the isothermal oxidation resistance of both  $Ti_5Si_3$  and  $Mo_5Si_3$ . The lattice parameter of  $Ti_5Si_3$  is significantly changed by ternary interstitial additions, indicating the extensive solubility of  $Ti_5Si_3$  for such additions. The level of similar additions affects the phase assemblage of  $Mo_5Si_3$ . Hardness and toughness values from indentation measurements for selected compositions are given.



15. V. D. Kristic and M. D. Vlajic, "Conditions for Spontaneous Cracking of a Brittle Matrix due to the Presence of Thermoelastic Stresses", *Acta. Metall.*, 31: 139-144, 1983.
16. J. Selsing, "Internal Stresses in Ceramics", *J. Am. Ceram. Soc.*, 44: 419, 1961.
17. S. S. Manson, Chap. 7 in *Thermal Stress and Low-Cycle Fatigue*, McGraw-Hill, New York, 1966.
18. Y. Kim, W.-J. Lee and E. D. Case, "The Measurement of the Surface Heat Transfer Coefficient for Ceramics Quenched into a Water Bath", *Mat. Sci. Eng.*, A145: L7-L11, 1991.

APPENDIX C:  
EVALUATION OF  $A_5Si_3Z_x$  INTERMETALLICS  
FOR USE AS HIGH TEMPERATURE STRUCTURAL MATERIALS

A paper published in *Processing and Fabrication of Advanced Materials-III*<sup>1</sup>

Andrew J. Thom, Mitchell K. Meyer, Youngman Kim, and Mufit Akinc  
Ames Laboratory and Department of Materials Science and Engineering

**Abstract**

Refractory intermetallic silicides are receiving increasing consideration for use as high temperature structural materials.  $A_5Si_3$  compositions are particularly interesting due to their ability to incorporate a variety of interstitial ternary additions. These ternary additions present a unique opportunity to potentially tailor physical properties. Previous experimental work has shown that these additions can decrease the inherent thermal expansion anisotropy of  $Ti_5Si_3$ . This paper reviews some of the literature with respect to binary and ternary silicides of the form  $A_5Si_3Z_x$ . Recent experimental work by the authors on two promising compositions,  $Ti_5Si_3$  and  $Mo_5Si_3$ , is discussed. Interstitial additions substantially improve the isothermal oxidation resistance of both  $Ti_5Si_3$  and  $Mo_5Si_3$ . The lattice parameter of  $Ti_5Si_3$  is significantly changed by ternary interstitial additions, indicating the extensive solubility of  $Ti_5Si_3$  for such additions. The level of similar additions affects the phase assemblage of  $Mo_5Si_3$ . Hardness and toughness values from indentation measurements for selected compositions are given.

---

<sup>1</sup>Reprinted with permission from Processing and Fabrication of Advanced Materials-III 1994, 413-438. Copyright © The Minerals, Metals & Materials Society.

## I. Introduction

Intermetallics as a class of materials have received considerable attention within the past decade for use as high temperature structural materials. A primary interest is for use in aerospace applications. The performance of an aircraft engine depends on its design, and therefore on the available materials. The latest design in turbine engines utilizes an active cooling of the turbine blades through intricate internal cooling passages. Such cooling allows the turbine blades to operate at temperatures where the combustion gases in contact with the blade approach the melting point of the turbine alloy. Nearly 20% of the compressor delivery air is used for cooling turbine components in some current jet engines [1]. Additionally, turbine blade construction has seen the advent of expensive processing schemes with the use of directionally solidified and single crystal turbine blades instead of conventionally cast blades. Increases in performance and efficiency continually push toward higher operating temperatures. Any significant improvement will necessitate the development of a new materials system.

Several comprehensive articles have been recently written summarizing the status of intermetallic research with respect to use as high temperature structural materials [2,3,4,5,6]. Due to the large number of intermetallic compounds which exist, and because of the time and expense involved in characterizing potential material systems, a common evolving theme is that research must be limited to those systems which demonstrate some reasonable potential for success. Potential materials must be evaluated

with respect to critical material properties to determine if they warrant further investigation. New structural applications envision operating temperatures up to 1600°C. Several selection criteria have been recommended by Anton et al. for determining candidate material systems [2]. Adequate oxidation resistance is required, and intermetallics with substantial concentrations of aluminum, chromium, or silicon are desirable since they are more likely to form protective scales. Materials should possess a compositional homogeneity range. The ability to vary stoichiometry as well as incorporate interstitial additions is important. In order to achieve useful strength and creep resistance, melting points in excess of 1600°C are required. Generally, single phase materials have an upper operating temperature of between 0.5-0.7T<sub>m</sub> [7]. This necessitates compounds with melting points between 1600-2700°C. Strength to density, or specific strength, must be considered. In order to minimize centrifugal stresses, density should not exceed that of current commercial nickel based superalloys (8.5 g/cm<sup>3</sup>).

Many materials in the general class of intermetallic silicides meet these initial requirements. More specifically, the class of transition metal silicides A<sub>5</sub>Si<sub>3</sub> (A=Ti, Nb, Ta, Mo, Zr, Cr, W) are particularly interesting. The compound Ti<sub>5</sub>Si<sub>3</sub> has received some attention in the past few years. This material is particularly attractive because of its high melting point of 2130°C, adequate oxidation resistance, and low density of 4.32 g/cm<sup>3</sup>. Mo<sub>5</sub>Si<sub>3</sub> is also a candidate high temperature structural material. Unlike MoSi<sub>2</sub>, it is expected to have good high temperature creep resistance due to a large and complex unit cell and expected large Burger's vector. Limited experimental data supports this assumption [8].

Ti<sub>5</sub>Si<sub>3</sub> and Mo<sub>5</sub>Si<sub>3</sub> based materials are being investigated in parallel to determine their usefulness as high temperature materials. Both compounds present certain problems that make them undesirable for use as stoichiometric, undoped materials. For example,

$\text{Mo}_5\text{Si}_3$  has poor oxidation resistance, in contrast to the adequate oxidation resistance of  $\text{Ti}_5\text{Si}_3$  up to  $800^\circ\text{C}$ . On the other hand,  $\text{Ti}_5\text{Si}_3$  shows considerable transgranular microcracking on cooling from consolidation temperatures, while  $\text{Mo}_5\text{Si}_3$  is more forgiving. The microcracking is due to high thermal expansion anisotropy. For these reasons, the two materials were investigated using slightly different approaches, as detailed below.

## II. Literature Review

### 1. Phase Diagrams

While similar in many respects, the refractory metal-silicon and transition metal silicon systems also exhibit notable differences. Refractory (Mo, W, Ta) metals form only a few compounds with silicon along the binary composition range. Figure 1 shows the molybdenum-silicon phase diagram, with small terminal solid solubility ranges and three compounds. Of the three compounds, only  $\text{MoSi}_2$  has been well characterized; it is well known for excellent oxidation resistance in the  $700^\circ\text{C}$ - $1700^\circ\text{C}$  range.  $\text{MoSi}_2$ , however, is not used as a high temperature structural material in the monolithic state, since it has a high creep rate above  $1000^\circ\text{C}$  [9].  $\text{Mo}_5\text{Si}_3$  has a homogeneity range of about 3 at.% silicon. A high melting eutectic is formed with  $\text{MoSi}_2$  at 54 at.% silicon.

Figure 2 shows the titanium-silicon phase diagram. This system contains five intermetallic compounds. All compounds except  $\text{Ti}_5\text{Si}_3$  exist as line compounds.  $\text{Ti}_5\text{Si}_3$  is the most refractory compound and congruently melts within a 2.5 at.% silicon homogeneity range.

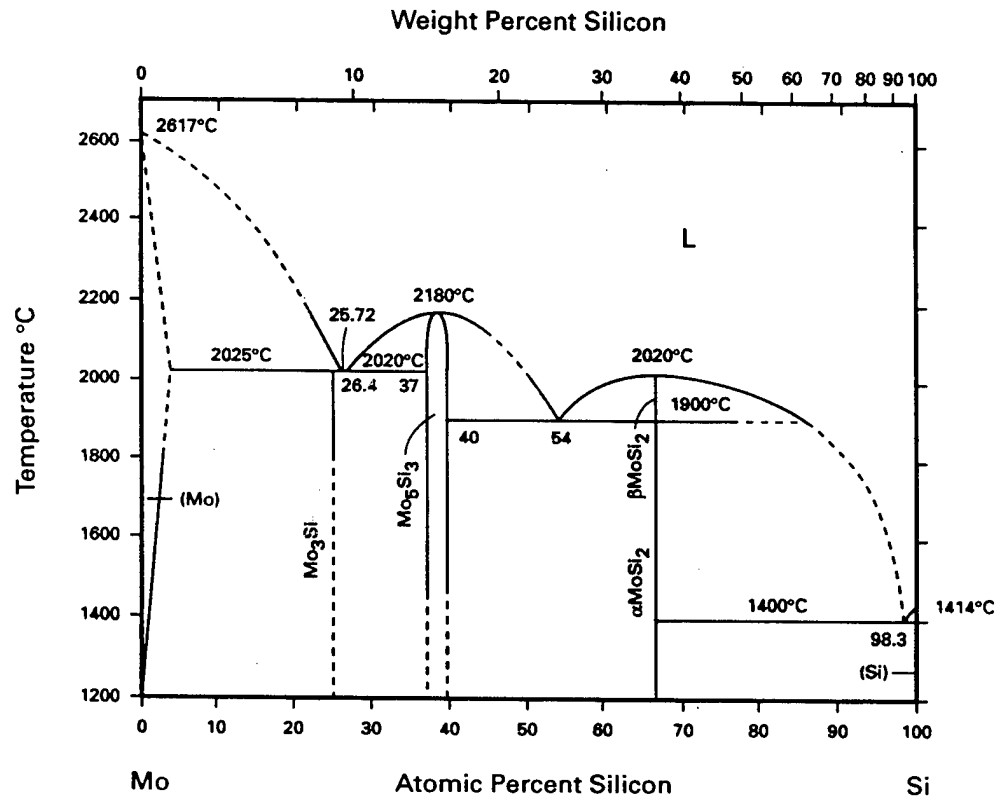


Figure 1: Mo-Si binary phase diagram [10].

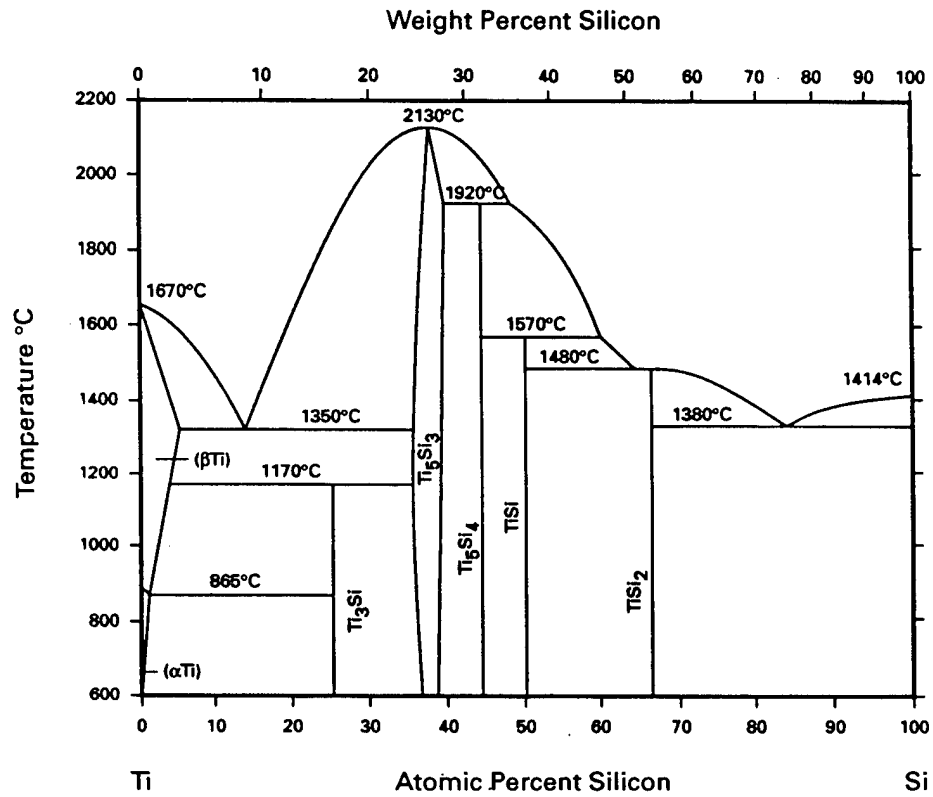


Figure 2: Ti-Si binary phase diagram [10].

## 2. Crystal Structure of $A_5Si_3$ Compounds

Transition metal silicides of the form  $A_5Si_3$ , which belong to the more general class of  $A_5X_3$  phases, crystallize into three structures: tetragonal  $Cr_5B_3$ -type ( $T_2$  phases), tetragonal  $W_5Si_3$ -type ( $T_1$  phases), and hexagonal  $Mn_5Si_3$ -type [11]. During the preparation and characterization of transition metal silicides, Nowotny and collaborators [12,13] observed that different samples of the same  $A_5Si_3$  composition crystallized in both the  $W_5Si_3$  and  $Mn_5Si_3$  structures. As compositional purity was increased, many pure  $M_5Si_3$  binary phases crystallized in the tetragonal  $W_5Si_3$  structure. Small concentrations of Z atoms ( $Z=B, C, N, O$ ) were found to stabilize a ternary hexagonal  $A_5Si_3Z_x$  phase which is isomorphous with the  $Mn_5Si_3$  structure. These interstitially stabilized  $A_5Si_3Z_x$  phases were coined Nowotny phases.

The  $Mn_5Si_3$ -type structure is characterized by chains of metal and silicon atoms in the [001] or c-direction. An [001] projection of the unit cell is shown in Figure 3. Mn1 atoms form linear chains at  $(1/3, 2/3, z)$  and  $(2/3, 1/3, z)$  with  $z=0, 1/2$ . Mn2 atoms form chains of trigonal antiprisms at the corners of the unit cell with  $z=1/4, 3/4$ . Silicon atoms (Si) form trigonal layers which create chains of irregular trigonal antiprisms at  $z=1/4, 3/4$ . The  $Mn_5Si_3$  structure incorporates a wide variety of atoms in the interstitial sites at the corners of the unit cell [14,15,16,17] at  $z=0, 1/2$ . Linear chains of interstitial atoms occupy the centers of trigonal antiprisms of the Mn2 atoms. In Nowotny phases, the stabilizing element Z occupies these interstitial sites. Substitution of Si atoms for Mn1 atoms or Z atoms for Si atoms may also occur [11].

$Mo_5Si_3$ , in the absence of impurities, has a body centered tetragonal crystal structure of space group  $I4/mcm$  (No. 140). Synthesis of  $Mo_5Si_3$  was first claimed in 1950 by Brewer et al. [18] who identified the stoichiometry of the compound as  $Mo_3Si_2$ . In 1955, Aronsson [19] identified the correct stoichiometry and crystal structure as



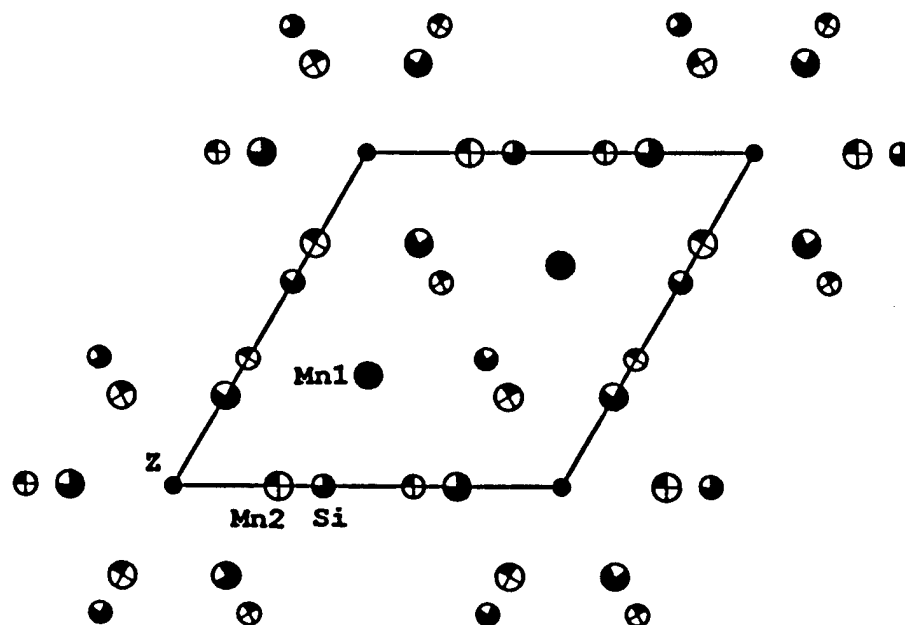


Figure 3: [001] projection of the Mn<sub>5</sub>Si<sub>3</sub>-type unit cell. Atoms are shaded according to their height.

tetragonal  $W_5Si_3$ -type, and another neutron diffraction study [20] confirmed the  $W_5Si_3$  structure. The ternary Mo-Si-C phase, which has the stabilized  $Mn_5Si_3$ -type hexagonal structure, was reported in 1954 by Nowotny et al. [12] Parthe' et al. [21] did a neutron diffraction study of  $Mo_{4.8}Si_3C_{0.6}$  in 1965 and confirmed the  $Mn_5Si_3$  structure type.

The true structure of  $Ti_5Si_3$  is less clear. It has not been established whether  $Ti_5Si_3$  is a true pure binary  $Mn_5Si_3$  structure or a Nowotny phase. In 1951 Pietrokosky and Duwez [22] characterized  $Ti_5Si_3$  as possessing the hexagonal  $Mn_5Si_3$ -type structure. Hexagonal lattice parameters,  $a=7.444 \text{ \AA}$  and  $c=5.143 \text{ \AA}$ , were measured by Quakernaat and Visser [23] from a relatively pure sample which fit the theoretical composition and showed an impurity content of carbon, boron, nitrogen, and oxygen of less than 500 ppm, 1000 ppm, 10000 ppm, and 1000 ppm, respectively. They were unable to determine the presence or absence of nitrogen below 10000 ppm and concluded that  $Ti_5Si_3$  might be a nitrogen stabilized Nowotny phase. Appropriate interstitial additions may significantly affect the bonding of the structure to change the thermal expansion, oxidative, and mechanical behavior.

### 3. Mechanical Properties

Mechanical properties data for  $A_5Si_3$  family compounds is scant. In 1991, Anton and Shah [8] included  $Mo_5Si_3$  in a group of seven intermetallic compounds selected for testing as high temperature structural materials. The results of these tests are shown in Table I. Note the low compressive creep rate of  $Mo_5Si_3$  at  $1200^\circ\text{C}$ , measured as  $4 \times 10^{-8} \text{ sec}^{-1}$ . The creep rate of  $MoSi_2$  in the same work was measured as  $2.1 \times 10^{-7} \text{ sec}^{-1}$ .  $Mo_5Si_3$  also exhibited considerable ductility in this study, and an anomalously low activation energy for creep. The ultimate tensile strength of the material was very low, with failure occurring by transgranular cracking. The ductile behavior of  $Mo_5Si_3$  in this

test may be due to the microstructure of the arc cast test specimens. Although no grain size information was provided by the authors, arc melting generally produces a large grain (100-1000  $\mu\text{m}$ ) material. Large grained  $\text{Mo}_5\text{Si}_3$  may crack transgranularly on cooling due to thermal expansion anisotropy. Transgranular fracture has been observed in  $\text{Mo}_5\text{Si}_3$  prepared in this work with an average grain size greater than 15  $\mu\text{m}$ . It is possible that the measured properties presented in Table I represent the properties of microcracked specimens.

Kim et al. [24] has derived an expression for estimating the critical grain size for cracking in materials with anisotropic thermal expansion. The degree of thermal expansion anisotropy in  $\text{Mo}_5\text{Si}_3$  has not been measured, so this analysis can not yet be applied to  $\text{Mo}_5\text{Si}_3$ . However, for  $\text{Ti}_5\text{Si}_3$ , we calculate that average grain size larger than 4  $\mu\text{m}$  will induce internal strain large enough to cause microcracking.

Table I. Mechanical Properties for Arc Cast  $\text{Mo}_5\text{Si}_3$  [8]

Property	Value	Notes
fracture strength	12 MPa	tensile
creep exponent (n)	1.9	1200°C
creep rate	$4 \times 10^{-8} \text{ sec}^{-1}$	1200°C, 69 MPa
creep activation energy	10 kcal/mole	1200°C, 69 MPa
ductile to brittle transition	none found up to 1200°C	ductility noted may be due to microcracking

Liu et al. [25] observed extensive microcracking for arc-melted and cast  $\text{Ti}_5\text{Si}_3$ . A slight decrease in microcracking was achieved by adjusting alloy composition to Ti-33Si-4Zr-4Cr. Cast specimens, even with a post HIP process, exhibited low fracture strengths of  $< 100$  MPa with transgranular fracture. Frommeyer et al. [26] tested HIPed monolithic  $\text{Ti}_5\text{Si}_3$  and a unidirectionally solidified  $\alpha$ -Ti- $\text{Ti}_5\text{Si}_3$  eutectic alloy. Dramatic improvement in room temperature fracture toughness was observed for the eutectic alloy. Bulk  $\text{Ti}_5\text{Si}_3$  toughness was about  $2 \text{ MPa} \cdot \sqrt{\text{m}}$ , and this increased to  $12 \text{ MPa} \cdot \sqrt{\text{m}}$  for the eutectic alloy. Monolithic  $\text{Ti}_5\text{Si}_3$  was brittle below the observed BDTT of  $850\text{-}950^\circ\text{C}$ . Above  $1000^\circ\text{C}$   $\text{Ti}_5\text{Si}_3$  deformed plastically, and from  $1000$  to  $1500^\circ\text{C}$  flow stress decreased from  $1048$  to  $50$  MPa. The eutectic alloy showed a room temperature flow stress of about  $1080$  MPa which decreased to  $150$  MPa at  $1000^\circ\text{C}$ . Monolithic  $\text{Ti}_5\text{Si}_3$  exhibited power law creep behavior ( $n=3$ ) with creep stress decreasing from  $240$  to  $44$  MPa at a strain rate of  $10^{-7} \text{ sec}^{-1}$  between  $900$  and  $1200^\circ\text{C}$ .

#### 4. Oxidation Resistance

$\text{Ti}_5\text{Si}_3$  and  $\text{Mo}_5\text{Si}_3$  differ considerably in oxidation behavior.  $\text{Ti}_5\text{Si}_3$  has the potential to form a duplex oxide scale composed of both titania and silica, both of which can act as passivating layers. In contrast, the formation of molybdenum oxide on  $\text{Mo}_5\text{Si}_3$  is undesirable and can lead to catastrophic oxidation. An early investigation of oxidation in the Ti-Si system was by Paine et al. [27], who tested sintered plates in dry air at  $1260^\circ\text{C}$  for  $100$  hours. Good oxidation resistance was reported in spite of the inability to synthesize single-phase compositions.  $\text{TiSi}_2$  was reported to experience mass gains of  $2.2$  and  $4.4 \text{ mg/cm}^2$  at  $1260$  and  $1370^\circ\text{C}$ . Anton and Shah [28] performed cyclical oxidation testing of arc-cast  $\text{Ti}_5\text{Si}_3$  at  $1149^\circ\text{C}$ . After  $50$  hours the mass gain was  $30.76 \text{ mg/cm}^2$ . An external brown oxide was observed, and x-ray diffraction of the oxidation products

indicated 75-80 vol%  $\text{TiO}_2$  (rutile), 20 vol% hexagonal  $\text{Ti}_5\text{Si}_3$  and < 5vol% tetragonal  $\text{SiO}_2$  ( $\alpha$ -cristobalite). Liu et al. [25] produced alloys of Ti-29Si-8Cr, Ti-33Si-4Cr-4Zr, and Ti-36.5Si by arc melting and casting. Isothermal oxidation at 800°C in air showed parabolic oxidation for the last two alloys with a mass gain of 0.88 and 0.98 mg/cm<sup>2</sup> at 120 hours. The alloy of lowest silicon content showed linear oxidation with a mass gain of 1.8 mg/cm<sup>2</sup> at 120 hours. All three alloys formed adherent scales.

There has been widespread interest in the mechanism of oxidation resistance of  $\text{MoSi}_2$  [29,30,31,32,33,34]. It is expected that the same basic oxidation mechanisms are operative for  $\text{Mo}_5\text{Si}_3$ . Although  $\text{MoSi}_2$  exhibits excellent oxidation resistance at temperatures greater than 800°C in air, it exhibits catastrophic oxidation failure at certain combinations of temperature and oxygen partial pressure. This low temperature catastrophic oxidation is known as pest oxidation. The temperature range for pest oxidation is a function of extrinsic specimen properties. It has been reported that dense polycrystalline and single crystal  $\text{MoSi}_2$  samples are immune to pest [34].

Bartlett et al. [35] plotted regions of active and passive oxidation of  $\text{Mo}_5\text{Si}_3$  based on experimental data and calculation of the rate at which silicon from the substrate silicide is made available for oxidation. Bartlett's analysis shows that at temperatures below 1000°C, passive oxidation occurs only at oxygen partial pressures below 100 Pa. As temperature is increased to 1600°C, a dense oxide layer is formed at much higher oxygen partial pressure. The same work reports that  $\text{Mo}_5\text{Si}_3$  did not form a protective scale in 101 kPa of oxygen at temperatures from 484°-1600°C. Shah and Anton [8] reported catastrophic oxidation of arc cast  $\text{Mo}_5\text{Si}_3$  within 20 cycles to 1149°C. The oxidation product was  $\alpha$ -cristobalite.

### III. Experimental Procedure

$\text{Ti}_5\text{Si}_3$  [24] and  $\text{Mo}_5\text{Si}_3$  were synthesized by arc-melting the elements under an argon atmosphere using a non-consumable electrode.  $\text{Ti}_5\text{Si}_3$  buttons were milled to -325 mesh ( $<43\text{ }\mu\text{m}$ ) powder in a WC lined impact mill.  $\text{Mo}_5\text{Si}_3$  buttons were milled in a molybdenum lined impact mill with molybdenum media. X-ray diffraction showed that a small amount of  $\text{Mo}_3\text{Si}$  was present, apparently due to silicon volatilization on arc melting. The stoichiometry was adjusted back into the  $\text{Mo}_5\text{Si}_3$  phase field by adding 0.5 wt.% excess silicon. Chemical analysis by laser mass spectrometry, inert gas fusion, and combustion analysis was performed on some materials.

Submicron size intermetallic powders were uniaxially pressed into bars and pellets. The green bodies were coated with boron nitride and HIPed in borosilicate encapsulating glass.  $\text{Ti}_5\text{Si}_3$  was HIPed at 206 MPa and  $1250^\circ\text{C}$ , while  $\text{Mo}_5\text{Si}_3$  was HIPed at 275 MPa and  $1300^\circ\text{C}$ . Both compositions were held at pressure and temperature for 10 hours. A slow cooling rate of  $1\text{-}2^\circ\text{C}/\text{min}$  was used to minimize bulk thermal stresses and reduce cracking. One billet of  $\text{Mo}_5\text{Si}_3$  was reactively HIPed in a tantalum can by consolidating elemental molybdenum and silicon powder at  $1440^\circ\text{C}$  and 275 MPa.

Room temperature hardness and fracture toughness were measured by Vickers indentation technique. Property determinations were made on a minimum of 20 indentations. Fracture toughness was estimated from indentation cracking using the method of Anstis et al. [36]. Ninety-nine percent (99%) confidence intervals were calculated for hardness and fracture toughness. Some preliminary four-point bend tests were performed using an articulating fixture as recommended by Quinn and Morrell [37] and others.

Specimens for thermal oxidation studies were prepared by cutting coupons from HIPed specimens. Samples were suspended in a vertical tube thermogravimetric analyzer and heated at 20°C/min in flowing air.  $\text{Ti}_5\text{Si}_3$  coupons were polished through 0.05  $\mu\text{m}$   $\text{Al}_2\text{O}_3$  abrasive and oxidized in synthetic 'zero' air (mixture of 79% $\text{N}_2$ -21% $\text{O}_2$ , free of  $\text{H}_2\text{O}$ ).  $\text{Mo}_5\text{Si}_3$  specimens were polished through 0.3  $\mu\text{m}$   $\text{Al}_2\text{O}_3$  abrasive and oxidized in flowing 'breathing quality' air. Continuous isothermal oxidation was measured for up to 400 hours. ESCA depth profiles were performed on some oxidized specimens. Depth profiling was performed using a 4 kV  $\text{Ar}^+$  ion mill. Etch rates of about 15Å/min for  $\text{SiO}_2$  on Si are expected.

#### IV. Results

##### 1. Microstructure and Mechanical Properties

X-ray diffraction patterns of  $\text{Ti}_5\text{Si}_3$  based materials indicate that the powders were essentially single phase  $\text{Ti}_5\text{Si}_3$  with the  $\text{Mn}_5\text{Si}_3$ -type structure. Minor amounts of impurity are probably present since each pattern contained a few unidentified peaks. This is expected since arc-melting is a particularly aggressive method of synthesis. Oxygen is particularly difficult to eliminate. Corbett and collaborators [16] have shown that reactive sintering for extended periods at temperature in sealed, non-reactive containers is required to synthesize relatively pure samples of  $\text{Mn}_5\text{Si}_3$ -type materials.

Alloys of the composition  $\text{Ti}_5\text{Si}_3\text{Z}_x$  were synthesized by arc-melting where  $\text{Z}=\text{B}$ ,  $\text{C}$ ,  $\text{N}$ ,  $\text{O}$  and  $x=0.25$ ,  $0.50$ ,  $0.75$ . Recent determinations of the  $\text{Ti-Si-Z}$  ( $\text{Z}=\text{C}$ ,  $\text{N}$ ,  $\text{O}$ ) phase diagrams [38,39,40] show that  $\text{Ti}_5\text{Si}_3$  has an appreciable solubility for these interstitials. These phase diagrams and our diffraction data indicate that  $\text{Ti}_5\text{Si}_3$  can accommodate several at.% carbon, nitrogen, or oxygen. Additionally, a silicon homogeneity range of a few at% is still maintained. The effect of these additions on the

thermal expansion anisotropy and oxidative properties of  $\text{Ti}_5\text{Si}_3$  is currently being investigated.

Table II gives qualitative phase analysis by x-ray diffraction of some  $\text{Mo}_5\text{Si}_3$  based materials produced. As carbon is added to  $\text{Mo}_5\text{Si}_3$ , the tetragonal  $\text{W}_5\text{Si}_3$ -type structure forms a two phase microstructure with the hexagonal  $\text{Mn}_5\text{Si}_3$ -type Nowotny phase. At one formula unit of carbon, the material is single phase hexagonal  $\text{Mn}_5\text{Si}_3$ . Relatively large boron additions do not stabilize the hexagonal Nowotny phase. Boron additions to  $\text{Mo}_5\text{Si}_3$  up to one formula unit cause formation of a two phase microstructure consisting of tetragonal  $\text{Mo}_5\text{Si}_3$  and tetragonal  $\text{MoB}$ .

Figure 4 shows the microstructure of HIPed  $\text{Ti}_5\text{Si}_3$  samples made from two powders impact milled for differing times [24]. The large grain sample was made from

Table II: Qualitative X-Ray Phase Analysis of Arc Melted  $\text{Mo}_5\text{Si}_3(\text{B,C})_x$

Composition	Phase Analysis <sup>1</sup> (qualitative)
$\text{Mo}_{2.6}\text{Si}_3$	$\text{Mo}_5\text{Si}_3$ (T) / $\text{MoSi}_2$ eutectic
$\text{Mo}_{4.93}\text{Si}_3$	$\text{Mo}_5\text{Si}_3$ (T)
$\text{Mo}_5\text{Si}_3$	$\text{Mo}_5\text{Si}_3$ (T) + trace $\text{Mo}_3\text{Si}$
$\text{Mo}_5\text{Si}_3\text{C}_{0.1}$	$\text{Mo}_5\text{Si}_3$ (H + T)
$\text{Mo}_5\text{Si}_3\text{C}_{0.5}$	$\text{Mo}_5\text{Si}_3$ (H + T)
$\text{Mo}_5\text{Si}_3\text{C}$	$\text{Mo}_5\text{Si}_3$ (H)
$\text{Mo}_5\text{Si}_3\text{C}_{1.5}$	not determined
$\text{Mo}_5\text{Si}_3\text{B}_{0.1}$	$\text{Mo}_5\text{Si}_3$ (T) + trace $\text{MoB}$
$\text{Mo}_5\text{Si}_3\text{B}_{0.5}$	$\text{Mo}_5\text{Si}_3$ (T) + $\text{MoB}$
$\text{Mo}_5\text{Si}_3\text{B}$	$\text{Mo}_5\text{Si}_3$ (T) + $\text{MoB}$

<sup>1</sup> T =  $\text{W}_5\text{Si}_3$  type; H =  $\text{Mn}_5\text{Si}_3$  type



HIPed  $\text{Ti}_5\text{Si}_3$  powders milled to -325 mesh. The fine grained sample was made from powder milled an additional six hours after sieving -325 mesh. The -325 mesh sample has an average grain size of 12  $\mu\text{m}$ . Transgranular microcracking is evident in larger grains, indicating that grain boundaries are stronger than one or more crystallographic directions within the grains. Further milling of the powder for six hours produced a microcrack-free sample on HIPing with an average grain size of 1-2  $\mu\text{m}$ . The Vicker's hardness of the fine grained, microcrack free sample was  $17.1 \pm 0.7$  GPa ( $1749 \pm 68$   $H_V$ ) under 1.96 N indentation load. The Vicker's hardness of the larger grained, microcracked sample was  $9.1 \pm 0.5$  GPa ( $924 \pm 56$   $H_V$ ) under identical load. Some hardness values reported in the literature are  $968 \pm 30$   $H_V$  [26] and  $1283 \pm 67$   $H_V$  [41]. The values obtained in this study were lower for the microcracked specimen and significantly higher for the non-microcracked specimen.

The microcracking observed in the larger grained  $\text{Ti}_5\text{Si}_3$  is believed to be caused by anisotropy in the thermal expansion and elastic modulus which results from the hexagonal symmetry of  $\text{Ti}_5\text{Si}_3$ . Thermal expansion anisotropy is a potential source of microcracking during thermal cycling [42]. For a noncubic polycrystalline body, microscopic stresses develop during cooling from the processing temperature as a result of the thermal expansion anisotropy and crystallographic orientation mismatch across grain boundaries. This thermal expansion anisotropy was measured by the method of high temperature x-ray diffraction [43]. The thermal expansion coefficients along the a-axis and c-axis are approximately constant over the temperature range of 298-873K and are:  $\alpha_a = 8.7 \pm 0.2$  ppm/K and  $\alpha_c = 20.4 \pm 0.4$  ppm/K. No values of  $\alpha_a$  and  $\alpha_c$  are available in the literature for comparison. The bulk CTE value estimated from x-ray diffraction is 11.6 ppm/K, compared to the literature value of 11 ppm/K for 450-1350K [44].

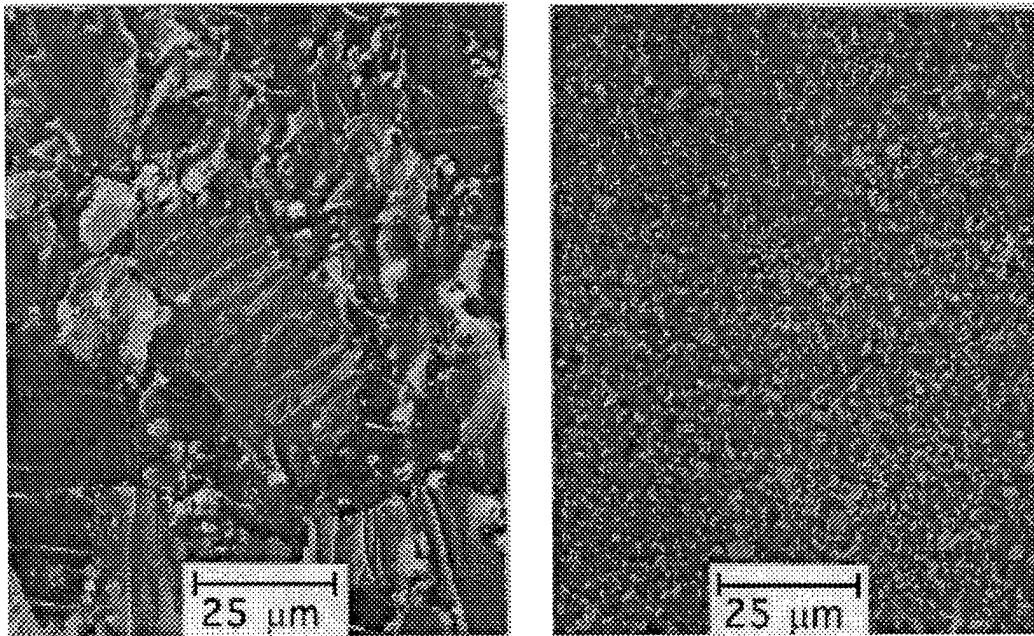


Figure 4: Polarized light micrographs of HIPed  $\text{Ti}_5\text{Si}_3$ . (a) -325 mesh powder  
(b) six hour milled, -325 mesh powder

In order to determine the effect of addition of interstitial atoms on the thermal expansion anisotropy, the thermal expansion of  $\text{Ti}_5\text{Si}_3\text{C}_{0.9}$  was also measured [43]. The addition of carbon to  $\text{Ti}_5\text{Si}_3$  caused expansion in the room temperature c-parameter and contraction in the a-parameter. The CTE of  $\text{Ti}_5\text{Si}_3\text{C}_{0.9}$  from 298-873K along the a-axis and c-axis is  $9.4 \pm 0.3$  and  $17.9 \pm 0.6$  ppm/K, respectively. Compared to  $\text{Ti}_5\text{Si}_3$  ( $\alpha_a = 8.7$  and  $\alpha_c = 20.4$  ppm/K), the decrease in  $\alpha_c$  and increase in  $\alpha_a$ , while causing little change in the overall bulk behavior, significantly reduced the CTE anisotropy from  $\Delta\alpha = 11.7$  to  $\Delta\alpha = 8.5$ . While still a significant CTE anisotropy, reductions of this type are expected to reduce the development of residual stresses during cooling from the processing temperature. The extent of microcracking should decrease, thus increasing the ability to process highly anisotropic  $\text{Mn}_5\text{Si}_3$ -type materials.

No microcracking is seen in HIPed  $\text{Mo}_5\text{Si}_3$  for grain size smaller than 15  $\mu\text{m}$ . The addition of carbon to  $\text{Mo}_5\text{Si}_3$  appears to increase hardness, as seen in Table III, which shows microhardness (9.8 N load) values for identically prepared specimens of similar grain size. The hardness increase may correspond to an increase in the amount of carbon stabilized  $\text{Mn}_5\text{Si}_3$  structure present. At one formula unit of carbon ( $\text{Mo}_5\text{Si}_3\text{C}$ ) the material is 100% hexagonal  $\text{Mn}_5\text{Si}_3$  phase, and the highest hardness values are obtained. As the amount of carbon increases past one formula unit, hardness values again decrease. Maloy et al. [45] made a 2 weight percent carbon addition to  $\text{MoSi}_2$  and recorded improved fracture toughness and hardness values. They attributed these gains to the reduction of  $\text{SiO}_2$  present in the grain boundaries of  $\text{MoSi}_2$  and to the presence of  $\text{SiC}$  in the microstructure. Density values are given in Table III as percent of measured pycnometric powder density, since density has a large bearing on hardness. Fracture toughness values are similar to those quoted for  $\text{MoSi}_2$  [46] for the indentation technique. Values of Young's modulus used to calculate fracture toughness were estimated from the

literature [47]. The modulus of the carbon doped compositions was unknown, and so fracture toughness values were not calculated. The partially lamellar  $\text{Mo}_5\text{Si}_3/\text{MoSi}_2$  microstructure and the two phase  $\text{Mo}_5\text{Si}_3\text{B}$  material may exhibit a slight increase in fracture toughness over  $\text{Mo}_5\text{Si}_3$ . This is not completely clear, however, due to the difference in porosity between the two materials and the uncertainty in Young's modulus.

Preliminary 4-point bend tests were completed on  $\text{Mo}_5\text{Si}_3$  specimens that were reactively HIPed in a tantalum can. The HIPed billet had a bulk density of 72.5% of theoretical. Specimens were loaded in 4-point bending at a rate of 1.0 mm/minute. Average strength of the bars was 92.4 MPa, with 95% confidence interval limits of 80-105 MPa. As expected in these initial 'trial runs' the specimens have low strength due to low specimen density. The strength of these specimens does, however, show great improvement over the value of 12.5 MPa as measured in tension by Anton and Shah [8] for arc cast specimens.

Table III. Micro-Indentation Data for  $\text{Mo}_5\text{Si}_3(\text{B,C})_x$  at 9.8 N Load

Composition	Hardness (GPa)	Density (% theoretical)	$K_{Ic}$ ( $\text{MPa}\cdot\text{m}^{1/2}$ )
$\text{Mo}_5\text{Si}_3$	$12.0\pm0.25$	97.4	$2.9\pm0.36$
$\text{Mo}_5\text{Si}_3\text{C}_{0.1}$	$12.0\pm0.25$	85.6	
$\text{Mo}_5\text{Si}_3\text{C}_{0.5}$	$12.2\pm0.28$	80.6	
$\text{Mo}_5\text{Si}_3\text{C}$	$12.8\pm0.28$	85.3	
$\text{Mo}_5\text{Si}_3\text{C}_{1.5}$	$11.7\pm0.37$	a	
$\text{Mo}_5\text{Si}_3\text{B}$	$11.8\pm0.30$	84.4	$3.4\pm0.17$
$\text{Mo}_5\text{Si}_3/\text{MoSi}_2$ eutectic	$11.4\pm0.15$	87.8	$3.5\pm0.19$

<sup>a</sup>Crystal structure not determined, theoretical density unknown.

## 2. Oxidation Resistance

Kinetic data for the oxidation of four  $\text{Mo}_5\text{Si}_3$  based materials at  $1000^\circ\text{C}$  in flowing air are summarized in Table IV. A comparison plot of the oxidation of the four compositions is shown in Figure 5, which includes the initial ramping up to temperature at  $20^\circ\text{C}/\text{min}$  (the first 50 minutes of plot). The oxidation of  $\text{Mo}_5\text{Si}_3\text{B}$  is shown in Figure 6, with features typical of the four compositions studied. Note that initially the specimen exhibits a mass gain, followed by a rapid mass loss, followed by a slower steady state mass change. The initial transient behavior is due to formation and volatilization of molybdenum trioxide, which has a significant vapor pressure starting at  $700^\circ\text{C}$  [48].  $\text{MoO}_3$  crystals, identified by x-ray diffraction, are found to condense in the cooler regions of the TGA apparatus. As  $\text{MoO}_3$  volatilizes, it leaves areas of higher silicon activity that oxidize to  $\text{SiO}_2$ .

Table IV: Kinetics of  $\text{Mo}_5\text{Si}_3(\text{B,C})_x$  Oxidation

Composition	Kinetic Model	K <sup>1</sup>	Run Time(hrs)
$\text{Mo}_5\text{Si}_3$	linear	$-3.2 \times 10^{-2}$	80
$\text{Mo}_5\text{Si}_3\text{B}$	parabolic	$+4.0 \times 10^{-4}$	200
Eutectic	linear	$-1.0 \times 10^{-3}$	240
$\text{Mo}_5\text{Si}_3\text{C}_{0.1}$	linear	-0.690	40

<sup>1</sup> This is in units of  $\text{mg}/(\text{cm}^2 \text{ hr})$  for linear model  
and  $\text{mg}^2/(\text{cm}^4 \text{ hr})$  for parabolic model

$\text{Mo}_5\text{Si}_3$  shows linear oxidation kinetics, indicating that the oxidation is reaction rate controlled. An SEM micrograph of the oxide scale (Figure 7) shows that it is cracked and porous and may not be acting as a complete diffusion barrier to oxygen. At  $800^\circ\text{C}$  under the same oxidizing conditions  $\text{Mo}_5\text{Si}_3$  exhibited severe pest after only 16 hours. The oxidation of  $\text{Mo}_5\text{Si}_3\text{C}_{0.1}$  in flowing air at  $1000^\circ\text{C}$  was also catastrophic. The specimen

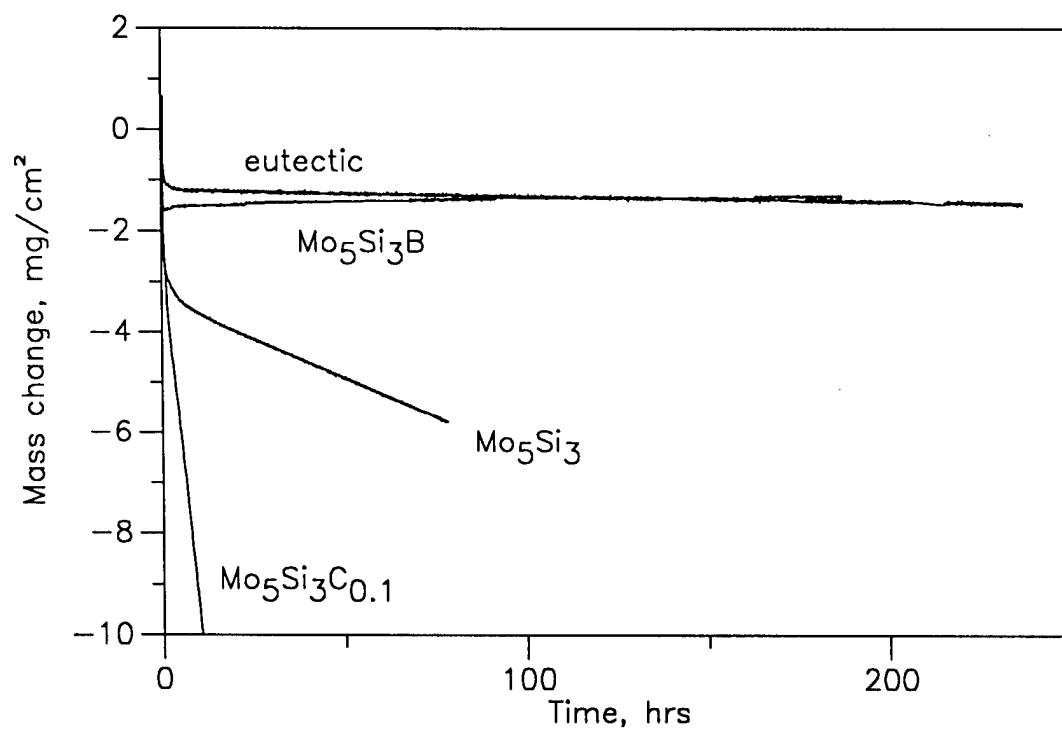


Figure 5. Oxidation of  $\text{Mo}_5\text{Si}_3$ -based compositions in flowing breathing air ( $1000^\circ\text{C}$ ). Note initial mass gain, then loss due to formation and volatilization of molybdenum oxides. See Table IV for kinetic data.

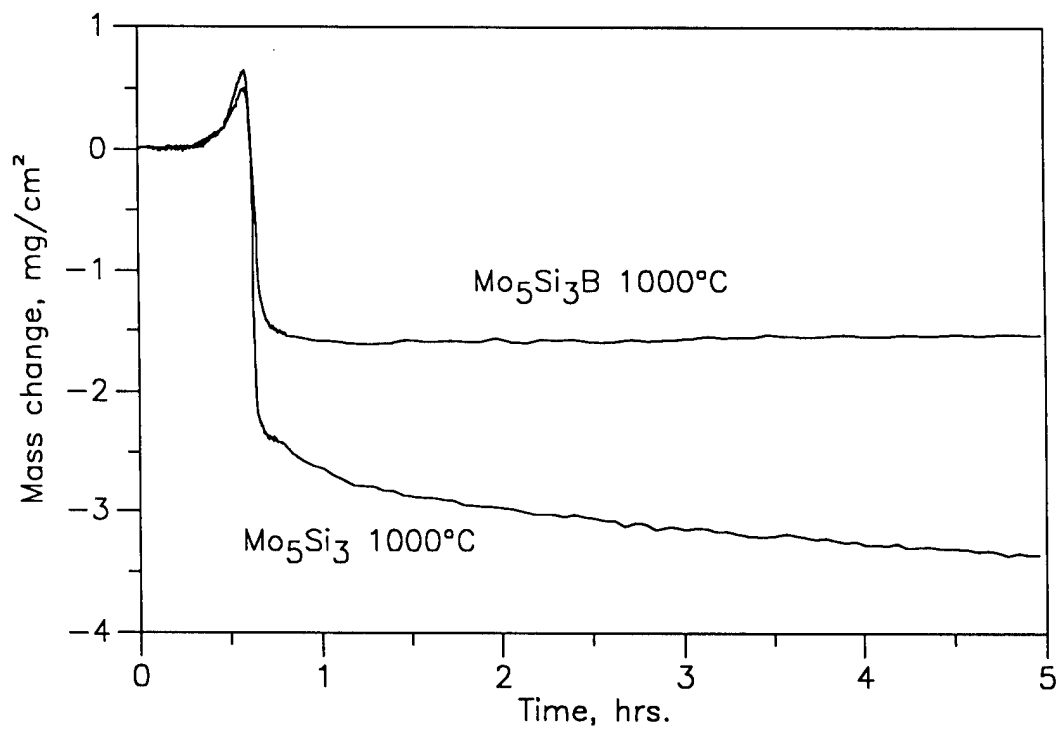
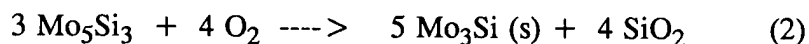
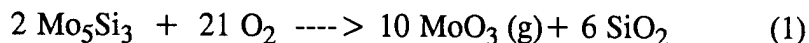


Figure 6: Oxidation of  $\text{Mo}_5\text{Si}_3\text{B}$  and  $\text{Mo}_5\text{Si}_3$  showing features typical of all compositions investigated.

exhibited fast linear kinetics, and a large section of scale spalled from the specimen after 40 hours. The scale was determined to be  $\alpha$ -cristobalite by x-ray diffraction.

The  $\text{Mo}_5\text{Si}_3/\text{MoSi}_2$  eutectic composition (54 at% Si) showed improvement in oxidation behavior relative to  $\text{Mo}_5\text{Si}_3$  and  $\text{Mo}_5\text{Si}_3\text{C}_{0.1}$ . The oxidation rate was slow and linear, showing continual mass loss. The steady state mass loss after 200 hours of oxidation is approximately the same as the steady state mass gain of  $\text{Mo}_5\text{Si}_3\text{B}$ , showing a thirtyfold improvement in linear oxidation rate over  $\text{Mo}_5\text{Si}_3$ . The scale formed exhibits small cracks and some porosity.

The oxidation of  $\text{Mo}_5\text{Si}_3$  may proceed by either or both of the net reactions



A mass loss on oxidation indicates that reaction (1) is dominant, while a net mass gain indicates that reaction (2) is operative. Thermodynamically, the free energy of formation of silica is much lower than that of any molybdenum oxide. Given sufficient silicon activity, the Si-SiO<sub>2</sub> equilibria should fix the oxygen partial pressure at the oxidation interface to a value below that required for molybdenum oxidation, and reaction (1) should not occur. Apparently, in the case of the three materials discussed above, silicon activity at the oxidation interface is low. The low silicon activity precludes Si-SiO<sub>2</sub> equilibria from being established, and oxygen partial pressure rises high enough at the interface to form MoO<sub>3</sub>. Volatilization of MoO<sub>3</sub> leads to a mass loss.

The addition of boron to form the nominal composition  $\text{Mo}_5\text{Si}_3\text{B}$  gives a dramatic increase in oxidation resistance, as can be seen in Figures 5 and 6. Note that the specimen



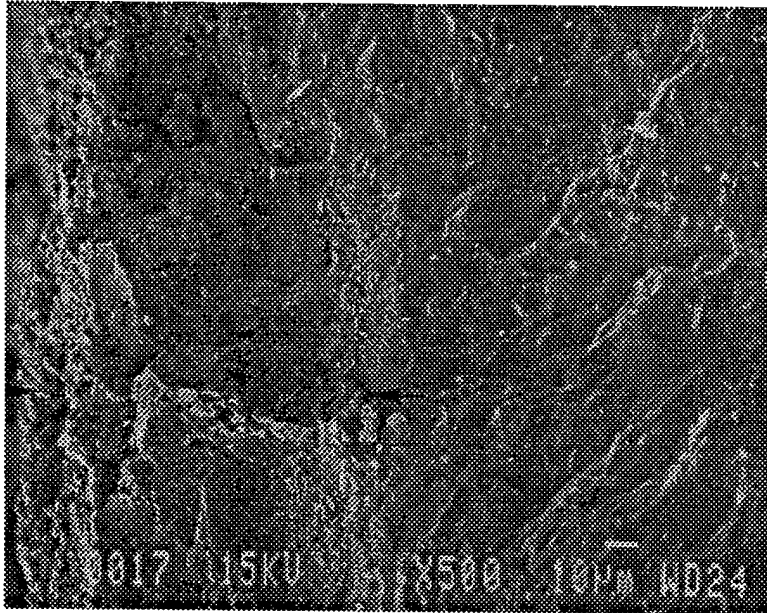


Figure 7: Micrograph of oxidized surface of  $\text{Mo}_5\text{Si}_3$  exposed to flowing air at  $1000^\circ\text{C}$  for 80 hours showing porous nature of scale consistent with linear oxidation kinetics.

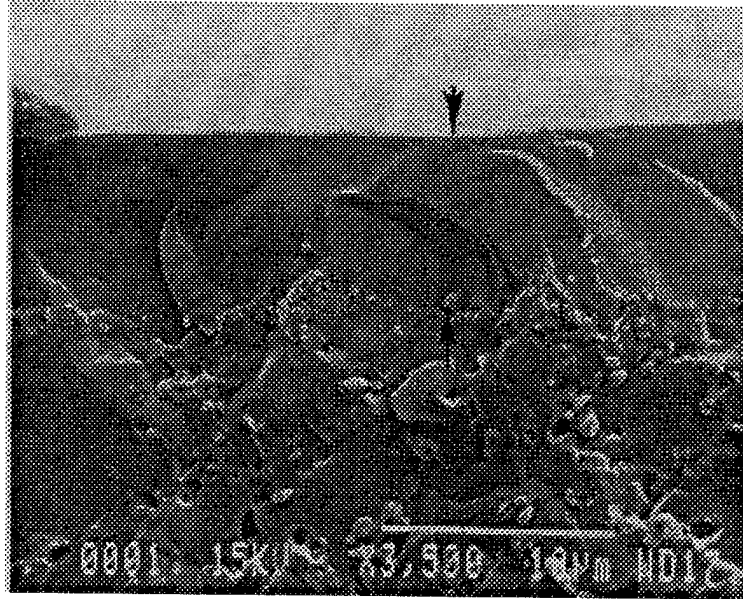


Figure 8: SEM of scale cross section of  $\text{Mo}_5\text{Si}_3\text{B}$  oxidized in flowing air for 410 hours at  $1000^\circ\text{C}$ . Scale shows no cracking or porosity and is quite homogeneous.

exhibits a mass gain in the steady state oxidation regime. The mass gain is parabolic, indicating classic formation of a passive protective scale and a net oxidation reaction similar to equation (2). The parabolic rate constant is  $4 \times 10^{-4} \text{ mg}^2/\text{cm}^4 \cdot \text{hr}$ . After oxidation for 400 hours at  $1000^\circ\text{C}$ , the specimen forms a dark, blue-black scale. The scale formed is about  $6 \text{ }\mu\text{m}$  thick, as shown by a cross sectional view of a fractured oxidation coupon (Figure 8). Examination of the oxidized surface shows largely a featureless glassy phase, with occasional crystalline islands, little porosity, and no cracks. The crystalline areas appear to be of the same composition as the glassy regions when viewed with back scattered electron imaging (BSE).

The mechanism for the improvement in oxidation resistance with boron addition is under investigation. Possible roles that boron may play are as a diffusion aid, as a glass modifier, or as a reactant participating in oxidation equilibria. As an example of a diffusion aid, consider the case of silicon carbide. A small addition of boron allows  $\beta\text{-SiC}$  to be sintered below  $2000^\circ\text{C}$ , two hundred degrees lower than undoped material [49]. The mechanism for the improved sinterability in the case of silicon carbide is suspected to be the creation of carbon vacancies as a result of doping with boron. The increase in the number of carbon vacancies may enhance diffusion [50,51]. In the case of  $\text{Mo}_5\text{Si}_3$ , boron may enable a defect mechanism that allows silicon to diffuse to the reaction interface faster than oxygen diffuses through the scale, insuring adequate silicon activity at the oxidation interface.

An ESCA (electron spectroscopy for chemical analysis) depth profile of oxidized  $\text{Mo}_5\text{Si}_3\text{B}$  gave information on the composition of the scale. ESCA chemical state information is altered during ion etching, but it appears that the scale formed is a borosilicate glass. The depth profile shows that the outer  $15\text{-}30\text{\AA}$  of the scale has low boron concentration. Deeper into the scale, boron concentration (in the oxide state) rises

and levels off. There is no evidence of molybdenum in the scale. The boron depletion in the outer regions of the scale is likely due to volatilization of  $B_2O_3$ , which has a vapor pressure of  $5 \times 10^{-2}$  Pa at  $1000^\circ\text{C}$  [48]. Borosilicate glass has a lower viscosity and higher thermal expansion coefficient than silica glass, and may help to heal any cracks that form due to scale growth stresses or thermal cycling. Mueller et al. [52] found that  $\text{Mo}(\text{Ge},\text{Si})_2$  alloys have better low temperature oxidation resistance than  $\text{MoSi}_2$ . The mechanism is suspected to be a closer thermal expansion match to the substrate intermetallic and decreased viscosity of the silicon-germanium oxide surface layer. It is possible that boron may play the same role as germanium in increasing oxidation resistance of  $\text{Mo}_5\text{Si}_3$ .

Alternatively, boron may be involved in oxidation reaction equilibria similar to that of silicon. The free energy of formation of boron oxide is more negative than that of molybdenum oxide. Thermodynamically, silica will be the first oxide to form. As the silicon supply near the oxidation interface falls and  $P_{\text{O}_2}$  rises, boria will form. The total supply of oxide formers (boron + silicon) in  $\text{Mo}_5\text{Si}_3\text{B}$  is higher than the total supply of oxide formers in  $\text{Mo}_5\text{Si}_3$ . It is less likely that the oxidation interface will become both boron and silicon depleted in  $\text{Mo}_5\text{Si}_3\text{B}$ , keeping  $P_{\text{O}_2}$  low at the oxidation interface and preventing  $\text{MoO}_3$  formation. Additionally, the volume of oxide formed per unit of substrate consumed will be larger due to the boron addition.

Isothermal oxidation of  $\text{Ti}_5\text{Si}_3$  was investigated from  $700$ - $1000^\circ\text{C}$  in dry synthetic air to characterize the development of the complex oxide structure [53]. At each temperature, an experiment was conducted at low and high flow rates of synthetic air. Samples at  $700^\circ\text{C}$  showed mass gains of less than  $0.1 \text{ mg/cm}^2$  after 120 hours. At  $700^\circ\text{C}$ , the external surface was slightly tarnished, indicating the presence of a thin film. ESCA indicated predominately  $\text{TiO}_2$  on the surface plus a minor amount of  $\text{SiO}_2$ . After ion milling for 15 minutes, the Ti peaks (in the oxide chemical state) were still very

strong, indicating that the external  $\text{TiO}_2$  layer is several hundred Angstroms thick. This type of scale development is consistent with the room temperature passivating layer which forms on  $\text{Ti}_5\text{Si}_3$ . Initially, both titania and silica nuclei form due to their similar free energies of formation. However, since diffusion of oxygen in titania is much faster, formation of the titania layer dominates.

For temperatures from 800-1000°C, the samples showed initial transient oxidation followed by assumption of a higher rate of mass gain. This transition to a higher rate occurred at shorter times as temperature increased. At 800°C the external layer contains a mixture of  $\text{TiO}_2$  and  $\text{SiO}_2$ . This was determined by both ESCA and EDS dot mapping. BSE and dot maps of the cross section of an 800°C oxidized sample are shown in Figure 9. A 10-12  $\mu\text{m}$  thick external layer covers a 150  $\mu\text{m}$  thick reaction layer. This external layer consists of essentially a titanium rich matrix phase ( $\text{TiO}_2$ ) with silicon rich phase interspersed ( $\text{SiO}_2$ ). The BSE image shows the unoxidized  $\text{Ti}_5\text{Si}_3$  as the bright phase. Dark dendrites are growing through a lighter colored matrix phase. The X-ray dot map shows that the dendrite phase is rich in Ti and depleted in Si, possibly  $\text{TiO}$ , while the lighter matrix phase is rich in Si and lower in Ti, verified to be  $\text{TiSi}_2$  by electron microprobe analysis (EMPA).  $\text{Ti}_5\text{Si}_3$ (bright phase),  $\text{TiSi}_2$ (dark matrix phase),  $\text{TiO}$ (darker dendrites), and  $\text{TiO}_2/\text{SiO}_2$ (darkest outer layer) match the anticipated atomic number contrast of the BSE image. At 900-1000°C the linear rate constants were not dependent on gas flow. Therefore, surface effects such as supply of oxidant are not a rate-determining step. Oxidation at 1000°C causes growth of a dense outer 10  $\mu\text{m}$  layer of rutile with an underlying stratified morphology consisting of interspersed silica. Spalling was not clearly detected during isothermal oxidation, but during cooling some spalling occurred.

These oxidation kinetics are similar to those observed for titanium [54]. This indicates that the rate controlling mechanisms for oxidation of titanium may be operative for  $\text{Ti}_5\text{Si}_3$ . Oxidation of titanium is characterized by a transition from parabolic to linear kinetics as the external rutile scale begins to spall. Stratified scale growth occurs, and a dense outer rutile layer reaches a limiting thickness of 15-20  $\mu\text{m}$  and begins to spall [55]. Smeltzer [56] explained the linear kinetics as the result of oxide growth by grain boundary diffusion of oxygen through rutile. Kofstad [57] proposed that sintering and grain growth of the rutile scale decreases the relative contribution of grain boundary diffusion. Eventually, volume diffusion dominates and the rate becomes parabolic. However, grain growth decreases plasticity of the scale and thus should decrease scale adherence.

A dramatic improvement in oxidation resistance resulted from the addition of carbon to  $\text{Ti}_5\text{Si}_3$ . Alloys of  $\text{Ti}_5\text{Si}_3\text{C}_x$  were prepared by arc-melting. Table V shows the alloys synthesized and the chemical analysis for carbon content as determined by combustion analysis.

Figure 10 shows the effect of increasing carbon content on oxidative stability at 1000°C compared to fine-grained undoped  $\text{Ti}_5\text{Si}_3$  at 700°C and 800°C. The addition of carbon has significantly lowered the mass gain. After 60 hours, fine-grained undoped

Table V: Chemical Analysis of  $\text{Ti}_5\text{Si}_3\text{C}_x$

Alloy Composition	Sample ID #	C (wt%)
$\text{Ti}_5\text{Si}_3$	C0	484 ppm
$\text{Ti}_5\text{Si}_3\text{C}_{0.25}$	C1	0.921
$\text{Ti}_5\text{Si}_3\text{C}_{0.50}$	C2	2.10
$\text{Ti}_5\text{Si}_3\text{C}_{0.75}$	C3	2.56
$\text{Ti}_5\text{Si}_3\text{C}_{0.90}$	C4	3.10

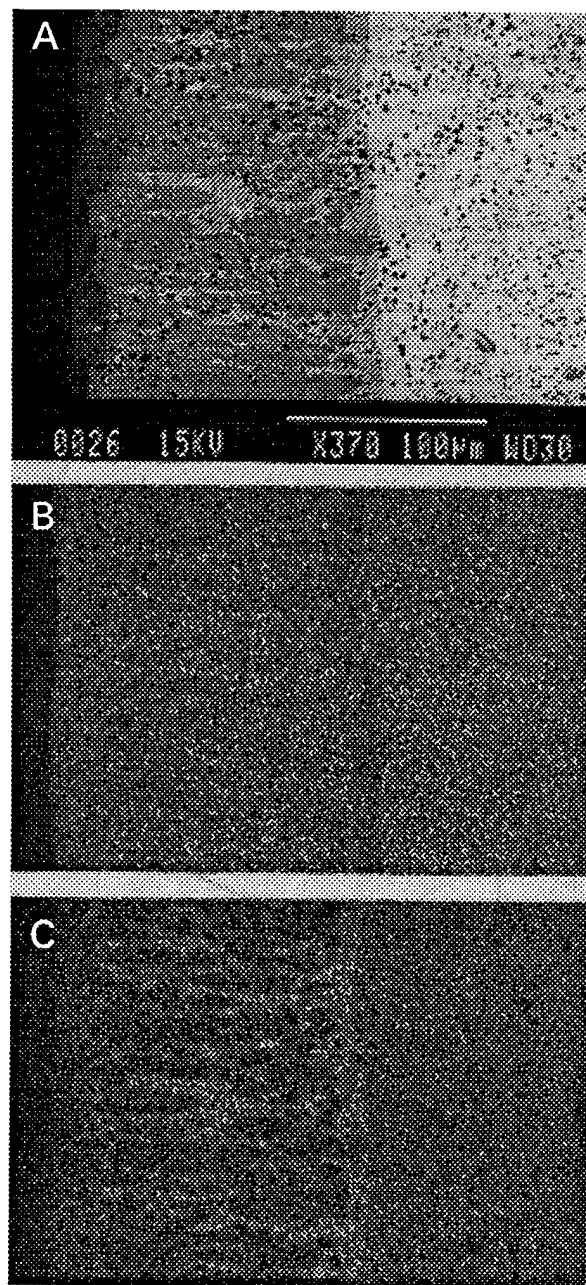


Figure 9: (a) BSE image of  $\text{Ti}_5\text{Si}_3$  oxidized at  $800^\circ\text{C}$  in synthetic air, (b) Titanium EDS dot map, (c) Silicon EDS dot map.

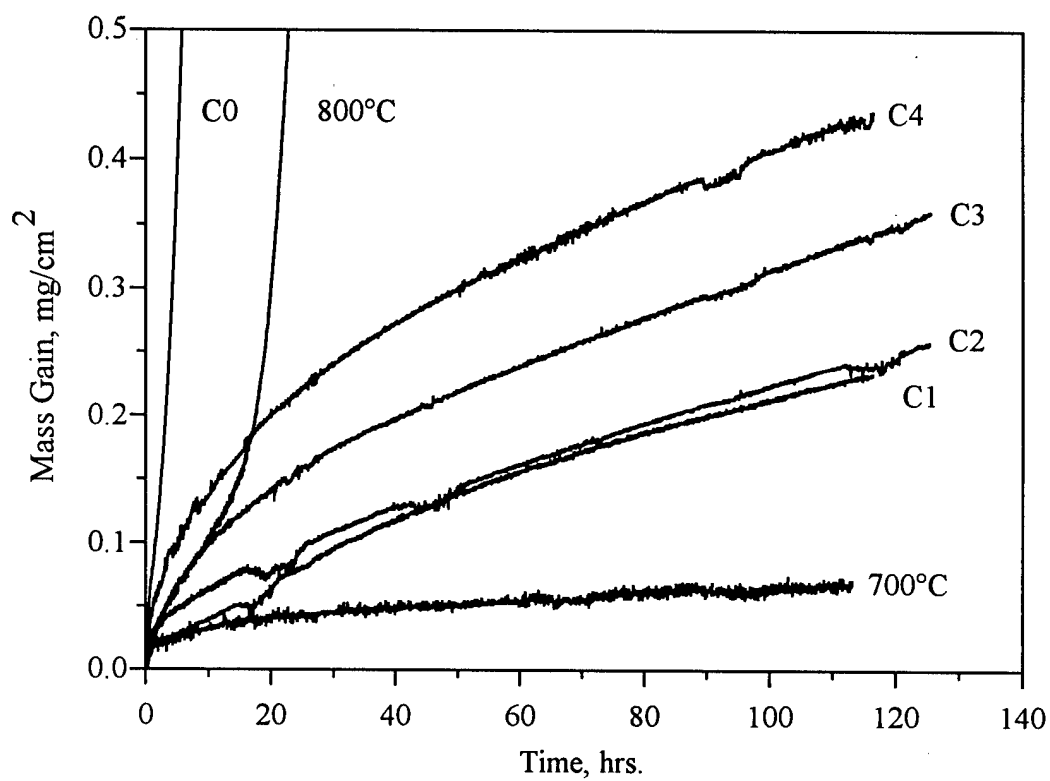


Figure 10: Isothermal oxidation of  $\text{Ti}_5\text{Si}_3\text{C}_x$  in zero air at  $1000^\circ\text{C}$  compared to  $\text{Ti}_5\text{Si}_3$  oxidized at  $700^\circ\text{C}$  and  $800^\circ\text{C}$ .



Ti<sub>5</sub>Si<sub>3</sub> shows a mass gain of about 14 mg/cm<sup>2</sup>. The mass gain for carbon doped samples varies from 0.2-0.4 mg/cm<sup>2</sup>, almost two orders of magnitude lower. The isothermal oxidation resistance of Ti<sub>5</sub>Si<sub>3</sub>C<sub>x</sub> compositions at 1000°C is increased by nearly 300°C, similar to that of undoped Ti<sub>5</sub>Si<sub>3</sub> at 700°C. Carbon doped samples show parabolic oxidation kinetics after an initial transient period of about 30 hours. These parabolic constants are given in Table VI. Parabolic rate constants for alloys C1 and C2 are similar to that of Mo<sub>5</sub>Si<sub>3</sub>B.

Table VI: Parabolic Rate Constants for Ti<sub>5</sub>Si<sub>3</sub>C<sub>x</sub> at 1000°C

Alloy	k <sub>p</sub> (mg <sup>2</sup> /cm <sup>4</sup> /hr)
C1	5.2 x 10 <sup>-4</sup>
C2	5.9 x 10 <sup>-4</sup>
C3	9.8 x 10 <sup>-4</sup>
C4	1.51 x 10 <sup>-3</sup>

X-ray diffraction of the scale surface indicated presence of TiO<sub>2</sub> (rutile). ESCA of the surface indicated the presence of both TiO<sub>2</sub> and SiO<sub>2</sub>. For alloy C1, TiO<sub>2</sub> and SiO<sub>2</sub> are present in nearly equal amounts during the first two minutes of ion milling, about 30 Å into the scale. At the scale surface of alloy C3, the ratio of TiO<sub>2</sub> to SiO<sub>2</sub> is much higher. In both compositions, TiO<sub>2</sub> is the predominant phase in the scale at depths greater than 30 Å. The analysis of carbon in the scale is inconclusive since it is difficult to distinguish between initial surface contamination (adventitious carbon) and that due to the sample composition.

BSE examination indicates the external scale to be between 2-4 μm thick. The scale is of a duplex nature as shown in Figure 11. In the BSE micrograph the bright phase

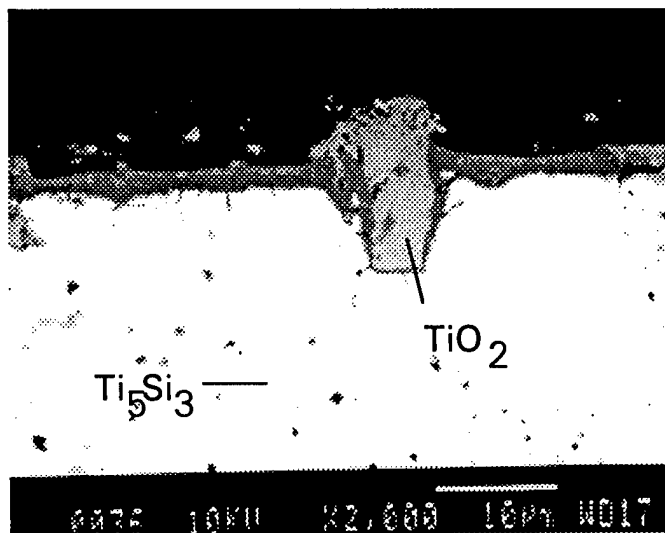


Figure 11: BSE image of  $\text{Ti}_5\text{Si}_3\text{C}_{0.75}$  oxidized at  $1000^\circ\text{C}$  in synthetic air for 120 hours.

is the base material alloy ( $\text{Ti}_5\text{Si}_3$ ), the dark inner scale is  $\text{SiO}_2$ , and the gray outer scale is  $\text{TiO}_2$ . The scale was analyzed by EMPA. Quantitative analysis could not be made due to the thinness of the scales. Qualitative analysis shows high titanium and low silicon concentration in the gray outer scale. High silicon and low titanium concentration is detected in the darker underlying scale.

The increased oxidation resistance of  $\text{Ti}_5\text{Si}_3\text{C}_x$  may be related to the formation of an underlying continuous  $\text{SiO}_2$  layer. This continuous layer does not form in undoped specimens. The formation of this  $\text{SiO}_2$  layer is likely promoted by the increased silicon activity or decreased titanium activity at the scale/alloy interface due to the interstitial carbon. The actual mechanism is the topic of further investigation.

## V. Summary

Refractory and transition metal intermetallic silicides have been demonstrated to be potential high temperature structural materials. Both  $\text{Ti}_5\text{Si}_3$  and  $\text{Mo}_5\text{Si}_3$  possess attractive properties, but both materials cannot be used as pure single phase materials due to inherent limitations. The addition of interstitial atoms to these materials dramatically improves their oxidation resistance. It is anticipated that these interstitial additions may also have similar beneficial effects on the mechanical properties.

## Acknowledgements

Ames Laboratory is operated for the U. S. Department of Energy by Iowa State University under contract number W-7405-ENG-82. This research was supported by the Office of Basic Energy Science, Materials Science Division.

The authors wish to thank Jim Anderegg for ESCA measurements.

### References

1. G. R. Loble, "Development of Aeroengine and Airframe Materials for Civil Airlines to Beyond the Year 2000," Civil Aviation, 12 (1993), 29-33.
2. D. L. Anton, D. M. Shah, D. N. Duhl, and A. F. Giamei, "Selecting High-Temperature Structural Intermetallic Compounds: The Engineering Approach," J. Metals, Sept. (1989), 12-17.
3. A. I. Taub and R. L. Fleischer, "Intermetallic Compounds for High-Temperature Structural Use," Science, 243 (1989), 616-621.
4. P. J. Meschter and D. S. Schwartz, "Silicide-Matrix Materials for High-Temperature Applications," J. Metals, Nov. (1989), 52-55.
5. D. M. Shah, D. Berczik, D. L. Anton, and R. Hecht, "Appraisal of other Silicides as Structural Materials," Mat. Sci. Eng., A155 (1992), 45-57.
6. K. S. Kumar and C. T. Liu, "Ordered Intermetallic Alloys, Part II: Silicides, Trialuminides, and Others," J. Metals, June (1993), 28-34.
7. H. J. Frost and M. F. Ashby, Deformation-Mechanism Maps: the Plasticity and Creep of Metals and Ceramics, (Oxford: Pergamon Press, 1982).
8. D.L. Anton and D.M. Shah, "High Temperature Properties of Refractory Intermetallics," Mat. Res. Soc. Symp. Proc., vol. 213, ed. Johnson, Pope, and Steigler (Pittsburgh, PA: Materials Research Society, 1991), 733-738.
9. J.J. Petrovich, "MoSi<sub>2</sub> based High-Temperature Structural Silicides," MRS Bulletin, July (1993), 35-40.
10. Thaddeus B. Massalski et al., eds., Binary Alloy Phase Diagrams, vol. 3 (Materials Park, OH: American Society for Metals, 1990), 2666, 3370.
11. H. Nowotny, "Alloy Chemistry of Transition Element Borides, Carbides, Nitrides, Aluminides, and Silicides," Electronic Structure and Alloy Chemistry of the Transition Elements, ed. P. Beck (New York, NY: John Wiley & Sons, 1963), 179-220.

12. H. Nowotny, E. Parthe, R. Kieffer, and F. Benesovsky, "Das Dreistoffsystem: Molybdan-Silizium-Kohlenstoff," Mh. Chem., 85 (1954), 255-272.
13. H. Nowotny, B. Lux, and H. Kudielka, "Das Verhalten metallreicher, hochschmelzender Silizide gegenüber Bor, Kohlenstoff, Stickstoff und Sauerstoff," Mh. Chem., 87 (1956), 447-470.
14. E. Garcia and J. D. Corbett, "Chemistry of Polar Intermetallic Compounds. Study of Two  $Zr_5Sb_3$  Phases, Hosts for a Diverse Interstitial Chemistry," Inorganic Chem., 27 (1988), 2353-2359.
15. Y. Kwon, M. A. Rzeznik, A. Guloy, and J. D. Corbett, "Impurity Stabilization of Phases with the  $Mn_5Si_3$ -Type Structure. Questions Regarding  $La_5Sn_3$  and  $Zr_5Si_3$ ," Chem. Mater., 2 (1990), 546-550.
16. E. Garcia and J. D. Corbett, "Chemistry in the Polar Intermetallic Host  $Zr_5Sb_3$ . Fifteen Interstitial Compounds," Inorganic Chem., 29 (1990), 3274-3282.
17. Y. Kwon and J. D. Corbett, "Chemistry in Polar Intermetallic Compounds. The Interstitial Chemistry of  $Zr_5Sn_3$ ," Chem. Mater., 4 (1992), 1348-1355.
18. L. Brewer., A.W. Searcy, D. H. Templeton, and C.H. Dauben, "High Melting Silicides," J. Amer. Ceram. Soc., 33 (1950), 291.
19. B. Aronsson, "The Crystal Structure of  $Mo_5Si_3$  and  $W_5Si_3$ ," Acta Chem. Scand., 9 (1955), 1107-1110.
20. N. Christensen, "Preparation and Characterization of  $Mo_3Si$  and  $Mo_5Si_3$ ," Acta Chem. Scand. A, 37 (1983), 519-522.
21. E. Parthe', W. Jeitschko, and V. Sadagopan, "A Neutron Diffraction Study of the Nowotny Phase  $Mo_{5-1}Si_3C_{1-x}$ ," Acta Cryst., 19 (1965), 1031-1037.
22. P. Pietrokosky and P. Duwez, "Crystal Structure of  $Ti_5Si_3$ ,  $Ti_5Ge_3$ , and  $Ti_5Sn_3$ ," Trans. AIME, 191 (1951), 772-773.
23. J. Quakernaat and J. W. Visser, "Lattice Dimensions of Low-Rate Metalloid-Stabilized  $Ti_5Si_3$ ," High Temp.-High Press., 6 (1974), 515-517.

24. Y. Kim, A. J. Thom, and M. Akinc, "Processing and Properties of  $Ti_5Si_3$ ," Processing and Fabrication of Advanced Materials for High Temperature Applications-II, ed. T.S. Srivatsan and V.A. Ravi (Warrendale, PA: The Min., Met., and Mater. Soc., 1993), 189-208.
25. C. T. Liu, E. H. Lee, and T. J. Henson, "Initial Development of High Temperature Titanium Silicide Alloys" (Report ORNL-6435; Order No. DE88007860, 1988).
26. G. Frommeyer, R. Rosenkranz, and C. Ludecke, "Microstructure and Properties of the Refractory Intermetallic  $Ti_5Si_3$  Compound and the Unidirectionally Solidified Eutectic Ti- $Ti_5Si_3$  Alloy," Z. Metallkde., 81 (1990), 307-313.
27. R. M. Paine, A. J. Stonehouse, and W. W. Beaver, WADC Tech. Rep. 59-29-Part I, January 1960 (United States Air Force, Wright-Patterson Air Force Base, OH)
28. D. M. Shah, private communication with author, Pratt and Whitney, 15 September 1992.
29. C.D. Wirkus and D.R. Wilder, "High-Temperature Oxidation of Molybdenum Disilicide," J. Am. Ceram. Soc., 49 (4) (1966), 173-177.
30. R.E. Regan, W.A. Baginski, and C.A. Krier, "Oxidation Studies of Complex Silicides for Protective Coatings," Ceramic Bulletin, 46 (5) (1967), 502-509.
31. E. Fitzner, "Oxidation of Molybdenum Disilicide," Ceramic Transactions, vol. 10, ed. R.B. Tressler and M. McNallan (Westerville, OH: American Ceramic Society, 1989), 19-41.
32. C.G. McKamey, P.F. Tortorelli, J.H. DeVan, and C.A. Carmichael, "A Study of Pest Oxidation in Polycrystalline  $MoSi_2$ ," J. Mater. Res., 7 (10) (1992), 2747-2755.
33. P.J. Meschter, "Low-Temperature Oxidation of Molybdenum Disilicide," Metallurgical Trans. A, 23A (1992), 1763-1772 .
34. T.C. Chou and T.G. Nieh, "Mechanism of  $MoSi_2$  Pest During Low Temperature Oxidation," J. Mater. Res., 1 (8) (1993), 214-227.
35. R.W. Bartlett, J.W. McCamont, and P.R. Gage, "Structure and Chemistry of Oxide Films Thermally Grown on Molybdenum Silicides," J. Am. Ceram. Soc., 48 (11) (1965), 551-558.

36. G.R. Anstis, P. Chantikul, B.R. Lawn, and D.B. Marshall, "A Critical Evaluation of Indentation Techniques for Measuring Fracture Toughness: I, Direct Crack Measurements and II. Strength Method," J. Am. Ceram. Soc., 64 (9) (1981), 533-543.
37. G.D. Quinn and R. Morrell, "Design Data for Engineering Ceramics: A Review of the Flexure Test," J. Am. Ceram. Soc., 74 (9) (1991), 2037-2066.
38. W. Wakelkamp, "Diffusion and Phase Relations in the Systems Ti-Si-C and Ti-Si-N" (Ph.D. Dissertation, Technical University at Eindhoven, 1991), 83.
39. S. Sambasivan and W. T. Petuskey, "Phase Chemistry in the Ti-Si-N System: Thermochemical Review with Phase Stability Diagrams", accepted for publication, J. Mater. Res.
40. S. K. Choi, J. Goldstein, F. J. J. van Loo, and R. Metselaar, "Solid State Reactions and Phase Relations in the Ti-Si-O System at 1373K" from W. Wakelkamp, "Diffusion and Phase Relations in the Systems Ti-Si-C and Ti-Si-N" (Ph.D. Dissertation, Technical University at Eindhoven, 1991), 81.
41. G. V. Samsonov et al., "Relations between the Electron Work Function and Certain Physical Properties in Silicides of Group IV Transition Metals", Izvestiya Akademii Nauk SSSR, Neorganicheskie Materialy, 12 (5) (1976), 850.
42. A. G. Evans, "Microfracture from Thermal Expansion Anisotropy-I. Single Phase Systems", Acta Metallurgica, 26 (1978), 1845-1853.
43. A. J. Thom, M. Akinc, O. B. Cavin, and C. R. Hubbard, "Thermal Expansion Anisotropy of  $Ti_5Si_3$ ", accepted for publication, J. Mat. Sci. Letters.
44. T. Y. Kosolapova, Handbook of High Temperature Compounds: Properties, Production, Application (New York, NY: Hemisphere Publishing, 1990), 392.
45. S.A. Maloy, J.J. Lewandowski, and A.H. Heuer, "Effects of Carbon Additions on the High Temperature Mechanical Properties of Molybdenum Disilicide," Mat. Sci. Eng., A155 (1992), 159-163.
46. R.K. Wade and J.J. Petrovich, "Processing Temperature Effects on Molybdenum Silicide," J. Am. Ceram. Soc., 75 (11) (1992), 3160-3162.

47. S.R. Srinivasan and R.B. Schwartz, "Elastic Moduli of MoSi<sub>2</sub> Based Materials," J. Mater. Res., 7 (7) (1992), 1610-1612.
48. M.S. Chandrasekharaiah, "Volatilities of Refractory Inorganic Compounds," The Characterization of High Temperature Vapors, ed. J.L. Margrave (New York, NY: John Wiley, 1967).
49. S. Prochaska, U.S. Patent 4,004,934 (1977), 4,041,117 (1977), 4,081,284 (1978).
50. P. Elder and V.D. Krstic, "Effect of Surface Area on Densification of  $\beta$ -SiC Powders in the Presence of Boron and Carbon," Br. Ceram. Trans. J., 91 (3) (1992), 67-71.
51. R. Hamminger, G. Grathwohl and F. Thummler, "Microanalytical Investigation of Sintered SiC," J. Mater. Sci., 18 (1983), 3154-3160.
52. A. Mueller, G. Wang, R.A. Rapp, E.L. Courtright and T.A. Kircher, "Oxidation Behavior of Tungsten and Germanium-Alloyed Molybdenum Disilicide Coatings," Mat. Sci. Eng., A155 (1992), 199-207.
53. A.J. Thom, Y. Kim, and M. Akinc, "Effect of Processing on Oxidation of Ti<sub>5</sub>Si<sub>3</sub>," Mat. Res. Soc. Symp. Proc., vol. 288, ed. by Baker, Darolia, Whittenberger, and Yoo (Pittsburgh, PA: Materials Research Society, 1993), 1037-1042.
54. P. Kofstad, High Temperature Oxidation of Metals (New York, NY: John Wiley, 1966).
55. A. I. Kahueci and G. Welsch, "Oxidation of Titanium Alloys," Environmental Degredation of Engineering Materials III, ed. M. R. Louthan (University Park, PA: Pennsylvania State University, 1987), 47-53.
56. W. W. Smeltzer, R. R. Haering, and J. S. Kirkaldy, "Oxidation of Metals by Short Circuit and Lattice Diffusion of Oxygen," Acta Metallurgica, 9 (1961), 880-885.
57. P. Kofstad, J. Less-Common Metals, "Note on the Defect Structure of Rutile (TiO<sub>2</sub>)," 13 (1967), 635-638.